Geology and Geochemistry of the Terrace Bay Batholith, N. Ontario

Kira Arnold

Submitted in partial fulfilment of the requirements for the degree of

Master of Science in Geology

Abstract

The Terrace Bay Batholith is a 25 km long oval shaped granitoid intrusion located in the western portion of the Schreiber-Hemlo greenstone belt, part of the larger Wawa-Abitibi terrane. The pluton was emplaced at 2689±1.1 Ma and intrudes *circa* 2720 Ma metavolcanic rocks of the Schreiber assemblage. The purpose of this study was to classify the Terrace Bay Batholith petrographically and geochemically in order to investigate the petrogenesis and tectonic setting in which the pluton formed, and to characterize the association with gold and base metal mineralization.

Detailed mapping of the pluton can separate the pluton into three mineralogically distinct lithologies: granodiorite (typically consisting of medium to coarse quartz and feldspar phenocrysts with a groundmass of fine-grained amphibole, biotite, disseminated magnetite, and sulphide minerals), a monzogranite (composed of medium-grained quartz and feldspar with increased amounts of potassium feldspar and amphibole relative to the granodiorite), and a diorite (composed of medium-grained amphibole and plagioclase with little to no quartz or potassium feldspar present). Two types of hydrothermal alteration are present in the pluton: a chlorite-epidote and a pervasive hematite alteration. These are present across the pluton, and always in proximity to cross-cutting regional scale faults or shears; however, no association was found between gold mineralization and regional structures.

Whole-rock geochemical analyses were undertaken on 147 samples from the Terrace Bay Batholith. Geochemically, the pluton is a homogenous calc-alkaline pluton, with minimal geochemical change between lithologies. The pluton exhibits trace element signatures that are characteristically arc-related signatures: fractionated heavy rare earth elements, negative high field strength element anomalies, enrichment of Th over light rare earth elements and enrichment of light rare earth elements. The fractionated heavy rare earth elements and the Th-Nb-La systematics are consistent with formation in a subduction zone at depths where garnet is stable. The Sr/Y and La/Yb signatures support formation within the garnet stability field and suggest small amount of slab-derived melt incorporated into the mantle wedge. The isotopic signature suggests that the pluton underwent minimal crustal contamination as shown by the depleted primitive mantle $\boldsymbol{\varepsilon}_{Nd}$ values ranging from +2.16 to +2.49.

The emplacement of the pluton was determined to be through multiple injections in the intrusion from a single source. The pluton underwent prolonged fractional crystallization, creating subtle mineralogical lithologies with no geochemical differences. The homogeneous nature of the pluton suggests it is unlikely that there were numerous pulses because these would result in more variation across the pluton.

Rhenium-Osmium isotope data were obtained on molybdenite to obtain an age of mineralization for the pluton, yielding a value of 2671±12 Ma. The molybdenum mineralization is spatially associated with gold mineralization in the pluton, suggesting that they were deposited from the same hydrothermal event. As is common in Archean cratons, this age of mineralization is syn- to post- both D_2 and regional metamorphism, as well as postdating the emplacement of the pluton. The gold and molybdenum mineralization in the pluton is generally disseminated throughout with local occurrences hosted in quartz veins. Although these exhibit elevated gold and molybdenum values there is no distinct mineralization style characterized with gold deposits. These features can be explained by the magmatic vapor-dispersed system theory which suggests that when a pluton is emplaced at depth, the aqueous phase will remain dispersed throughout the pluton instead of concentrating in economic amounts.

Acknowledgements

First, I would like to thank Dr. Pete Hollings for his guidance, insight and support throughout my Masters project. His patience when reviewing my work and discussing complex Archean tectonic theories was much appreciated. I would also like to thank Seamus Magnus for all of his guidance, support and patience in the field and during the writing of these thesis, without his guidance I might still be wandering around the cliffs of Terrace Bay. Another big thanks to my field assistants, Lucas Wolfe, Mallory Metcalf, Haley Aldred, Maddison Hodder, Gabrielle Klemt and Joshua Nguyen for their outstanding work and endurance through the rough terrain over the two field seasons. Additional thanks go to local prospector Wayne Richards and the Richards family for all the help and knowledge of the map area and treating us like family during our field seasons.

Thanks to Mark Smyk, Mark Puumala and Dorothy Campbell and the rest of the Residents Geologist Program of Thunder Bay Office for the discussion in the field and the continuous support and outstanding knowledge of the field area. Further thanks to the Geoscience Laboratories, Ontario Geological Survey in Sudbury for in-kind support for the analysis of rock samples.

Many thanks to Anne Hammond and Kristi Tavener for producing pristine thin sections for this project. In addition, I would like to thank Sherri Strong (Memorial University- Nd isotopes), Robert Creaser (University of Alberta Radiogenic Isotope Facility- Re-Os isotope) for their help in collecting, interpreting and understanding all isotope data.

Most of all I would like to thank my friends and family for their continuous support and encouragement throughout this project, it would not have been possible without you all.

Table of Contents

List of Figures

List of Tables

Chapter 1: Introduction

1.1 Objective

The purpose of this project was to study the Terrace Bay Batholith in the western end of the Schreiber-Hemlo greenstone belt in order to characterize and investigate the petrogenesis of the pluton and related gold and base metal mineralization. This study focused on describing the lithology and geochemistry of the Terrace Bay Batholith, as well as the mineralization and alteration throughout the pluton. A combination of petrography, mapping and geochemistry was used to describe the igneous textures and examine areas of alteration and mineralization.

1.2 Location

The Terrace Bay Batholith is located along the north shore of Lake Superior in the Wawa-Abitibi terrane. The study area is located in the western Schreiber-Hemlo greenstone belt, in the Priske, Strey and Syine townships (Fig. 1.1). The Terrace Bay batholith is approximately 25 km long and 8 km wide covering an area of 109 km^2 with the southern border under Lake Superior. Highway 17 cuts through the batholith with access also possible along the shore of Lake Superior, on ATV trails, power lines and train tracks.

1.3 Granitoids

Granitoids are the most abundant plutonic rocks in the upper continental crust (Frost et al., 2001). Granite *sensu lato* includes a wide range of rock types but are broadly phaneritic rocks that contain quartz, plagioclase and alkali feldspar (Le Maitre et al., 2005). Granitoid rocks generally have a medium to coarse grainsize,

which reflects the slow cooling process and the presence of volatiles (Le Maitre et al., 2005).

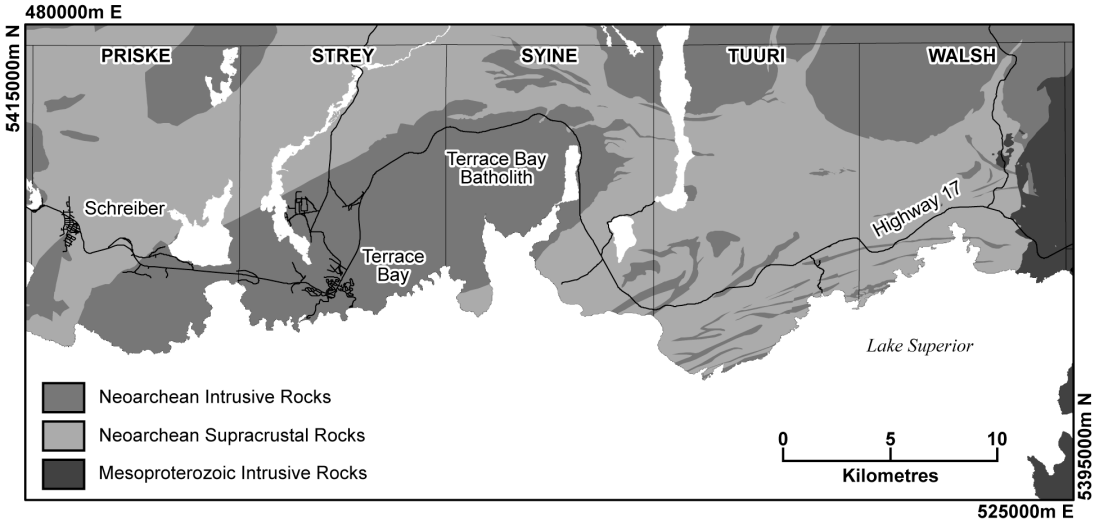

Figure 1.1. Location of the study area showing the Schreiber assemblage and townships boundaries. From Magnus and Arnold (2016).

Granitoid rocks generally have a medium- to coarse-grained size, which reflects the slow cooling process and the presence of volatiles (Le Maitre et al., 2005). Hydrous minerals such as hornblende and biotite are the dominant mafic phases. Other common textures are granophyric or graphic textures, showing the eutectic quartz-alkali feldspar-plagioclase exsolution (Frost et al., 2001; Beakhouse, 2007).

Many classification systems have been proposed for granites, all with some validity but also drawbacks due to the wide variety of granitoids (Frost et al., 2001). Classification schemes have used a variety of different features including mineralogy, geochemistry, isotopes, source regions, and genetic processes. The most favoured systems are the IUGS, and S-I-A-M classifications (LeMaitre et al., 1989).

Although no one system can best represent the variations in granites, each have specific advantages.

The IUGS classification system can be readily applied to most granitic rocks. Granites are classified based upon the mineralogical composition and amounts of quartz, plagioclase and alkali-feldspars (Streckeisen, 1974). The IUGS system further subdivides granites into granodiorite, granitoids and alkali-feldspar granites.

The S and I classification scheme for granites known as the alphabetic classification, was proposed by Chappell and White (1974). The scheme classifies granites based on geochemistry and distinctive compositional features that were inherited from the source. The classification scheme was initially based on granites studied in the Lachlan Fold Belt, Australia (Chappell and White, 1974). The classification was originally separated into two distinct types (I and S) but other types (M and A) have been added to explain variations in granites (Loiselle and Wones, 1979; White, 1979).

I-type granites are metaluminous to weakly peraluminous with silica contents from 56-77 wt.%. Chappell and White (1974) suggested that I-type granites were derived from a mafic, meta-igneous source. The I-type compositions are variable from tonalite, granodiorite, quartz diorite and quartz monzodiorite, with mineralogy of hornblende, biotite, magnetite, and sphene (Chappell and White, 2001). S-type granites are interpreted to have formed from melting of a metasedimentary source, resulting in strongly peraluminous, relatively potassic and higher silica compositions (64-77 wt.%; Chappell and White, 1974). They are

commonly leucogranites with biotite, cordierite, ilmenite muscovite, garnet, and monzonite. The S-type granites are mica rich, typically muscovite but biotite is common in mafic varieties, as the sedimentary source results in an increase in aluminum, sodium and calcium (Chappell and White, 2001).

Barbarin (1999) developed a classification scheme that used a combination of mineral assemblages, field and petrographic analysis, geochemical and isotopic signatures. It is a genetic classification because it separates and classifies granites into six specific types that each relate to a geodynamic environment and origin (Barbarin, 1999). The six classifications are; Muscovite-bearing Peraluminous Granitoids (MPG), Cordierite-bearing Peraluminous Granitoids (CPG), K-rich Calc-alkaline Granitoids (KCG), Amphibole-bearing Calc-alkaline Granitoids (ACG), Mid-ocean Ridge Tholeiitic Granitoids (RTG), Peralkaline and Alkaline Granitoids (PAG) (Barbarin, 1999). Although this classification scheme is specific and breaks down granitoids based upon many attributes it is not widely used due to the complexity of the scheme.

The tectonic classification scheme purposed by Pearce et al. (1984) uses trace element discrimination diagrams, to determine the tectonic environment such as; ocean ridge, volcanic arc, within plate boundary, and collisional. The discrimination diagrams used are Nb vs. Y, Ta vs. Y, Rb vs. (Y+Nb), and Rb vs. (Y+Ta) (Pearce et al., 1984).

A volumetrically significant Archean granitoid type are the TTG suite (tonalite, trondhjemite and granodiorite). Tonalite, trondhjemite and granodiorite are the dominant component of Archean terranes such as the Superior Province

(Beakhouse, 2007). Approximately 90% of the juvenile continental crust generated between 4.0 and 2.5 Ga belongs to the TTG suites (Martin et al., 1997, 2005). It has been suggested that TTG's formed from partial melting of subducted basaltic crust and the assimilation of crustal material, although it is suggested that there may be interaction between the partial slab melts and the mantle wedge (Martin et al., 1997, 2005; Frost et al., 2006; Beakhouse, 2007). Tonalite, trondhjemites and granodiorites are silica rich (>64 wt.% SiO_2) with a mineralogical composition of quartz, plagioclase and minor K-feldspar. The tonalite, trondhjemites and granodiorites are characterized by a restricted mineralogical range (tonalite to granodiorite), where biotite and hornblende are the dominant mafic components. Accessory minerals include titanite, epidote, apatite and zircons (Martin et al., 1997, 2005; Beakhouse, 2007). The suite is subdivided into two groups, low-Al TTG and high-Al TTG. Low-Al TTG characteristically have <15% Al_2O_3, low Sr but higher HFSE (including Zr and Nb) abundances (Martin et al., 1997, 2005; Beakhouse, 2007). Whereas high-Al TTG are characterized by elevated Al (>15% Al_2O_3), Sr and low Yb and Y contents (Martin et al., 2005; Beakhouse, 2007).

1.4 Mineralization in Granites

Granitic rocks can host a variety of mineralization styles due to the diversity and complexity of the deposits and the association of elements such as Sn, W, U, Th, Mo, Nb, Ta, Be, Li, Y, Zr, Be, As, Cu, Au, Pb, Zn, Ag, and REE (Cerny et al., 2005; Sial et al., 2011). Granite-hosted ore deposits include hydrothermal deposits (vein and greisen type), orogenic deposits, rare element pegmatites, intrusion related Au, skarn, uranium, porphyry-style mineralization, tin tungsten and rare metal granites.

The genetic relationship between granites and ore deposits is commonly highly variable, making it difficult to distinguish why certain deposits have economic concentrations and others not (Cerny et al., 2005).

Gold deposits formed in metamorphic environments are diverse in terms of age, geometry, structural controls, host rocks, metamorphic grade, temperature and pressures, wall rock alteration and metal associations (Groves et al., 2003; Dubé and Gosselin, 2007). Orogenic gold deposits typically develop in terranes that have undergone moderate- to high-T, low- to moderate-P metamorphism, and are commonly associated with the generation of large volumes of granitic melts and major crustal-scale fault zones. Lode gold deposits are thought to have formed during compressional to transpressional deformation events, in accretionary and collisional orogens, whereas the mineralization is commonly controlled by 2^{nd} to 3^{rd} order faults from the translithospheric structures (Groves et al., 2000, 2003; Goldfarb et al., 2005). Mineralization in orogenic deposits commonly formed during D_2- D_4 deformation events, normally 20 to 100 m.y after the deposition of volcanic and sedimentary host rocks (Groves et al., 2000, 2003). The metamorphic grade ranges from lower greenschist to amphibolite, but most commonly deposits are associated with greenschist grade metamorphism (Groves et al., 2000, 2003). Consistent geological characteristics of orogenic gold deposits are low sulfide volumes, low salinity, CO_2-rich ore fluids (Goldfarb et al., 2001). They are commonly found along convergent margins between major lithological boundaries (Dubé and Gosselin, 2007). Distal spatial relationships with intrusions are common with the possibility of a genetic connection between orogenic gold and granitoid intrusions

(Groves et al., 2003; Dubé and Gosselin, 2007). Commonly chemical and structural traps determine if gold will precipitate in an economic form. Chemical traps include banded iron formations, tholeiitic basalts, and black slate (Goldfarb et al., 2001; Groves et al., 2003; Dube and Gosselin, 2007). Structural traps that favour gold deposition include fold hinges, dilatational jogs along faults or shear zones and zones of competency contrast (Groves et al., 2003; Dube and Gosselin, 2007).

Vein-type hydrothermal mineralization commonly occurs in high-level, felsic and highly fractionated granites, that are typically silica rich, peraluminous to metaluminous, and less commonly alkaline (Cerny et al., 2005). Vein deposits, as described by Cerny et al. (2005), consist of single veins, lodes, sheeted or stockwork vein systems, that can be directly hosted in the granite or in the wall rock zone in the surrounding supracrustal rocks. Veins can range from subvertical to horizontal and range in thickness from millimeters to tens of centimeters. Veins are commonly filled with quartz and ore minerals with well developed alteration around the vein, that vary from silicic, through feldpathic to muscovite (Cerny et al., 2005). The deposits can host to economic amounts of Sn, W, Sn-W, W-Mo and Mo with a range of associated elements such as Cu, Pb, Zn, Ag (Cerny et al., 2005).

Intrusion related gold deposits have a wide range of features and vary based on the individual intrusion. The depth of formation can range from <1 km to >8km (Goldfarb at el., 2001, 2005). Hart et al. (2000) classified the deposits based on the spatial relationship to the intrusion, stating that intrusion hosted deposits have mostly sheeted and lesser stockwork veins with mineral assemblage of Au-Bi+/- Te, As, Mo, W. Deposits proximal to the intrusion, located within the host rock but still

in the metamorphic aureole of the intrusion commonly exhibit mineralization of W+/- Cu, Au and Cu-Bi-Au+/- W (Hart et al., 2000). In contrast, deposits distal to the intrusion beyond the limits of the aureole, commonly include auriferous, mesothermal to epithermal quartz sulphide veins along faults (Hart et al., 2000). Distal deposits typically host mineralization of Au-As-Sb+/- Hg. A similar style of deposit to the intrusion-related deposits are the reduced intrusion-related deposits (RIRG). Goldfarb et al. (2005) state that they differ from other intrusion-related deposits in that the granitoids have a reduced primary oxidation state, have a shallow to moderate crustal setting (2-8 km) and form late in the orogenic cycle. The intrusions are granodioritic to granitic, sub-alkaline and metaluminous to weakly peraluminous (Goldfarb et al., 2005). The ore assemblage typically contains gold with bismuth and/or tellurium-bearing phases and locally molybdenum and/or scheelite.

Chapter 2: Regional Geology

2.1 Archean Superior Province

The Superior Province is one of the Earth's largest Archean cratons at ~1,572,000 km^2, and is located in the center of North America (Fig. 2.1). The Superior Province is composed of long broad belt-like subprovinces that preserve a record of the late Archean Kenoran Orogeny (Goodwin, 1991; Stott, 1997). The Superior Province is bounded by Paleoproterozoic orogenies: the Churchill Province to the east, north and west, the Southern Province to the south and the Mesoproterzoic Grenville Province to the southeast. The boundaries are dominantly tectonic zones and unconformities (Percival, 2007).

The Superior Province is composed of granite-greenstone terranes separated by metasedimentary belts, plutons and high-grade gneiss terranes (Card, 1990). The was subdivided into subprovinces, using differences in lithological variations, metamorphic grade, structural features, isotopic age of rock units, metallogenic characteristics as well as geophysical attributes (Card and Ciesielski, 1986). The subdivision boundaries are typically zones of structural or metamorphic transition but are often difficult to distinguish (Card and Ciesielski, 1986). Volcano-plutonic subprovinces such as the Wawa-Abitibi, Wabigoon and Uchi are dominantly comprised of metavolcanic and metasedimentary supracrustal sequences intruded by syn- to post-orogenic granitic plutons (Fig. 2.1; Stott, 1997). The metamorphism in the subprovinces generally ranges from sub-greenschist to greenschist and increases outwards to amphibolite facies in the presence of plutons (Card and Ciesielski, 1986).

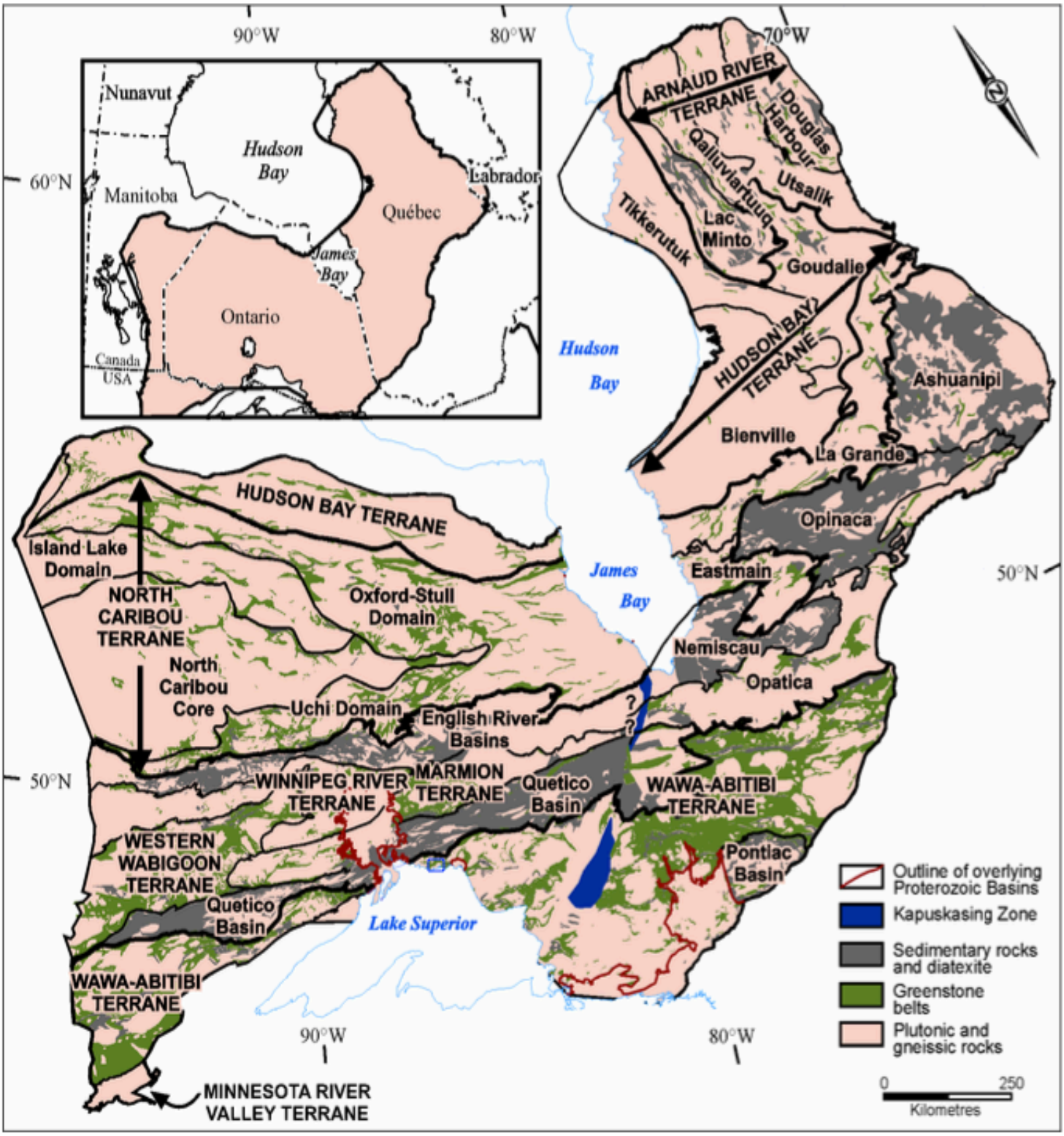

Figure 2.1. Map of the Superior Province, with updated terranes and domains (from Stott, 2010).

The metasedimentary subprovinces such as the Quetico, Pontiac and English River (Fig. 2.1) consist mainly of supracrustal sedimentary rocks including turbiditic greywacke and pelites that have under gone low-grade greenschist to lower amphibolite metamorphism and been intruded by S-type granites (Thurston et al., 1991). The plutonic subprovinces such as the Winnipeg River (Fig. 2.1) are distinguished by a lack of supracrustal rocks but massive felsic plutonic rocks instead. The plutonic rocks include tonalitic gneiss and more massive felsic plutons ranging between sodic to potassic in composition (Card and Ciesielski, 1986). Lastly, the high-grade gneiss subprovinces such as the Kapususkasing Structural Zone and Pikwitonei (Fig. 2.1) are characterized by plutonic and supracrustal rocks that have undergone intermediate to high pressure upper amphibolite to granulite facies metamorphism, displaying domal structural features that suggest multiple phases of deformation (Card and Ciesielski, 1986; Stott, 1991).

Stott et al. (2010) redefined the subdivisions of the Superior Province by using a classification based on more recent data including: regional mapping, geophysical surveys, geochronology, geochemical analysis and isotopes. Using this classification a superterrane is an amalgamation of two or more terranes before the Neoarchean assembly of the Superior Province. Terranes previously known as subprovinces, are tectonically bounded regions, with internal characteristics that are distinct from bordering regions formed prior to the Neoarchean assembly of the Superior Province (Stott et al., 2010). Terranes can be further subdivided into

domains; i.e. younger parts of a terrane, sharing a common basement or containing juvenile crust (Stott et al., 2010).

The Kenoran Orogeny is thought to represent an amalgamation of continental fragments from 2710-2660 Ma (Stott, 1997), representing a 40 million year long period of tectonism leading to the assembly of the Superior Province (Percival, 2007). Five Neoarchean events have been distinguished as separate phases of the Kenoran Orogeny; the Northern Superior, Uchian, Central Superior, Shebandowanian, and Minnesotan (Percival, 2007). The Northern Superior orogeny occurred ~2.72-2.71 Ga, when the Northern Superior and North Caribou superterranes collided, trapping the Oxford-Skull domain (Percival, 2007). The Uchian orogeny (~2.72-2.70 Ga) was preceded by arc magmatism in the North Caribou superterrane, before the subduction and collision of the Winnipeg River terrane into the North Caribou superterrane (Percival, 2007). The suture zone between the Winnipeg River terrane and North Caribou superterrane is covered by the sedimentary rocks of the English River Basin, which were deposited after 2.7 Ga (Percival, 2007). The Central Superior orogeny involved the amalgamation of the Wabigoon terrane to the composite Superior superterrane and the beginning of the subduction of the Wawa-Abitibi terrane (Percival, 2007). The Shebandowanian orogeny (~2.69 Ga) led to the juxtaposition of the Wawa-Abitibi terrane into the Superior Province (Percival, 2007). Lastly the Minnesotan orogeny (~2.68 Ga) to the collision between the Minnesota River Valley terrane and the Superior Province forming the Pontiac Basin (Percival, 2007; Stott et al., 2010).

2.2 Wawa Terrane

The Wawa Terrane is a ~2.7 Ga aggregation of Archean greenstone belts and granitoid plutons, located in the Superior Province along the north shore of Lake Superior (Fig. 2.2; Williams et al., 1991; Polat and Kerrich, 2000). The eastern extent of the Wawa Terrane is the Kapuskasing Tectonic zone where it transitions into the Chapleau block of the Abitibi Terrane (Percival, 2007). The northern boundary of the terrane overlies the metasedimentary rocks of the Quetico subprovince, whereas to the south the Wawa terrane is cut by the Montreal River fault and is unconformable with the Proterozoic supracrustal rocks of the Animikee Basin in the west (Williams et al., 1991).

The Wawa terrane is composed of six greenstone belts; the Gamitagama, Mishibishu, Michipicoten, Dayohessarah-Kabinakagami, Schreiber-Hemlo, and Shebandowan belts. Separated by the Pukaskwa and the Black Pic batholiths (Fig. 2.2). Polat et al. (1998) showed that the Schreiber-Hemlo assemblages have similar geochemistry to the White River-Dayohessarah greenstone belts indicating that the latter is possibly a continuation of the Schreiber-Hemlo greenstone belt. Williams (1991) showed that the metamorphic grade across the Wawa terrane is heterogeneous with grades up to amphibolite facies in areas proximal to granitoid intrusions compared to the greenschist facies in the supracrustal rocks. The greenstone belts of the Wawa subprovince are typically composed of metamorphosed komatiite, basalt, dacite and rhyolite (Williams et al., 1991). The volcanic rocks in the Wawa greenstone belts can be separated into two main stages: 2.75-2.70 Ga intra-oceanic tholeiitic basalt-komatiite sequences and 2.72-2.69 Ga

bimodal tholeiitic to calc-alkaline arc sequences consisting of basalts, andesites and rhyolites (Polat and Kerrich, 2000).

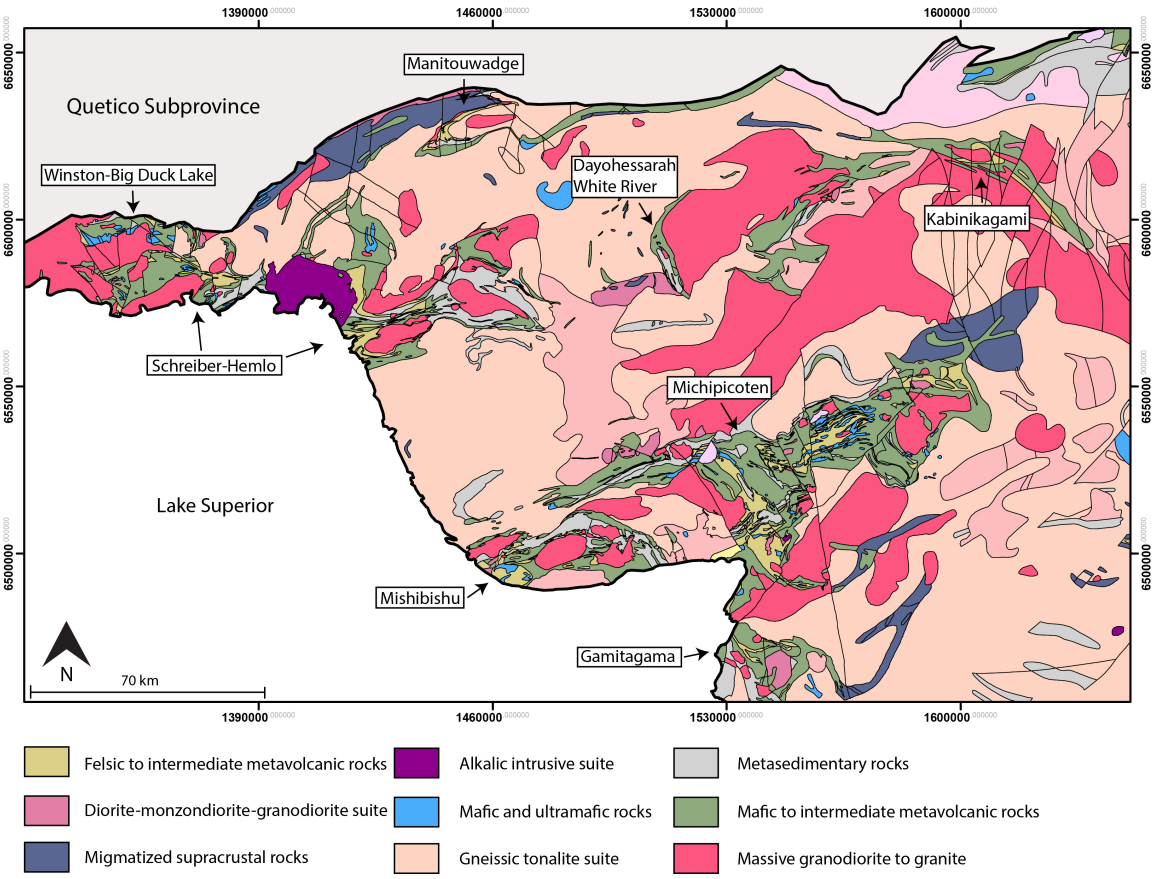

Figure 2.2. The eastern Wawa Terrane with the associated greenstone belts. (Modified from Stott et al., 2010).

Primary igneous textures and pillows are well preserved outside of major shear zones and intrusions (Polat and Kerrich, 2000). The associated metasedimentary rocks include turbiditic wacke, minor conglomerate and iron formation (Williams et al., 1991). The Wawa terrane is thought to represent an Archean intra-oceanic convergent plate margin (Kerrich and Xie, 2002).

The 2.72 Ga Greenwater and Manitouwadge assemblages are consistent with an oceanic setting and formed as part of an arc-back-arc system (Percival, 2007). There are significant massive sulphides deposits in the Shebandowan, Winston Lake and Manitouwadge greenstone belts, consistent with an oceanic setting (Percival, 2007). The greenstone belts are interpreted to represent collages of oceanic plateaus, oceanic islands arc, and trench turbidites that were all assembled in a subduction-accretion complex (Polat and Kerrich, 2000). Following juxtaposition, the lithologies were intruded by syn-kinematic TTG (tonalite, trondhjemite and granodiorite) plutons and ultramafic to felsic dykes and sills (Polat and Kerrich, 2000).

2.3 Schreiber-Hemlo Belt

The Schreiber-Hemlo greenstone belt trends west from the town of Schreiber to White River in the east. The belt is subparallel with the contacts of the Black-Pic batholith, and is separated into two sections by the Coldwell alkali complex (Fig. 2.3). There are three assemblages present in the Schreiber-Hemlo greenstone belt; the Hemlo-Black River, Heron Bay and the Schreiber assemblages (Williams et al., 1991; Polat et al, 1998). The Hemlo-Black River and Heron Bay assemblages are found to the east of the Coldwell complex.

The two assemblages are separated by the Lake Superior-Hemlo fault zone; the older Hemlo-Black River (2.77 Ga) to the north of the fault and the younger Heron Bay (2.70 Ga) to the south (Williams et al., 1991; Polat et al., 1998). The supracrustal rocks within the Hemlo side of the belt mainly consist of tholeiitic basalts overlain by calc-alkaline volcanic rocks, intercalated with and overlain by

sedimentary rocks particularly in the eastern half of the belt. The greenstone belt was intruded by multiple granitic intrusions that range from syn-volcanic to post-orogenic (Muir, 2002; Beakhouse and Davis, 2005). The Schreiber assemblage is located to the west of the Coldwell complex and has been considered to be temporally equivalent to the Hemlo-Black River assemblage (Williams et al., 1991; Beakhouse and Davis, 2005).

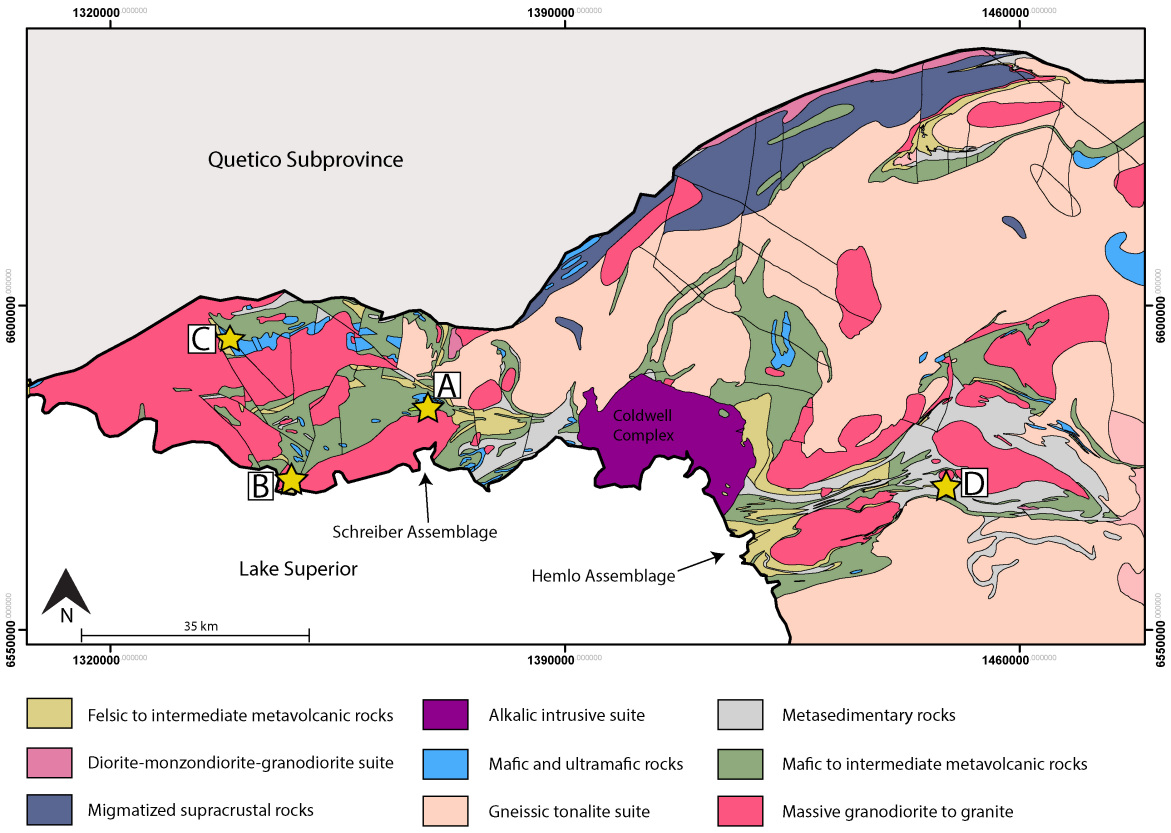

Figure 2.3. The Schreiber-Hemlo greenstone belt and the surrounding plutons, as well as the alkaline Coldwell Complex. The active and past producing mines in the region, A. The Empress mine, B. North Shores mine, C. Winston Lake Mine, D. Hemlo Mine (Modified from Stott, 2010).

Mineralization in the Schreiber-Hemlo area includes the past-producing volcanogenic massive sulphide (VMS) style zinc copper silver deposit at Winston

Lake, where sphalerite mineralization occurs at the contact between a layered gabbro and the altered felsic volcanic rocks primarily tuff and pyroclastic units (Fig. 2.4; Kerrich et al., 2008; Lodge, 2012). It is underlain by mafic to felsic volcanic flows and pyroclastic rocks and overlain by tholeiitic pillow basalts, the volcanic rocks are intruded by gabbroic sills (Kerrich et al., 2008). The deposit produced 3.1 million tonnes at a grade of 16% Zn, 1% Cu, 30.1 g/t Ag, 1.0 g/t Au (Lodge, 2012). The Hemlo gold mine is the only producing mine in the region. It is described as a lode gold deposit located in the Hemlo assemblage of the Schreiber-Hemlo greenstone belt (Fig 2.4; Muir, 2002). The Hemlo mine has averaged gold grade of 5.04 g/t Au at 93 million tonnes of ore with reserves and resources of 24 million tonnes at 2.21 g/t Au and 41 million tonnes at 1.41 g/t Au (Puumala et al., 2018). The Hemlo mine is hosted in felsic to intermediate volcanic to volcaniclastic rocks (Muir, 2002). Gold mineralization in common in the Schreiber and Terrace Bay area, as many historical gold mines operated between 1896 to 1941 with a total of production in the Schreiber region of 3100 ounces Au (Magnus and Walker, 2015; Puumala et al., 2016). Multiple abandoned artisanal gold mines including the Empress, North Shores, Hays Lake, and Gold Range mines are located within a kilometer of the contact with the Terrace Bay Batholith (Williams et al., 1991). The Empress mine (Fig. 2.4) operated from 1895 to 1900 producing 112 ounces of gold from 1100 tonnes of ore (Puumala et al., 2016). The North Shores mine (Fig. 2.4) yielded 2441 ounces at an average grade of 0.64 ounces per ton gold (Puumala et al., 2016).

2.3.1 Schreiber Assemblage

The Schreiber assemblage comprises supracrustal rocks that extend from the Coldwell Complex westward to Schreiber and northwards to Big Duck Lake (Fig. 2.5). The Schreiber assemblage is comprised of circa 2720 Ma volcanic rocks, circa 2698 Ma and 2690 Ma siliciclastic sedimentary rocks, and intrusions with an age range of 2689 Ma to 2667 Ma (Kamo, 2016; Kamo and Hamilton, 2017; Davis and Sutcliffe, 2017). Polat et al. (1999) recognized three major rock types throughout the supracrustal assemblage: tholeiitic mafic volcanic rocks, calc-alkalic mafic to felsic volcanic rocks and sedimentary (turbidites) rocks. The tholeiitic volcanic rocks are typically pillowed, massive or foliated flows, tuffs and fragmental units and are intruded by pods and lenses of gabbro and peridotite (Polat et al., 1999). The felsic volcanic rocks are fragmental ranging from crystal to lapilli tuffs to breccias, with clast sizes ranging from coarse to fine (Williams et al., 1991; Magnus and Arnold, 2016). The sedimentary rocks are typically composed of sand dominated turbidites, interlayered slate and iron formation (Polat et al., 1999). Carter (1988) proposed that the contact between the calc-alkalic and the tholeiitic metavolcanic rocks is a sulphide-bearing graphitic shale that could represent a tectonic contact. Both volcanic and siliciclastic sedimentary sequences are intruded by syn-kinematic mafic to felsic dykes and sills (circa 2690-2680 Ma) and TTG (Polat et al., 1999). All of the mentioned lithologies have been cut by (circa 2680-2674 Ma) late lamprophyre dykes (Polat et al., 1999). The metamorphic grade of the area is upper greenschist facies but increases to amphibolite when in proximity to

plutonic intrusions (Williams et al., 1991; Polat et al., 1999). The complex structural history of the Schreiber assemblage includes isoclinal folding and the Jackfish-Middleton-McKellar Harbour shear zone (JMMHSZ), which cross-cuts the Schreiber assemblage (Williams, 1989).

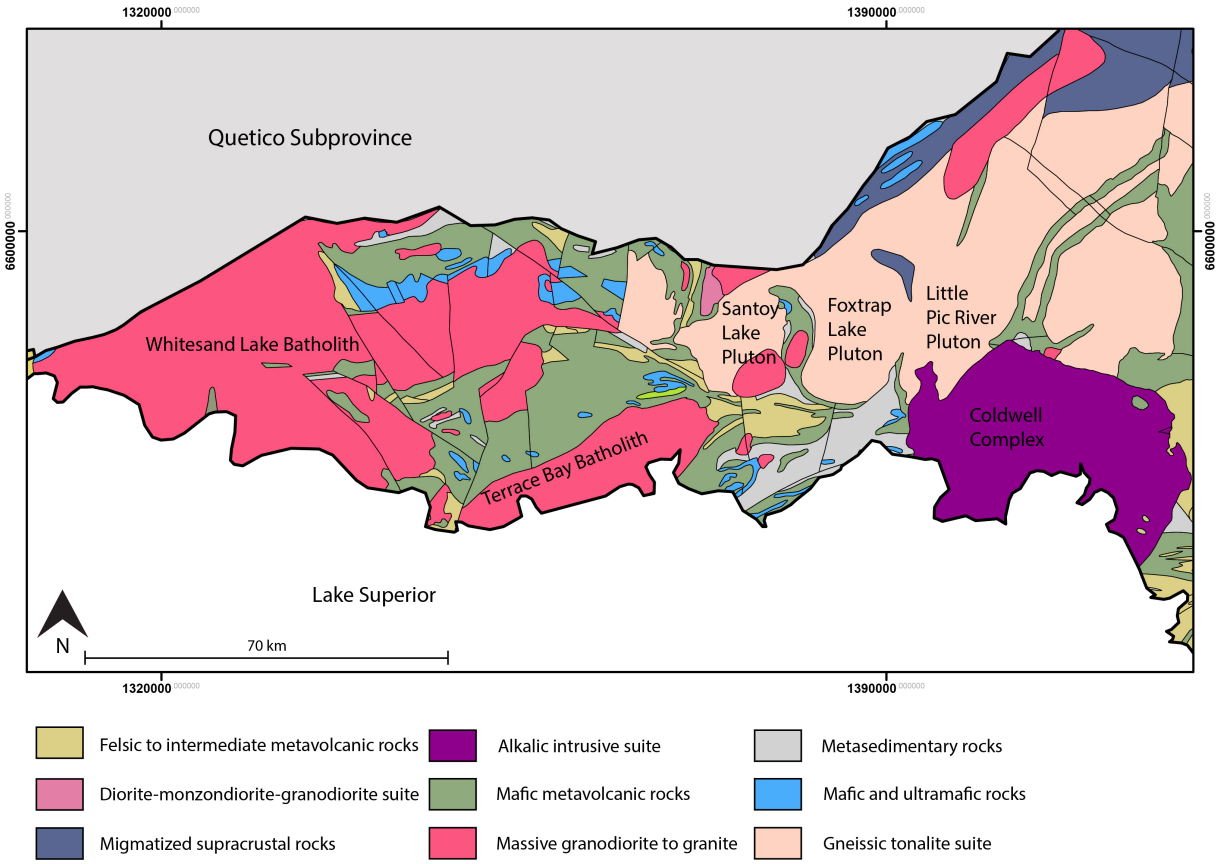

Figure. 2.4. The Schreiber assemblage and the associated plutons (Modified from Stott et al. 2010).

2.4 Previous Work

The earliest mapping done in the region was completed by Hopkins (1921) who mapped the Schreiber-Duck Lake area (Fig. 2.6). This was followed by Harcourt and Bartley (1938) who mapped the Schreiber area (Fig. 2.6). Walker (1967) published two maps of the Jackfish-Middleton area along with a report describing the geology and structures (Fig. 2.6). Carter (1979, 1980, 1981a, b, c, d) completed a

detailed mapping project (with the OGS), of the Schreiber-Terrace Bay area (Fig. 2.6). The Terrace Bay Batholith was partially mapping and examined by Marmont (1984), to determine geological relationships and genesis of the pluton in conjunction with Carter's mapping of the Schreiber-Terrace Bay area in the 1970's. The most recent work in the area was part of a four year mapping project by Ontario Geological Survey (OGS) in the Walsh, Tuuri, and Syine townships (Magnus and Walker, 2015; Magnus and Arnold, 2016; Magnus, 2017; Magnus and Hastie, 2018; Fig. 2.6). The pluton was also mentioned in OGS studies of the felsic intrusive of the Hemlo greenstone belt and Archean lode gold deposits (Beakhouse, 2001, 2007). There has been increasing interest in gold exploration within the pluton and surrounding supracrustal rocks in recent years (Sanatana Resources Inc, 2017; Puumala et al., 2016, 2018). Small scale stripping and drilling has been completed by prospectors and companies in the eastern end of the pluton.

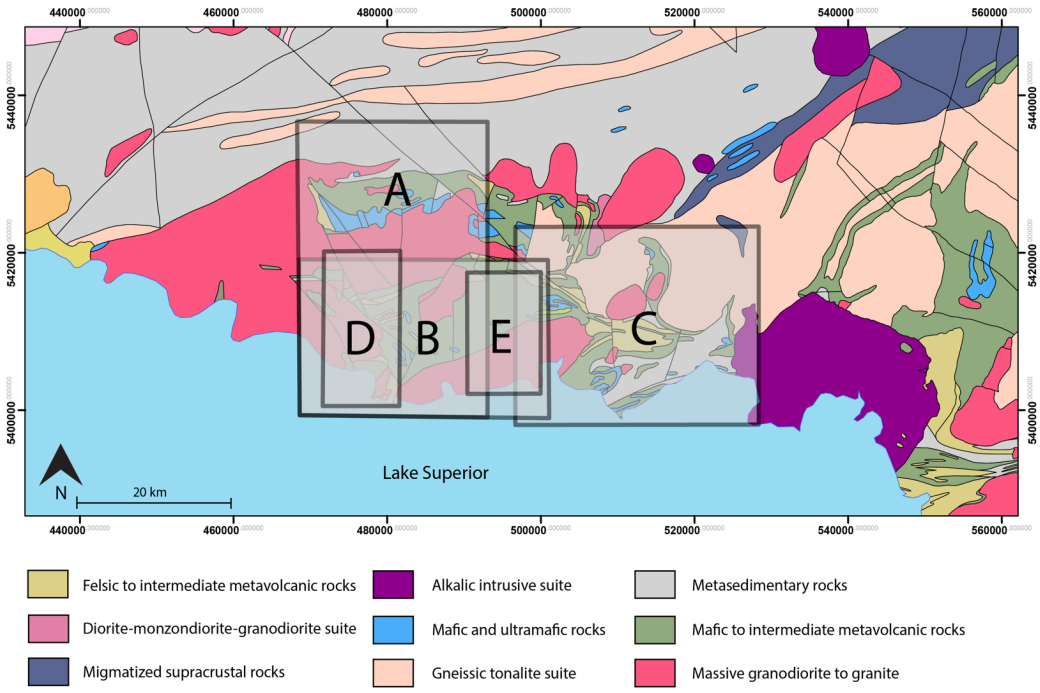

Figure 2.5. Previous mapping project in the Schreiber-Terrace Bay area. A. Hopkins (1921) B. Harcourt and Bartley (1938) C. Walker (1967) and Magnus et al. (2015, 2016, 2017) D. Carter (1979, 1980) E. Carter (1979, 1980) (Modified from Stott et al. 2010).

Chapter 3: Methodology

3.1 Regional and Trench Mapping

Regional mapping of the pluton took place during the summers of 2016 and 2017. The mapping project was completed in partnership with the Ontario Geological Survey (OGS). The pluton is approximately 25 km long and 5 km wide and was mapped at a scale of 1:20 000. During the summer of 2016 approximately three weeks of work was completed which included one detailed trench map and 44 stations. In the summer of 2017 approximately four weeks of work were completed and 95 stations along with five trench maps were completed to fill in gaps in the study area.

Prospector Wayne Richards excavated eight trenches of areas near the contact with the greenstone belt while prospecting for gold occurrences in the pluton (during 2015 and 2017). These trenches were mapped in detail to investigate the relationship of the gold occurrences to the granite.

3.2 Petrography

Fifty six samples were selected for petrography and polished thin sections were prepared at Lakehead University. The samples were selected from around the pluton with emphasis on samples that showed alteration, mineralization or variation in the rock type. Detailed petrography was undertaken using transmitted and reflected light microscopy in order to define the mineralogy, textures, alteration, mineralization and rock types. An Olympus B51 microscope equipped with an Olympus DP-70 camera was used for transmitted and reflected light petrography.

3.3 Whole-Rock and trace element geochemistry

One hundred and forty seven samples were submitted to the Geoscience Laboratories of the Ministry of Northern Development and Mines in Sudbury, Ontario. The samples underwent analysis for whole rock geochemistry including; specific gravity, ICP-MS with closed vessel multi acid digestion, lead fire assay with ICP-MS finish, as well X-ray fluorescences (XRF) for major and trace elements. The samples were pulverized in a 99.8% pure aluminum oxide ball mill. Loss on ignition (LOI) was determined gravimetrically by heating at 100°C under a nitrogen atmosphere and then at 1000°C under an oxygen atmosphere until a constant weight loss was measured. Major and selected trace element concentrations were determined by wavelength-dispersive X-ray fluorescence spectrometry with a XRF-PANalytical instrument on borate fused glass discs (major elements) and pressed powder pellets (trace elements). Trace elements were analyzed by XRF to allow comparison with data generated by inductively coupled plasma-mass spectrometry (ICP-MS). The samples also underwent lead fire assay with an ICP-MS finish to determine the values of gold, platinum and palladium. All analyses performed during the course of this study utilized standards, duplicates of samples and blanks as part of the normal procedures of the GeoLabs (reported in appendix E). The geochemical data was normalized to anhydrous values. The major and trace element geochemistry was interpreted with ioGAS software.

3.4 Rhenium-osmium geochronology

Rhenium - osmium geochronology on one molybdenite sample that was found within the granodiorite was completed at the University of Alberta Radiogenic Isotope Facility. Molybdenite is enriched in Re and contains insignificant Os, meaning that all ^{187}Os derives from ^{187}Re decay. The sample was processed by metal free crushing, then gravity and magnetic concentration methods, to obtain a molybdenite mineral separate for Re-Os age dating. The ^{187}Re and ^{187}Os concentrations in the molybdenite were determined by isotope dilution mass spectrometry using Carius-tube, solvent extraction, and anion chromatography as outlined in detail by Selby and Creaser (2004). Rhenium and osmium isotope ratios were measured using negative thermal ionization mass spectrometry techniques. The isotopic analysis used a ThermScientific Trition mass spectrometer by Faraday collector.

3.5 Samarium-neodymium isotopes

Seven samples were analyzed for Sm-Nd isotopes. Three samples were chosen of the most unaltered granodiorite and three of the monzogranite that occurs along the contact of the pluton and one samples from the diorite in the center of the pluton. The samples were chosen based on rare-earth element primitive mantle normalized profiles. The samples were analyzed at the Earth Resources Research and Analysis Facility at Memorial University, St. John's, Newfoundland. Whole rock powders were dissolved in Savilex© Teflon capsules using a mixture of HF and HNO_3. Prior to acid digestion, a mixed $^{150}Nd/^{149}Sm$ spike was added to each sample. After digestion, the samples were dried and taken back up in various

mixtures of HCl. Samples were then loaded into a column containing cation exchange resin where Sr fractionation can be isolated followed by collection of bulk rare earth elements (REEs). This bulk sample was then dried, taken up in HCl and loaded on a second column containing Eichrom© Ln resin to isolate Sm and Nd separately from the other REEs. Samarium and neodymium concentrations were determined using a multi-collector Finnigan Mat 262 mass spectrometer (TIMS) in dynamic mode for isotopic composition determination. Instrumental mass fractionation of Sm and Nd were corrected using a Raleigh law relative to $^{146}Nd/^{144}Nd = 0.7219$ and $^{152}Sm/^{147}Sm = 1.783$. The reported $^{143}Nd/^{144}Nd$ ratios were corrected for the deviation from repeated duplicates of the standard JNdi-1 ($^{143}Nd/^{144}Nd = 0.512115$; Tanaka et al., 2000). Replicates of the standards give a 6-month mean value of $^{143}Nd/^{144}Nd = 0.512102 \pm 14$ (2SD, n=18) for JNdi-1. Analyses of the USGS standard BCR-2 was included in each batch using a separate dissolution and thus provides the best estimate of the reproducibility of an individual analysis.

3.6 Back-scatter electron petrography

Back-scatter electron petrography was performed on six carbon coated thin sections at Lakehead University using an SEM-EDS JEOL 5900 scanning electron microscope equipped with an Oxford energy X-ray spectrometer (EDX) dispersion system with a resolution of 139eV. The SEM was used to conduct quantitative analyses of the minerals, with a 15mm working distance and an accelerating voltage of 20kV. The following well characterized mineral and synthetic standards were used: jadeite (Na, Al); wollastonite (Ca, Si); orthoclase (K); ilmenite (Fe, Ti);

periclase (Mg); Mn-hortonolite (Mn); apatite (F, P); barite (Ba and S); $SrTiO_3$ (Sr); and KCl (Cl).

Chapter 4: Field Relations and Petrography Results

4.1 Field and petrographic observation

The Terrace Bay Batholith has been separated into three main rock types: granodiorite, diorite and monzogranite (Fig. 4.1). During field mapping, rock names were assigned based upon field observations (Station locations in Appendix A). Lithological names are based upon the field observations for consistency. The pluton has been cross-cut by dykes of different varieties including Archean to Proterozoic gabbro, lamprophyres and late stage granites.

4.1.1 Granodiorite

The majority of the pluton is composed of massive, relatively homogeneous, equigranular to porphyritic granodiorite to monzogranite. Local porphyritic varieties contain medium- to coarse-grained quartz and/or potassium feldspar phenocrysts in a groundmass of fine-grained quartz, plagioclase and potassium feldspars, amphibole and biotite with minor magnetite, sulphide minerals, chlorite, titanite and epidote. The classification of these rocks as granodiorite to monzogranite is based on field estimates of the modal percentage of quartz, plagioclase and alkali feldspar plotted on a QAP diagram (Fig. 4.3). The granodiorite throughout the pluton is massive, relatively homogenous, equigranular and locally quartz porphyritic. It consists of medium- to coarse-grained quartz and feldspar phenocrysts with a groundmass of fine-grained amphibole, biotite and disseminated magnetite and sulphide minerals (Fig. 4.2a, b).

Petrographically the granodiorite consists of plagioclase, potassium feldspar, quartz, amphibole, biotite, ± chlorite, ± titanite, ± epidote, ± sulphides (Fig. 4.2c, d;

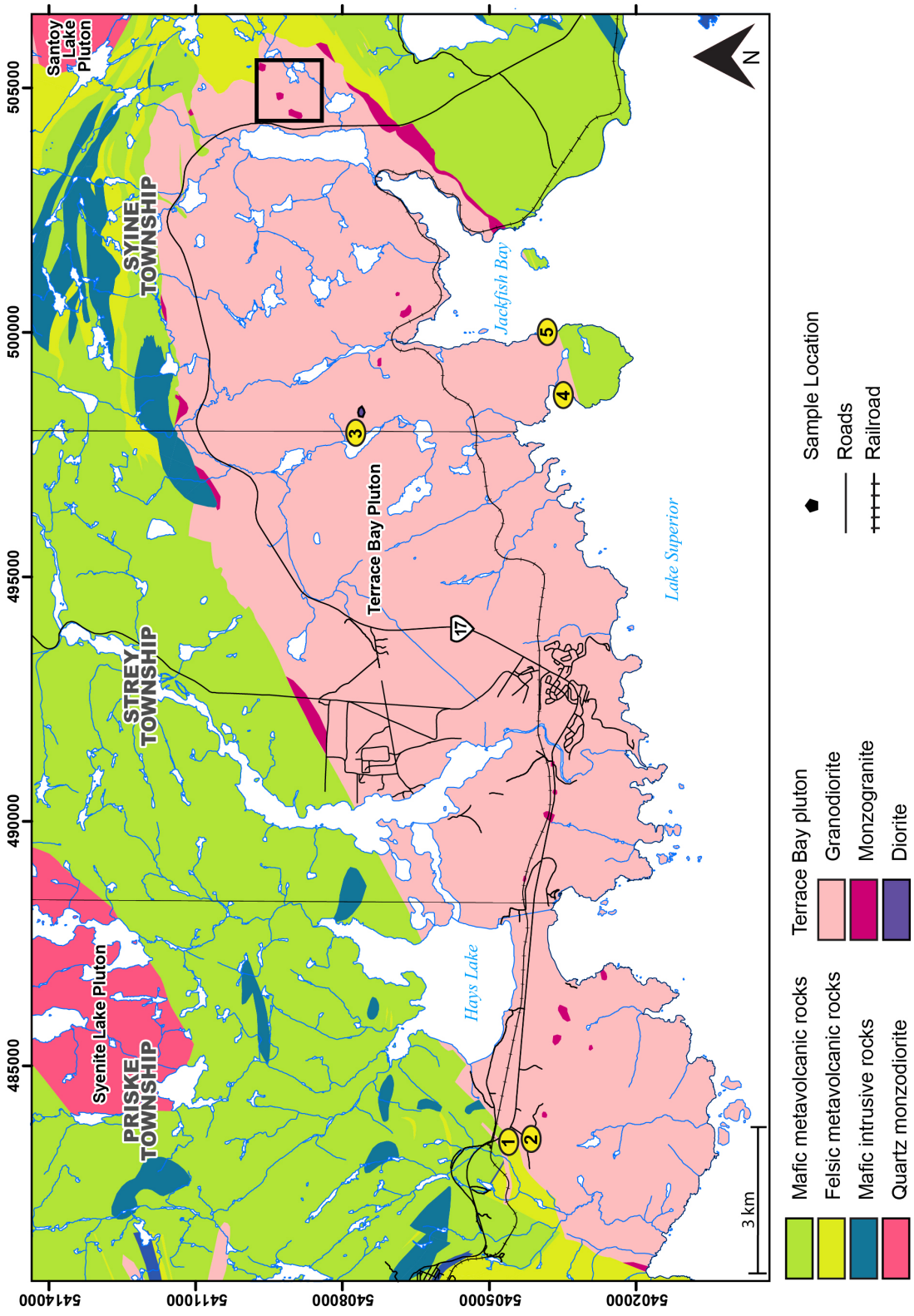

Figure 4.1 Simplified bedrock geology map of the Terrace Bay Batholith and the surrounding greenstone belt in the Priske, Strey and Syine townships. 1) Molybdenum occurrence; UTM 483500 5404390; 2) Amphibole clusters; UTM 482666 5404085; 3) Amphibole rimmed pyroxene; UTM 497999 5407765 4) Western Victoria Cape contact; UTM 498608 5403311; 5) Eastern Victoria Cap contact; UTM 500047 5403726. Black box represents where trenches are located.

full petrographic descriptions in Appendix B). The mafic phases of the granodiorite are dominantly amphibole (5% to 15%) and biotite (5% to 10%). The amphibole and biotite crystals are commonly altered to chlorite. The groundmass of the granodiorite is composed of fine-grained plagioclase 40%, potassium feldspar 30%,

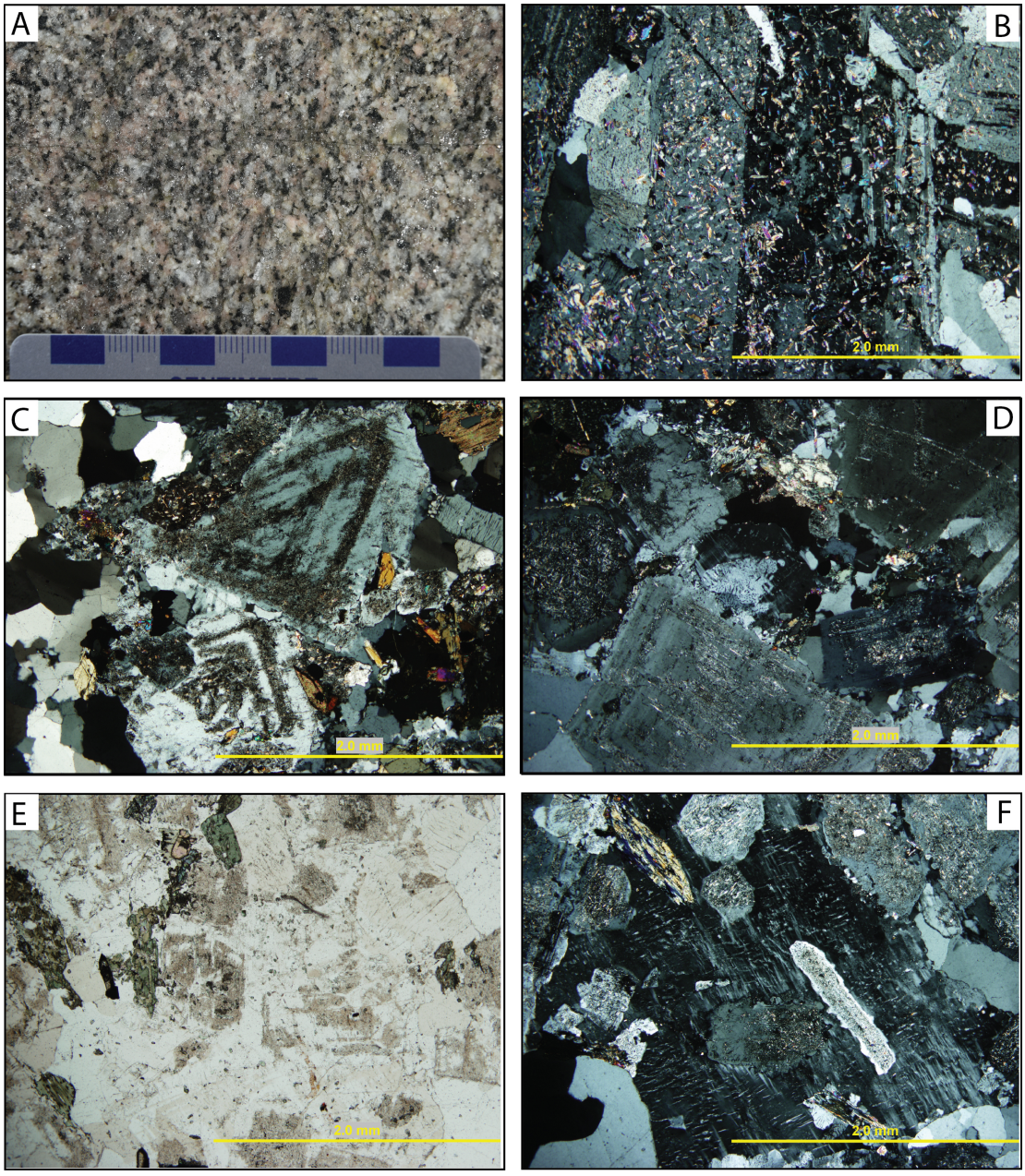

Figure 4.2 Field and petrographic photographs of the granodiorite. A) Massive granodiorite (station 16KAA043A). B) Coarse-grained sericite alteration on plagioclase (Sample 16KAA006).C) Zoned plagioclase phenocrysts (Sample 17KAM030). D) Minor sericite alteration on plagioclase phenocrysts (Sample 16KAA005). E) Amphiboles and titanite in ppl (Sample 16KAA004). F) Perthitic lamellae (Sample 16KAA004).

quartz 20% ± 5% amphibole and 5% biotite. When plotted on the QAP diagram the granodiorite plots within the granodiorite and monzogranite fields (Fig. 4.3).

The plagioclase mainly occurs as phenocrysts but is also found as fine-grained crystals in the groundmass. Plagioclase generally displays simple twins or Carlsbad twinning; the simple twins are more frequent in the coarser phenocrysts. The medium- to coarse-grained plagioclase and potassium feldspar phenocrysts typically display zonations, commonly defined by sericite (Fig. 4.2c). Potassium feldspar is interstitial between the plagioclase and quartz crystals and displays tartan twinning, which is commonly distorted by the presence of perthitic lamellae

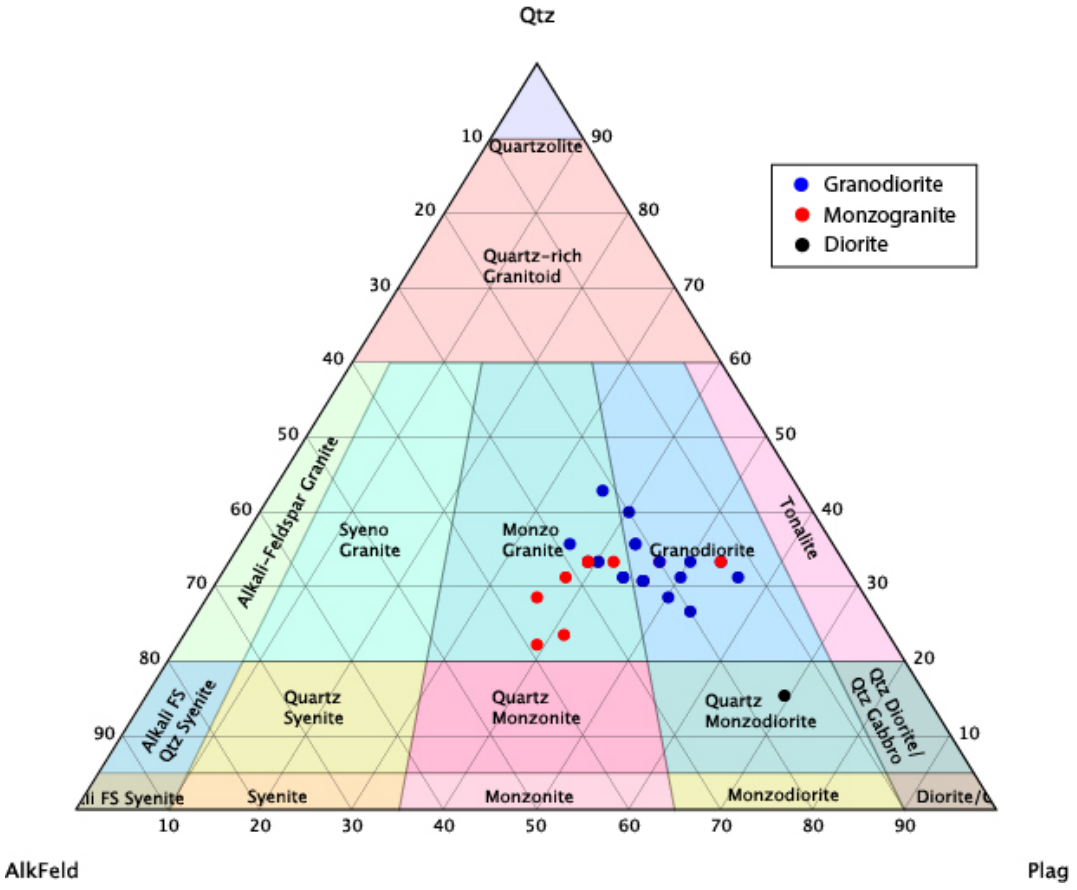

Figure 4.3 QAP diagram showing the lithologies of the Terrace Bay Batholith based on petrography. Modified from Streckeise (1974).

(Fig. 4.2e, f).The potassium feldspar phenocrysts are commonly poikilitic with amphibole, quartz and titanite. The potassium feldspars show sericite alteration which varies in intensity (Fig. 4.2 b, c, d). It ranges from very fine-grained to fine-grained sericite/white mica which has entirely replaced the primary feldspar crystal. The potassium feldspars display seritization, but not as intensely as the plagioclase crystals.

Quantitative analysis was performed to determine the composition of the feldspars, amphibole, and pyroxenes. Six samples were selected for feldspar analysis, three granodiorites and three monzogranites with 20 grains analyzed from the six samples (Table 4.1; full results in Appendix C). The plagioclase feldspars were determined based off the oxide analysis to be dominantly oligoclase with minor albite whereas the potassium feldspars were classified as orthoclase. The amphiboles in the pluton were determined to be magnesio-hornblendes using the IMA classification system of Leake et al., (1997) (results in Appendix C). Pyroxene crystals were found in the center of the pluton approximately 3 km from the contact with the supracrustal rocks and were analyzed by SEM-EDS (Fig. 4.1). The pyroxene crystals are rimmed by amphiboles (Fig. 4.4a, b).

Table 4.1 Feldspar mineral composition, modal abundances of type of feldspar are based on crystals analyzed by SEM-EDS.

Sample number	Lithology	Orthoclase	Anorthite	Albite	Oligoclase	Anorthoclase
16KAA026A	Granodiorite	100%	0%	0%	0%	0%
17KAM036B	Granodiorite	50%	0%	0%	50%	0%
16KAA020A	Monzogranite	25%	0%	25%	50%	0%
17KAM042A	Granodiorite	90%	0%	0%	10%	0%

The pyroxene cores were determined to be diopside and augite with the amphibole rims comprised of magnesio-hornblende similar to the other amphiboles in the pluton. Clusters of the amphibole crystals were only seen in the west end of the pluton (Fig. 4.1). The clusters are up to 5 cm across and the edges are anhedral, with feldspars and quartz crystals sporadically throughout the cluster (Fig. 4.4 c, d)

Multiple outcrops in the center of the pluton, as well as sporadic outcrops near the contact with the volcanic rocks, host very coarse-grained phenocrysts of potassium feldspar, ranging in size from 1 cm to 3 cm (Fig. 4.5a, b). The crystals increase in abundance towards the center of the pluton, displaying random orientation (Fig. 4.5a, b), whereas near the supracrustal contact there are only sporadic occurrences. The crystals typically host inclusions of plagioclase,

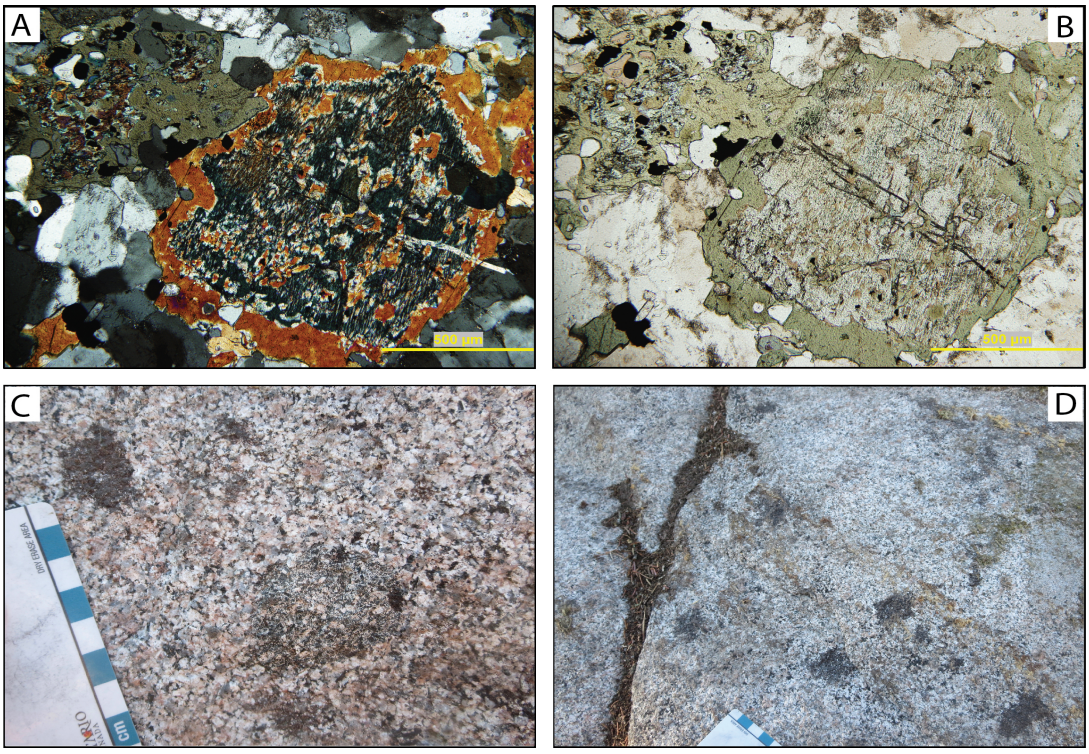

Figure 4.4. Photomicrographs A) Amphibole rimmed pyroxene crystal in XPL (Station 17KAM036A). B) Amphibole rimmed pyroxene crystal in PPL. Field photographs C and D) Field photographs of amphibole clusters (station 17KAM077).

amphibole, biotite and titanite and perthitic exsolution lamellae are present (Fig. 4.5c, d). Some of the crystals have macroscopic zonations suggesting compositional variations. Multiple zoned K-feldspar crystals show a decreasing trend of orthoclase (Or) composition towards the center of the crystal. Whereas barium concentrations decrease outwards from the center to rim from 2.89 to 0.51 wt.% Ba, barium is only present in potassium feldspars. The outer rim of the crystal generally has a composition of pure orthoclase (Or) decreasing from rim to core, these crystals typically decrease in orthoclase from Or_{100} to $Or_{91.6}$ (Fig. 4.6). Multiple examples of pure orthoclase were found in the samples analyzed.

Primary exsolution textures observed include graphic and myrmekitic textures as well as perthitic lamellae (Fig. 4.5e, f). The intensity of the textures varies between samples, commonly they occur in and along phenocrysts of the potassium feldspar. The potassium feldspar and the plagioclase regularly exhibited perthitic textures in coarse phenocrysts (Fig. 4.5d).

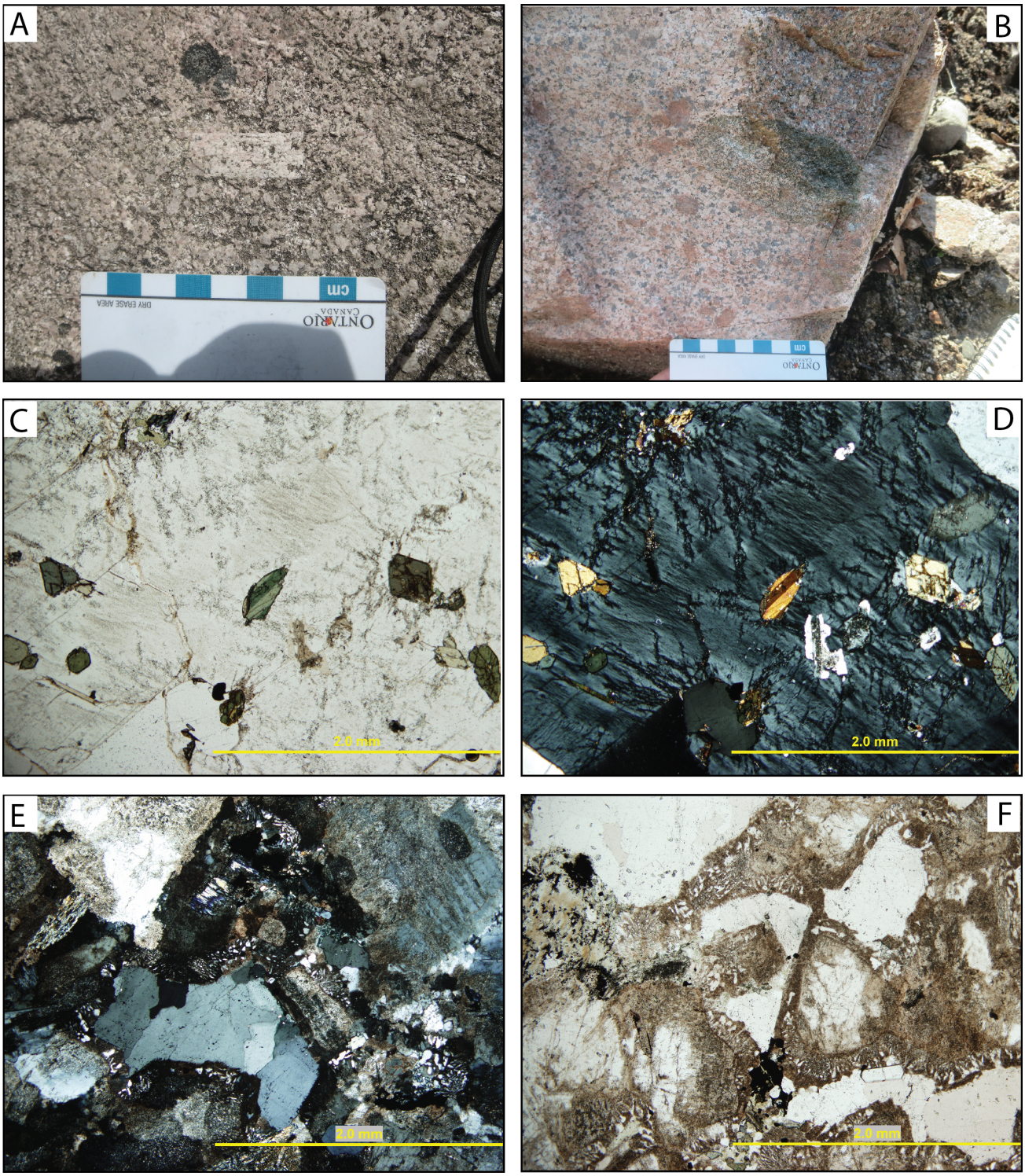

Figure 4.5 A) Coarse-grained feldspar phenocrysts (UTM 498666 5407536, station 17KAM040a). B) Cluster of k-feldspar phenocrysts (UTM 498666 5407536, station 17KAM040a). C) Inclusions in coarse-grained feldspar phenocrysts in PPL (UTM 498666 5407536, station 17KAM040a). D) Inclusions in coarse-grained feldspar phenocrysts in XPL (UTM 498666 5407536, station 17KAM040a). E) Graphic texture in XPL (Station 16KAA013). F) Graphic texture in PPL. (Station 16KAA013)

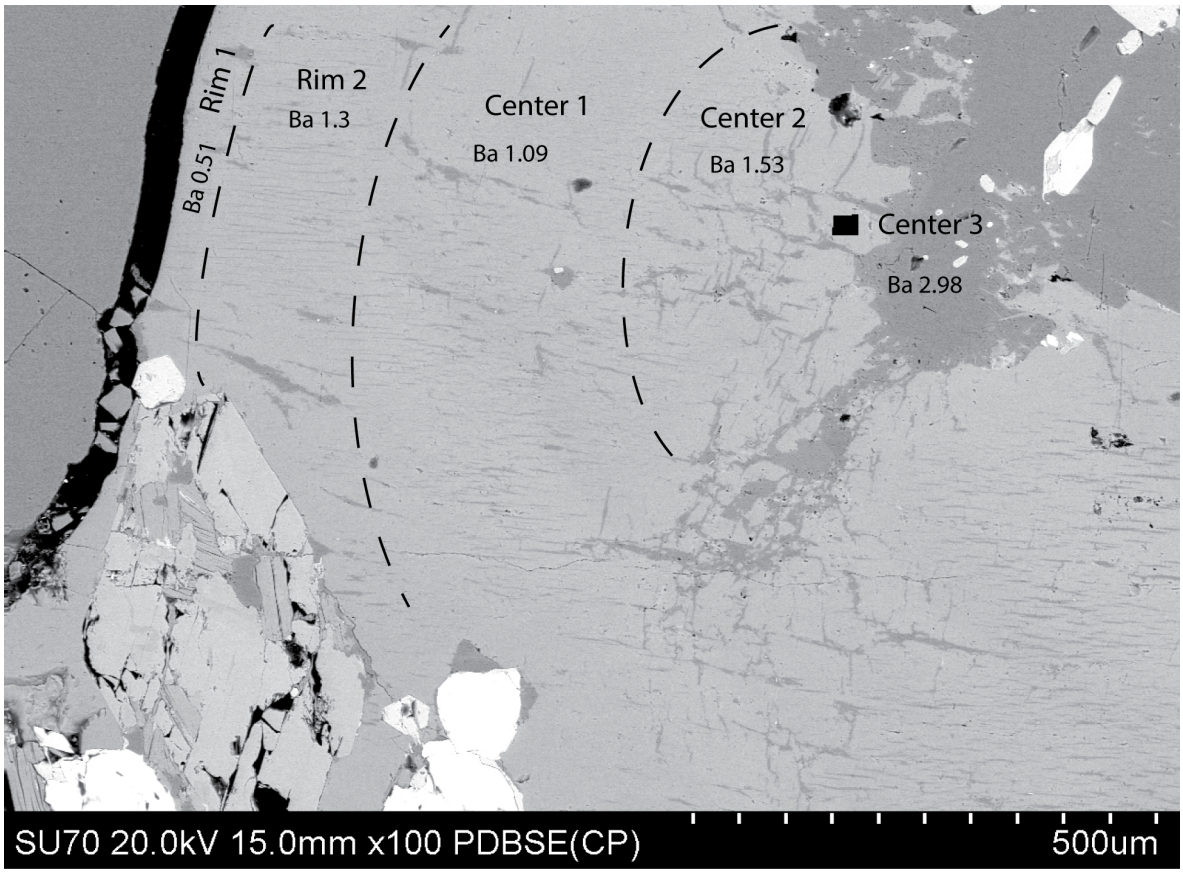

Figure 4.6 Zonations across a coarse-grained potassium feldspar phenocryst, Ba = barium in wt.% (UTM 498666 5407536, station 17KAM040a).

4.1.2 Diorite

An outcrop of diorite was found in the center of the pluton, approximately 3.7 km from the contact with the greenstone belt (Fig. 4.1). The outcrop is 15 m long and approximately 2 m high (Fig. 4.7a). The diorite is composed of medium-grained amphibole, biotite and plagioclase and has an average magnetic susceptibility of 0.219 x 10^{-3} SI units (Fig. 4.7b). There are areas that have an increased potassium feldspar content, giving the diorite a pinker colour suggesting that it could be a monzodiorite (Fig. 4.7c). Trace amounts of quartz crystals are present in the diorite. The contacts between the diorite and the surrounding granodiorite were not observed due to overburden cover.

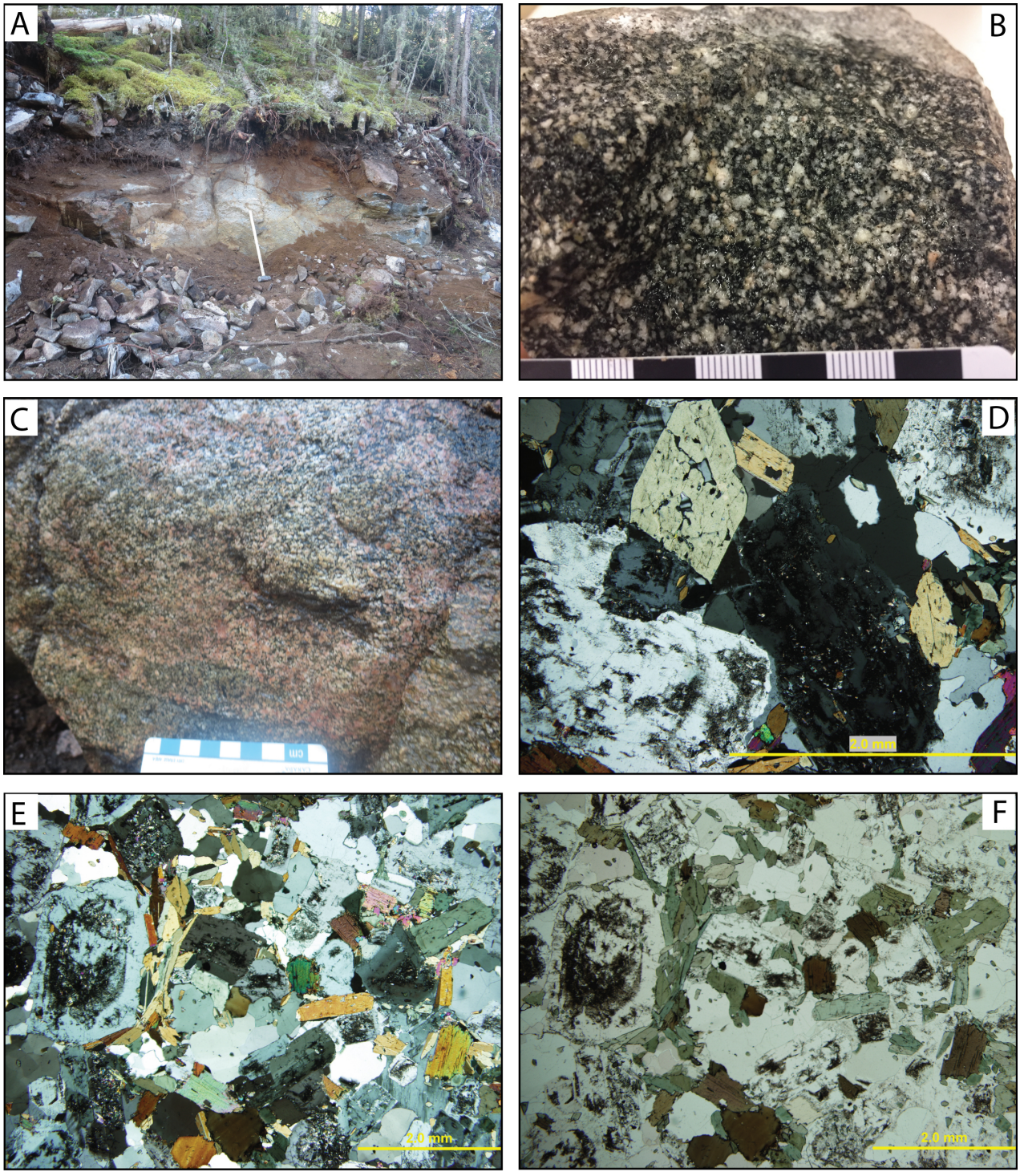

Figure 4.7 Field and petrographic photographs of diorite (UTM 498372 5407657; Station 17KAM039B). A) Outcrop photo; B) The medium-grained diorite, showing plagioclase and amphiboles; C) Areas of increased potassium feldspar; D) Photomicrograph of feldspar and amphiboles in XPL; E) Photomicrograph of feldspar and amphiboles in XPL; F) Photomicrograph of feldspar and amphiboles in PPL.

The diorite phase was also found at the western end of the pluton near the contact, this was a smaller 10 m by 4 m outcrop (Fig. 4.1). Based on petrographic modal analyses, they are composed of roughly 20% amphibole, 45% plagioclase and 5% biotite with trace amounts of quartz and potassium feldspar (Fig. 4.7d, e, f). On the QAP diagram, it plots in the quartz monzodiorite field (Fig. 4.3).

4.1.3 Monzogranite

Although the pluton is relatively homogenous, there are areas where the rocks are pink to red in colour, with increased potassium feldspar content up to 25-35 modal% indicating a monzogranite (Fig. 4.8). Amphibole contents in the monzogranite are higher than in the granodiorite with 10 to 25%.

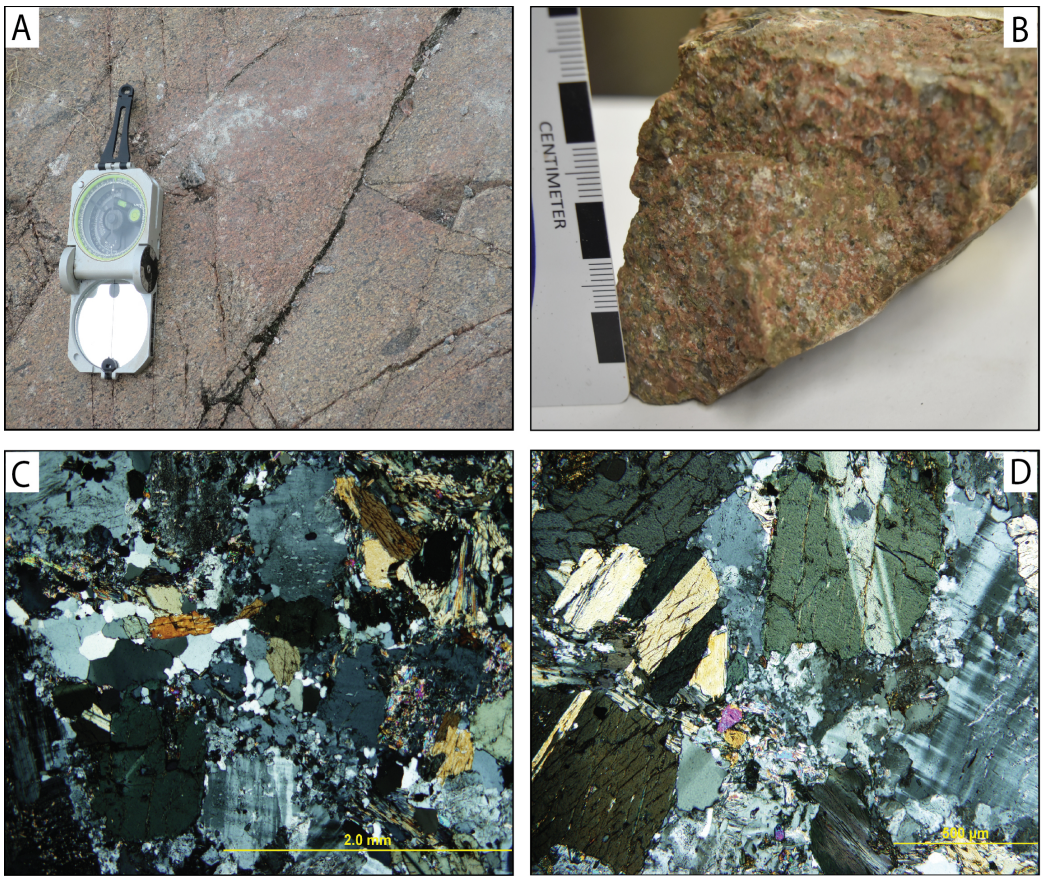

Figure 4.8. Field and petrographic photographs of monzogranite. A) Monzogranite photo (Station 16KAA020; UTM 502146 5404765). B) Hand sample, showing quartz phenocrysts in the potassium feldspar groundmass. (Station 17KAM048A). C & D) Photomicrographs of interstitial potassium feldspar and amphibole displaying simple twinning (Station 16KAA020; UTM 500362 5406771).

Petrographically the monzogranite has up to 25% quartz, 20-35% plagioclase, 25-35% potassium feldspar, 10-25% amphibole with trace biotite and sulphides with secondary chlorite and epidote. Both feldspars display a similar sericitic alteration to the granodiorite. The monzogranite that occurs along the contact with the supracrustal rocks shows an increased amphibole content compared to the granodiorite (Fig. 5.1). This monzogranite is seen in five separate outcrops along the contact but is not continuous, with numerous outcrops in the center of the pluton.

4.1.4 Xenoliths

The pluton contains xenoliths that range in size from centimeters to a meter in scale. Xenoliths increase in abundance towards the contact with the surrounding supracrustal rocks (Fig. 4.9a). Two types of xenoliths were observed in the pluton. The first is a fine-grained mafic and composed primarily of amphibole and biotite with little to no felsic minerals present (Fig. 4.9a). The second type is a fine-grained felsic rock, which is less common, and is similar to the diorite with increased amounts of quartz and feldspars compared to the mafic xenoliths (Fig. 4.9b). The contacts between the irregular xenoliths and the surrounding intrusive rocks are typically sharp. The mafic xenoliths are composed primarily of subhedral amphibole (40%) and anhedral biotite (30%), with lesser amounts of plagioclase (>25%), generally occurring in the matrix (Fig. 4.9c, d). Trace amounts of calcite, epidote and quartz can be seen sporadically throughout. It was not possible to sample the felsic xenoliths for petrography or geochemistry because of the glacially polished outcrop surfaces.

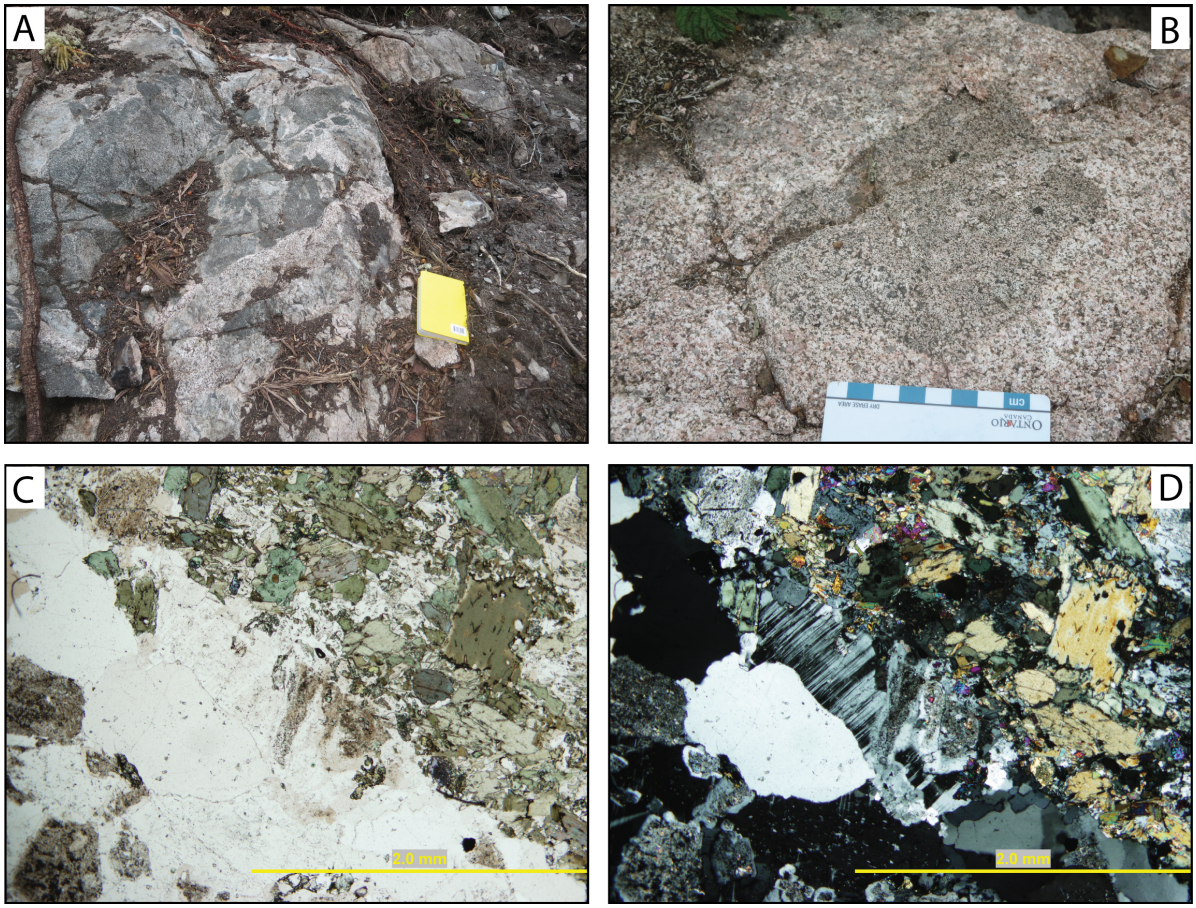

Figure 4.9. Field and petrographic photos of xenoliths A) Mafic xenoliths (Station 17KAM084; UTM 505049 5409740). B) Felsic Xenoliths (Station 17KAM049; UTM 500786 5406887). C & D) Photo micrograph of mafic xenolith contact with the granodiorite in PPL and XPL (16KAA006B; UTM 497372 5410520).

4.1.5 Dykes

Many types of dykes cross-cut the pluton, including granitic, lamprophyre, diabase and meta-gabbroic dykes. The gabbroic dykes range from 10s of cm to meters in width and cross-cut many of the large highway outcrops (Fig. 4.10a). The lamprophyre dykes are smaller with widths up to 40 cm (Fig. 4.10b). Both types of dykes commonly cross-cut the pluton with sharp boundaries and because of the significant age difference they were not the focus of this study. The granitic dykes, characteristically exhibit pegmatitic and aplitic textures, and were composed of

quartz, potassium and plagioclase feldspar with minor amounts of mafic minerals such as amphibole and biotite. The pegmatitic dykes consist of plagioclase, potassium feldspar and quartz with trace chlorite (Fig. 4.11c, d). The groundmass is composed of very fine-grained feldspar and quartz, the feldspars display sericite alteration so it was difficult to determine the variety of feldspar.

Figure 4.10. Cross-cutting dykes. A) Lamprophyre dyke (Station 16KAA006; UTM 497390 5410502); B) Gabbro dyke (Station 16KAA007; UTM 498307 5410970); C) Aplitic dyke (Station 17KAM015; UTM 48065 5403367); D) Pegmatitic dyke (Station 16KAA021; UTM 504208 5407257).

Aplitic dykes are typically zoned, with a potassium rich margin and a quartz and plagioclase rich center. The granitic dykes, both pegmatitic and aplitic, vary in width from 1cm - 30 cm. The pegmatitic dykes occasionally have quartz veins

through the center (Fig. 4.10c, d). One aplitic dyke in the center of the pluton displayed sporadic coarse-grained plagioclase feldspar phenocrysts (Fig. 4.11c, d). Locally, quartz veins cross-cut the pegmatitic dykes.

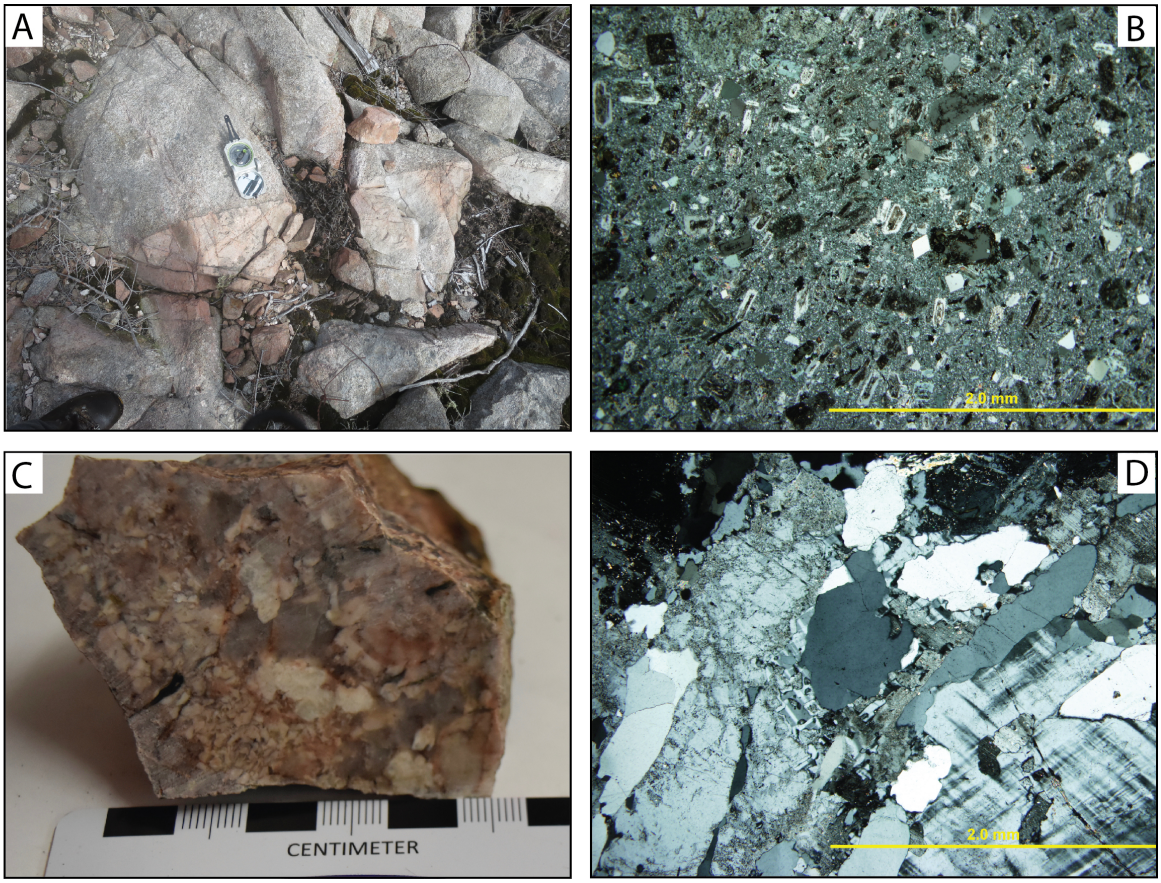

Figure 4.11. A) Aplitic dyke cross-cutting granodiorite. (Station 17KAM038; UTM 498005 5407652). B.) Photomicrograph of aplitic dyke, showing the fine-grained groundmass of feldspar and quartz (Station 17KAM038B; UTM 498005 5407652). C). Pegmatitic dykes with quartz, plagioclase and potassium feldspar (Station 16KAA33b; UTM 500451 5411679). D) Photomicrograph of pegmatitic dyke, showing macro graphic exsolution textures between feldspars and quartz in XPL (Station 16KAA021C; UTM504206 5407245).

4.1.6 Contact relationships with supracrustal rocks

The contact with the supracrustal rocks is not fully exposed around the pluton due to erosion and overburden. Where observed the contact between the granodiorite and the supracrustal rocks tends to be very chaotic, although there are only two outcrops that display a sharp contact (Fig. 4.12). Locally, granitoid dykes

extend from the pluton into the surrounding metavolcanic rocks. One outcrop along the northern contact with the volcanic rocks showed a gradual contact with numerous entrained xenoliths, and cross-cutting pegmatitic and aplitic dykes (Fig. 4.12 c, d). Some contacts show the cross-cutting relationships and entrainment of the surrounding volcanic rocks. Locally, large sections of the volcanic rocks that are highly foliated and strained are cross-cut by late dykes and veins (Fig. 4.12c, d, f). Pegmatitic and aplitic dykes increase in abundance in proximity to the contact with the supracrustal rocks, representing a later phase of the pluton.

Only two examples of the southern contact with the volcanic rocks are exposed along the Cape Victoria point (Fig. 4.1). The western contact with the volcanic rocks is gradual similar to elsewhere in the pluton. Large granitic dykes ranging in size from 10cm to 2 m cross cut the volcanic rocks up to 500-600 m from the contact (Fig. 4.12e). On the eastern side of the point the contact was only observed in a section just below the waters surface, but it was sharp, with dykes and veins of the granodiorite that intrude into the volcanic rocks. Aplitic and pegmatitic dykes cross-cut the granodiorite and volcanic rocks (Fig. 4.12b).

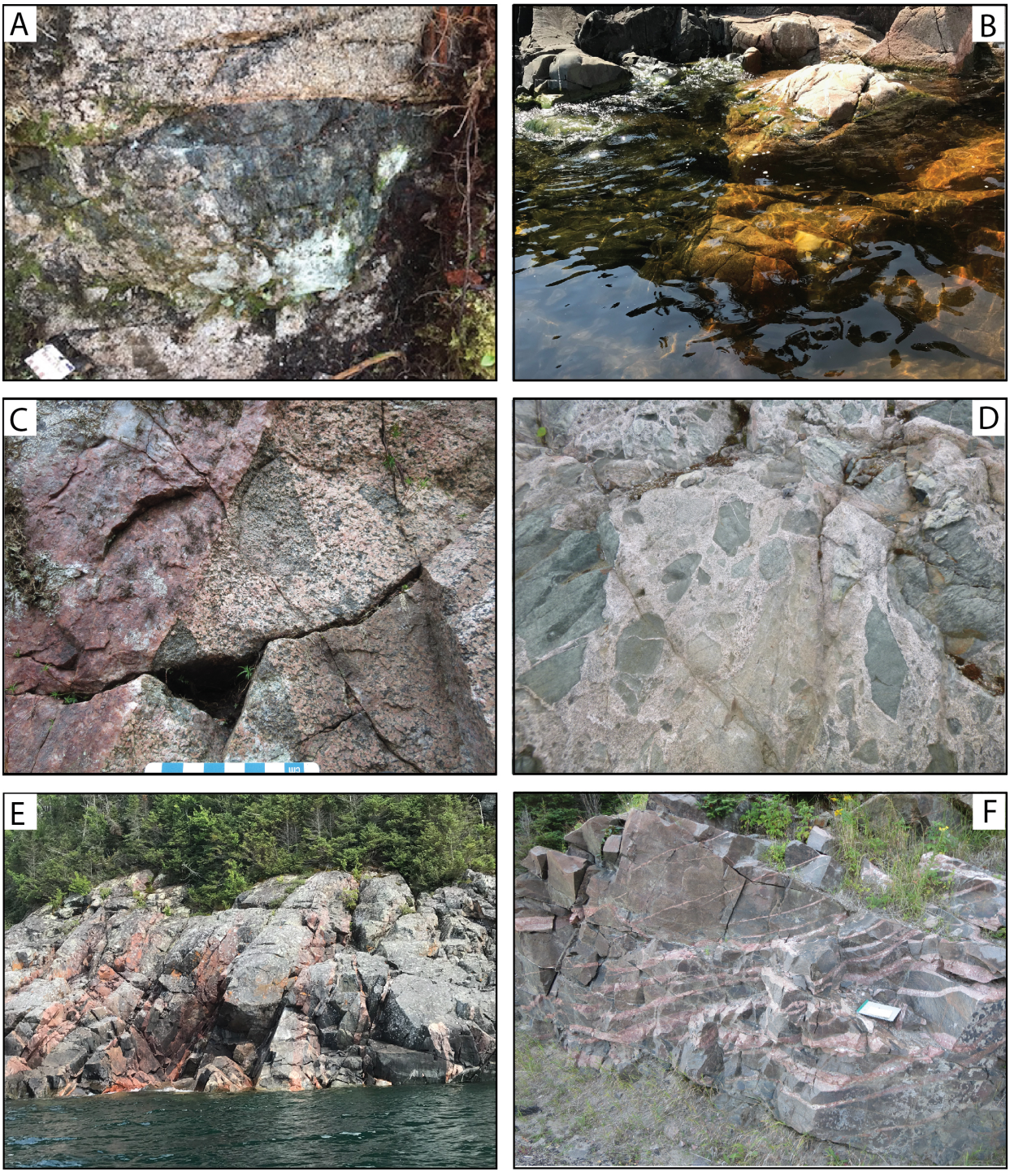

Figure 4.12 Field photographs of contact between pluton and supracrustal assemblage. A) Sharp contact between granodiorite and amphibolite (Station 18EM007; UTM 495250 5410500). B) Contact with supracrustal rocks on east side of Victoria cape (UTM 498663 5403321). C) granodiorite cross-cut by late pegmatitic veins and mafic xenoliths (Station 16KAA033; UTM 500444 5411686). D) Granodiorite with mafic xenoliths and late stage veins and dykes (Station 16KAA038; 504888 5410854). E) Granitic dykes on west side of Victoria Cape (UTM 500018 5403616). F) Late stage aplitic dykes cross-cutting supracrustal rocks (Station 16KAA021; UTM 504198 5407254).

4.2 Deformation and Alteration

4.2.1 Structural observations

The pluton is generally massive but exhibits a structural fabric in proximity to cross-cutting structures and proximal to the contact with the surrounding supracrustal rocks. The foliations across the batholith have a weak northeast trend that is prominent across the pluton (Fig. 4.13). The pluton is cross-cut by a multitude of shears and fractures in a broad range of orientations. They appear chaotic but when separated out into areas a clear structural trend is seen with the direction of shearing (Fig. 4.14). The eastern portion of the pluton shows north-south and east-west shearing (Fig. 4.14a). The west end shows a general northwest shear direction with two shears with east-west orientation (Fig. 4.14c). The shears located in the center of the pluton are sporadic (Fig. 4.14b). It is clear that two prominent structural features are present, the north-south shear movement that is seen across the pluton and then the east-west movement in the eastern end of the pluton. Although the pluton has been cross-cut by shear zones of varied orientations, the number of shearing events cannot be determined with this data. The orientation of these structural features corelates with regional-scale fabrics and shear zones in the supracrustal rocks surrounding the pluton (Fig. 4.13). One northeast trending feature, which strikes parallel to the Augasabon river (Fig. 4.15a), can clearly be seen cross-cutting the granodiorite, but because of the over burden no offsets were observed. The second shear runs from the northern contact in the western end of the pluton into Lake Superior.

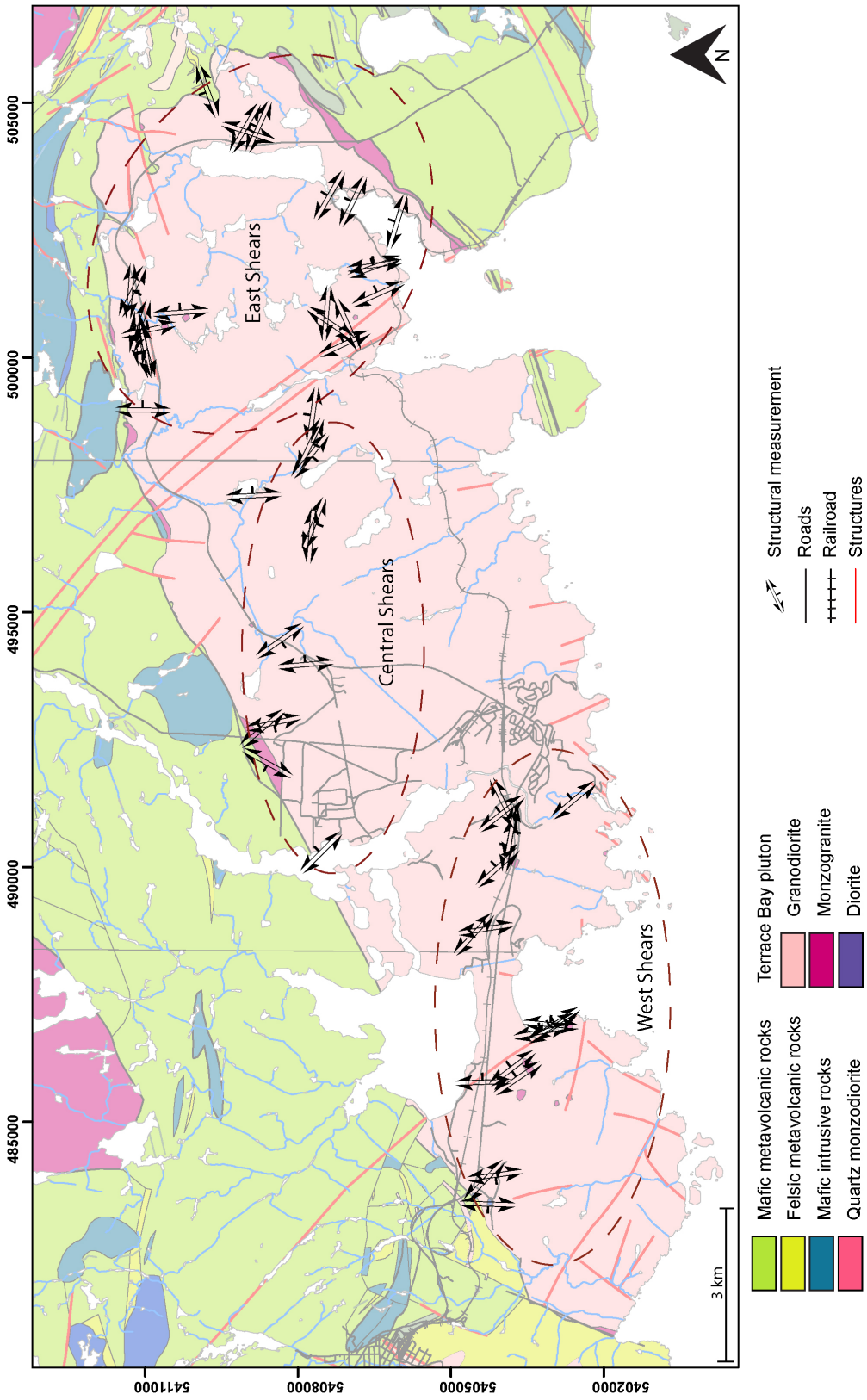

Figure 4.13. Simplified geology map, showing the location of shear zones in the pluton.

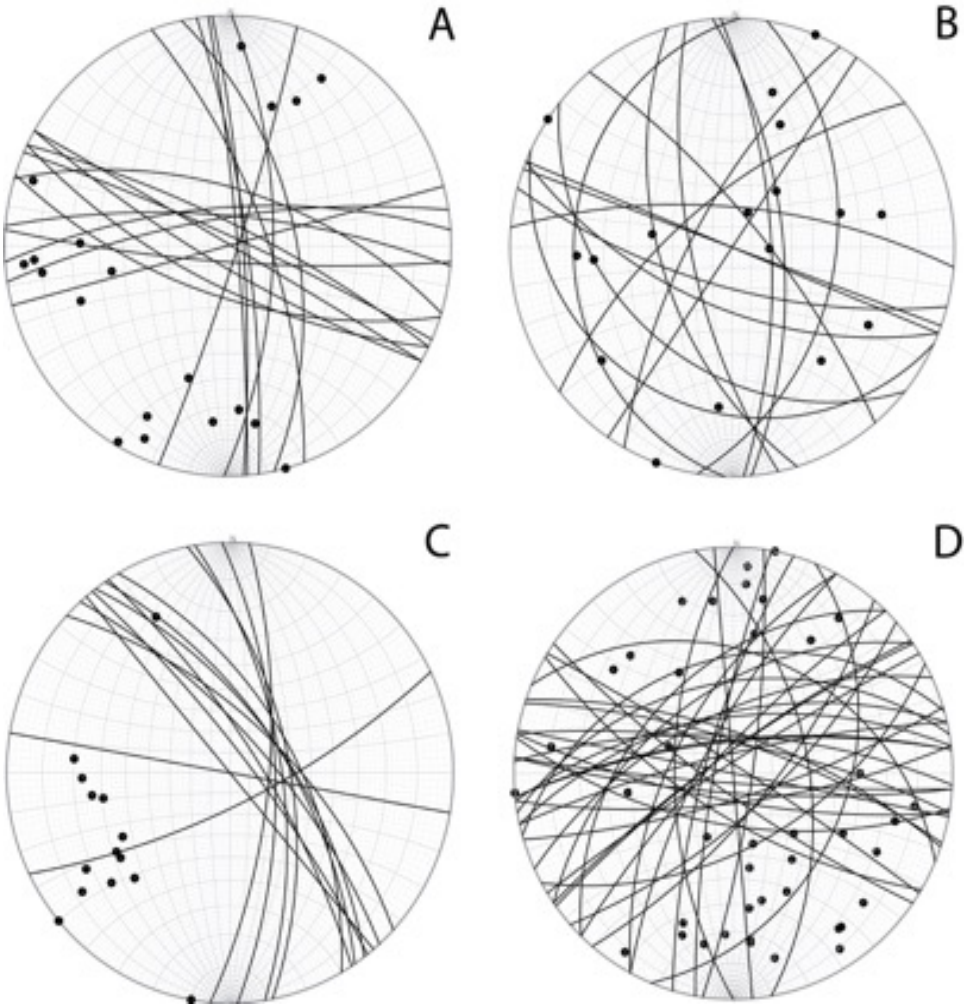

Figure 4.14 Stereonets showing direction of shearing and foliation. A) Orientation of shearing in the eastern end of the pluton. B) Orientation of shearing in the center of the pluton. C) Orientation of shearing in the western end of the pluton. D) Direction of foliation across the pluton.

Dextrally offset quartz veins were present showing the movement along the shear (Fig. 4.15b, d, e).

Off set quartz veins have also been found in outcrops surrounding the largescale structures. The best examples are from the western end of the pluton, where the quartz veins are offset multiple times with a (dextral) offset of 2-3 cm (Fig. 4.15f).

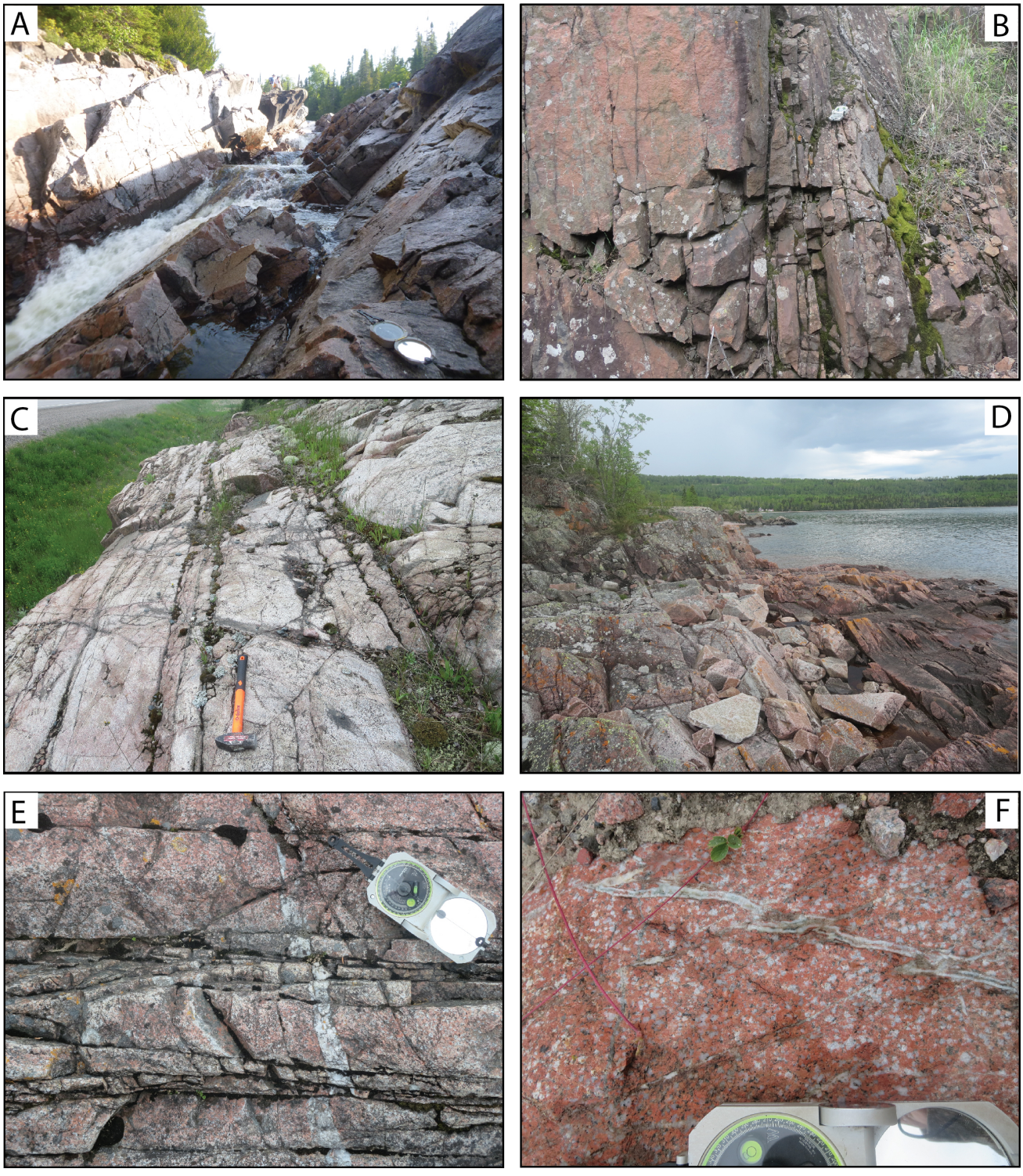

Figure 4.15. Field photos of structures. A) Northeast shear running up the Agasabon River (Station 17KAM072; UTM 483498 5404527). B) North-south shear (Station 17KAM043; UTM 503326 5407137). C) East-west shear along highway (Station 17KAM059; UTM 500243 5410886). D)Northwest-southeast shearing (Station 17KAM019; UTM 486936 5402728). E) Offset quartz vein by northwest-southeast movement (Station 17KAM019; UTM 486936 5402728). F) Quartz vein offset by north-south movement (Station 17KAM073; UTM 490588 5403655).

Similar offsets were also found in other areas along the same large-scale structure (Fig. 4.15e). In the eastern end of the pluton, north-south structures are prominent across the area (Fig. 4.15b), but there are also east-west shears that cross-cut the pluton. The most prominent example of the east-west movement is seen in a highway outcrop near the northern contact with the supracrustal rocks where the shear strikes parallel to the highway for 20 m (Fig. 4.15c).

4.2.2 Chlorite-Epidote alteration

Small areas (<1 m) of intense chlorite-epidote and sericite alteration occur locally in the pluton. Due to the intensity of the alteration the rocks are fissile. Commonly the altered rocks occur as small veinlets that run parallel to quartz veins or structures (Fig. 4.16a, b). The most extensive example of this alteration was observed in the North Zone trench, where a 70 cm wide zone was observed (Fig. 4.16b). This zone of alteration is recessively weathered due to the intensity of alteration. The zone is comprised primarily of fine-grained plagioclase, quartz, and potassium feldspar with secondary chlorite, epidote and calcite in the groundmass with relict quartz and feldspar phenocrysts that are intensely altered by sericite. Phenocrysts are highly altered by very fine-grained sericite and possible epidote and feldspar crystals with little to no relic twinning (Fig. 4.16c). The feldspar phenocrysts appear to have been reduced in grainsize, but are heavily altered making it difficult to distinguish the exact composition. Calcite, chlorite and epidote can be seen occurring along the edge of the phenocrysts. In plane polarized light the phenocrysts are a light brown/green colour, with darker areas that are more prominently altered (Fig. 4.16c, d). The samples also have trace to 2% sulphide

mineralization (pyrite, chalcopyrite). Potassium feldspar phenocrysts are perthitic with mild sericite alteration, mostly along the fractures of the crystals. No primary amphibole and biotite are preserved having been altered to chlorite.

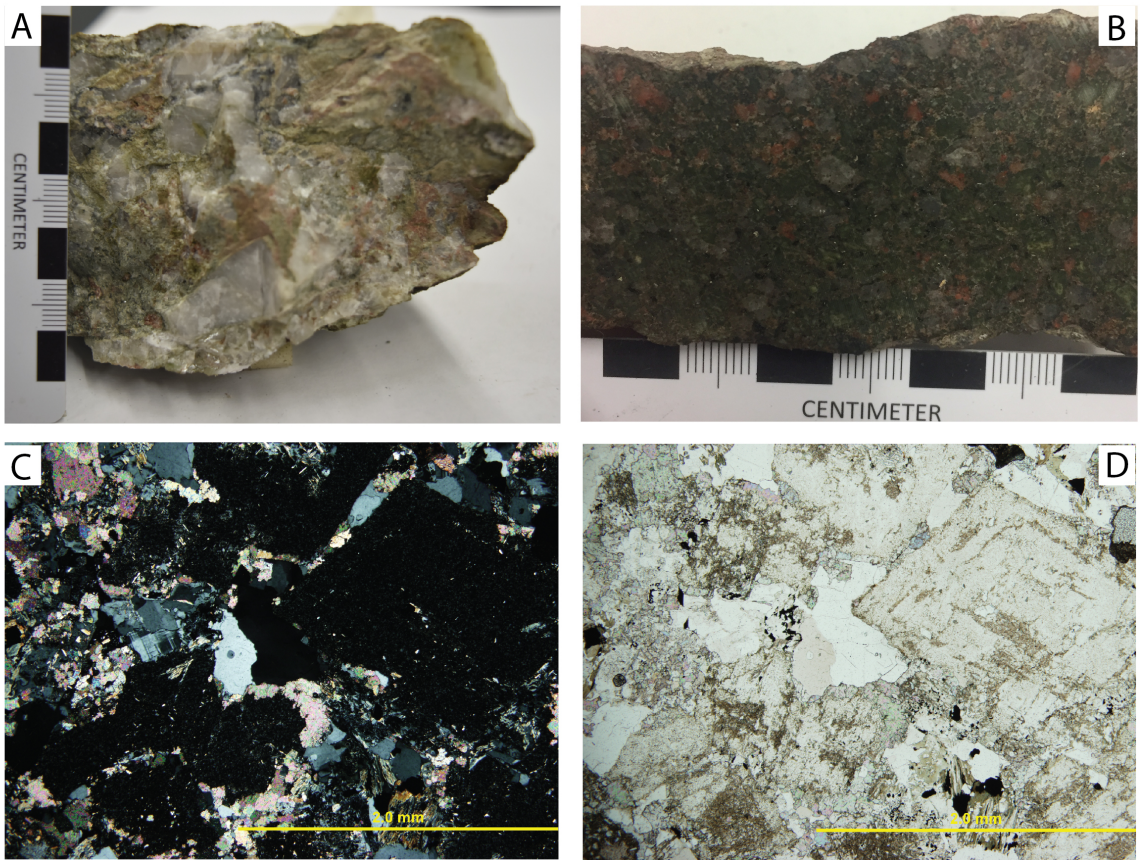

Figure 4.16. Hand sample and petrographic photos of the chlorite and epidote alteration. A) Chlorite-epidote alteration occurring along a quartz vein (Station 17KAM062B; UTM 502364 5406589). B) Epidote-chlorite altered zone, showing coarse relic feldspar phenocrysts in a groundmass of chlorite and epidote (Station 16KAA019C; UTM 504675 5408534). C) Photomicrograph of completely altered feldspars in XPL (Station 16KAA019C; UTM 504675 5408534) D) Photomicrograph of completely altered feldspars in PPL (Station 16KAA019C; UTM 504675 5408534).

4.2.3 Hematite alteration

Hematite alteration was observed across the pluton. The hematite alteration overprinted the primary mineralogy and textures. Groundmass compositions are also obliterated and composed of fine- to very fine-grained hematite, chlorite, sericite, epidote and calcite (Fig. 4.17). The outcrops that are highly altered are less

competent and tend to be recessively weathered. The areas of alteration are dominantly found in proximity to regional-scale shears and faults that cross-cut the pluton. The phenocrysts of feldspar have only relic twinning, are heavily sericite

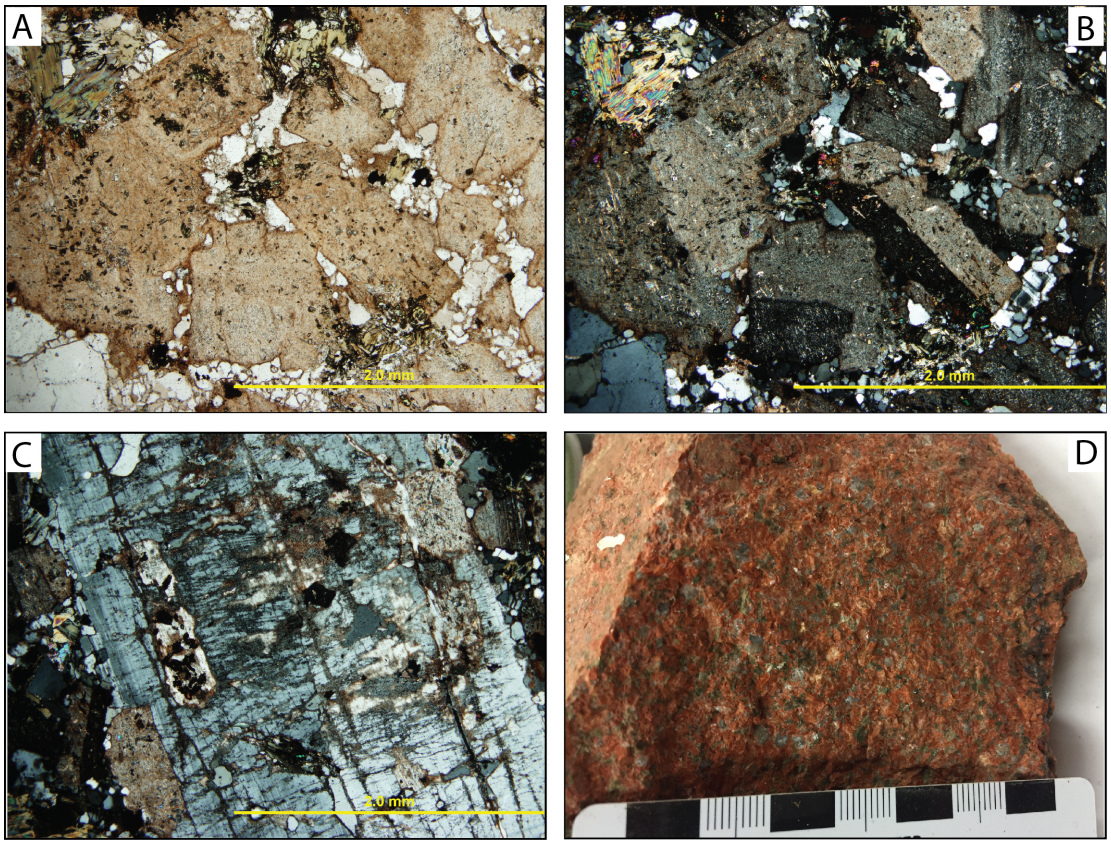

Figure 4.17. Petrographic and hand sample photos of hematite alteration. A) Photomicrograph of completely altered feldspar in PPL (Station 17KAM022B; UTM 504846 5409295). B) Photomicrograph of completely altered feldspar in XPL (Station 17KAM022B; UTM 504846 5409295). C) Photomicrograph of potassium feldspar phenocrysts with relic perthitic twinning (Station 17KAM022B; UTM 504846 5409295). D) Hand sample photo of hematite alteration (Station 17KAM093A; UTM 485361 5402928).

altered and overprinted by very fine-grained hematite. In plane polarized light the feldspars are dusted red, suggesting the presents of hematite (Fig. 4.17a, b, c). The phenocrysts can be poikilitic, with quartz, epidote and minor calcite. The sericite is generally very fine-grained but can occur as fine-grained laths (Fig. 4.17c). Quartz is

generally the most resistant to alteration. Calcite also occurs along fractures throughout the samples.

No primary amphibole or biotite were present, having been completely altered to chlorite. Two samples contained clinopyroxene phenocrysts in the highly hematite altered samples displaying simple twinning. In these samples the felspars have been completed altered to sericite and no primary textures are preserved. Less than 5% quartz was present in the samples. Some relic twinning can be seen in the coarse potassium feldspar phenocrysts (Fig. 4.17d).

4.3 Mineralization

The pluton generally contains disseminated pyrite and less commonly chalcopyrite with minor galena. Select areas are host to massive, coarse cubic pyrite as well as chalcopyrite (Fig. 4.18). The pluton is host to sporadic gold anomalies, generally in the eastern end of the batholith. Gold mineralization has been found both in the granodiorite and the cross-cutting quartz veins. Galena was also found to be hosted in the quartz veins (Fig. 4.18d). The North Zone and the Hematite Zone trench host gold values upwards of 1400 ppb. The two highest gold values (1407 ppb and 500 ppb) were hosted in the granodiorite, with the next highest value of 300 ppb to 159 ppb hosted in quartz veins. Molybdenite was found sporadically throughout the pluton, occurring with trace amounts of pyrite and chalcopyrite (Fig. 4.19). The molybdenite is frequently fine-grained and disseminated throughout quartz veins that cross cut the pluton, giving the quartz veins a grey colour (Fig. 4.19a, b, c). One occurrence on the southern contact with Lake Superior comprises a

40 cm wide vein that contains sulphide staining along with slivers of granodiorite caught up in the veining (Fig. 4.19a).

Figure 4.18. Molybdenum and pyrite in granodiorite. A) Quartz vein with disseminated molybdenum (Station 17KAM063; UTM 501865 5406189). B) Coarse-grained molybdenum in granodiorite (Station 17KAM072; UTM 483502 5404524). C) Coarse-grained molybdenum in quartz veins (Station 17KAM072; UTM 483502 5404524). D) Medium grained pyrite in monzogranite (Station 17KAM201; UTM 540680 5408520

The vein has areas that are a dusty grey in colour, due to the presence of disseminated molybdenum. This grab sample returned values of 44 ppm Mo, similar to molybdenum values in other areas in the batholith. Station 17KAM072A near the western end of the pluton is an exception to the typical molybdenum mineralization, as it contains coarse-grained molybdenum in both the granite and the cross-cutting quartz veins (Fig. 4.1; 4.19c). The molybdenum present in the

granite is disseminated but can be found as coarse pods up to 2 cm wide. Coarse pockets of molybdenum were found at station 17KAM072, along the western contact with the supracrustal rocks (Fig. 4.19b). The stockwork quartz veins cross-cuts the outcrop typically have disseminated sulphides, including pyrite and molybdenite.

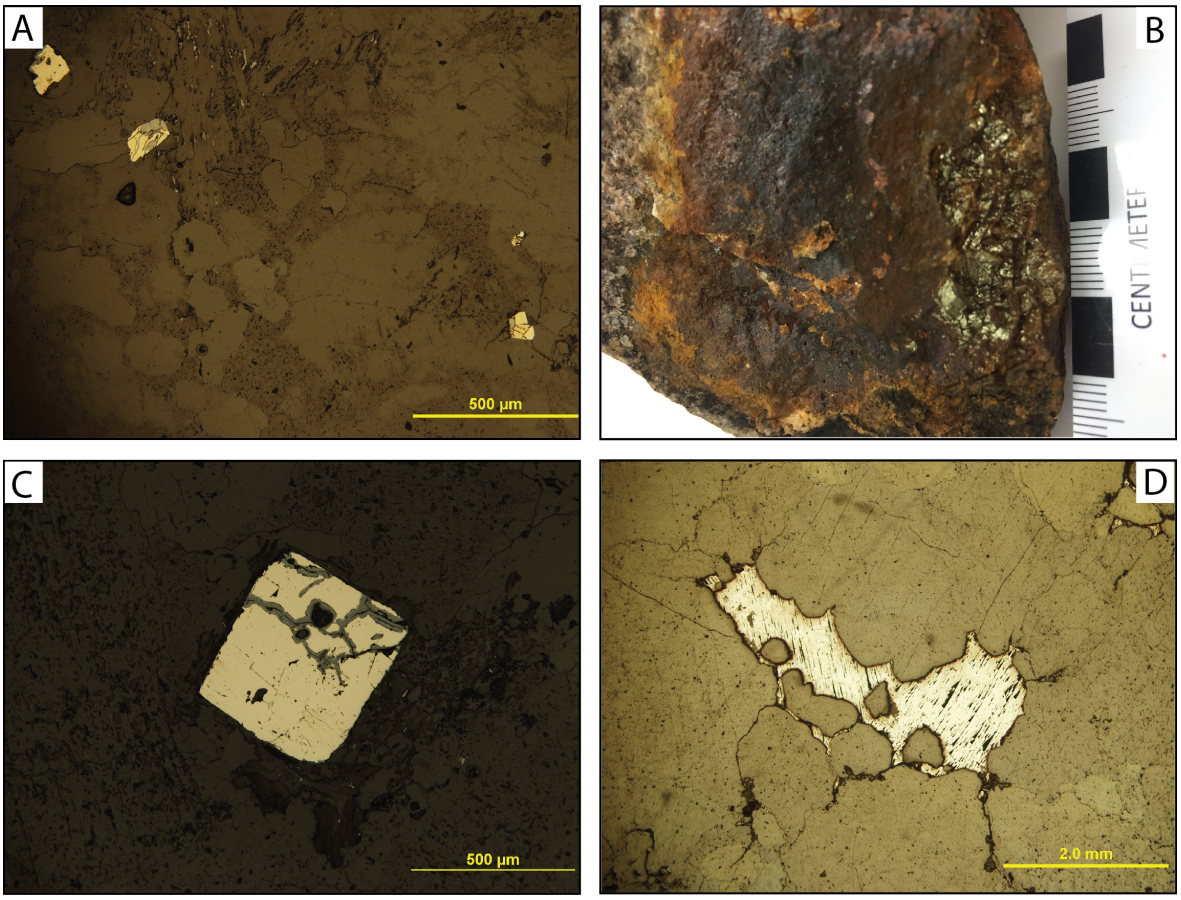

Figure 4.19. Photographs of mineralization. A) Photomicrograph of disseminated pyrite in granodiorite (Station 17KAM030; UTM 502461 5405593). B) Hand sample of massive pyrite and chalcopyrite (Station 16KAA019A; UTM 540681 5408528). C) Cubic pyrite with hematite alteration along edges and fractures (Station 16KAA019A; UTM 540681 5408528). D) Galena occurring in fractures in a quartz vein (Station 16KAA018A; UTM 504423 5408670).

4.4 Mineralized trenches

Mineralized trenches were mapped to determine the association with the pluton. Area of interest were stripped by local prospectors during gold exploration

in the area in 2016. The quartz veins that cross-cut the trenches, have a north-south and north-west trend and are mainly found in the east end of the pluton, where the trenches cover a 10 km area (Fig. 4.1). All trench maps are presented in Appendix D.

4.4.1 The North Zone

The North Zone is a stripped trench approximately 25m by 12m, in the northeast corner of the pluton (Fig. 4.1). The North Zone was stripped after grab samples in the area returned elevated gold values. The North Zone is composed of granodiorite crosscut by multiple parallel quartz veins with interstitial stock work veining (Fig. 4.20). The granodiorite is massive with no distinct foliation and disseminated pyrite and chalcopyrite (Fig. 4.21e). The outcrop hosts mafic xenoliths that range in size from 2 cm up to 26 cm. The outcrop is crosscut by a 7 cm wide pegmatitic vein at 288°/58°S. The composition of the pegmatitic vein was dominantly quartz, plagioclase and potassium feldspar. The vein has a distinct chill margin with fine-grained margins and increasing crystal size towards the middle. The outcrop was also crosscut by smaller aplitic veins ranging in size from 1 cm to 2 cm with similar orientations as the pegmatitic veins. Some areas of the granodiorite are sulphide rich and so appear rusty on surface. A distinct zone of epidote and chlorite altered granodiorite, oriented 018°/85° (SE), overprints the granodiorite and the stacked quartz veins.

The veins exposed on the surface have an average strike of 121° with dips between 26° and 41° (SW). The vein widths range between 1 cm to 15 cm, with the smaller veins exhibiting pinching and swelling. The quartz appears as sheeted veins that dip to the south.

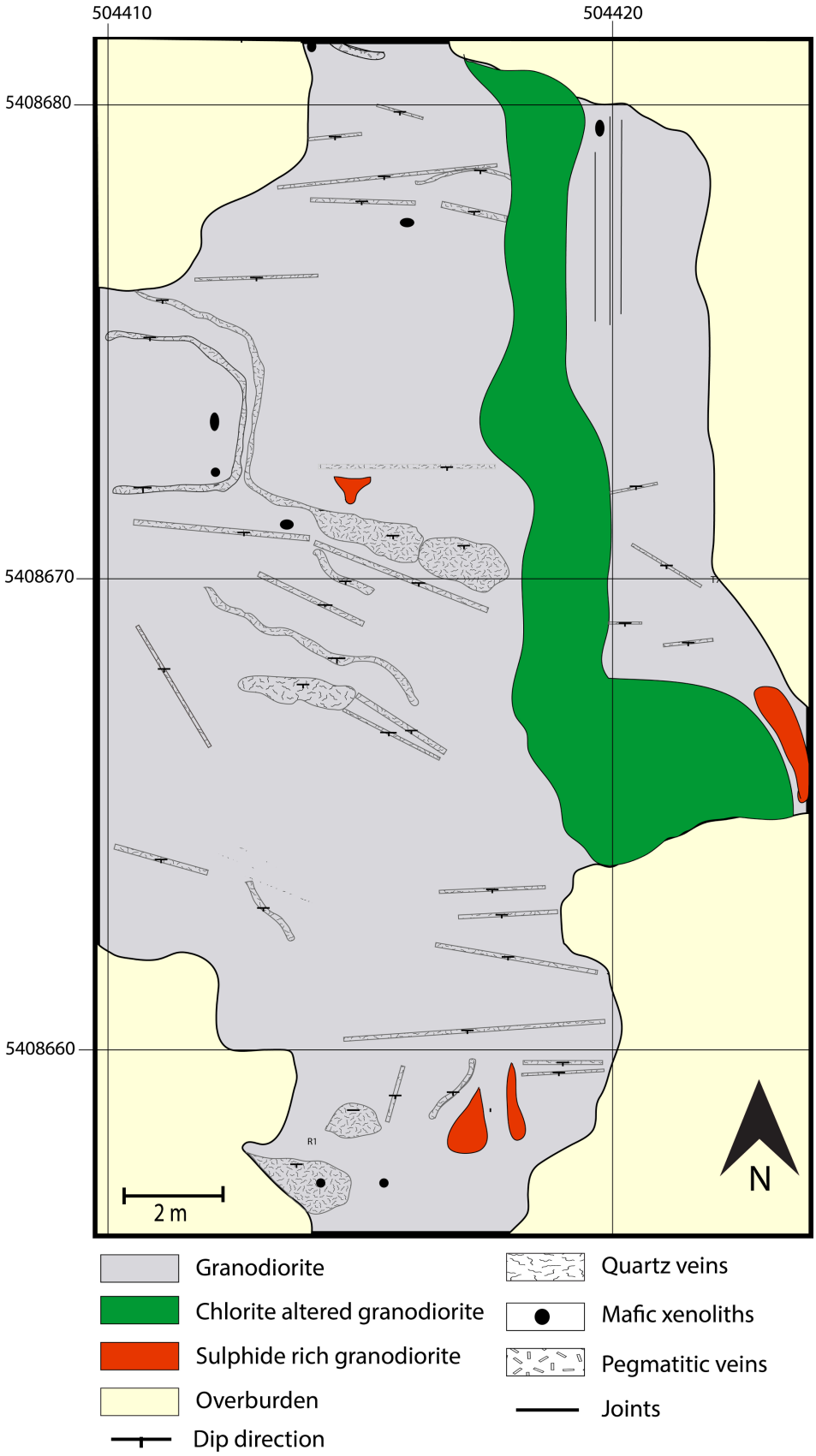

Figure 4.20 Trench map of North Zone.

In between the parallel sheet veins there are fine stock work quartz veins that originate from the sheet veins. Black tourmaline occurs as >1 cm wide veins along joints and fractures and along some of the quartz veins. Pyrite, chalcopyrite and galena are present in veins and disseminated in the granodiorite around the veins.

4.4.2 The Hematite Zone

The Hematite Zone is a stripped exposure located to the southeast of the North Zone. The zone is dominantly massive, unaltered, grey granodiorite with horizontal quartz veins occurring at the top of the outcrop. Several horizontal veins crosscut the granodiorite, ranging in width from 0.5 cm to 15 cm and consistently striking 210° with a near-horizontal dip of 5° (NW). Several vertical quartz veins with black tourmaline along the vein walls occur at the south end of the outcrop. Veins in both orientations host sulphide minerals, including pyrite and chalcopyrite. The granodiorite below the horizontally stacked quartz veins yielded gold values of 90 to 1407 ppb. Rare vertical quartz veins are present approximately 15 m to the south. Vertical veins range in width from 1 cm - 5 cm at an orientation of 313°/59°(SE). The vertical veins host little to no visible mineralization but have black tourmaline occurring along the contact with the granodiorite. Trace amounts of disseminated pyrite were identified in the veins.

A 40 cm wide zone of sheared, hematized granodiorite that has been highly altered is located on the northern end of the hematite Zone. There is little to no competent rock present in the sheared area, which trends at 294°/ 85°(SE) over 7 m before abruptly ending. Along the northern margin of the shear is a 20 cm wide calcite vein, that has areas of euhedral rose bud style calcite crystals.

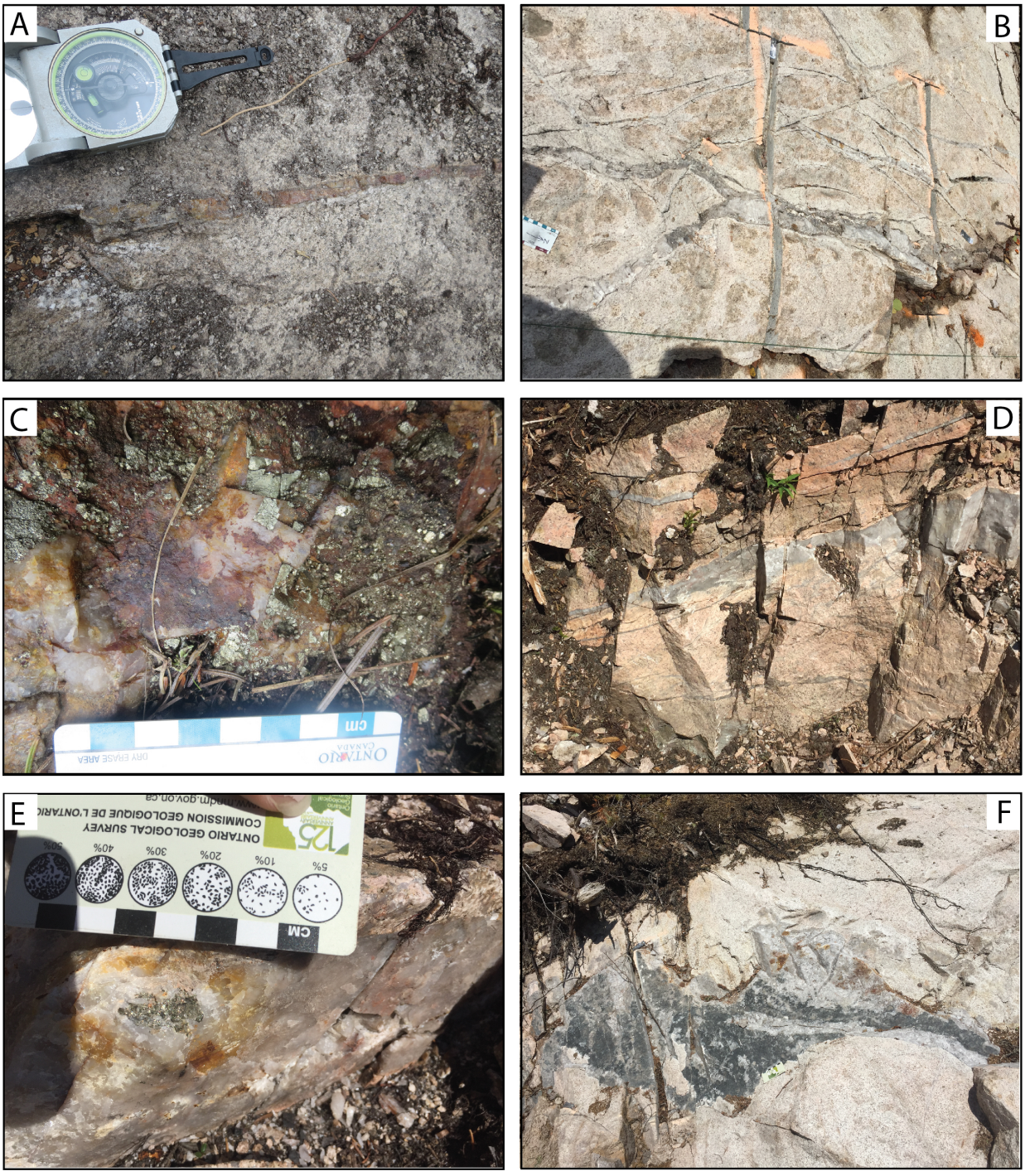

Figure 4.21 Field photos of mineralized trenches. A) Sulphide rich quartz vein (Trench 3). B) Bifurcated quartz vein (Station 17KAM022, Top of hill trench; UTM 504850 5409296). C) Massive cubic pyrite (Station 17KAM022, Top of hill trench; UTM 504850 5409296). D) Stacked quartz veins (Station 16KAA019, North Zone; UTM 540681 5408528). E) Chalcopyrite and pyrite mineralization (Station 16KAA019, North Zone; UTM 540681 5408528). F) Tourmaline veins (Station 17KAM022, Top of hill trench; UTM 504850 5409296).

4.4.3 Trench One

The 5 m by 6 m outcrop of is a grey homogeneous granodiorite. The outcrop is cut by quartz veins, up to 3 cm in width. Some of the quartz veins have abundant pyrite with minor chalcopyrite. Mafic xenoliths occur across the outcrop ranging in size from 3 cm - 5 cm. Tourmaline veins also cross-cut the outcrop parallel to the north-south quartz veins. The quartz veins all strike north-south with dips ranging from 30°- 53°(SE-SW).

4.4.4 Trench Two

Trench Two is located 5 m from Trench One and is approximately 4 m by 5 m. The outcrop was a grey/white homogeneous granodiorite. Trench Two has fewer quartz veins than Trench One but they were up to 10 cm in width, vary in size. Mafic xenoliths are common across the outcrop, ranging in size up to 8 cm. The quartz veins all dip to the west, and strike run north-south. A diabase dyke cross-cuts the outcrop at the north-west end. Structures run east-west across the outcrop, but no distinct offsets were observed. Disseminated pyrite and chalcopyrite are found in the quartz veins.

4.4.5 Trench Three

Located west three meters from Trench 2, Trench Three is approximately 7 m by 10 m, and consists of a grey homogeneous granodiorite. The outcrop is cross cut by stacked quartz veins. The veins range in size from 1 cm to 10 cm, and many of the veins vary in size. The quartz veins trend north south with dips ranging between 36° and 60°. Pyrite and minor chalcopyrite are commonly present in the undulating veins (Fig. 4.21a). The quartz veins extend across the entire length of the outcrop,

with very few pinching out. Trench three also has shears that run perpendicular to the veins in an east-west direction, but it these are less common.

4.4.6 Top of the Hill Trench

The Top of the Hill Trench is approximately 30 m long and 15 m wide. Unlike the other trenches it is cross-cut by over five diabase dykes that run horizontally across the trench (Fig. 4.22). The dykes range up to 10 cm in thickness and are perpendicular to the quartz veins but cross-cut the veins. In some cases, the dykes intruded on top of each other stacking upwards on the outcrop. Tourmaline was found along the contacts of the quartz veins and as sheets. The quartz veins run perpendicular to the outcrop with approximately north-south strike and dips between 50° to 70° (Fig. 4.21b). The widths of the veins ranging from 1 cm to 20 cm. The quartz veins have minor amounts of disseminated pyrite with minor chalcopyrite, but in some cases the veins have black tourmaline occurring along the edge of the vein, similar to the veins in the North and Hematite Zone trenches (Fig. 4.21e, f). There are areas that host massive sulphides, generally cubic pyrite but did not return significant gold values (Fig. 4.21e). The veins occasionally splay and bifurcate into multiple veins and stockwork veining is common between the sheet veins (Fig. 4.21b). The veins are broadly parallel are to be stacked on top of each other similar to the North Zone trench. Tension gash quartz veins are present in one section of the trench, cutting the exposed diabase sills.

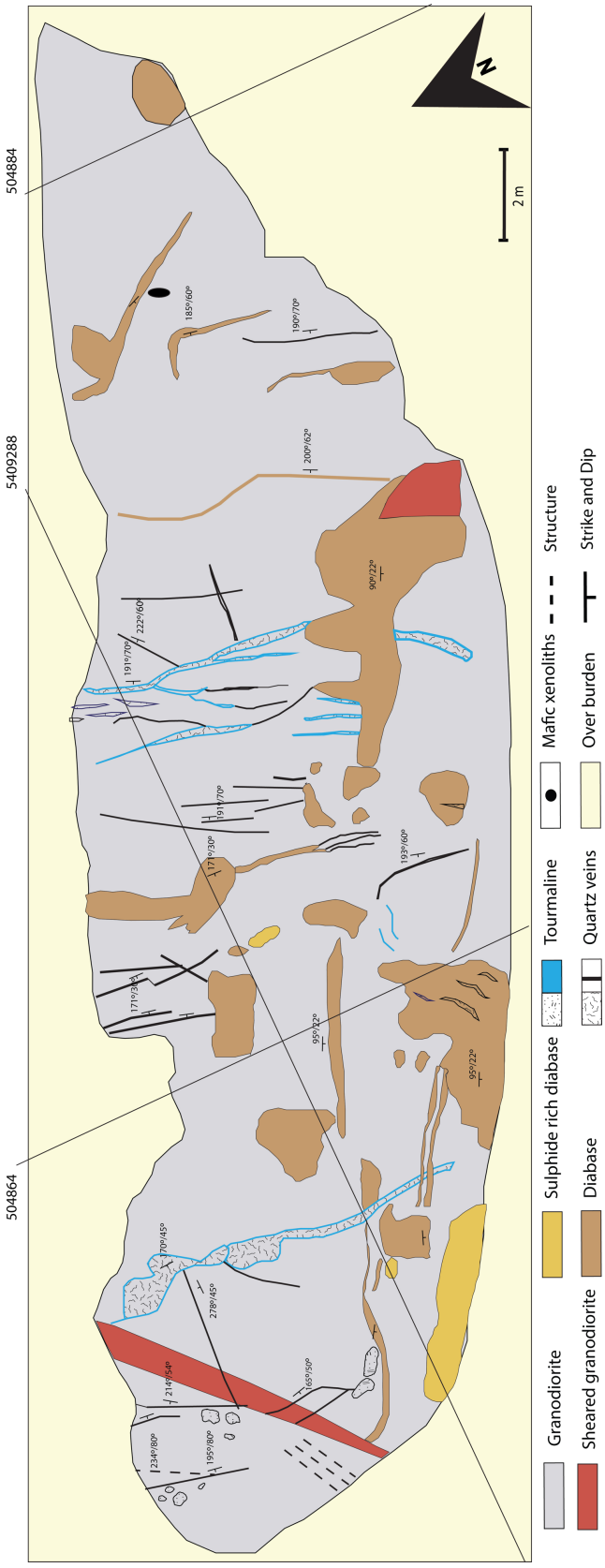

Figure 4.22 Trench map of top of the hill trench.

Chapter 5: Whole Rock and Isotope Geochemistry Results

5.1 Whole rock geochemistry

Major and trace element analysis of 147 field samples was completed to characterize the Terrace Bay Batholith in order to evaluate the genesis and tectonic environment. Geochemistry will be used to investigate if the different units have distinct geochemical signatures. The mafic xenoliths that occur within the pluton will also be described.

Harker diagrams plotting Al_2O, MgO, K_2O, Na_2O, TiO_2 and P_2O_5 versus SiO_2 and plots of SiO_2 versus Th, Y, Yb, Nb, Sr, Rb, U and Zr are shown in Figures 5.1 and 5.2. The elements which show a linear trend are interpreted to be immobile whereas the elements which have a large scatter are considered to have been mobile during metamorphism and hydrothermal metasomatism (Rollinson, 1993). All samples have been recalculated to a 100% volatile free basis to account for variations in the loss on ignition (LOI). Most rock types display linear patterns on Figures 5.1 and 5.2, but show scatter in the Al_2O_3, $K_2O$and Na_2O plots, indicating mobility of these oxides, most likely caused by metamorphism and the alteration of the primary mineralogy.

The altered granodiorite samples were plotted on the Harker diagrams to show that there is an increased mobility in Al_2O_3, K_2O, Fe_2O_3 and Na_2O plots when compared to the unaltered lithologies. In general, high field strength elements (HFSE) Th, Zr, Hf, Ti, Nb, Ta, P, Y, and rare-earth elements (REE) are typically immobile during hydrothermal alteration or metamorphism (Rollinson, 1993). The immobile elements better reflect the primary geochemical signature of the rocks.

These immobile elements such as La, Th, Y, Yb, Ti and Zr are the elements used for rock classification and to infer tectonic settings. Full geochemical results are presented in Appendix E.

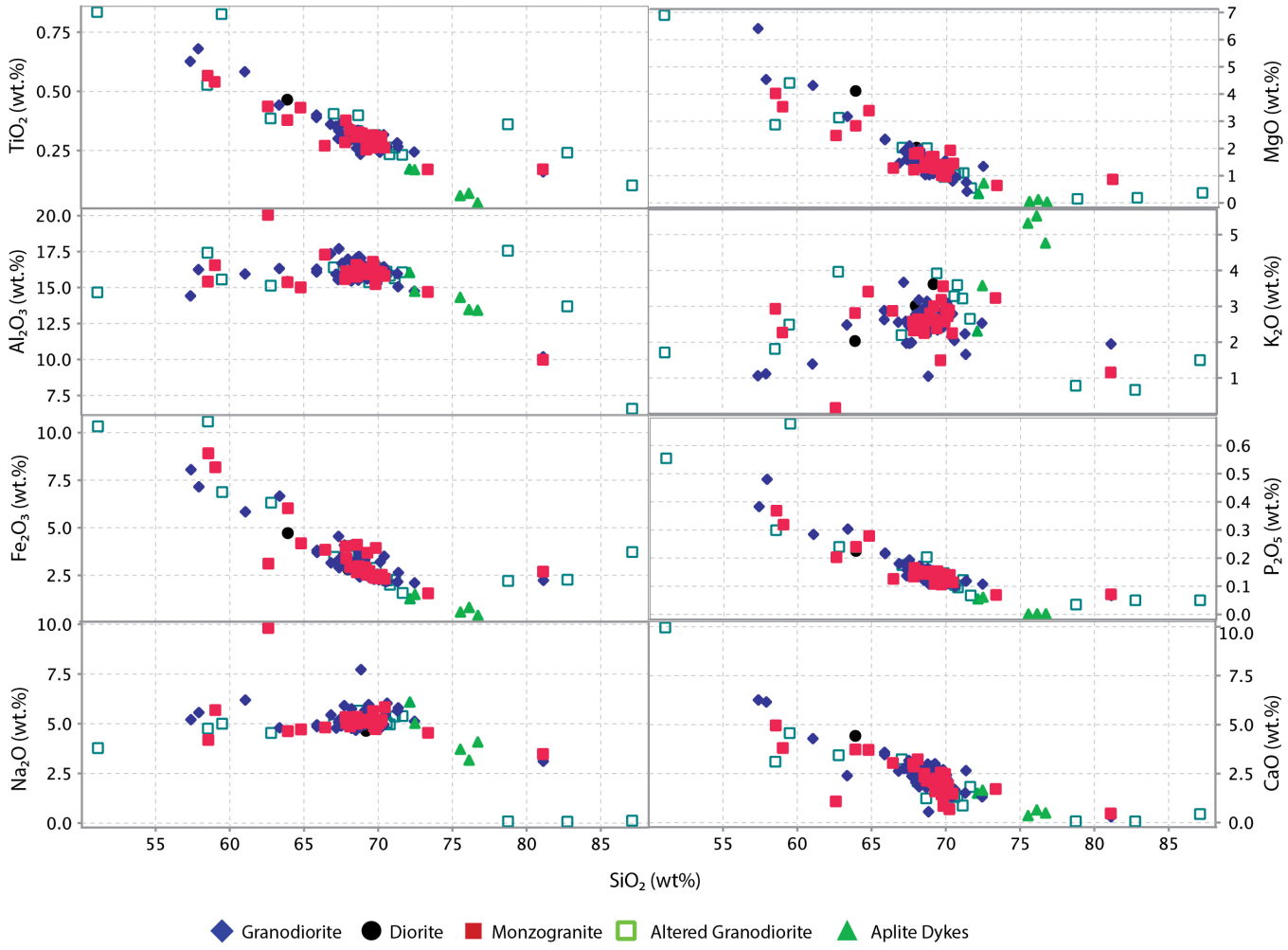

Figure 5.1: Variation diagrams of SiO_2 versus major element oxides for each lithology

5 .1.1 Granodiorite

Seventy samples were selected from the granodiorite for geochemical analysis. The granodiorite is characterized by anhydrous SiO_2 values of 57- 81 wt.%, Fe_2O_3 of 1-8 wt.%, TiO_2 of 0.1 - 0.6 wt. %, MgO of 0.2 – 6 wt.% and Mg # (100x(Mg/Mg+Fe)) of 13.7 – 44.3. Gold values ranges from 0.7 ppb to 500 ppb, with

an outlier of 1407 ppb, and Mo ranges from 0.82 ppm to 45.86 ppm with mean values of 12.08 ppb and 3.83 ppm respectively. The granodiorite has a mean Cu content of 13.6 ppm with one outlier of 3022.7 ppm. On primitive mantle normalized diagrams, the granodiorite is characterized by negative Nb and Ti anomalies (Nb/Nb*= 0.05-0.26; Ti/Ti*= 0.10-0.31) as well as negative Zr and Hf anomalies (Zr/Zr*= 0.38-1.73; Hf/Hf*= 0.37- 1.69; Fig. 5.3A). A majority of the samples show elevated LREE values (La/Sm_n values of 2.89- 11.4) and depleted HREE (Gd/Yb values ranges from 1.19- 3.29; Fig. 5.3A).

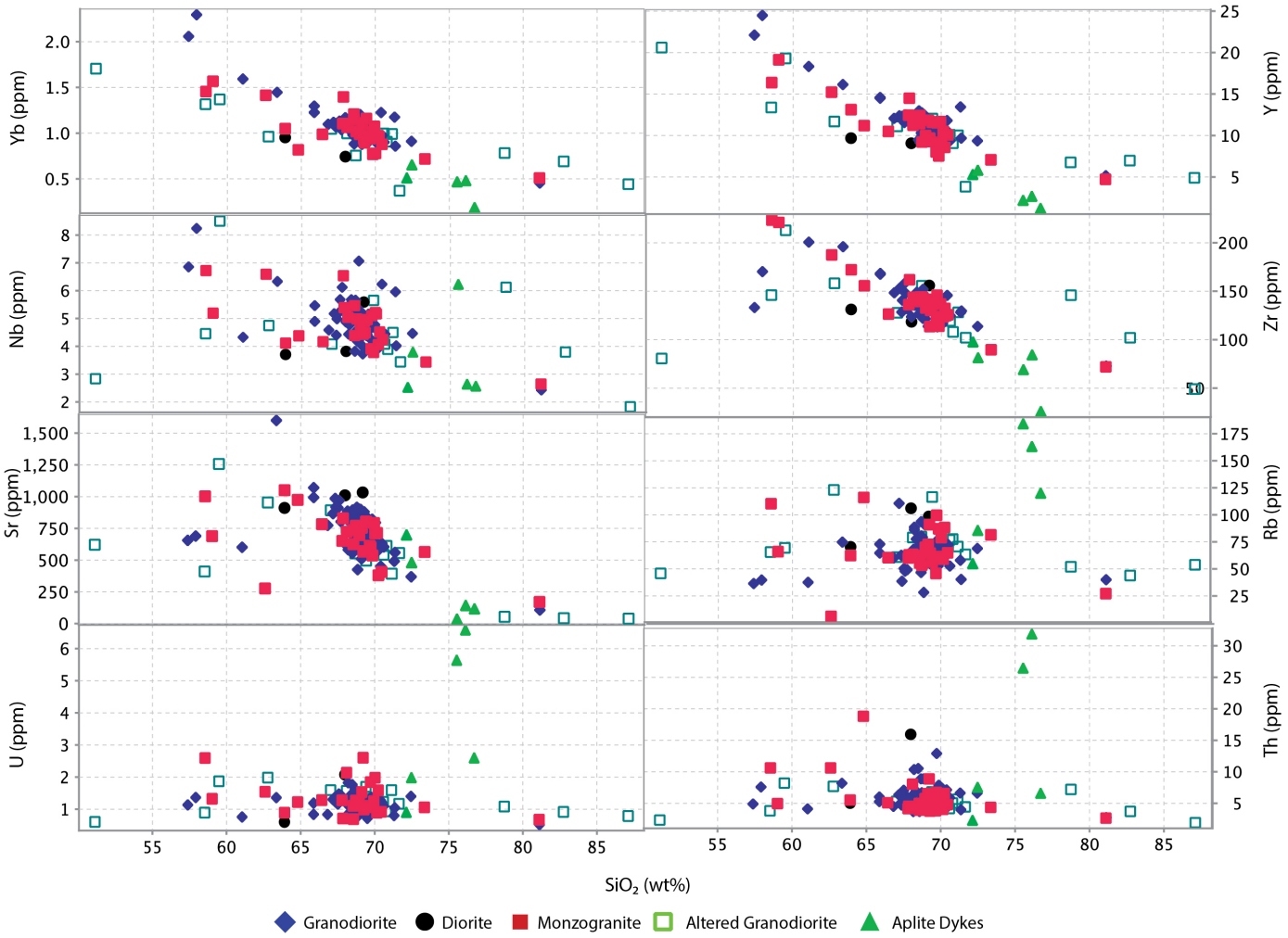

Figure 5.2: Variation diagrams of SiO_2 versus trace elements for each lithology.

5.1.2 Monzogranite

Twenty-five samples of the monzogranite were selected for geochemistry. The monzogranite is characterized by anhydrous SiO_2 values of 58- 82 wt.%, Fe_2O_3 of 1-10 wt. %, TiO_2 of 0.17-0.8 wt. %, MgO of 0.1- 6 wt. %, K_2O of 0.16-3.96 wt. % and Mg# of 24.26 – 44.7. The whole rock Au content range from 0.3 ppb to 32 ppb and Mo ranges from 0.72 ppm to 8.01 ppm, with mean values of 4.024 ppb and 2.39 ppm, respectively. When plotted on a primitive mantle normalized diagram, the majority of the samples show similar trends to the granodiorite with negative Nb and Ti anomalies (Nb/Nb*= 0.05- 0.24; Ti/Ti*= 0.1-0.4; Fig. 5.3B), whereas the negative Zr and Hf anomalies are weaker in the monzogranite (Zr/Zr*=0.55- 0.99; Hf/Hf*=0.52- 0.95). The monzogranite displays the same LREE enrichment (La/Sm_n = 2.5 – 7.2) and depleted HREE (Gd/Yb= 1.5- 4.93; Fig. 5.3B) as the granodiorite.

5.1.3 Diorite

Three samples were submitted for the diorite, it is characterized by anhydrous SiO_2 values of 63-69 wt.%, Fe_2O_3 of 2-4 wt. %, TiO_2 of 0.29- 0.46 wt. %, MgO of 0.09- 0.04 wt. %, and Mg # of 37.09- 46.56. The gold contents range from 1.1 to 3 ppb and Mo ranges from 0.99 ppm to 2.3 ppm, with mean values of 2.5 ppb and 1.69 ppm, respectively. The diorite exhibits the same negative Nb and Ti anomalies as the other lithologies (Nb/Nb*= 0.08-0.13; Ti/Ti*= 0.27-0.17). The diorite has a very weak negative Zr and Hf anomalies (Zr/Zr*= 0.62-0.89; Hf/Hf*= 0.64-0.83; Fig. 5.3C). On a primitive mantle normalized spider diagram the diorite displays similar LREE enrichment (La/Sm_n = 4.36-4.35) and fractionated HREE (Gd/Yb_n= 2.89-3.52 Fig. 5.3C).

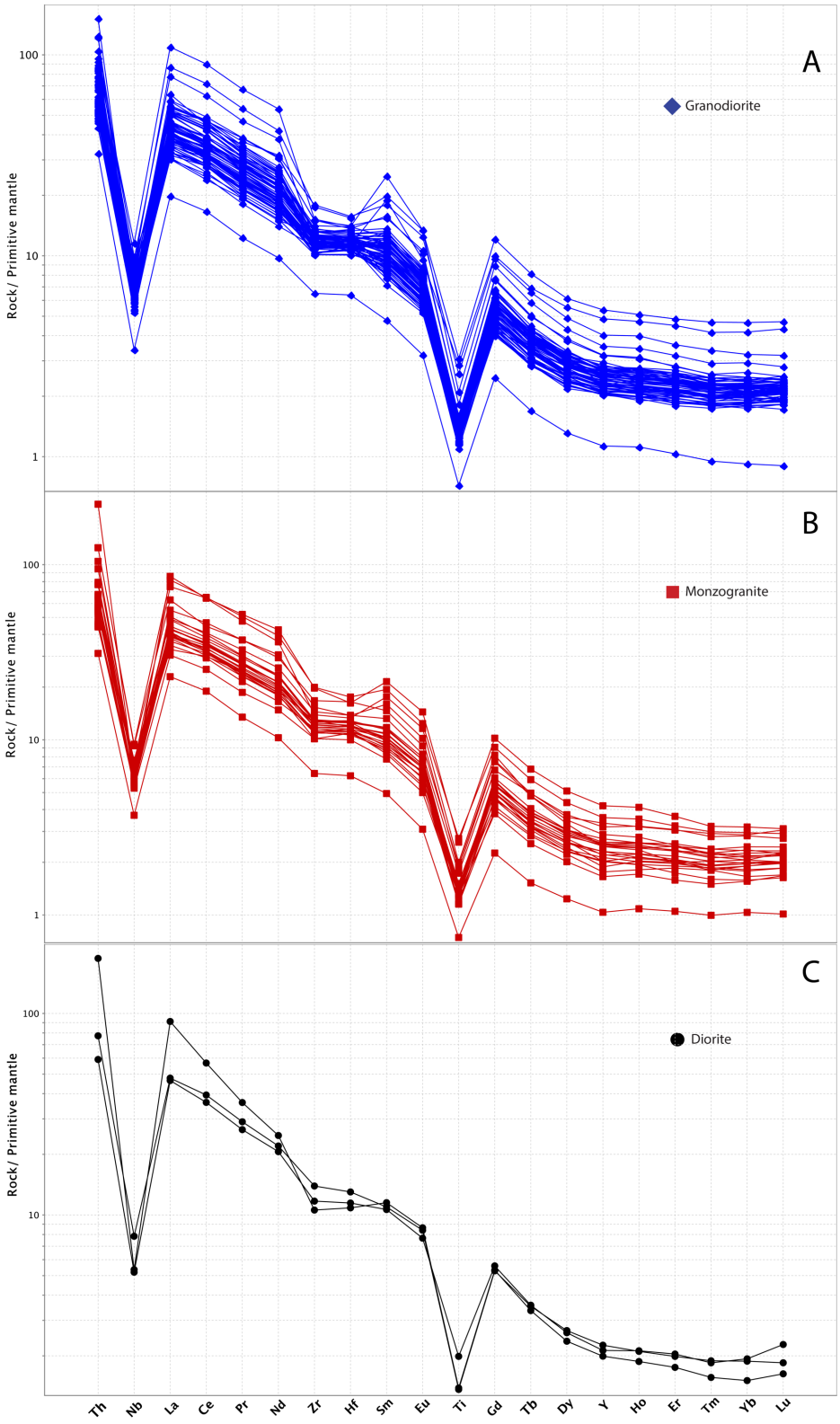

Figure 5.3: Primitive mantle normalized plots for the samples from the granodiorite (A), monzogranite (B), and diorite (C). Normalizing values from Sun and McDonough (1989).

5.1.4 Mafic Xenoliths

The mafic xenoliths have anhydrous SiO_2 values of 45.0-51.7 wt. % and Fe_2O_3 and MgO values of 13.8-21.5 wt. % and 4.88-7.6 wt. %, respectively. On a primitive mantle normalized diagram the xenoliths display LREE enrichment (La/Sm_n values

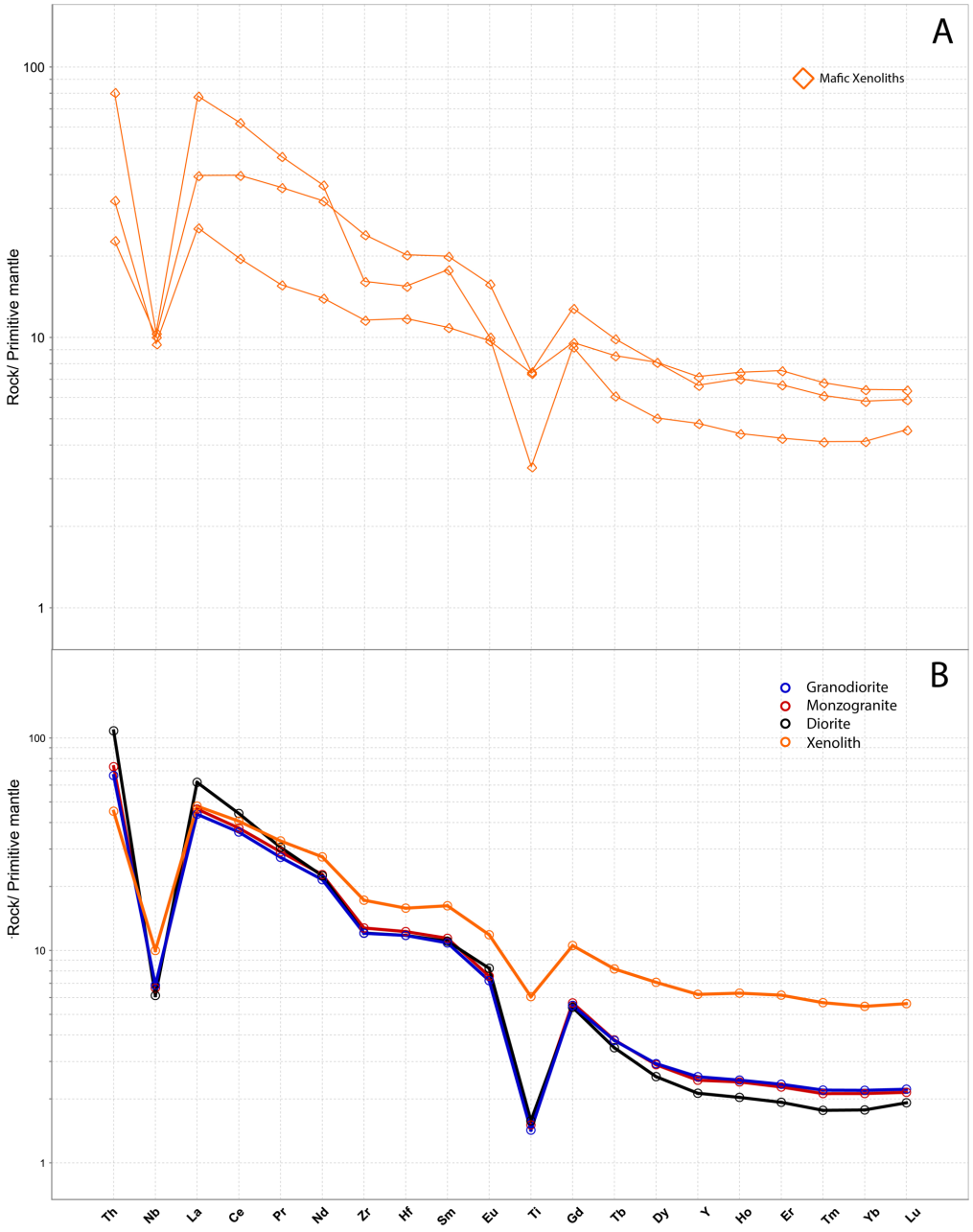

Figure 5.4: Primitive mantle normalized plots for the samples from the Mafic Xenolith (top, A) and the mean values of each lithology (bottom, B). Mean values: Granodiorite n= 70, Monzogranite n=25, Diorite n= 3, Mafic Xenolith n= 3. Normalizing values from Sun and McDonough (1989).

of 1.98-4.38) and fractionated HREE (Gd/Yb values ranges from 1.49-2.23, Fig. 5.4A). The xenoliths have moderate to weak negative Nb and Ti anomalies (Nb/Nb* = 0.10-0.28 and Ti/Ti*= 0.23-0.66; Fig. 5.4A).

5.2 Neodymiun–samarium isotopes

Seven samples were analyzed for Nd- Sm isotopes in order to investigate the magmatic source and tectonic setting in which the rocks formed. Representative and least altered samples from the granodiorite, monzogranite and diorite were chosen for this study. The results are summarized in Table 5.1 and full results provided in Appendix F.

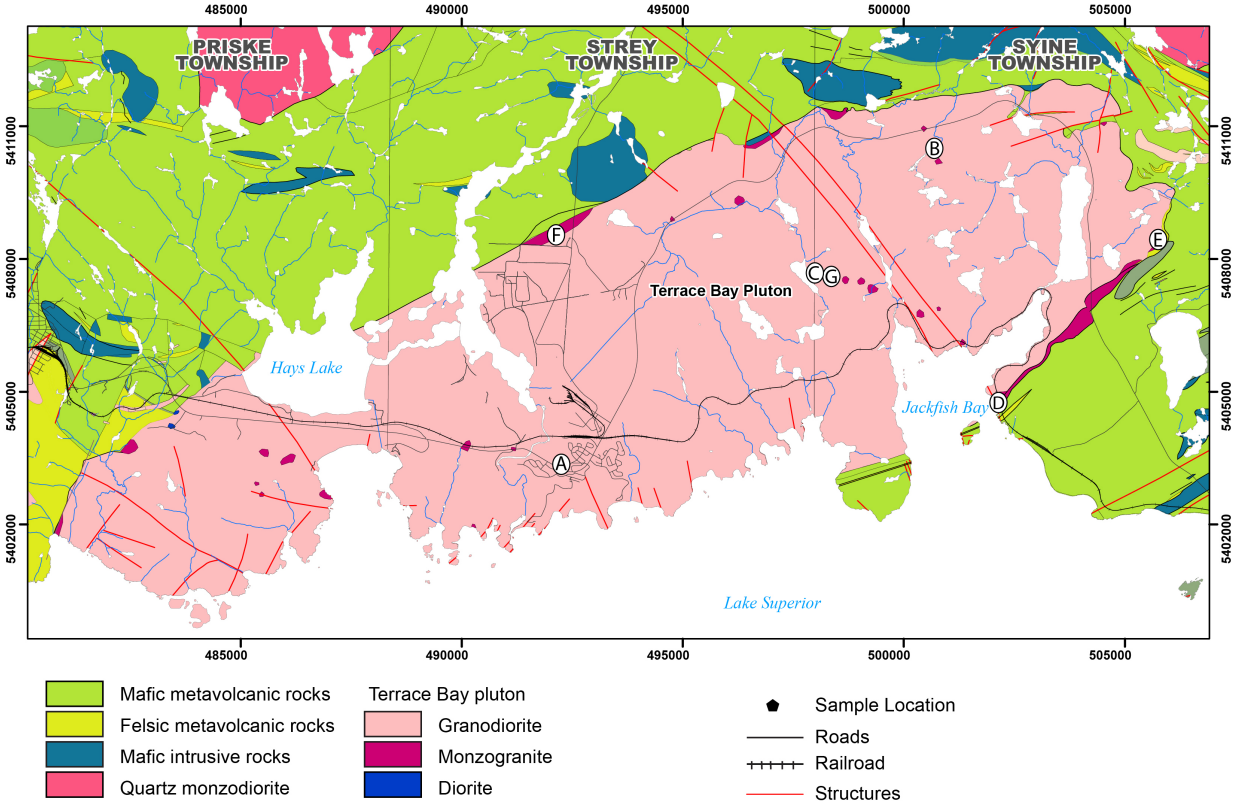

Figure 5.5 Sample locations of the Sm-Nd isotope samples. A: Station 17KAM024A UTM 505898 5403317; B: Station 17KAM007A UTM 500690 5410489; C: Station 17KAM038A UTM 498009 5407647; D: Station 16KAA020A UTM 502116 5404952; E: Station 17KAM074A UTM 505898 5408314; F: Station 17KAM025A UTM 492139 5408522; G: Station 17KAM039B 498239 5407615.

An age of 2689 Ma (Kamo, 2018) was used to calculate the ε_{Nd} values for the granodiorite and monzogranite samples with three samples selected from each lithology. The samples of the granodiorite were selected from the center of the pluton. The whole rock Sm and Nd values for granodiorite range from 3.58- 4.57 and 21.9-29.0. The samples have initial $^{143}Nd/^{144}Nd$ values of 0.50926-0.5093 and a range of ε_{Nd} values from 2.23 to 3.69 (Table 5.1). The monzogranite samples were selected from a marginal phase along the contact with the supracrustal rocks with initial $^{143}Nd/^{144}Nd$ values of 0.50926-0.50927 and have a range of ε_{Nd} values from 2.16 to 2.33 (Table 5.1). The whole rock Sm and Nd values for the monzogranite range from 4.5-7.09 and 26.7-41.42. The diorite age of 2690 Ma (Kamo, 2018) was used to calculate the εNd values for the one diorite sample. The diorite sample has initial $^{143}Nd/^{144}Nd$ value of 0.50927 and an ε_{Nd} value of 2.39 (Table 5.1). The average whole rock Sm and Nd values for the diorite are 4.72 and 27.9, respectively.

Table 5.1 Sm-Nd isotope results.

Sample	Lithology	$^{143}Nd/^{144}Nd$ current	$^{143}Nd/^{144}Nd$ Initial	ε_{Ndt}	Age (Ma)
17KAM024A	Granodiorite	0.511043	0.50926	$2.239 \pm_{0.138}$	2689
17KAM007A	Granodiorite	0.511030	0.50926	$2.282 \pm_{0.157}$	2689
17KAM038A	Granodiorite	0.511020	0.50928	$2.498 \pm^{0.138}$	2689
16KAA020A	Monzogranite	0.511074	0.50926	$2.207 \pm^{0.138}$	2689
17KAM074A	Monzogranite	0.511067	0.50926	$2.160 \pm^{0.138}$	2689
17KAM025A	Monzogranite	0.511056	0.50927	$2.335 \pm^{0.138}$	2689
17KAM039B	Diorite	0.511053	0.50927	$2.396 \pm^{0.138}$	2690

5.3 Rhenium - Osmium Isotopes

One sample of molybdenite from the granodiorite was sent to the University of Alberta to be dated using ^{187}Re-^{187}Os. The sample was of the coarse-grained

molybdenite from the eastern end of the pluton (Fig. 5.6). The results yielded a molybdenum mineralization age of 2671+/- 12 Ma (Table 5.2).

Table 5.2: Results of the rhenium-osmium analyses of a molybdenite sample from the Terrace Bay Batholith.

Re ppm	^{187}Re ppm	^{187}Os ppb	Model Age (Ma)	±2σ (Ma)
48.10	30.23	1376	2671	12

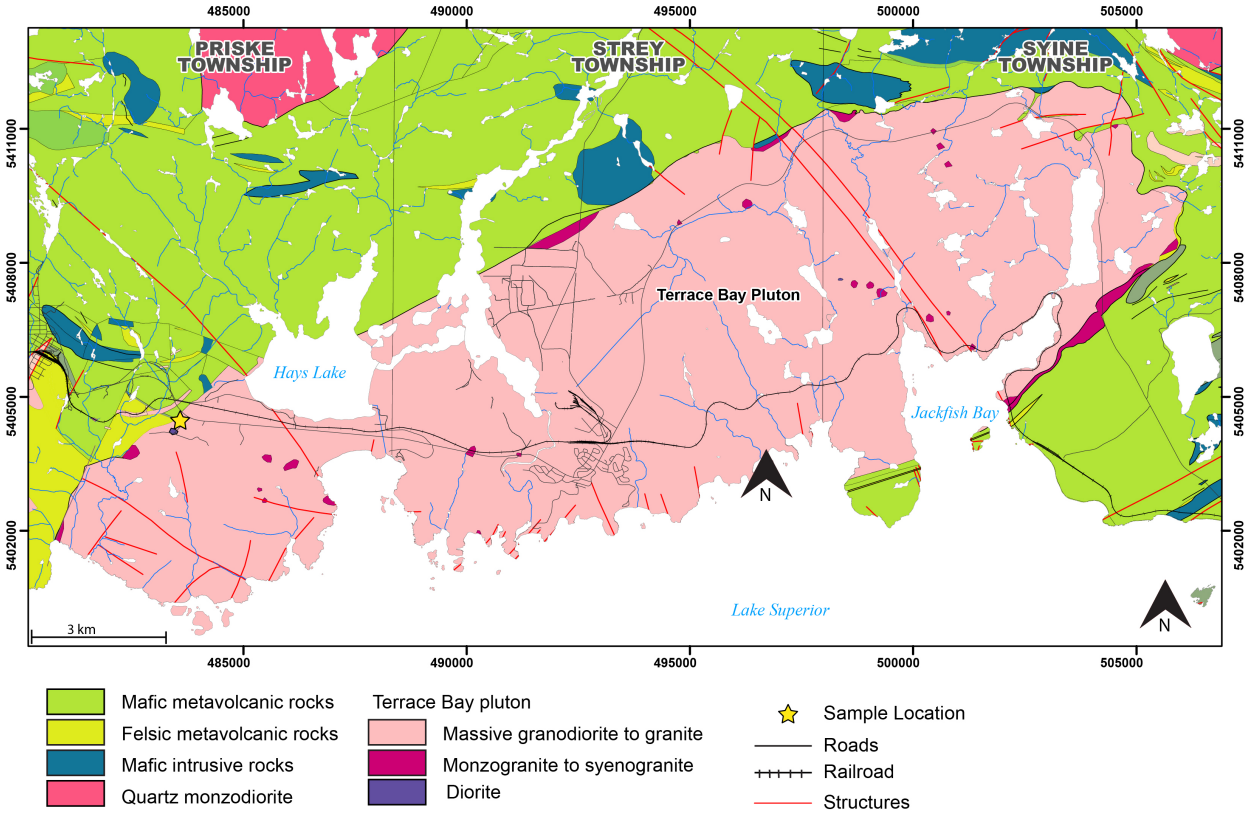

Figure 5.6 Location of sample taken for Re-Os geochronology. (A: Station 17KAM072, UTM 483501 5404524).

Chapter 6: Discussion

6.1 Petrography

The granodiorite in the Terrace Bay Batholith has been subdivided into three distinct lithological units: a massive, locally quartz and potassium feldspar porphyritic granodiorite; a pink to red equigranular monzogranite and a massive diorite (Chapter 4). The mineralogy of the Terrace Bay Batholith does not vary significantly between lithologies, with compositional changes predominantly controlled by variations in the modal abundance of the constituent minerals. All lithologies are characterized by the stable mineral assemblages of quartz, plagioclase, K-feldspar, amphibole, biotite, magnetite and titanite. The key differences between lithologies is an increase in K-feldspar and a decrease in plagioclase and quartz in the monzogranite lithologies compared to the granodiorite, as well as an increased amount of amphibole and biotite. When plotted on a QAPF diagram both the granodiorite and monzogranite plot within the range of granodiorite to monzogranite, whereas the diorite falls entirely in the monzodiorite field (Fig. 4.3).

A pervasive hematite alteration is present sporadically across the pluton, always occurring in proximity to large-scale faults and shear zones. The zones of alteration are characterized by intensely altered feldspars with up to 80% replacement by very fine-grained sericite/white micas overprinted by hematite. The hematite alteration occurs as a very fine-grained dusting across the samples, with quartz crystals generally showing the least amount of hematite alteration, typically less than 15%. Samples from the zones of alteration were not used for geochemical classification because of the increased mobility potential for elements.

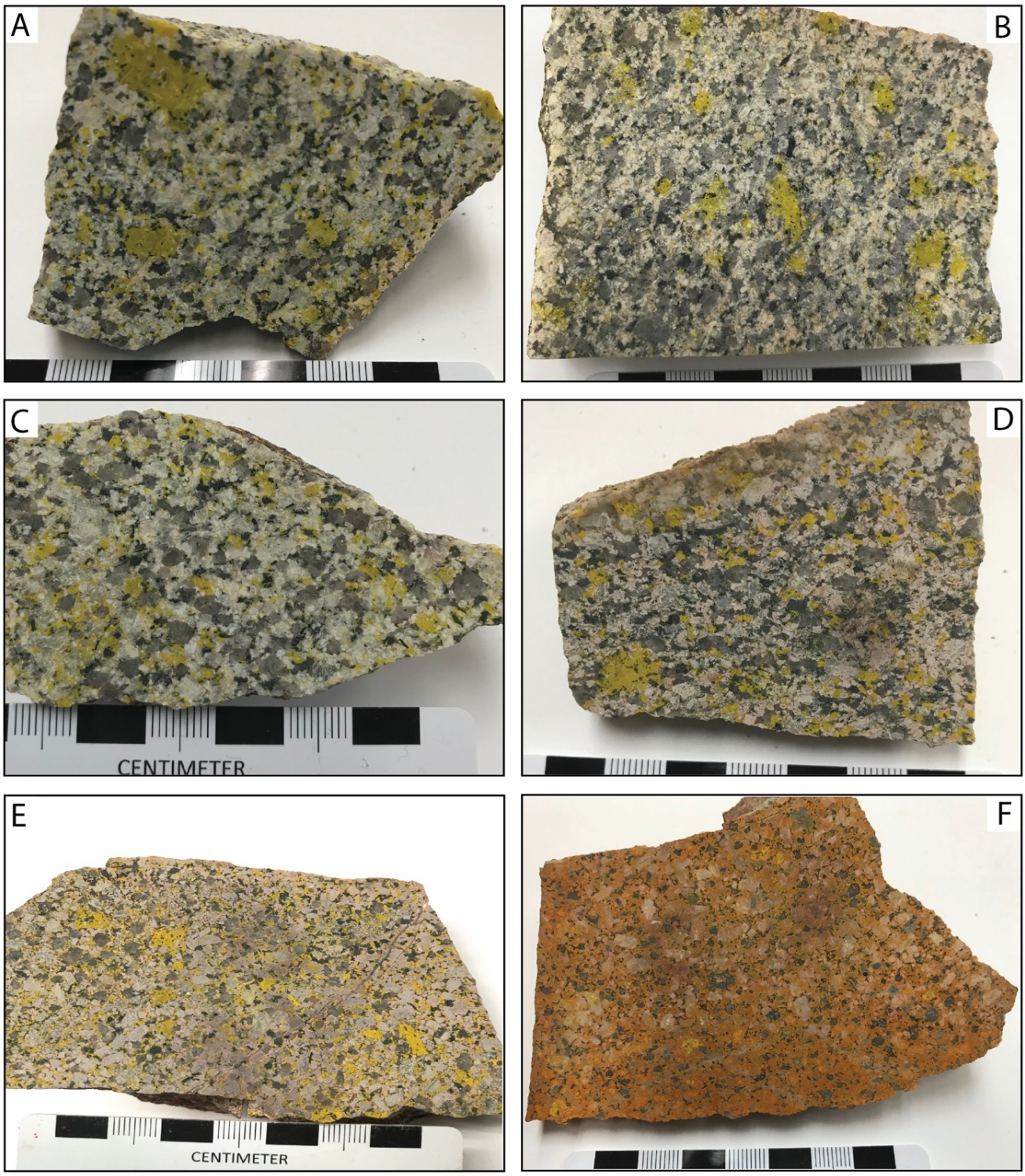

Figure 6.1. Photographs of lithologies showing sodium cobaltinitrite staining. A) Granodiorite (station 17KAA026 UTM: 497547 5404904. B) Granodiorite (station 17KAM032A UTM: 503185 54061166). C) Granodiorite (station 16KAA025A UTM: 493719 5402538). D) Monzogranite (station 16KAA020A UTM: 502116 5404952). E) Monzogranite (station 17KAM089A UTM: 490265 5401952). F) Hematite alteration (station 17KAM093A UTM: 485361 5402928).

Figure 6.1 shows photographs of the granodiorite, monzodiorite and hematite alteration after sodium cobaltinitrite staining to show potassium feldspars. Photographs 6.1a, b and c are granodiorite, with sporadic potassium feldspar phenocrysts primarily occurring as interstitial material. In the monzogranite (Fig. 6.1d, e) potassium feldspars are more evenly distributed throughout the samples and occur interstitially. The hematite alteration sample includes some fine-grained potassium feldspar grains, but the distinct red colour coming from fine-grained hematite is overprinting the mineralogy.

The pluton has undergone greenschist facies metamorphism with alteration of mafic minerals to chlorite, and feldspars to epidote and sericite. The effect of metamorphism is seen across the pluton, but dominantly occurs as less than 25% alteration of a given sample. Sericite alteration of feldspars occurs in varying degrees of intensity from weak to intense (Fig. 4.2). The metamorphic chlorite alteration varies from minor to complete alteration of amphibole and biotite. It is distinguished from the hydrothermal alteration based on the fact that the hydrothermal alteration overprints any effects of metamorphism.

Only 15 outcrops were identified that show intense hydrothermal alteration to hematite, sericite, chlorite and calcite (Fig. 6.2). The hematite and epidote/chlorite alteration were dominantly found in proximity to large-scale shear zones and faults that cross-cut the pluton, in outcrops ranging in size from 10 to 20 m. This suggests that these structures likely acted as pathways for hydrothermal fluids. The structures that cross-cut the pluton are shown in Figure 6.2 as red lines, in relation to outcrops of hematite alteration. Only three areas of alteration do not occur in proximity to a large-scale fault or shear zones.

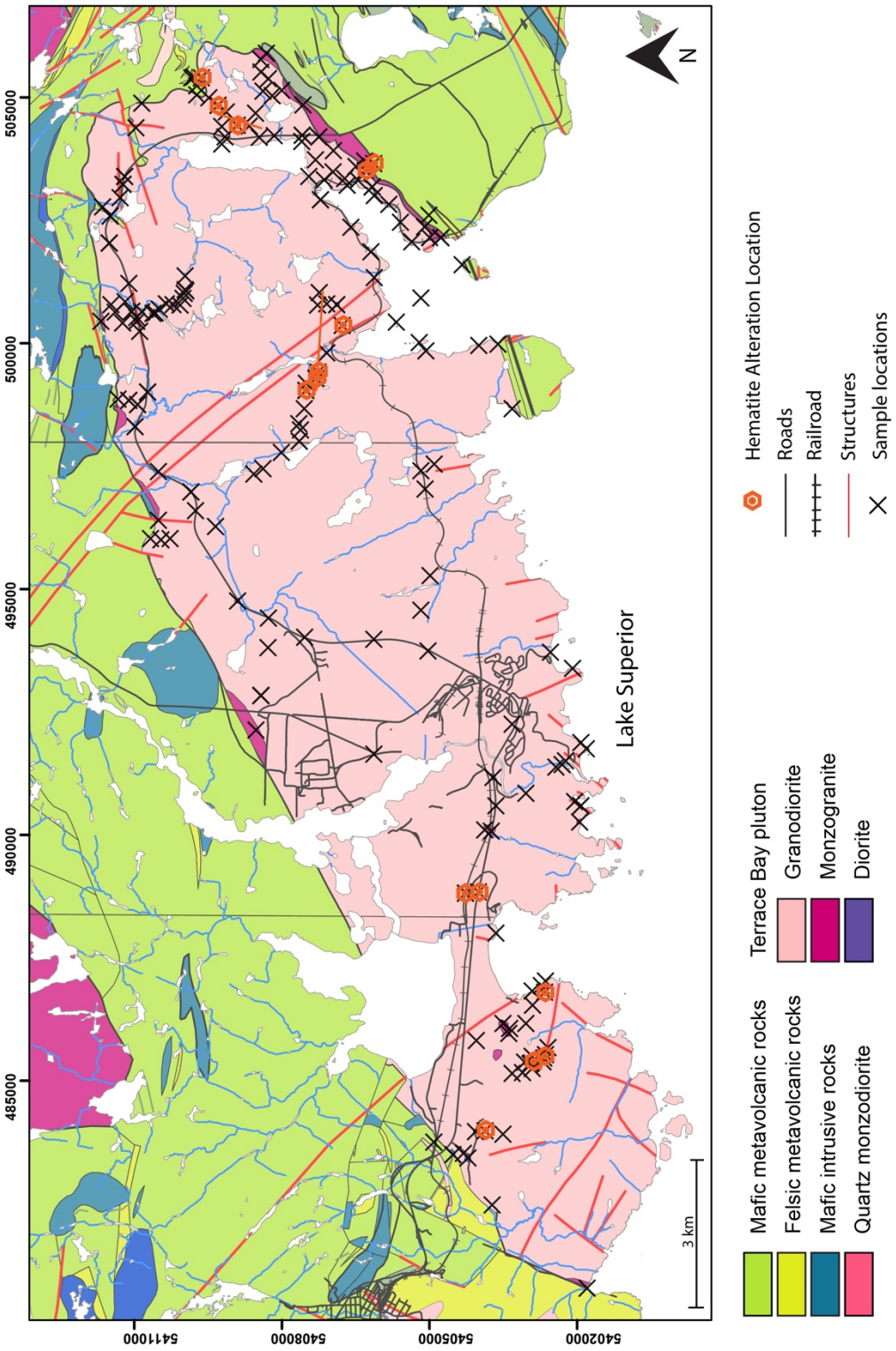

Figure 6.2. Structural and alteration map of the Terrace Bay Batholith. Modified from Stott et al. (2010).

The rest of the zones of alteration are all found near shear zones. The link between shear zones and increased degrees of metasomatism or mineralization has been suggested by many authors, who have suggested that shear zones make suitable fluid flow pathways (Kerrich et al., 1997; Oliver, 2001; Goldfarb et al., 2005). As the shear zones likely acted as pathways for hydrothermal fluids it is also likely that they were also conduits for mineralizing fluids in the pluton.

The chlorite-epidote alteration is primarily found along faults and fractures with quartz veins that cross-cut the pluton. The hematite alteration has overprinted the mineralogy (Fig. 6.1f). The magnetic susceptibility of the samples were recorded in the field. The replacement of magnetite by hematite is supported by the hematite altered granitoid sample having the lowest average value of $4.1x10^{-3}$ SI units, whereas an average value for the granodiorite was $8.3x\ 10^{-3}$ SI units and the monzogranite had an average value of $5.9x\ 10^{-3}$ SI units.

Pyroxenes are rarely found in the monzogranite but occur sporadically in the granodiorite. In one outcrop pyroxene phenocrysts were rimmed by amphibole (Fig. 4.4a, b). This is consistent with early crystallization of clinopyroxene in a more primitive magma that subsequently evolved to crystalize amphibole (Cao et al., 2018). This change in magma composition during crystallization, could have been trigged by an increase in magmatic water content (Cao et al., 2018). This texture is a rare but not uncommon feature in granitoids, as pyroxenes rimmed with amphiboles are also seen in plutons associated with the Hemlo assemblage of the belt (Beakhouse, 2007).

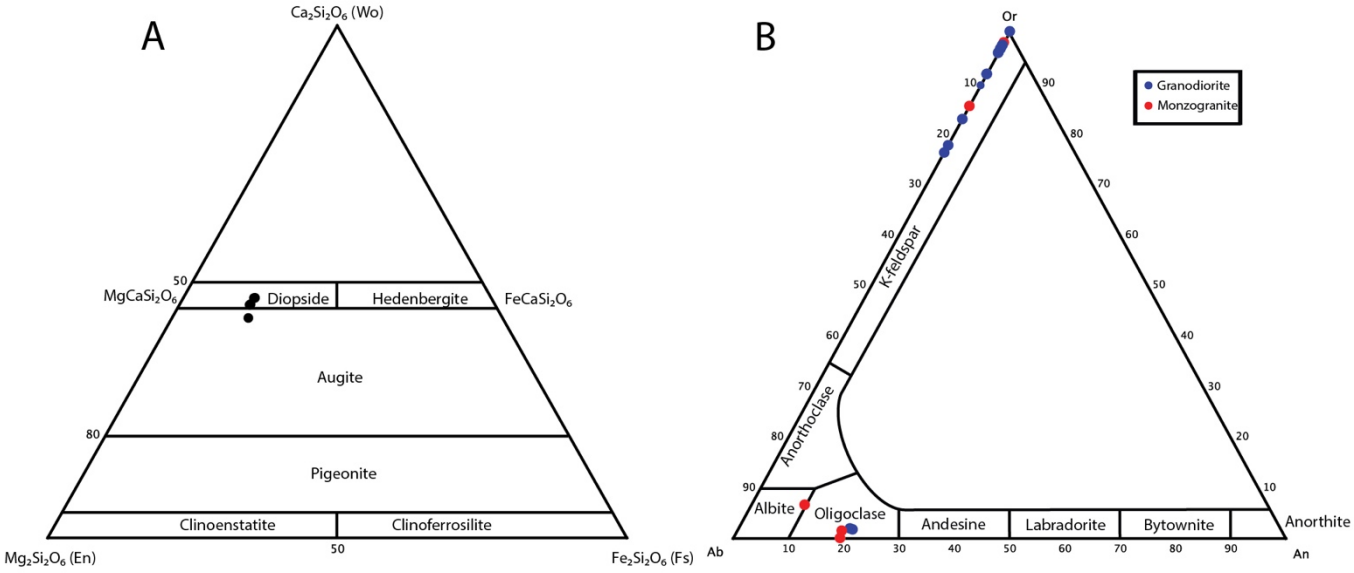

Figure 6.3 Mineral compositions of the Terrace Bay Batholith: A) Wollastonite (Wo)- Enstatite (En) – Ferrosilite (Fs) ternary diagram showing pyroxene compositions. B) Albite (Ab) – anorthite (An) – orthoclase (Or) ternary diagram showing plagioclase compositions.

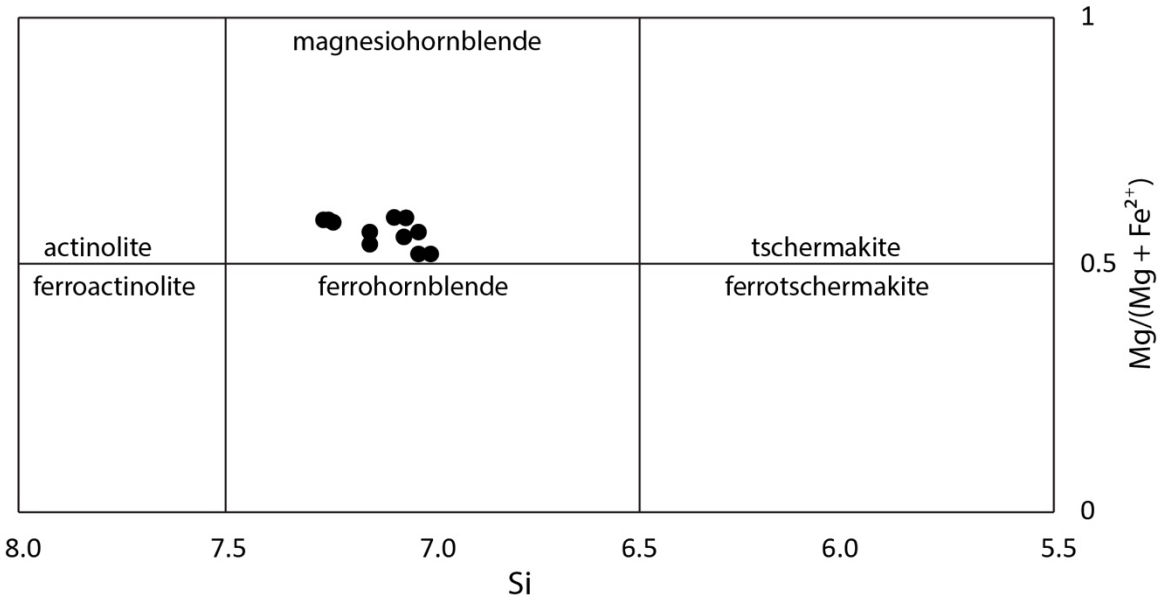

Figure 6.4 Amphibole composition of the Terrace Bay Batholith, after the IMA classification scheme of Leake et al. (1997).

The pyroxenes in the pluton all plot in the diopside to augite fields (Fig. 6.3a), whereas the amphiboles are primarily calcic variety, magnesio-hornblende (Fig. 6.4). The presence of calcic amphiboles is typical of a calc-alkaline magma (Castor and Stephens, 1992; Leake et al., 1997; Ridolfi et al., 2008).

The coarse-grained potassium feldspar phenocrysts that sporadically occur throughout the pluton have orthoclase rich rims but are albite rich in the center of the crystals with Ba also increasing towards the core. This suggests that the magma was initially Na and Ba rich, producing predominantly albite, but as the magma evolved and as the albite crystalized the magma became more potassium rich, switching to dominantly orthoclase with lower Ba contents. The potassium feldspar crystals are orthoclase in composition (Fig. 6.3b) and dominantly occur interstitially rather than as phenocrysts, suggesting they were one of the last phases to crystalize in the melt. Plagioclase feldspars are the dominant phenocryst phase in the granodiorite aside from the coarse-grained potassium feldspar phenocrysts and are mainly albite and oligoclase with one sample each of anorthite and anorthoclase (Fig. 6.3b). Albite and oligoclase were found in both the granodiorite and the monzogranite, there is no variation in feldspar composition between the different lithologies of the pluton. The presence of albite and oligoclase suggests that the magma had a low H_2O content which would suppress the formation of more An (calcic) rich feldspars such as anorthite and bytownite (Sisson and Grove, 1993).

The crystallization history of the pluton and a paragenetic sequence is summarized in Figure 6.5. The first minerals to crystalize in the intrusion were medium-grained plagioclase, fine- to medium-grained hornblende, biotite and fine-grained titanite and pyrite. Phenocrysts of plagioclase and quartz rarely have inclusions, suggesting earlier formation than potassium

feldspar and mafic minerals. Quartz occurs both as phenocrysts and interstitial grains, suggesting a second later crystallization similar to potassium feldspar. The majority of the potassium feldspar occurs as interstitial grains to the phenocrysts of plagioclase and quartz and can range in size up to 1cm (Fig. 4.2). Sporadic coarse-grained (2-4 cm) potassium feldspar phenocrysts commonly host very fine-grained inclusions of quartz, amphibole, biotite and titanite, suggesting a late crystallization. Potassium feldspar commonly has perthitic lamellae occurring in medium-grained interstitial crystals indicating exsolution of plagioclase and potassium feldspar. Primary pyroxene crystals are sometimes rimmed with amphibole showing a change in the magma composition. Amphibole and biotite phenocrysts occur around the feldspar and quartz, with amphiboles commonly containing inclusions of titanite and pyrite. Mafic minerals such as biotite and amphibole commonly occur as clusters of crystals around feldspar phenocrysts (Fig. 4.5c, d). Pyrite and titanite crystals occur as an early phase, commonly as inclusions in amphibole, biotite and rarely feldspar phenocrysts (Fig. 4.4c, d). Titanite grains are replaced by pyrite and possibly magnetite.

Sericite/white mica alteration of the plagioclase crystals varies in intensity from mild (> 25%) to intense (>75%). The potassium feldspar can have some white mica alteration, but it is generally minor compared to the plagioclase crystals. Fine-grained epidote occurs as an alteration product of feldspar phenocrysts and of feldspar in the groundmass. Chlorite occurs as an alteration product of amphibole and biotite, varying in intensity up to complete replacement. Calcite also occurs as a secondary alteration product commonly as clusters surrounding the chlorite (Fig. 4.16c, d).

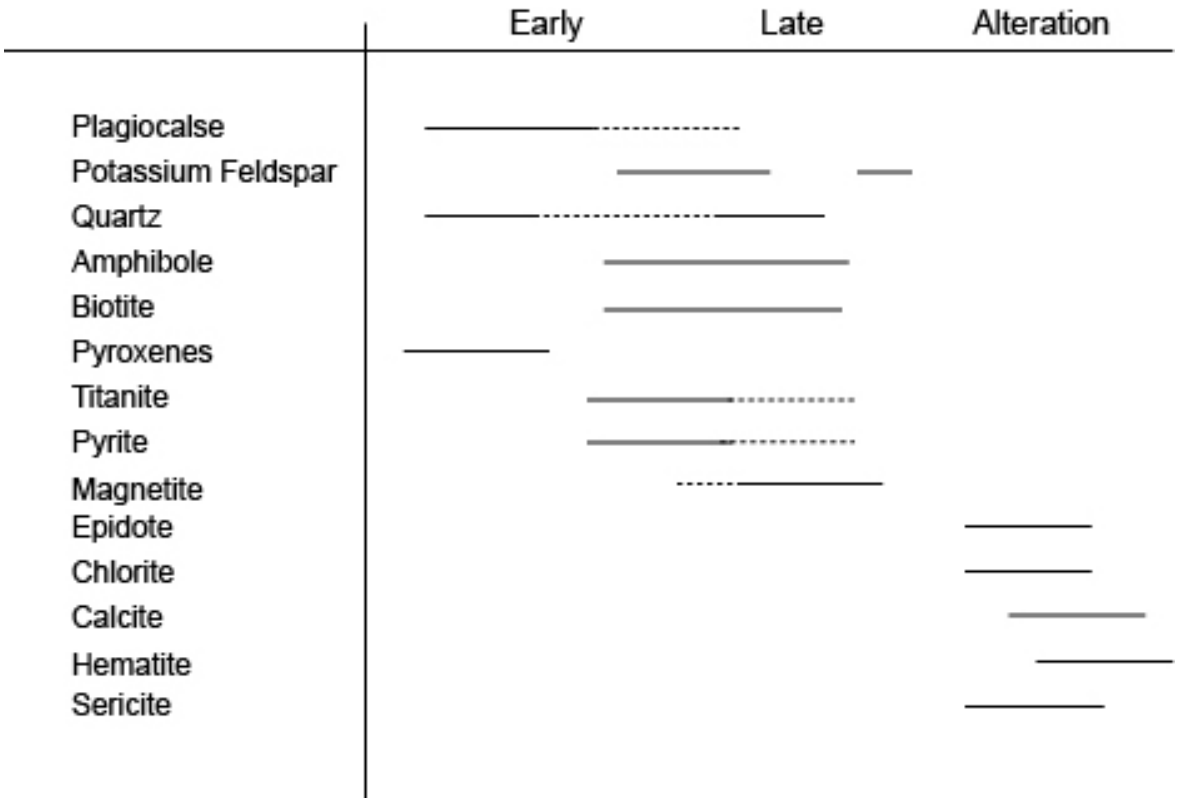

Figure 6.5 Paragenetic sequence of the Terrace Bay Batholith.

Hematite occurs as a late overprint across the samples, primarily in feldspars with intensity increasing in plagioclase crystals. The hematite alteration is very fine-grained, making it difficult to distinguish, but is red to slightly opaque in plain polarized light. The granodiorite groundmass is composed of very fine- to fine-grained plagioclase, potassium feldspar and quartz +/- hornblende and biotite. The plagioclase, quartz and potassium feldspar occur as interstitial material in the groundmass and show the least amount of alteration. Fine-grained magnetite is disseminated through the groundmass in and among the very fine-grained feldspars and quartz.

6.2 Geochemistry

Harker variation diagrams for major element oxides from the Terrace Bay Batholith display smooth geochemical trends. Plots of TiO_2, Fe_2O_3, MnO, MgO, CaO, P_2O_5 vs. SiO_2 wt.% show negative correlations (Fig. 5.1) whereas Na_2O, K_2O, and Al_2O_3 show weak positive and

bellshaped trends, but with significant scatter (Fig. 5.1). The hematite altered samples show scatter with all major elements, consistent with the more intense alteration (Figs. 4.16 and 17; 5.1 and 5.2) and consequently they will not be discussed further.

On major element Harker diagrams, the Terrace Bay Batholith does show some minor evolution across the pluton, but the majority of the samples cluster in the middle of the trend (Figs. 5.1 and 2). The late stage pegmatite and aplitic dykes are the most evolved, plotting at the end of the linear trends with the highest SiO_2 content (Fig. 5.1). The negative linear trends that are observed for major elements with the exceptions of Al, Na and K, can be explained by crystal fractionation and/or partial melting. The clustering of samples (83 out of 102) in the middle of the trend suggests that the pluton is geochemically homogeneous and has undergone relatively little fractionation, which for a pluton of this size (>100 km^2) is uncommon (Clemens and Stevens, 2012). The 17 samples that define the end of the linear trends are located primarily within the outer one kilometer of the pluton, they include monzogranite (n=7), granodiorite (n=6) and diorite (n=1), with the remainder being late stage dykes (Fig. 6.6). Ten of the samples are more primitive than the majority of the pluton with only two samples of each monzogranite and granodiorite being more evolved then the rest of the pluton. Potassium content shows a high degree of scatter when plotted against SiO_2, which is likely the result of remobilization during metamorphism, which is consistent with the alteration of hornblende and biotite to chlorite and epidote. Similar scattered trends are also seen in Al_2O_3 and Na_2O versus SiO_2, suggesting those elements were also mobile (Fig. 5.1). The granodiorite samples show the less variation compared to the other lithologies, suggesting it has undergone the least amount of element mobility. Mobility of Na and K makes it difficult to geochemically classify the pluton

using the TAS diagram. Negative linear trends are seen with MgO, CaO, P_2O_3, Fe_2O_3 vs. SiO_2 wt.% consistent with crystal fractionation of amphibole and biotite. The negative linear trends in MgO, TiO_2, and Fe_2O_3 can be explained by fractional crystallization of ferromagnesian

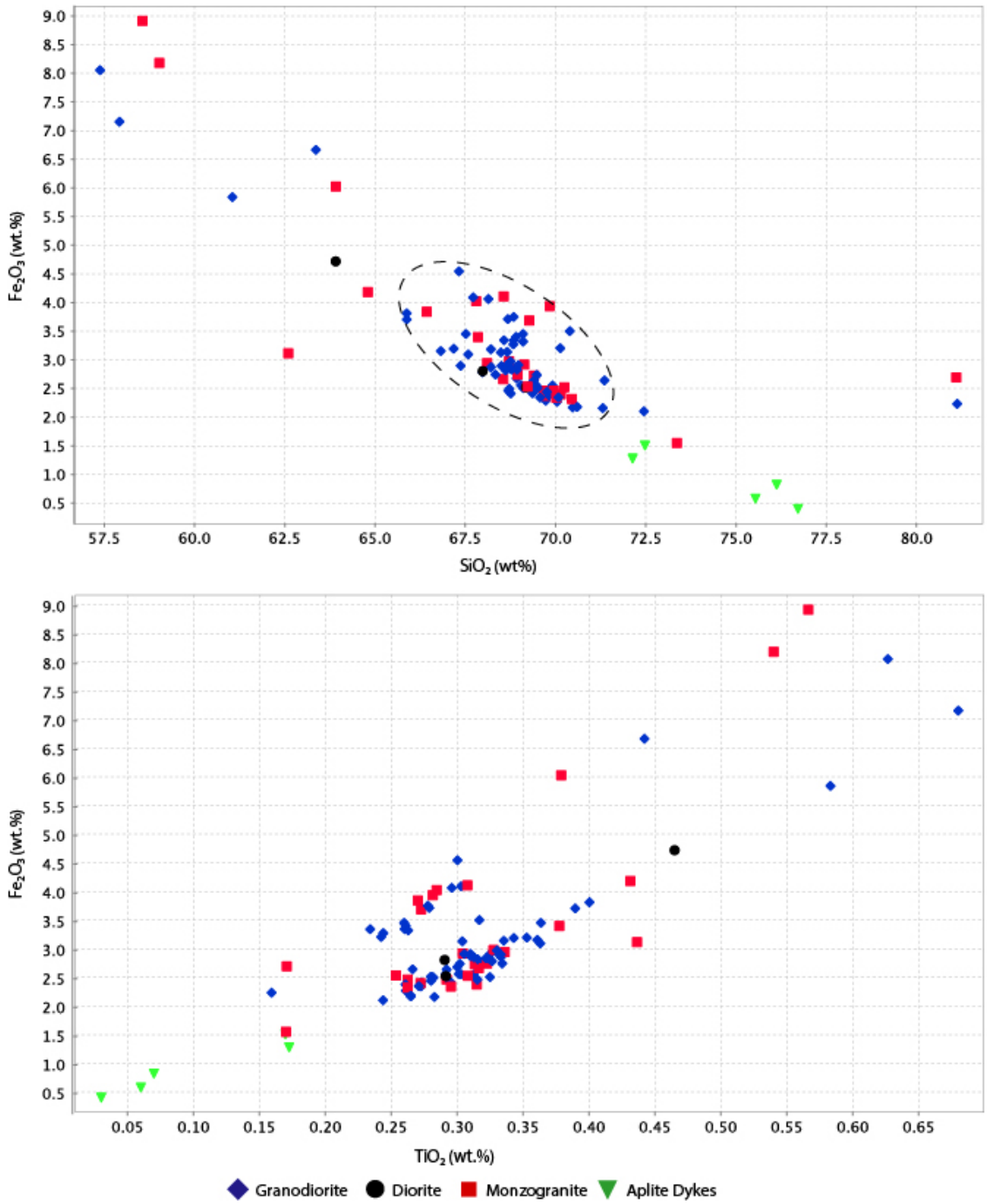

Figure 6.6 Variation diagrams Fe_2O_3 vs. SiO_2 and TiO_2. The Fe_2O_3 vs. SiO_2 displays the clustering of samples (circled by the dotted line) that occur along the linear trends. The Fe_2O_3 vs. TiO_2 display the two linear trends of Fe_2O_3.

minerals, particularly hornblende, biotite pyroxenes and Fe-Ti oxides during early evolution of the pluton. A correlation is observed for Fe_2O_3 against SiO_2 and TiO_2, with two subparallel negative trends (Fig. 6.6). Both trends include a mix of granodiorite and monzogranite, but samples of the higher trend only occur within the outer kilometer of the pluton. All of the samples are located within areas where supracrustal rocks are incorporated into the plutons and/or abundant xenoliths are found. Consequently, the two parallel trends suggest that the high Fe_2O_3 samples could be important due to the incorporation of supracrustal xenoliths. The increase in Fe_2O_3 vs. SiO_2 is likely due to the assimilation of the more mafic supracrustal rocks. The Terrace Bay Batholith follows the calc-alkaline trend of both Irvine and Baragar (1971) and Kuno (1968) when plotted on an alkalis-iron-magnesium (AFM) diagram (Fig. 6.7).

On trace element Harker diagrams, the Terrace Bay Batholith displays similar smooth geochemical trends to the major element oxides, consistent with fractionation. The LILEs (Rb; Fig. 5.1) show no correlation with SiO_2 whereas the tight correlation between SiO_2 and TiO_2 suggests a relatively high mobility of LILE and low mobility of HFSE. When plotting Zr vs. SiO_2 a slight negative trend can be seen (Fig. 5.2). The lithologies of the Terrace Bay Batholith are characterized by similar primitive mantle normalized patterns, with fractionated HREE, negative HFSE anomalies (Nb/Nb*=0.05-0.26; Ti/Ti*=0.37-0.31), enrichment of Th over LREE and enrichment of LREE (La/Sm_n=2.9-11.4). The diorite is characterized by higher La values (La= 31.9-62.8; mean=42.4) than the granodiorite (La=13.6-75.1; mean=30.4) and the monzogranite has values of La= 15-58 (mean=31.7). The fractionated HREEs (high La/Y; Fig. 6.7) and the Th-Nb-La systematics are consistent with formation in a subduction zone at depths where garnet is present (Drummond and Defant, 1990; Polat et al., 1998; Kerrich and Richards, 2007). The HREE

depletion and high La/Yb and Sr/Y ratios seen in the Terrace Bay Batholith have a number of possible causes including; partial melts involving garnet amphibolite, AFC (assimilation, fractional crystallization; DePaolo, 1981) or MASH processes (melting, assimilation, storage, homogenization; Hildreth and Moorebath, 1988; Richards, 2011). It is unlikely that the Terrace Bay Batholith underwent significant AFC or MASH processes to produce HREE depletion and high La/Yb and Sr/Y ratios, due to the primitive mantle signature of the ε_{Nd} values and major and trace element signatures (Fig. 6.8). The partial melting of oceanic crust in a subduction zone in the presence of garnet and absence of plagioclase in the residue, better explains the signatures (Richards, 2011).

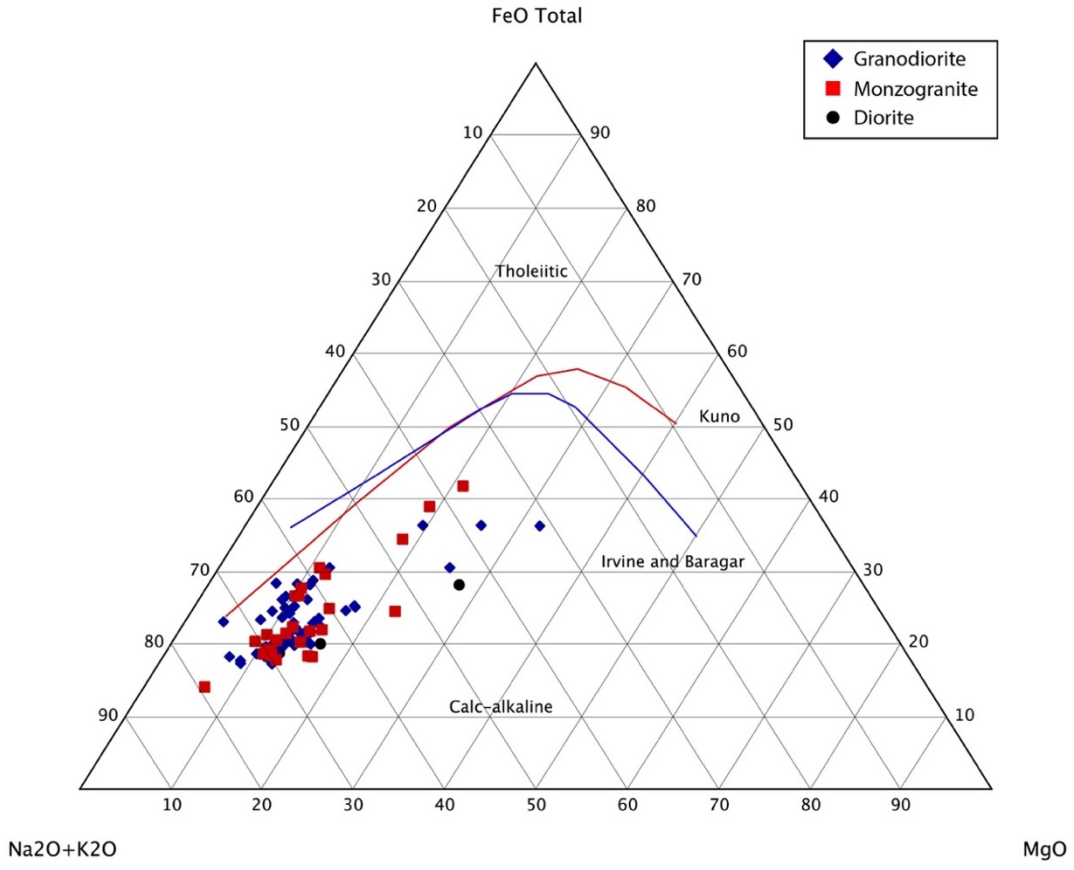

Figure 6.7 AFM diagram for the Terrace Bay Batholith. The lines separating tholeiitic from calc-alkaline from Kuno (1968; red), and Irvine and Baragar (1971; blue)

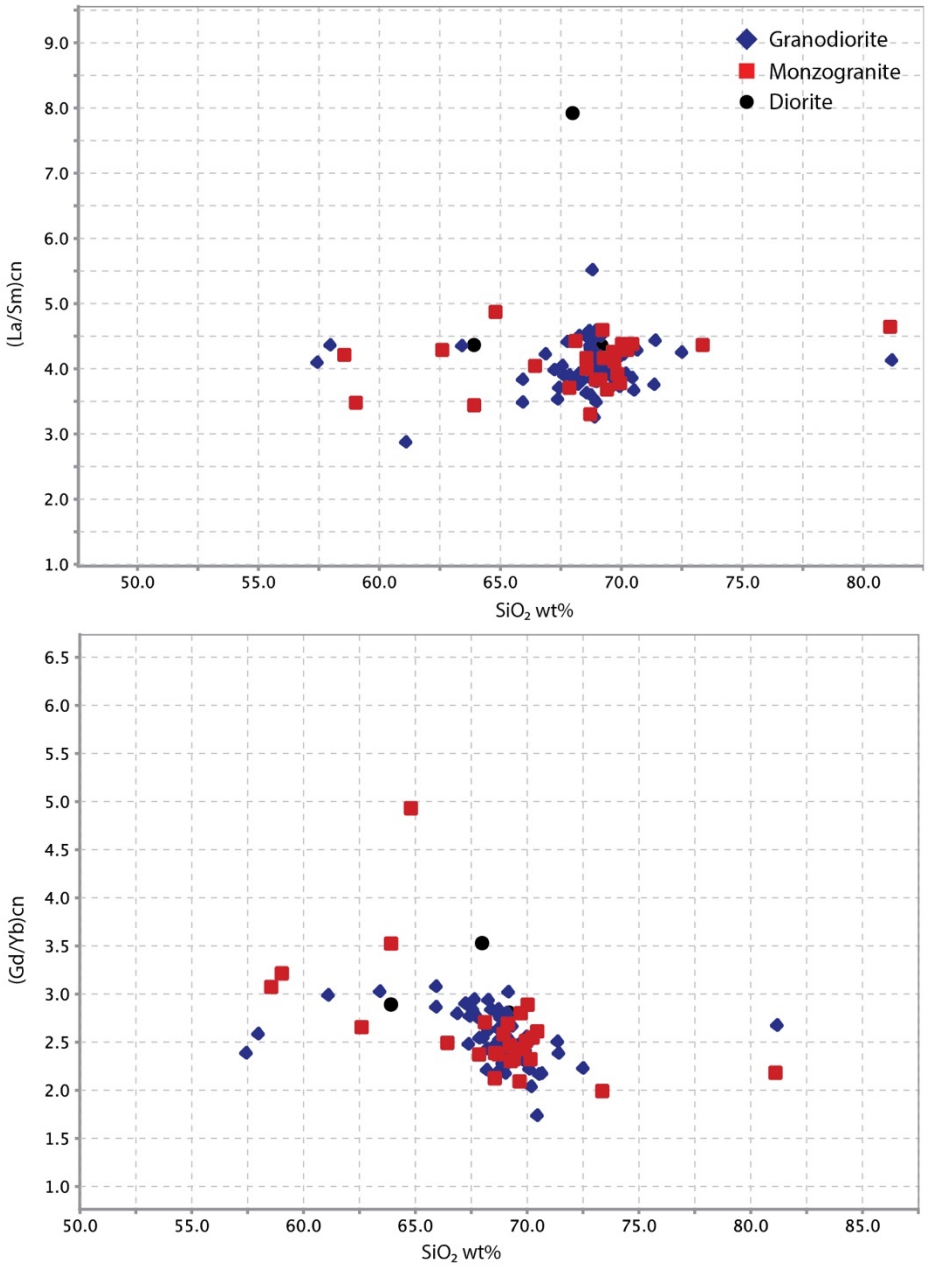

Figure 6.8 Chondrite normalized La/Sm_n vs. SiO_2 and Gd/Yb_n vs. SiO_2. Normalization values of Sun and McDonough (1989).

6.3 Isotopes

6.3.1 Rhenium-osmium geochronology

Molybdenite from the granodiorite dated in this study yielded an age of mineralization of 2671 +/- 12 Ma, 17 m.y younger than the granodiorite which has been dated at 2689 +/- 1 Ma (Kamo, 2016). The Re-Os age is similar to other molybdenite ages from the region, including ages of 2665 +/- 18 Ma, and 2674 +/- 12 Ma from Hemlo (Stein et al., 2000; Gorner, unpublished). The similar ages of mineralization suggest that there may have been a widespread molybdenum mineralization event throughout the region.

The Re-Os data can also be used to investigate the source of the molybdenite, based on the amounts of Re in the sample. It has been suggested that the metal source of deposits and the degree of magma fractionation control the Re content of molybdenite in granite hosted deposits (Stein et al., 2001a, b; Belvin, 2009; Sinclair et al., 2009). A mantle derived source would be enriched in rhenium with values > 100 pm, a mixture of mantle and crustal sources values would yield Re in the tens of ppm whereas a crustal source have the lowest values of <10 ppm (Berzina et al., 2005; Pasava et al., 2016). The Terrace Bay Batholith molybdenite contains 48 ppm rhenium. This is similar to I-type granites of the Bohemanian Massif and suggests that the Terrace Bay Batholith is derived from a mixed source of mantle and crustal consistent with geochemical evidence that the Terrace Bay Batholith is derived from above a subduction zone (Finger et al., 1997; Pasava et al., 2016). Molybdenite found in gold associated I-type granites from the Bohmenian Massif were analysed and found to host Re with mean values of 16-34 ppm (Pasava et al., 2016).

6.3.2 Neodymium Isotopes

The Sm-Nd isotope system is often used to constrain the source of a magmatic suite and helps identify the processes involved in petrogenesis (DePaolo and Wasserburg, 1976; DePaolo 1981a). The ε_{Nd} values have been calculated for six samples from the Terrace Bay Batholith using the chondrite uniform reservoir (CHUR) value at 2689 and 2690 Ma. The age of 2689 and 2690 was determined to be the age of crystallization of the Terrace Bay Batholith by U-Pb zircon dating (Kamo, 2016). Positive ε_{Nd} values are believed to result from a depleted source with respect to CHUR whereas negative value are interpreted to have formed from an enriched source that has undergone crustal contamination (DePaolo and Wasserburg, 1976). Partial melting and fractional crystallization of mantle derived magmas results in lower Sm/ Nd ratios than the source, resulting in the Earth's crust being enriched in LREE with lower Sm-Nd ratios than the depleted mantle reservoir (DePaolo and Wasserburg, 1976; Bennett and DePaolo, 1987; Champion, 2013).

The ε_{Nd} values are more enriched in the monzogranite than the granodiorite likely due to crustal contamination during emplacement. When comparing the values spatially the ε_{Nd} value increase towards the center of the pluton with the highest ε_{Nd} value of +2.49 at 17KAM038A, which is located 3 km from the contact with the supracrustal rocks, the next highest value is from the diorite at +2.39. This suggests that there is a slight increase in the primitive signature towards the center of the pluton. This trend can also be seen on the ε_{Nd} diagram (Fig. 6.9), the monzogranites have slightly more enriched values compared to depleted mantle. This decrease in values suggests that the monzogranite has undergone more contamination than the more primitive granodiorite. Due to the geochemical signatures being

the same between lithologies, a different source for the monzogranite is unlikely. The monzogranite primarily occurs at the contact with the surrounding supracrustal rocks. As discussed in Chapter 5, the contact relationship with the supracrustal rocks and the pluton is complicated and only occurs as a sharp contact in a select few areas, rather it is commonly gradational with a complex relationship. Consequently, the slight decreases in the ε_{Nd} value of the monzogranite, is likely due to crustal contamination during emplacement of the pluton. The slight decrease is larger than the +/-0.137 errors of the values, suggesting it is a true enrichment. It is useful to compare the ε_{Nd} values of the Terrace Bay Batholith to the values of the depleted mantle at the time, which has been estimated to be +3 under the western Superior Province at 2700 Ma (Tomlinson, 2004).

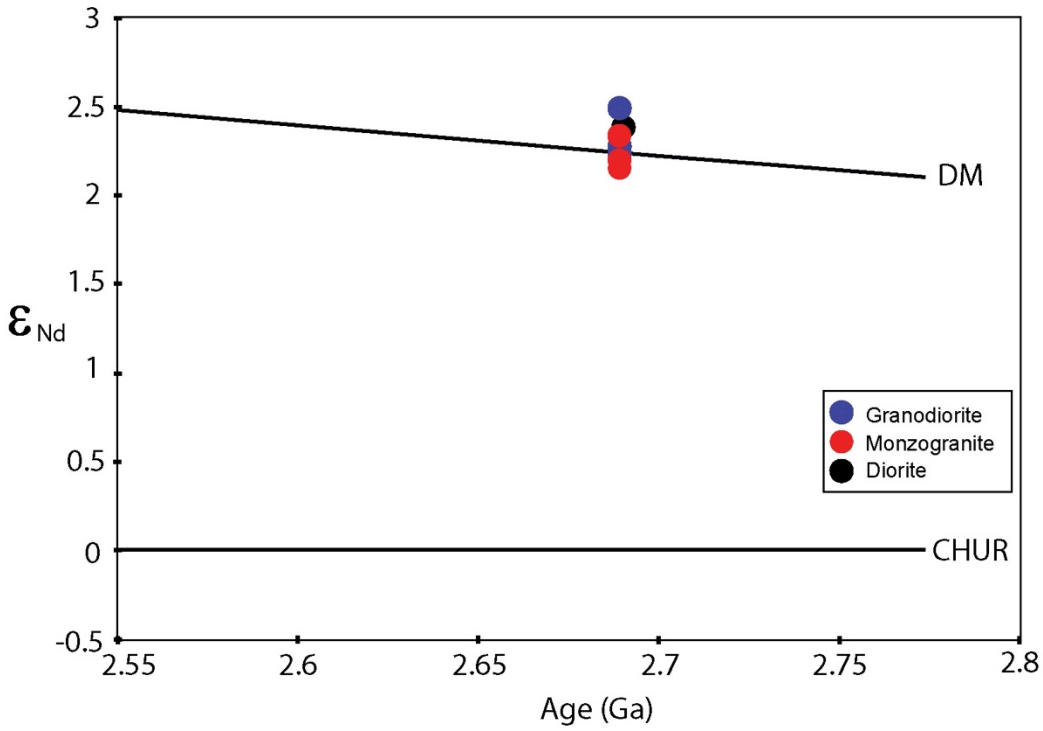

Figure 6.9 ε_{Nd} values as a function of crystallization ages showing Nd isotope data for the Terrace Bay Batholith. 1981a. (Curve described by ε_{Nd} (T) = 0.25T2-3T+8.5) DM: Depleted mantle, CHUR: Chondritic Uniform Reservoir.

Epsilon neodymium values of around +1 in Neoarchean rocks have been interpreted to represent mantle derived magmas with a small amount of older crustal contamination, such as contamination by an endogenic subduction-derived component in the mantle (Tomlinson, 2004; Polat et al. 1999). Neoarchean rocks with ε_{Nd} values less than +1 have likely undergone more significant exogenic crustal contamination (Tomlinson, 2004). Polat et al. (1999) reported Sm-Nd isotopic data for tholeiitic basalts and komatiites from the western Schreiber-Hemlo greenstone belt. The age used for ε_{Nd} calculation was 2700 Ma. These lithologies represent the age of volcanism on the Schreiber side of the greenstone belt and are the supracrustal rocks that the Terrace Bay Batholith intruded into. The tholeiitic basalts from the Schreiber area yielded ε_{Nd} values of +2.55 whereas the transitional basalts ranged from + 1.96 to +2.99 ε_{Nd} (Polat et al., 1999). Across the subprovince ε_{Nd} values for the komatiites ranged from +1.31 to +3.49 and for the basalts values ranged from +0.71 to +2.99 (Polat et al., 1999). The Terrace Bay Batholith ε_{Nd} values are similar to the basalts and komatiites from the Schreiber area, suggesting a similar depleted mantle source as the volcanic rocks (Polat et al. 1999). The positive but slightly less than depleted mantle data for the Terrace Bay Batholith, is consistent with the pluton being derived from a depleted mantle source, in an oceanic arc environment, where melts experience little to no crustal contamination (DePaolo, 1981a, 1981b; Tomlinson, 2004). Formation in a continental setting would cause the ε_{Nd} values to range around zero to negative values, due to the contributions of an older crustal component (DePaolo, 1981a, 1981b). The relatively minor contamination suggested by the isotope data is unusual for granites and may be explained by the supracrustal rocks being derived from the same source and having similar primitive ε_{Nd} signatures to the granitic melts (e.g, Polat et al., 1999).

Consequently, contamination by these rocks would not have a significant effect on the isotope signature of the granites.

DePaolo (1981b) suggested that granite plutons generally undergo some degree of contamination by crustal materials during the ascent of the magma through the crust, resulting in some decrease in ε_{Nd} values. Plutonic rocks from the Superior Province with ages between 2.74 to 2.69 Ma have been suggested to have been generated by partial melting of a garnet-bearing amphibole source which was contaminated by subducted sediments (~1-10%), causing small variations from the depleted mantle signature of ε_{Nd} +3.0 at 2700 Ma (Martin, 1987; Henry et al., 1998; Tomlinson, 2004). When compared to the Yilgarn Craton and the Baltic Shield which are examples of crustal contamination in arc related rocks, it is suggested that the arc environment in which the Terrace Bay Batholith formed likely incorporated crustal material that has been subducted into the mantle rather than during emplacement in the continental crust (Polat et al., 1998, 1999; Henry et al., 1998). In granites from Colorado, subduction derived contamination produces a primarily mantle derived signature of +3 to +1 whereas a crustal contamination produces a ε_{Nd} signature of +0.1 to -2.5 in intrusive rocks in Colorado (DePaolo, 1981a). Granites, specifically S-type granites, are generally derived from crustal sources, which would decrease the ε_{Nd} value to near zero or negative values (Chappell and White, 1974; DePaolo, 1981a), whereas primitive mantle-derived rocks formed within a continental setting will typically have negative ε_{Nd} values, caused by the incorporation of crust during AFC or MASH processes (DePaolo and Wasserburg, 1976; DePaolo, 1981a). The isotopic depletion is influenced by a number of factors, including the source of the melts, the isotopic composition of the contaminant and the thickness of the contaminate, which can all lead to

variations in isotopic enrichment (DePaolo and Wasserburg, 1976; DePaolo, 1981a). The syn-tectonic Shebandowan Lake pluton has an ε_{Nd} value of +2.3, which is consistent with derivation from a depleted mantle reservoir (Henry et al., 1998). The Terrace Bay Batholith has very similar ε_{Nd} values to the Shebandowan Lake pluton implying a similar source. When plotted on an ε_{Nd} vs $^{147}Sm/^{144}Nd$ plot, the Terrace Bay Batholith plots just below the depleted mantle origin field, similar to other plutons from the Wawa subprovince (Henry et al., 1998). This further suggests that the Terrace Bay Batholith did not undergo contamination by older crust during emplacement similar to other Archean plutons, but incorporated minor amounts of supracrustal rocks incorporated into a depleted mantle source during subduction.

6.4 Regional Plutons

6.4.1 Schreiber Assemblage Plutons

Numerous felsic plutons are located in the western Schreiber-Hemlo greenstone belt, eight of which are located within the Schreiber assemblage (Fig. 2.5). They vary from large plutons up to 40 km that have undergone regional deformation to small <5 km relatively undeformed plutons. Details of the plutons are summarized in Table 6.1. Previously a lack of geochronology of the plutons in the Schreiber assemblage has made it difficult to compare the granitoids to the eastern Hemlo assemblage, other than using geochemistry and mineralogy. With data collected in this study and new geochronological data from select plutons from the Schreiber assemblage the relationships between the two can be investigated (Kamo, 2016, 2018; Kamo and Hamilton, 2017; Davis and Sutcliffe, 2017).

The Terrace Bay Batholith is centrally located in the Schreiber greenstone belt. The western plutons include the Whitesand Lake Batholith, Crossman Lake Batholith, Syenite Lake

Table 6.1 Geochemical and petrographic descriptions of regional plutons and the Dog Lake granite chain (DLGC). S-type and I-type granites classification of Chappell and White (1974). With data from Hughes (2016), Kuzmich (2012) and Magnus and Hastie (2018).

Pluton name	Rock type	Mineralogy	Age (Ma)	S-type or I - type	ASI	ε_{Nd}	SiO_2
Terrace Bay Batholith	Granodiorite to monzogranite	Amphibole, biotite	2689	I	Metaluminous to weakly peraluminous	+2.1-+2.4	57-81%
Syenite Lake Pluton	Quartz monzodiorite	Biotite	2682		Metaluminous	N/A	68-74%
Schreiber pluton	Granite	Biotite, amphibole (Trace)	N/A		Metaluminous to peraluminous	N/A	57-69%
Crossman Lake batholith	Tonalite and granodiorite	Biotite, amphibole	N/A		Peraluminous	N/A	59-77%
Whitesand Lake batholith	Granodiorite, monzonite, and monzodiorite	Amphibole, biotite	N/A		Metaluminous to peraluminous	N/A	47-75%
Little pic River	Tonalite to granodiorite	Biotite, amphibole, titanite	2673		Metaluminous to peraluminous	N/A	51-73%
Foxtrap Lake	Granodiorite to granite	Biotite	2674		Peraluminous	N/A	59-73%
Santoy Lake	Granite	Biotite	2667		Metaluminous to peraluminous	N/A	64-75%
Steel River	Granodiorite	Biotite	2689		Metaluminous	N/A	64-69%
Mackenzie	Quartz monzonite	Amphibole, biotite	N/A	I	Peraluminous	n/a	63-68 %
Barnum Lake	Microcline phyric Monzonite/quartz-Monzonite	Amphibole, magnetite, biotite	2700	I	Metaluminous	+1.54	59-69%
Trout Lake	Monzonite/ Quartz-Monzonite, Syenite/Quartz Syenite, Granite	Amphibole, magnetite, biotite, garnet, muscovite	2700	I and S	Metaluminous to peraluminous	-1.45 to +2.11	57-67%

White Lily	Quartz Monzonite, Syenite/Quartz Syenite	Amphibole, magnetite, biotite	2700	I	Metaluminous to weakly peraluminous	+0.78 to +1.44	54-64%
Silver Falls	Syenite/Quartz Syenite, Granite	Amphibole, magnetite, biotite, garnet, muscovite	2700	I and S	Metaluminous to peraluminous	-0.08 to +1.09	65-73%
Penasen Lake	Monzodiorite	Amphibole, magnetite, biotite, pyroxene	2700	I	Metaluminous	n/a	49-55%
Cedar Lake	Diorite, Quartz Monzonite	Amphibole, Biotite	2680	I	Metaluminous	+1.8 to +3.1	62-67%
Heron Bay	Granodiorite	Amphibole, Biotite	2682	I	Metaluminous	+1.9 to +2.7	65-69%

and the Schreiber pluton (Fig. 2.5). The two largest plutons, the Crossman Lake and Whitesand Lake Batholiths show the largest variation in lithologies compared to the other intrusions in the Schreiber region. The Crossman Lake Batholith varies between tonalite and granodiorite, whereas the Whitesand Lake batholith varies from granodiorite, monzonite and monzodiorite. The only dated intrusion in the western end of the belt is the Syenite Lake pluton with an age of 2682 +/- 1.1 Ma (quartz monzodiorite; Magnus, 2017; Kamo, 2018; Magnus and Hastie, 2018). The plutons to the east of the Terrace Bay Batholith are the Santoy Lake, Foxtrap Lake, Little Pic River and the Steel River (Fig. 2.5). They vary from quartz monzodiorite, granite to tonalite, and are all metaluminous to weakly peraluminous. The youngest of the plutons are the Foxtrap Lake pluton at 2674.1 +/- 1.3 Ma, the Little Pic River pluton at 2673.4 +/- 1.4 Ma and the Santoy Lake pluton at 2667 +/- 4 Ma (Kamo, 2016, 2018; Kamo and Hamilton, 2017; Davis and Sutcliffe, 2017; Magnus, 2017; Magnus and Hastie, 2018). The Terrace Bay Batholith is the oldest dated

pluton in the region with a granodiorite age of 2689 +/- 1.1 Ma and the diorite age of 2690.64 +/- 0.91 Ma along with the Steel River pluton that has a similar age of 2689 +/- 2.0 Ma (Kamo, 2016, 2018; Kamo and Hamilton, 2017).

The 2689 +/- 1.1 Ma Terrace Bay Batholith is host to xenoliths that show D_1 deformation but only minimal amounts of D_2 deformation, suggesting the pluton was emplaced in a syn-tectonic setting (Kamo, 2016). The Whitesand and Crossman Lake Batholiths show similar regional deformation to the Terrace Bay Batholith, and host xenoliths that show D_1 foliations. Without a U-Pb age it is difficult to say with certainty that the Whitesand and Crossman Lake Batholiths are syn-tectonic but the deformation of the plutons and the presence of D_1 deformed supracrustal xenoliths provides good evidence to suggest such an age. The eastern plutons show little to no deformation suggesting that they are post tectonic, which is consistent with the younger ages. Two stages of plutonism are recognized in the western Schreiber-Hemlo greenstone belt based on the new geochronological data, a syn-tectonic stage comprising the Terrace Bay Batholith, Steel River pluton, and the Syenite Lake pluton (2690 to 2682 Ma) and a post-tectonic stage which is represented by the Foxtrap, Little Pic River and the Santoy Lake plutons (2674 to 2667 Ma).

The regional plutons show compositional differences when compared to the Terrace Bay Batholith, but they are broadly similar (Fig. 6.10). The Little Pic River, Whitesand, Syenite Lake, and Santoy Lake intrusions show similar rare earth element signatures to the Terrace Bay Batholith (Fig. 6.10). All of the plutons show similar signatures with negative HFSE anomalies, enrichment of LREE and fractionated HREE. This geochemistry is consistent with magmas derived from mantle melts in a suprasubduction zone environment (Hollings et al., 2011). The

flat trends of the Crossman Lake Batholith and the Steel River Pluton suggest that there may be geochemical evolution across the region with the syn-tectonic plutons having more fractioned HREE. The Crossman Lake batholith and Steel River pluton have relatively flat HREEs when compared to the Terrace Bay Batholith, which suggests a variation in source, a source similar to low Al-TTG melts in shallow and lower pressure conditions, above the garnet stability field (Beakhouse, 2007; Hollings et al., 2011). The Terrace Bay Batholith does overlap some of the regional plutons, but there is little overlap between the pluton and the post-tectonic plutons, suggesting that there may be a slight evolution of the plutonism in the region between the syn- to post- tectonic suites which is also seen the primitive mantle plots (Fig. 6.10). When plotted on an aluminum saturation index (ASI) diagram, the regional plutons show metaluminous to weakly peraluminous signatures similar to the Terrace Bay Batholith.

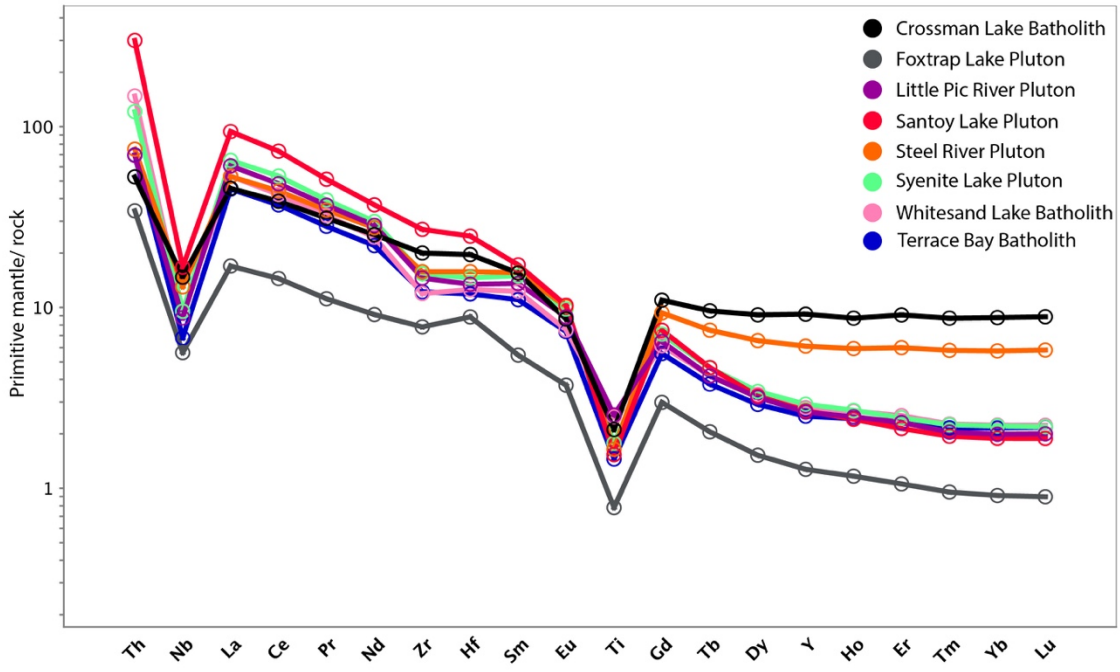

Figure 6.10 Primitive mantle normalized plots for the regional plutons compared to the Terrace Bay Batholith). Normalizing values from Sun and McDonough (1989). Average values are used; Crossman Lake Batholith n=10, Foxtrap Lake pluton n=17, Little Pic River pluton n= 11, Santoy pluton n=7, Steel River pluton n=7, Whitesand Lake Batholite n=7, Syenite Lake pluton n=3, Terrace Bay Batholith n=122.

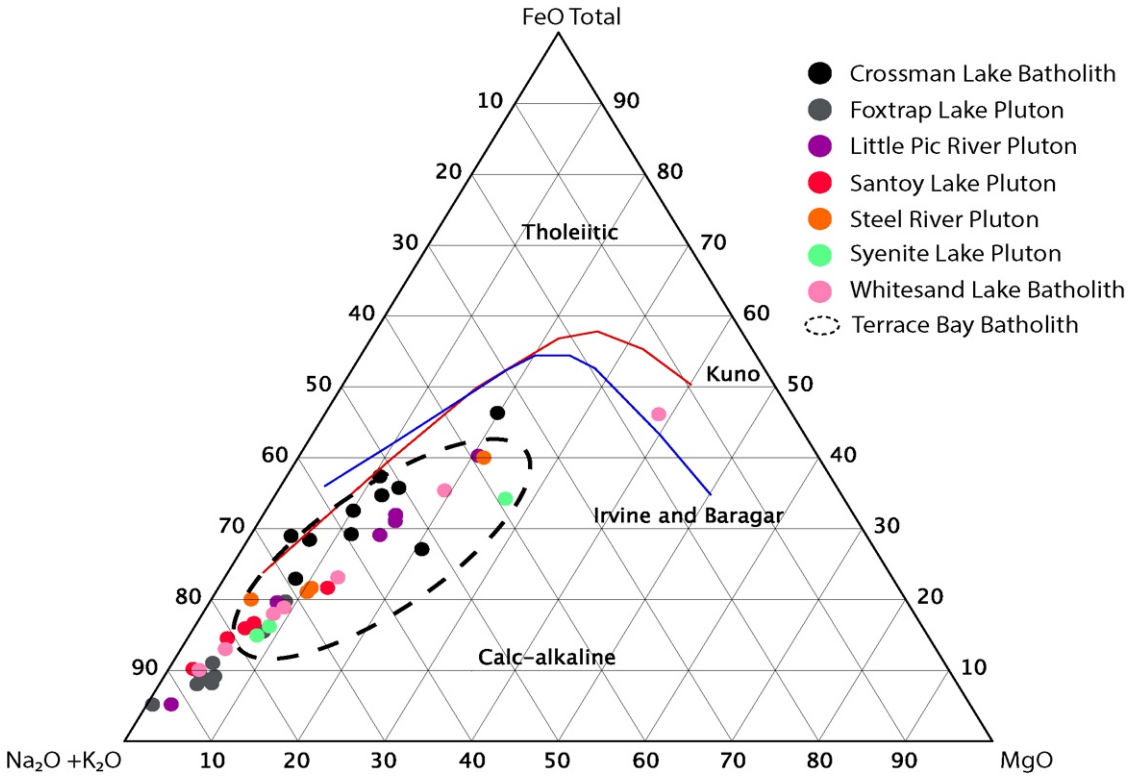

Figure 6.11. AFM diagram showing regional plutons and the overlap with the Terrace Bay Batholith. The lines separating tholeiitic from calc-alkaline from Kuno (1968; red), and Irvine and Baragar (1971; blue)

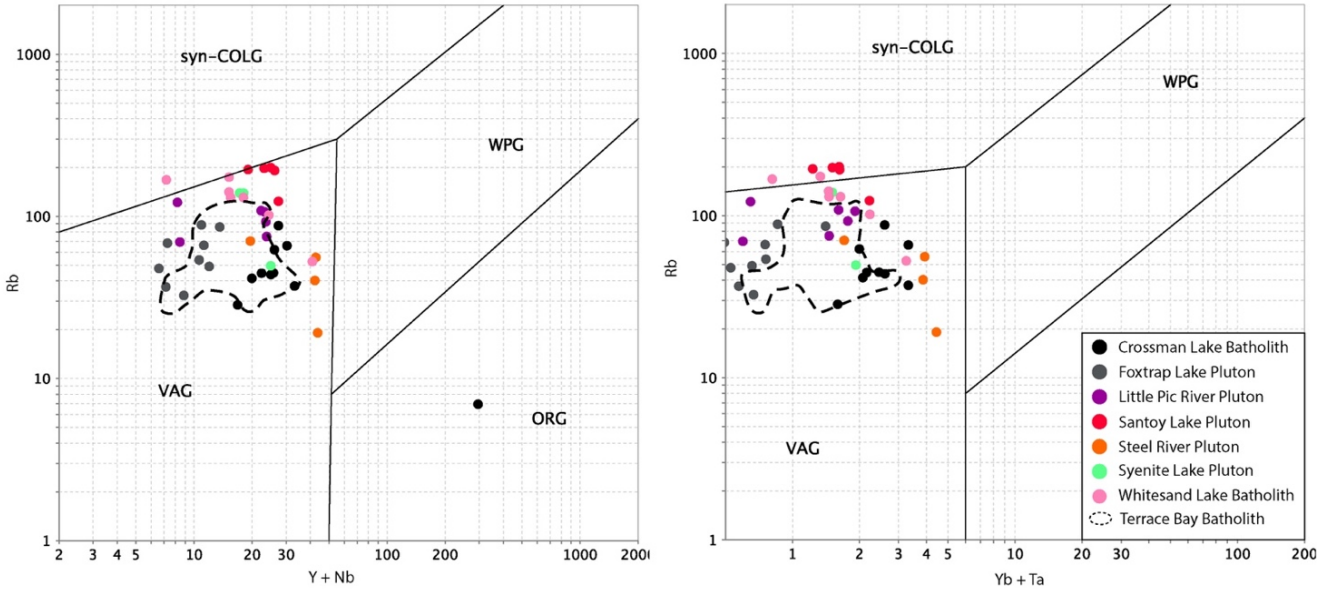

Figure 6.12 Pearce tectonic diagram plotting regional plutons compared to the Terrace Bay Batholith, modified from Pearce, (1984).

All the plutons plot in the calc-alkaline field of an AFM diagram (Fig. 6.11) and within the volcanic arc granite field of the Pearce tectonic diagram (Fig. 6.12).

6.4.2 Hemlo Assemblage

The Terrace Bay Batholith is similar to a group of plutons described by Beakhouse (2001) as syn-deformational plutons on the Hemlo side of the greenstone belt (Fig. 6.13). The Hemlo assemblage plutons are compositionally intermediate between younger mantle derived post-tectonic plutons and the TTG-type plutons of the region. Two plutons, the Heron Bay and Cedar Lake plutons from this stage will be compared to the Terrace Bay Batholith. The Heron Bay pluton is composed of three mineralogically similar granodioritic phases that are texturally variable, with a medium-grained granodiorite, transitional granodiorite and a plagioclase sub-porphyritic granodiorite (Beakhouse, 2001). The estimated age of the pluton is 2682 +/- 2 Ma (Beakhouse and Davis, 2005). The Cedar Lake pluton is composed of granodiorite with minor diorite to quartz monzodiorite, with a U-Pb zircon age of 2680.2 $\pm$ 1.1 Ma for the interior granodiorite and 2687 $\pm$ 3 Ma for the marginal phase (Corfu and Muir, 1989; Davis and Lin, 2003). The Heron Bay and Cedar Lake plutons, are strongly metaluminous, with elevated compatible elements, high Sr abundances and lack negative Eu anomalies (Beakhouse, 2001). The intermediate plutons are characterized by hornblende with minor clinopyroxene as the mafic mineral assemblage and enriched HFSE and REE. Beakhouse (2001) divided plutonism in the Hemlo side of the greenstone belt into three stages: i) Pre- D_1, possibly syn volcanism (ε_{Nd} values of +2.3 to +3.3); ii) Post- D_1, syn – D_2 units (ε_{Nd} values of +3.1 to +1.8); and iii) post- D1, syn to post D_2 units(ε_{Nd} values +2.4 to +1.7). The post- D_1, Syn – D_2 units and syn to post D_2 stages of plutonism are recognized in the Schreiber side of the greenstone belt, with the

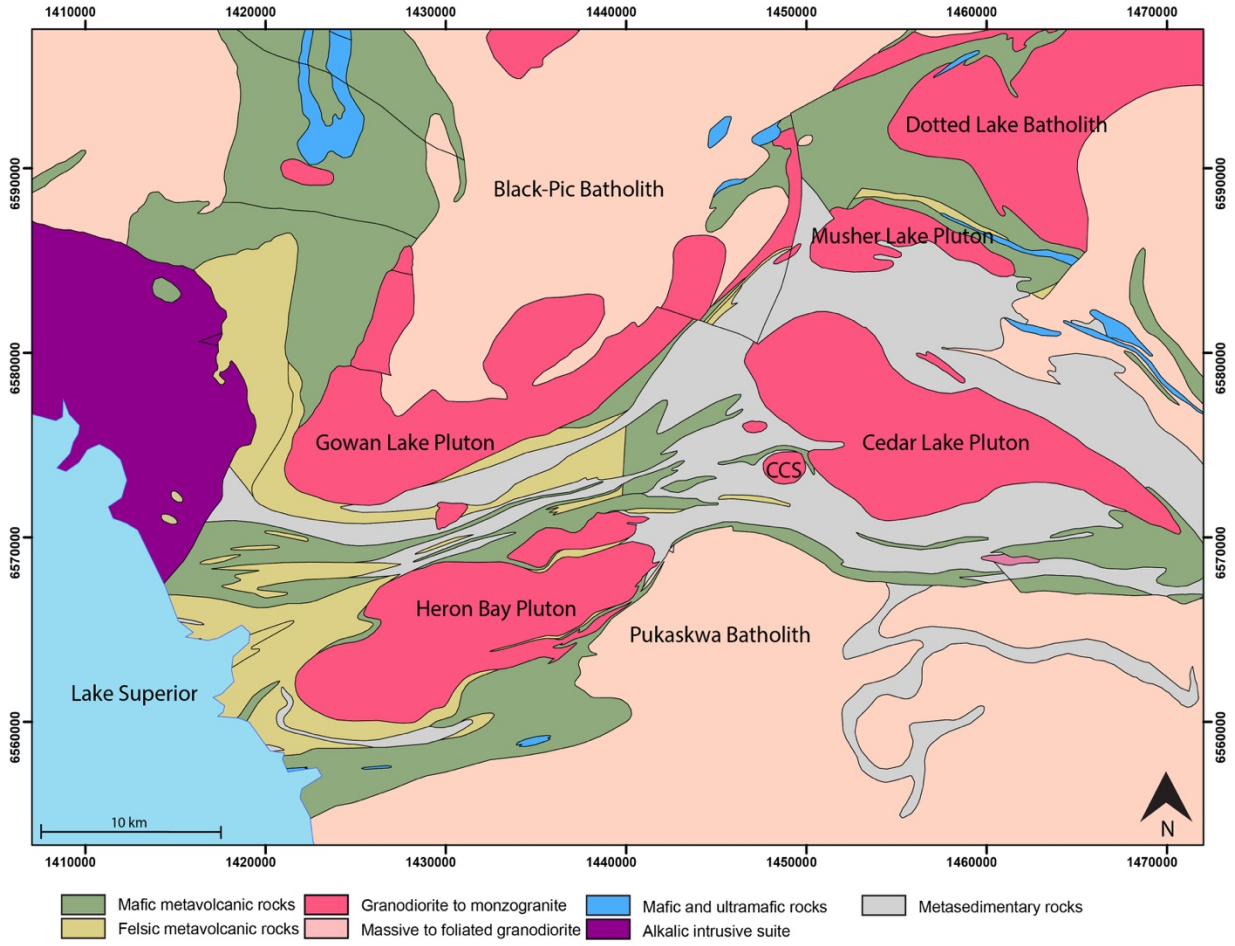

Figure 6.13 Regional map showing plutons of the Hemlo Assemblage. Modified from Stott et al., (2010).

Terrace Bay Batholith potentially representing the second stage of plutonism between TTG and the post-tectonic plutonism. The Terrace Bay Batholith has many similarities to the post D_1 plutons in the Hemlo area, including; mineralogy, geochemistry and primitive mantle ε_{Nd} isotopic signatures (ε_{Nd} = + 1.8 to +3.1). When comparing the Terrace Bay Batholith to the other two stages, the most distinct phase is the post-D_2 showing the least amount of similarities to the Terrace Bay Batholith as it is quartz poor with lower SiO_2, highly fractionated REE and abundant LILE (Stern et al., 1989; Beakhouse, 2001). The second phase of plutonism is interpreted to represent a transition in the magmatic history of the Hemlo greenstone belt

from dominantly basalt (slab) derived magmatism to a metasomatized mantle derived source (Beakhouse, 2001). As the Terrace Bay Batholith shows similar characteristics to the syn-tectonic plutons (second phase) of the Hemlo assemblage, a similar source can be assumed, consistent with geochemical data that suggests that the Terrace Bay Batholith formed during a transition from basaltic slab melt component to metasomatized mantle.

6.4.3 The Dog Lake Granite Chain

The Dog Lake granite chain (DLGC) is located within the Quetico subprovince just north of the boundary with the Wawa subprovince. The chain is composed of six oval granitic intrusions, located north of Thunder (Fig. 6.12). Kuzmich (2012) used petrographic and geochemical data to classify the intrusions as both I- and S-type (Table 6.1).

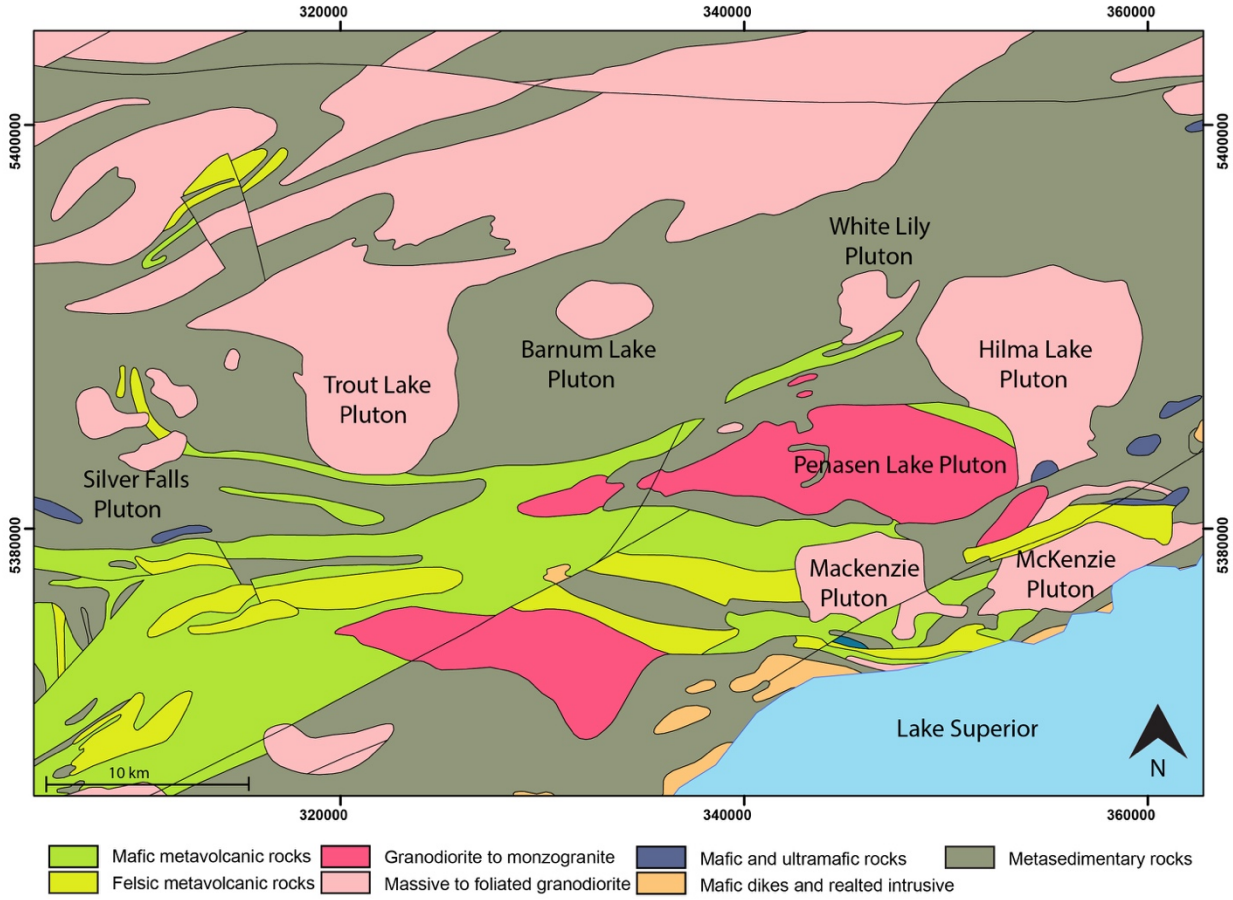

Figure 6.14 Regional map of the Dog Lake Granite Chain. Modified from Stott et al. (2010).

The I-type plutons can be subdivided into three lithological units i) microcline-phyric monzonite/quartz-monzonite, ii) syenite/quartz-syenite, and iii) monzodiorite. The I-type granites are massive, silica poor, largely metaluminous with mineral assemblages of hornblende + magnetite + sphene +/- pyroxene, with positive ε_{Nd} values of 1.44 to 2.11 (Kuzmich, 2012). The S-type granites in the DLGC are defined by peraluminous affinities, lower ε_{Nd} values of -1.44 to +1.09 and mineral assemblages of muscovite, biotite $\pm$ garnet. The S-type granites are more characteristic of the Quetico subprovince granites then the I-types which are similar to plutons of the Wawa subprovince (Williams, 1989). The Mackenzie granite is located below the DLGC but north of Thunder Bay, in the Quetico subprovince (Fig. 6.14). The Mackenzie granite is similar to the I-type intrusions of the DLGC. It is a massive, medium- to coarse-grained, quartz

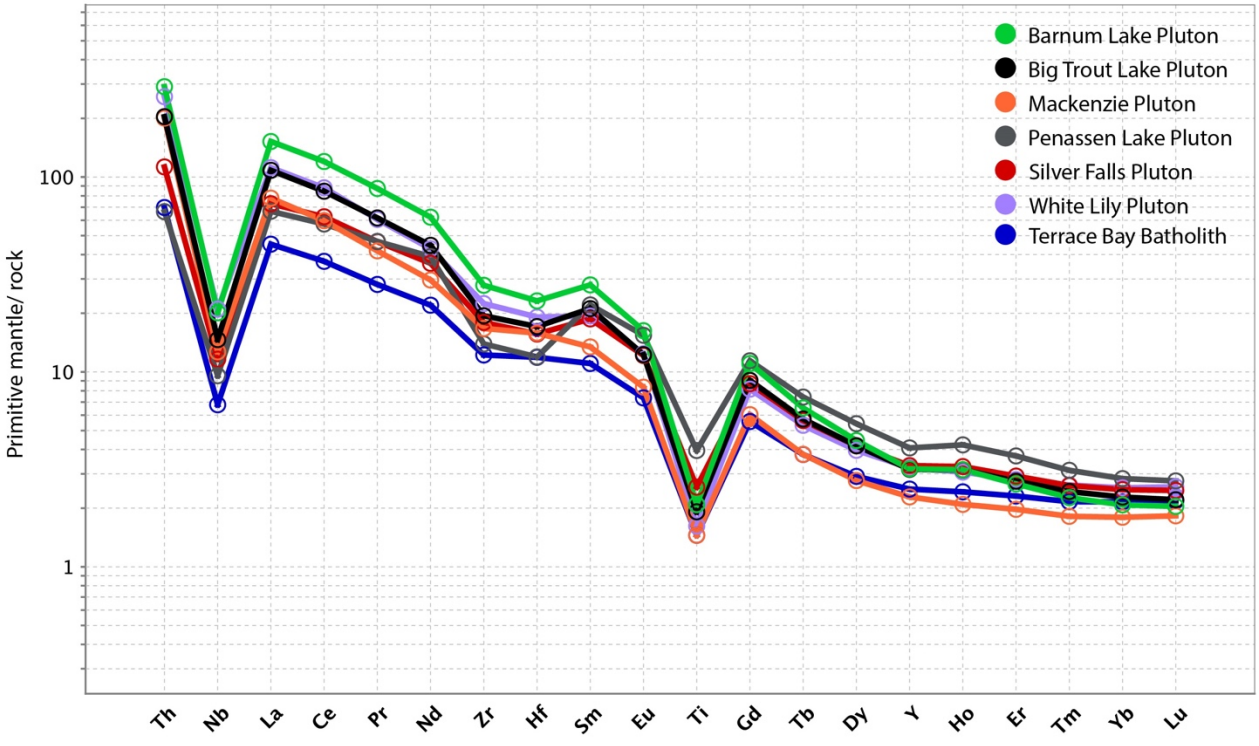

Figure 6.15. Primitive mantle normalized plots for the DLGC compared to the Terrace Bay Batholith. Normalizing values from Sun and McDonough (1989). Average values are used; Barnum Lake Pluton n= 8, Big Trout Lake Pluton n=11, Mackenzie Pluton n=16, Silver Falls Pluton n=5, Penassen Lake Pluton n=5, White Lily Pluton n=6, Terrace Bay Batholith n=122. Data from Kuzmich, (2012) and Hughes, (2016).

monzonite, with a mineral assemblage of plagioclase, potassium feldspar, quartz, amphibole, biotite, muscovite $\pm$ apatite, titanite, pyroxene and opaques (Hughes, 2016). Both the DLGC and the Mackenzie granite are thought to have formed from partial melting of the mantle wedge under the Wawa-Abitibi Terrane (Kuzmich, 2012; Hughes, 2016).

The Dog Lake granite chain and the Terrace Bay Batholith share a number of features: i) they are characterized by a similar mineralogy, ii) are calc-alkalic, ranging from metaluminous to weakly peraluminous, and display broadly similar negative HFSE anomalies (Fig. 6.15), and iii) they formed in a similar arc setting. However, the DLGC does display more variation between plutons than the Terrace Bay Batholith, with a range from I- to S-type. This likely reflects the different subprovinces that host the plutons, the Quetico basin plutons having undergone more crustal contamination by sedimentary material than the plutons of the Wawa subprovince. The ε_{Nd} values of the I-type plutons of the DLGC suggest a depleted mantle source with minimal contributions of crustal contamination, whereas the S-type plutons have negative values suggesting crustal contamination.

The Terrace Bay Batholith and the Dog Lake granites overlap when plotted on an ASI diagram, falling in both the metaluminous to weakly peraluminous fields. The Terrace Bay Batholith overlaps with the I-type lithologies of Big Trout Lake, Barnum Lake, Mackenzie granite and Silver falls plutons on the AFM diagram (Fig. 6.16). When both the Terrace Bay Batholith and the DLGC are plotted on a tectonic discrimination diagram they plot in the Volcanic Arc Setting, there is variation between the Terrace Bay Batholith and the DLGC (Fig. 6.17).

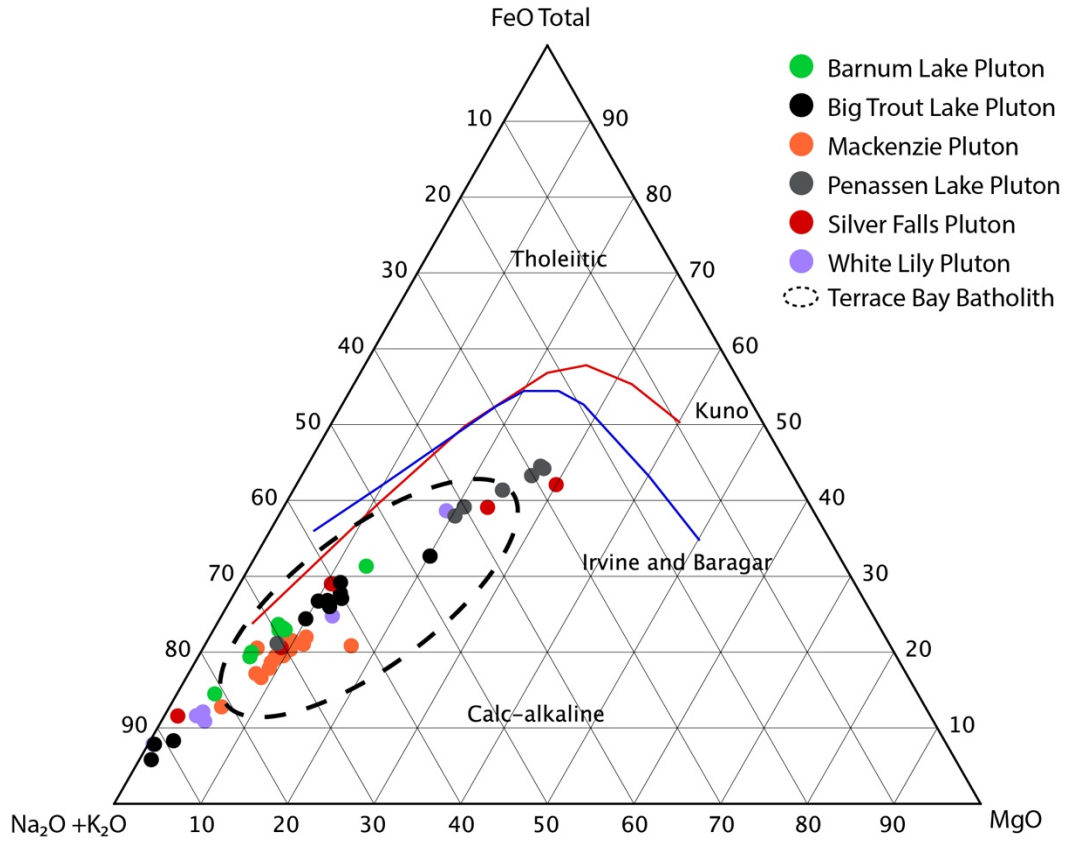

Figure 6.16 AFM diagram showing DLGC and the overlap with the Terrace Bay Batholith.The lines separating tholeiitic from calc-alkaline from Kuno (1968; red), and Irvine and Baragar (1971; blue). Data from Kuzmich, (2012) and Hughes, (2016).

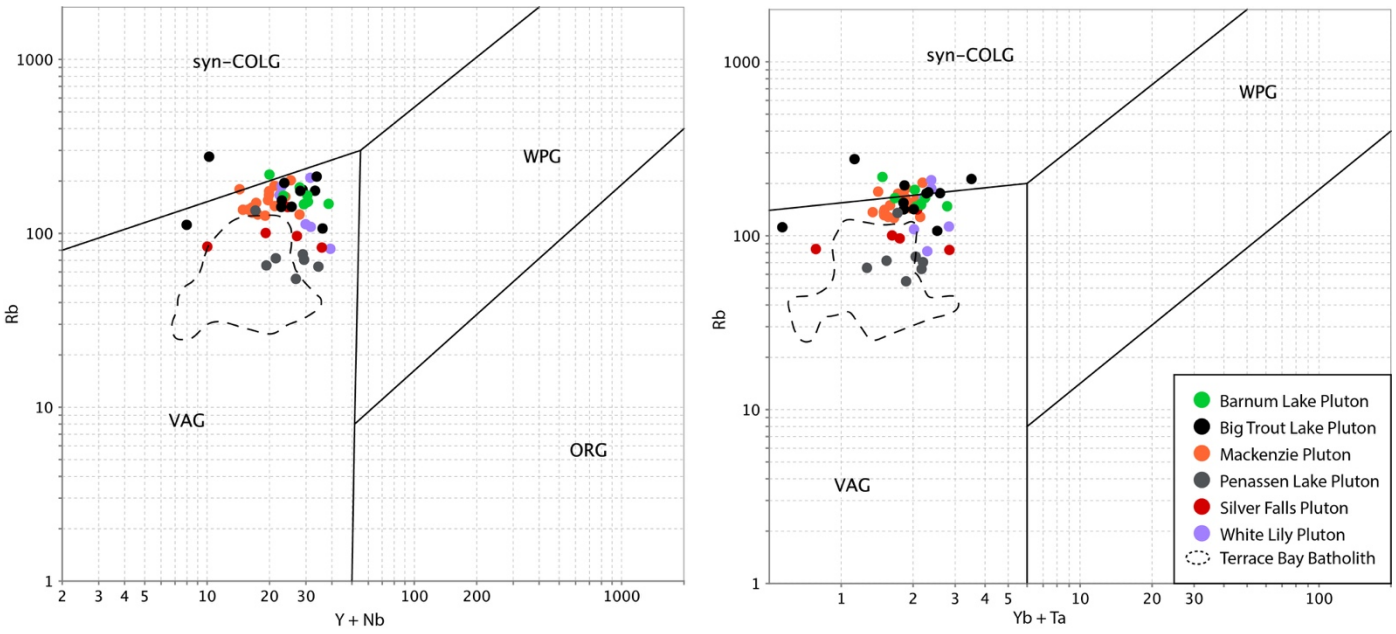

Figure 6.17 Pearce tectonic diagram plotting DLGC compared to the Terrace Bay Batholith, modified from Pearce, (1984). Data from Kuzmich, (2012) and Hughes, (2016).

The DLGC has higher Rb values, plotting near the boundary of the syn-collisional field, suggesting that the DLGC is more evolved then the Terrace Bay Batholith. The I-type granites of the DLGC have positive ε_{Nd} values of +1.09 to +2.11, falling within the lower range of the Terrace Bay Batholith. These ε_{Nd} values imply that the DLGC I-type granites were formed from a similar depleted mantle source with minimal crustal interaction (DePaolo, 1981a).

The similarities between the Terrace Bay Batholith and the DLGC suggest that they were derived from a similar depleted mantle source in an arc environment. It has been suggested that the I-type granites of the DLGC formed from melting of the mantle wedge beneath the Wawa-Abitibi island arc around 2700 Ma (Kuzmich, 2012). The Terrace Bay Batholith may well have formed from similar melting of the mantle wedge beneath the Wawa-Abitibi island arc ~10 m.y. later. This suggests that there was long lived regional subduction below the Wawa-Abitibi island arc, resulting in melting of the mantle wedge generating plutonism from 2700 Ma to 2667 Ma.

6.5 Mineralization

The Terrace Bay Batholith hosts numerous gold occurrences in the eastern end of the pluton, generally 5 m - 10 m in size but ranging up to 15 m - 20 m (Fig. 6.18a). The mineralization is generally hosted within quartz carbonate veins, although in rare cases gold can be found in the granodiorite in close proximity to quartz veins. In addition to the gold values mentioned in Chapter 4.3, company grab samples and RGP (Regional Geologist Program) grab samples have returned elevated Au values from the main gold occurrence in the pluton, the North Zone (Puumala et al., 2015; Sanatana Resources Inc, 2017).

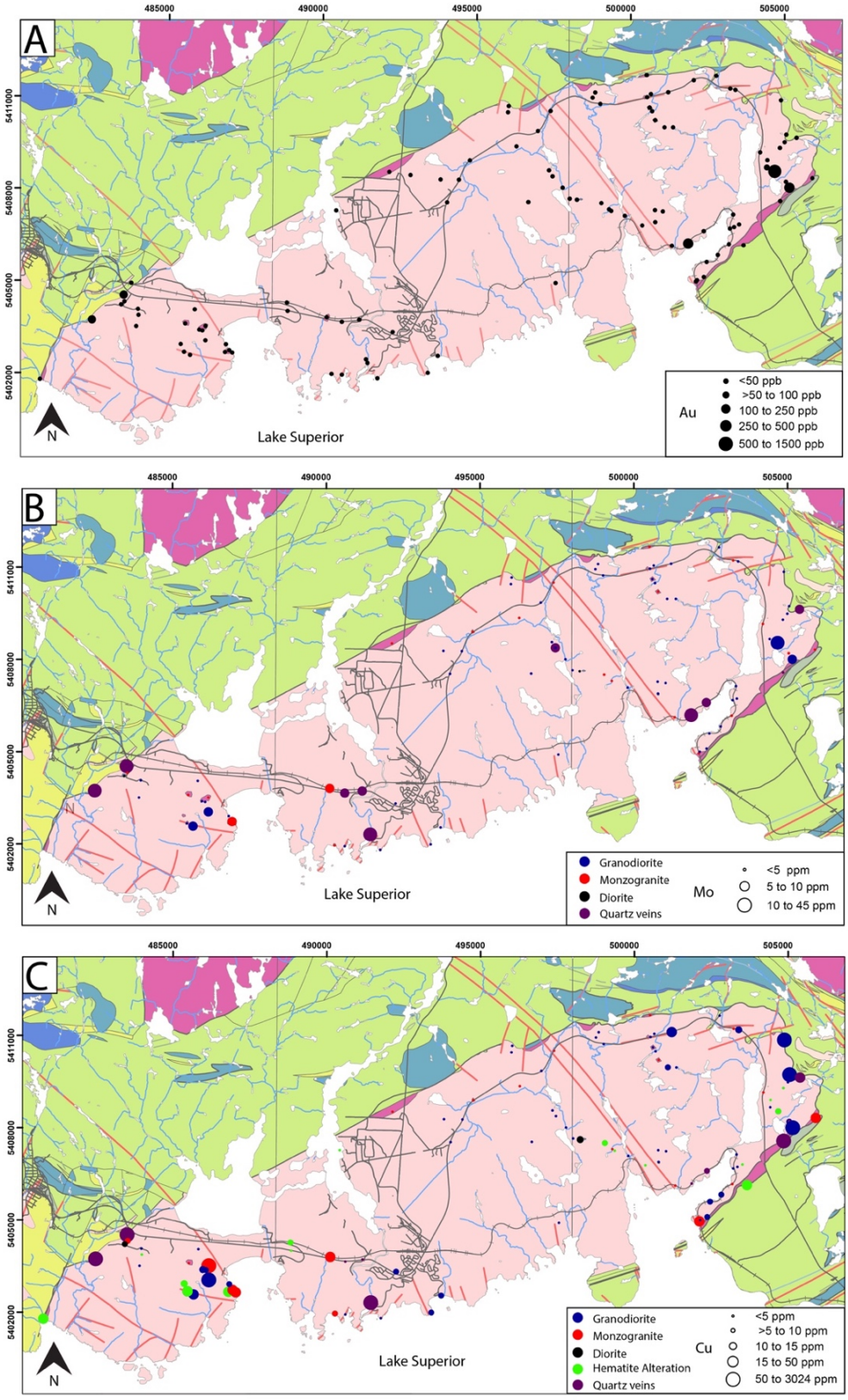

Figure 6.18. Mineralization distribution map: A) Au, B) Mo, C) Cu.

The North Zone trench has yielded grab sample values up to 16.2 g/t and 34.71 g/t from quartz veins (Puumala et al., 2015; Sanatana Resources Inc, 2017). Other occurrences along the eastern contact with the supracrustal rocks have returned values of 43.89 g/t in quartz veins. In addition to gold, molybdenite mineralization is found across the pluton, it is frequently found disseminated throughout quartz veins but also as blebs in the granodiorite with values up to 45 ppm (Chapter 4.3). Elevated copper anomalies are commonly found with the molybdenite mineralization with values of upwards of 3000 ppm (Fig. 6.18).

Five areas of elevated gold were identified by the author with Au values ranging between 250 ppb and 1500 ppb. These gold values are hosted in the granodiorite and quartz veins. Spatially there is a clear association between gold and molybdenum correlation (Fig. 6.18). All the areas with molybdenum above 10 ppm were found in the same areas as the elevated gold values, suggesting that the gold and molybdenum mineralization occurred as one event and made use of the same structural pathways. Therefore, the age of mineralization of the molybdenum likely also represent age of gold mineralization in the pluton. Copper values also show a correlation with molybdenum mineralization, with most of the elevated copper values occurring with elevated molybdenum and gold.

Rhenium-osmium geochronology of molybdenite, yielded an age of 2671 +/- 12 Ma. This age of mineralization is late tectonic and coincided with syn- to post- D_2 and metamorphism in the region. The emplacement of the pluton predates the mineralization, which is also common in gold deposits of the Yilgarn block of Australia (Groves et al., 2000, 2003; Dubé and Gosselin, 2007). This study provides the first a precise age of mineralization for the Schreiber side of the

greenstone belt and is similar to previous ages from the western Hemlo assemblage of 2665 +/- 18 Ma and 2674+/- 12 Ma (Stein et al., 2000; Gorner, unpublished).

Although the Terrace Bay Batholith has similarities to gold deposits that are discussed below, there is no evidence that the pluton itself hosts significant Au mineralization. There is a need to investigate further the source of gold to determine the exact mineralization potential of the pluton.

Gold deposits formed in metamorphic environments are diverse in terms of age, geometry, structural controls, host rocks, metamorphic grade, temperature and pressures, wall rock alteration and metal associations (Groves et al., 2003). Orogenic gold deposits typically develop in terranes that have undergone moderate- to high-T, low- to moderate-P metamorphism, and are commonly associated with the generation of large volumes of granitic melts. Distal relationships with certain intrusions are common with the possibility of a genetic connection between orogenic gold and granitoid intrusions (Groves et al., 2003; Dubé and Gosselin, 2007). Mineralization in orogenic deposits commonly formed during D_2-D_4 deformation events, normally 20 to 100 m.y. after the deposition of volcanic and sedimentary host rocks (Groves et al., 2000, 2003).

The Terrace Bay Batholith and the surrounding supracrustal rocks show potential for gold mineralization, it has features associated with gold deposits in metamorphic terranes and orogenic deposits: the presence of large-scale faults and shear zones that crosscut the pluton and the Jackfish-Middleton-McKellar Harbour shear zone that runs northwest-southeast above the pluton, greenschist to amphibolite grade metamorphism, the age and timing of the host rocks and mineralization are synchronous with other gold deposits in the Superior Province, the

supracrustal rocks are bimodal volcanic and sedimentary rocks with the potential to act as sulphur traps for fluids, and the plutonic associations (Goldfarb et al., 2001; Groves et al., 2003). The roof zone of large plutons are potential hosts for gold mineralization, due to the presence of thermal, fluid and geochemical gradients and fluxes, as well as the presence of structures related to emplacement of the pluton (Wall, 2000; Groves et al., 2003). Ore deposits can also form from circulation of meteoric fluids, those produced from thermal devolatization within aureoles, or fluids exsolved from a magma. This suggests that plutons may not be the direct source for fluids and metals but act as a heat engine for the systems (Groves et al., 2003). The pluton may not be well mineralized, but it may have acted as a heat source for the system, provided the fluids, or produced and influenced structures in the region (Belkabir et al., 1993; Groves et al., 2003; Dubé and Gosselin, 2007).

The mineralization in the Terrace Bay Batholith has similarities to vein-type hydrothermal mineralization and intrusion related gold deposits (Cerny et al., 2005; Goldfarb et al., 2005). The similarities included: i) mineralization hosted in parallel stacked sheet veins, with stockwork veining between sheets; ii) a correlation with Au mineralization and Mo, Cu, and iii) the presence of K-rich, metaluminous to peraluminous granites (Hart et al., 2000; Cerny et al., 2005; Goldfarb et al., 2005).

Although the pluton has many characteristics of intrusion related gold deposits, it lacks key features including metal associations with Bi, W, As, Te and Sb that are typical with intrusion related gold deposits, and zones of extensive hydrothermal alteration within and surrounding the pluton. The wall rock alteration that is commonly found around intrusion-related deposits (silicic, feldspathic or muscovite alteration; Cerny et al., 2005) is not present in

the Terrace Bay Batholith. As well intrusion related Au deposits are generally hosted within small 2-10 km^2 plutons, whereas the Terrace Bay Batholith is approximately 100 km^2 (Hart et al., 2000). Intrusion-related gold deposits are a relatively new deposit model, that is still being established, and consequently the model is variable, and most descriptions of intrusions-related gold deposits do not represent a single well-defined group but a number of different deposit styles with different tectonic settings, metal associations and ore fluids that are being grouped together under one deposit type (Groves et al., 2003). Intrusion related gold deposits can be broadly similar to orogenic deposits, in that the deposits associated with plutonic magmatism are not always in the granitoid but hosted in the surrounding supracrustal rocks. The supracrustal hosted deposits found in the Tintina gold province and the Pine Creek district of northern, Australia, are all examples of intrusion related gold deposits (Hart et al., 2000; Goldfarb et al., 2001; Groves et al., 2003).

The mineralization of the Terrace Bay Batholith does not fit one model but rather has characteristics similar to both intrusion-related deposits and orogenic gold deposits. The pluton is host to sporadic elevated gold occurrences, generally in quartz carbonate veins. It is surrounded by numerous historic gold occurrences (Chapter 2), that host up to an ounce per tonne gold (Puumala et al., 2016). The occurrence of gold mineralization in the contact aureole of the pluton suggests that the pluton could be an important factor in the gold mineralization in the area. This spatial and possibly temporal association between the emplacement of felsic plutons and gold mineralization in the supracrustal rocks has been noted as a factor in the formation of orogenic gold deposits (Groves et al., 1998, 2003; Goldfarb et al., 2001).

The late mantle derived plutons of the Hemlo assemblage were likely derived from hydrous magmas because of the abundance of hornblende and biotite, suggesting the Terrace Bay Batholith was also sourced from a hydrous magma because of the similar mineralogy. These magmas would likely evolving an aqueous magmatic volatile phase during crystallization (Beakhouse, 2007). Commonly in shallow (<2-3km) Phanerozoic hydrous systems, the present of a volatile phase during crystallization results in fracturing and brecciation of the supracrustal rocks creating porosity and permeability that is required for the presence of fluids (Beakhouse, 2007). The lack of fracturing and brecciation in the Terrace Bay Batholith, can be explained by the depth of emplacement. Beakhouse (2007) proposed that the plutons of the Hemlo assemblage were emplace at depths of 6-12 km, where the higher confining pressure can result in limited brecciation. Candela (1991) proposed the concept of a magmatic vapor-disperse system, which occurs when a pluton is emplaced at depths of approximately 6 to 12 km, and the aqueous phase will remains dispersed throughout the pluton. This commonly results in the formation of small uneconomic mineral occurrences. The lack of brecciation and the occurrence of small uneconomic mineral occurrences in the Terrace Bay Batholith are consistent with the 6-12 km depth of emplacement suggested by Beakhouse (2007) for the Hemlo assemblage plutons and the magmatic vapour-disperse system theory of Candela (1991).

This theory can help explain why the pluton exhibits elevated gold and molybdenum values, but no distinct mineralization associated with gold deposits. A direct correlation between mineralization and the pluton can only be generally defined based on this study; a more detailed investigation of the mineralization within the pluton and the surrounding

supracrustal rocks would be needed to determine the exact relationship of the mineralization to the pluton.

6.6 Tectonic setting and Genesis

6.6.1 Tectonic Setting

The Terrace Bay Batholith is an oval shaped granitic body that has intruded into the western Schreiber-Hemlo greenstone belt. Polat et al. (1998) proposed that the tectonic setting at the time was a subduction-accretion complex formed along a convergent plate margin. More specifically the Schreiber-Hemlo greenstone belt is an assemblage of oceanic plateaus (circa 2750-2700 Ma), oceanic island arcs (circa 2705-2697 Ma) and siliciclastic trench turbidites (circa 2705-2697 Ma), that has been intruded by syn- and post-tectonic arc granitoids (Polat et al., 1998). The belt underwent three major phases of deformation; two prior to, and one during the assembly of the Superior Province (Polat et al., 1998). The Terrace Bay granodiorite has been dated at 2689+/- 1.1 Ma (Kamo, 2016), and the diorite at 2690.64+/- 0.91 Ma (Kamo, 2018). The age of the diorite is within error of the granodiorite but could represent an earlier more mafic phase of the pluton.

This study has classified the Terrace Bay Batholith as a metaluminous to weakly peraluminous, calc-alkaline I-type granite, with a mantle Sm-Nd isotope signature. The Terrace Bay Batholith is characterized by an enrichment in LILEs and negative HFSE anomalies though all the samples, consistent with a suprasubduction zone environment (e.g, Drummond and Defant, 1990; Polat et al., 1998; Whalen et al., 2004; Richards and Kerrich, 2007; Hollings et al., 2011). The pluton plots within the volcanic arc granite field (VAG) with minimal scatter (Fig. 6.18). Geochemical and isotopic signatures of the Terrace Bay Batholith are consistent with the

suggested oceanic arc setting for the Schreiber greenstone belt (Polat et al., 1998, 1999). Strongly fractionated HREE and the LREE enrichment are all consistent with formation within a garnet stability field (Drummond and Defant, 1990; Polat et al., 1998; Frost et al., 2006; Richard sand Kerrich, 2007).

The positive ε_{Nd} values of the pluton, are consistent with a depleted mantle source (I-type) over a crustal-sedimentary source (S-type). Crustal contamination would result in prominent negative Eu anomalies, and depletion of Sr which are not seen in the Terrace Bay Batholith (Drummon and Defant, 1990). The mineral chemistry suggests that the magma was hydrous enough to stabilize and promote significant amphibole fractionation while suppressing plagioclase fractionation and driving the magma to high Sr/Y ratios. The negative Nb and Ti anomalies reflect the fractionation of amphibole in the melt as, amphibole can act a sink for HFSE during partial melting (Drummond and Defant, 1990; Frost et al., 2006). These chemical characteristics are thought to be consistent with an origin as partial melts of subducted oceanic

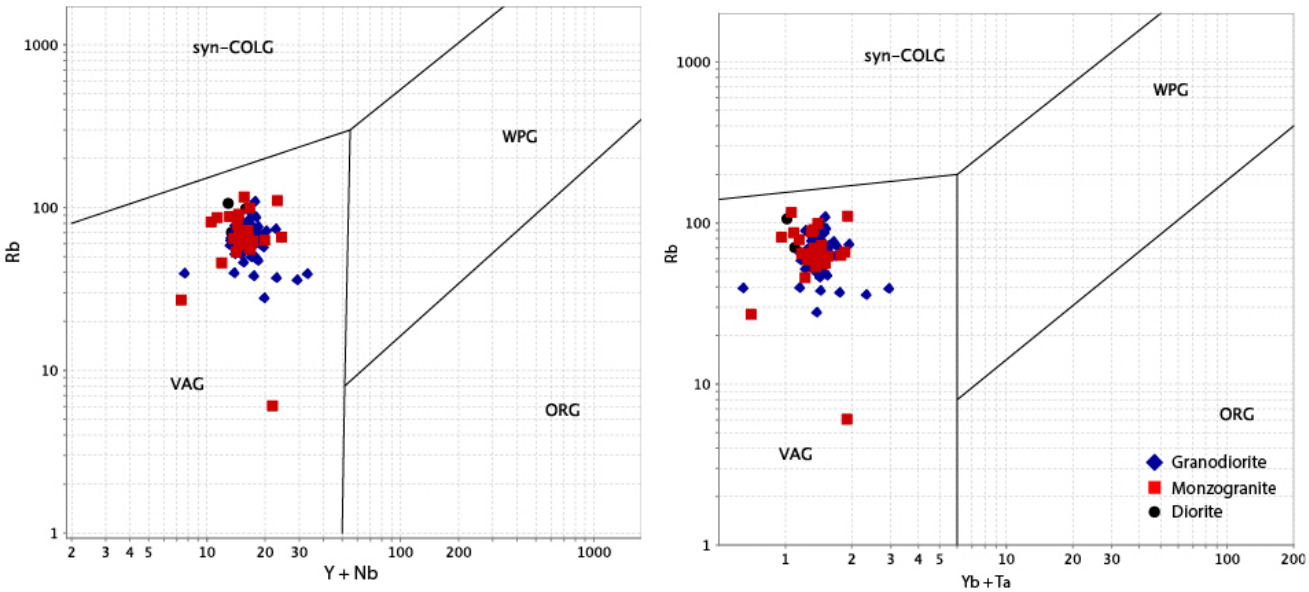

Figure 6.19 Pearce tectonic diagram plotting the Terrace Bay Batholith, using Pearce, (1984).

crust, that partially equilibrated with the metasomatized mantle wedge during ascent (Frost et al., 2006; Richards and Kerrich, 2007).

Trondhjemites, tonalites and granodiorites comprise around 90% of the Archean crust and are an important part of Archean plutonism (Martin et al., 2005). TTG melts, are thought to form from AFC and/or MASH processes at the base of the crust, where they incorporate some crustal material (Martin, 1987; Frost et al., 2006; Richards and Kerrich, 2007). This style of plutonism is dominant around >2700 Ma (Martin et al., 2005), 20-30 m.y. before the Terrace Bay Batholith was emplaced. The wide range of SiO_2 (57-81 wt.%) in the Terrace Bay Batholith is broadly consistent with average TTG SiO_2 values (~70%; Martin, 1987; Frost et al. 2006; Beakhouse, 2011). Other characteristics of the Terrace Bay Batholith that are consistent with TTG are elevated Al_2O_3 (14-18%) and NaO_2 (avg. 5.1%) and the metaluminous character (Martin, 1987). The TTG suites that intrude into the eastern side of the Schreiber-Hemlo greenstone belt have similarities with the Terrace Bay Batholith including; negative Ti and Nb anomalies, LILEs enrichment and fractionated HREE (Beakhouse, 2001; Whalen et al., 2004). The Terrace Bay Batholith has fractionated HREE (La/Yb_n= 12.1-42.7 avg.= 20.4) but not as highly fractionated as typical TTG (La/Yb_n= 16-102 avg.= 49; Martin, 1987; Whalen et al., 2004). When compared to Archean TTG suites the Terrace Bay Batholith lacks the Eu anomalies that are commonly associated with Archean TTG (Martin, 1987). This can be explained by increasing the formation of amphibole but suppressing the crystallization of plagioclase in the source, resulting in a lack of Eu anomaly that is seen in the Terrace Bay Batholith (Drummond and Defant, 1990; Kerrich and Richards, 2007; Richards, 2011).

While the Terrace Bay Batholith does have some geochemical similarities to TTGs, the lack of extremely fractionated HREE and Y, Eu anomalies, and the assimilation and incorporation of crust are not consistent with the TTG model. It is likely that the Terrace Bay Batholith formed in a similar arc setting to TTG melts, but that the evolution of the batholith was different from TTG intrusions. The pluton could potentially represent a late stage calc-alkaline intrusion that formed after the TTG stage of magmatism (Martin, 1987; Beakhouse, 2011). The transition from the extensive stage of TTG-type plutonic activity to a later stage of mantle derived calc-alkaline intrusions has been suggested to represent the terminal stage of Archean juvenile crust formation (Beakhouse et al., 1999; Beakhouse, 2001). When plotted on a Sr/Y vs. Y and La/Yb vs. Yb diagram, the Terrace Bay Batholith plots within the adakite like rocks field, suggesting they formed from melting of the down going slab in the garnet stability field (Fig. 6.19; Richards and Kerrich, 2007). Although Sr can be mobile in Archean systems the relatively constrained trend of Sr compared to K on Figures 5.1 and 5.2 suggests it has remained relatively immobile. The fact that the data also plot in the adakite field on the La/Yb plot which uses immobile elements also supports a slab melt origin. Due to the variations in geochemistry from TTGs, it is likely that the Terrace Bay Batholith is derived from the mantle wedge within the garnet stability field and may have had some incorporation from partial melts from subducted oceanic crust (Polat et al., 1999; Beakhouse, 2007).

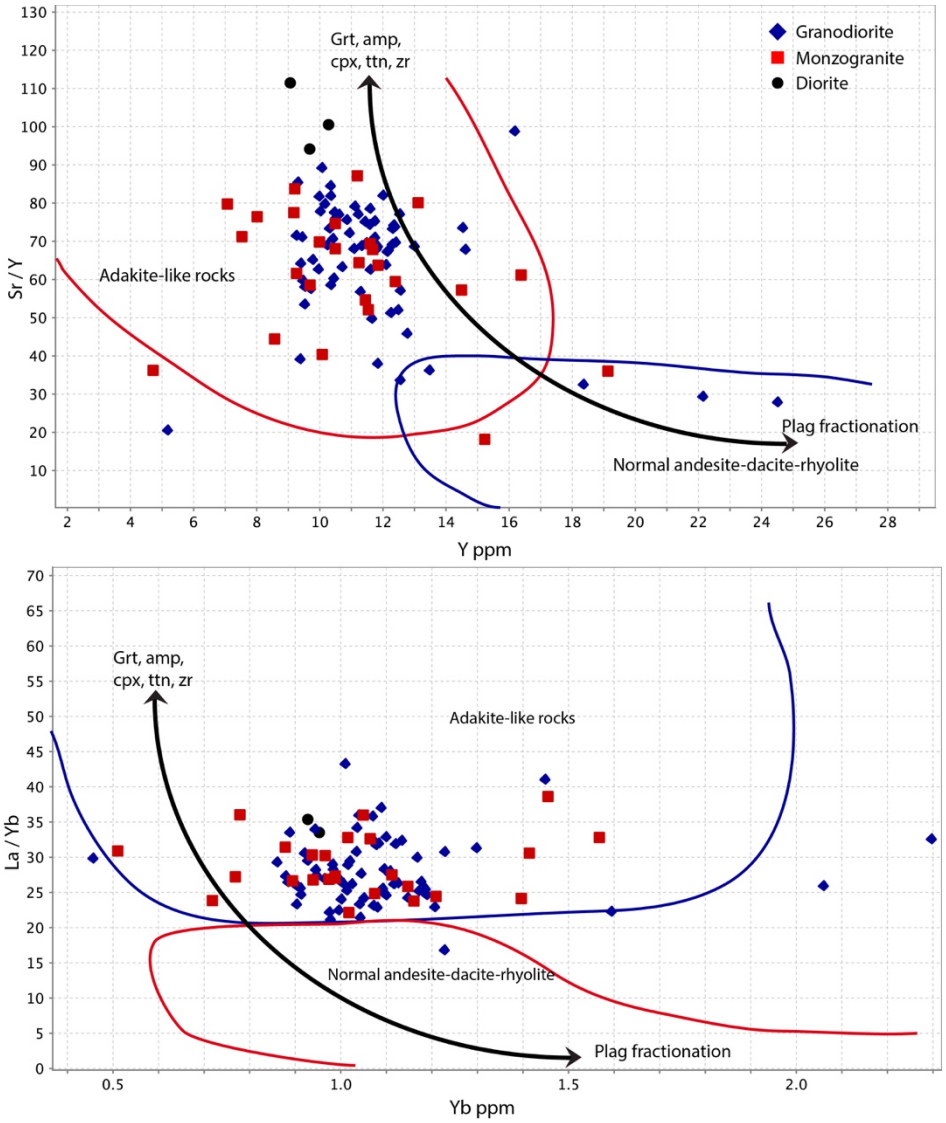

Figure 6.20 Plots of Sr/Y vs. Y and La/Yb vs. Yb for the Terrace Bay Batholith. Adakite fields from Richards and Kerrich (2007). Normal island-arc andesite-dacite-rhyolite fields from Castilla et al. (1990). Fractionation trends from Richards and Kerrich (2007). Grt= Garnet, Amp= Amphibole, Cpx= Clinopyroxene, Ttn= Titanite, Zr= Zircon.

6.6.2 Genesis

Granitoid magmatism involves four main stages; generation, segregation, ascent and emplacement (Petford et al., 2000). The presence of large homogenous intrusions are rare because it is generally accepted that plutons form from multiple injections into the magma chamber, that typically affect the geochemistry and mineralogy of the pluton (Clemens and Stevens, 2012). Granitic plutons emplaced in the upper crust are thought to be emplaced as

low-viscosity, crystal-poor magmas in tabular intrusions fed from depth by small magma batches rather than emplacement as large diapirs moving through the crust. The magma must be transported from the source region to final emplacement, generally along narrow conduits, as propagating dykes or pre-existing faults, or an interconnected network of active shear zones and structures (D'Lemos et al., 1992; Petford et al., 2000). Annen (2009) suggested that emplacement of granitic intrusions in an episodic process involving multiple pulses of magma into the chamber (Petford et al., 2000; Clemens and Stevens, 2012). The emplacement of granitic magma within crust occurs when there is a switch from upward to horizontal flow and can be controlled by a combination of mechanisms including; pre-existing or emplacement generated wall rock structures and density effects between the flow and its surroundings (Petford et al., 2000).

Variations in mineral composition can be influenced by a wide range of factors including bulk composition and late magmatic to sub solidus re-equilibration of mineral phases (Beakhouse, 2001). The similar geochemistry but variations in mineralogy in the Terrace Bay Batholith can be explained by magma being emplaced in pulses with the source magma staying consistent. If magma emplacement were episodic from one chamber or reserve in the lower crust, the geochemical signature would stay consistent throughout the emplacement causing differences in the mineralogy. The first pulse would experience the most crustal assimilation and contamination which can explain the slightly more evolved ε_{Nd} signatures of the monzogranite phase. It is suggested that with multiple pulses the evolution of the pluton would be the reverse of what is typical in a large cooling magma chamber, because the residual melt would become more felsic as a result of mafic mineral crystallization over time (Annen, 2008).

This evolution towards more felsic melts is seen in the Terrace Bay Batholith, the more mafic monzogranite along the contact grades to the felsic granodiorite in the center of the pluton. The presence of amphibole rimmed pyroxenes is an example of the more mafic primary magma. As well the mafic mineral clusters typically only occur within a kilometer of the contact with the supracrustal rocks. The diorite outcrop in the center of the pluton likely represents an autolith of the pluton that has been reincorporated into the magma, representing one of the earliest more mafic phases of the pluton. The other diorite outcrop located along the contact with the supracrustal rocks supports the theory of the diorite being an earlier phase of the pluton.

The multiple pulse theory is consistent with the pluton having formed from one source but would have undergone fractional crystallization, creating subtle mineralogical lithologies with no geochemical differences. The presence of only three lithological changes, suggests that there were not numerous pulses, because these would result in more variation across the pluton. The lack of sharp contacts between lithologies suggests that the transition would be gradational, which can be explained by the extended crystallization. The multiphase emplacement would allow the melt to begin to crystalize producing the monzogranite. The monzogranite would also be influenced by contamination of the supracrustal rocks which would not be isotopically distinguishable because the contaminants have a similar isotopic character. After partial crystallization of multiple pulses there would be a gradational change from more mafic rich along the contact to felsic in the center.

6.6.3 Genetic Model

Based on the petrographic, geochemical, mineralogical and isotopic evidence for the petrogenesis of the Terrace Bay Batholith, the pluton would have been emplaced during the initial stages of the collision of the Wawa-Abitibi terrane into the Wabigoon terrane, deforming the Quetico basin culminating at 2689-2684 Ma (Williams, 1991; White et al., 2003). First, the subduction of the oceanic lithosphere under the Wawa-Abitibi terrane, would have generated fluids derived by dehydration of the downgoing slab, metasomatizing the mantle wedge (Richards and Kerrich, 2007). Partial melting of the metasomatized mantle generated primitive mafic magmas at depth within the garnet stability field, potentially incorporating minimal amounts of slab derived melts. The mafic melts began to ascend due to a buoyancy contrast within the mantle wedge (Fig. 6.21; Richards and Kerrich, 2007). The mafic melt underplated the arc crust and underwent fractional crystallization evolving into an I-type granitic melt. The crust that the magma underplated and intruded into would have been oceanic crust, with a source composition similar to the magma, explain the lack of strong negative ε_{Nd} signatures (Myers, 1997). Newly formed granitic melt ascended along structural weaknesses in the Wawa-Abitibi terrane. The magma underwent very little crustal contamination during the ascent through the crust. Next the granitoid magma would have been emplaced at depth within the Wawa- Abitibi terrane by multiple injections (Petford et al., 2000; Beakhouse, 2007; Annen, 2009). Finally, the intrusion crystalized after multiple pulses of magma have entered pluton.

To summarize the Terrace Bay Batholith formed from partial melting of metasomatized mantle wedge within the garnet stability field, possibly with minor slab derived melts incorporated, before being emplaced into the bimodal volcanic sequence of the Schreiber-

Hemlo greenstone belt. The pluton was emplaced in multiple pulses derived from the same source magma creating mineralogically unique but geochemically similar lithologies. The geochemical and isotopic results from this study supports the previous work of Polat et al. (1998, 1999), with the model that the western Schreiber greenstone belt represents an Archean oceanic volcanic arc sequence.

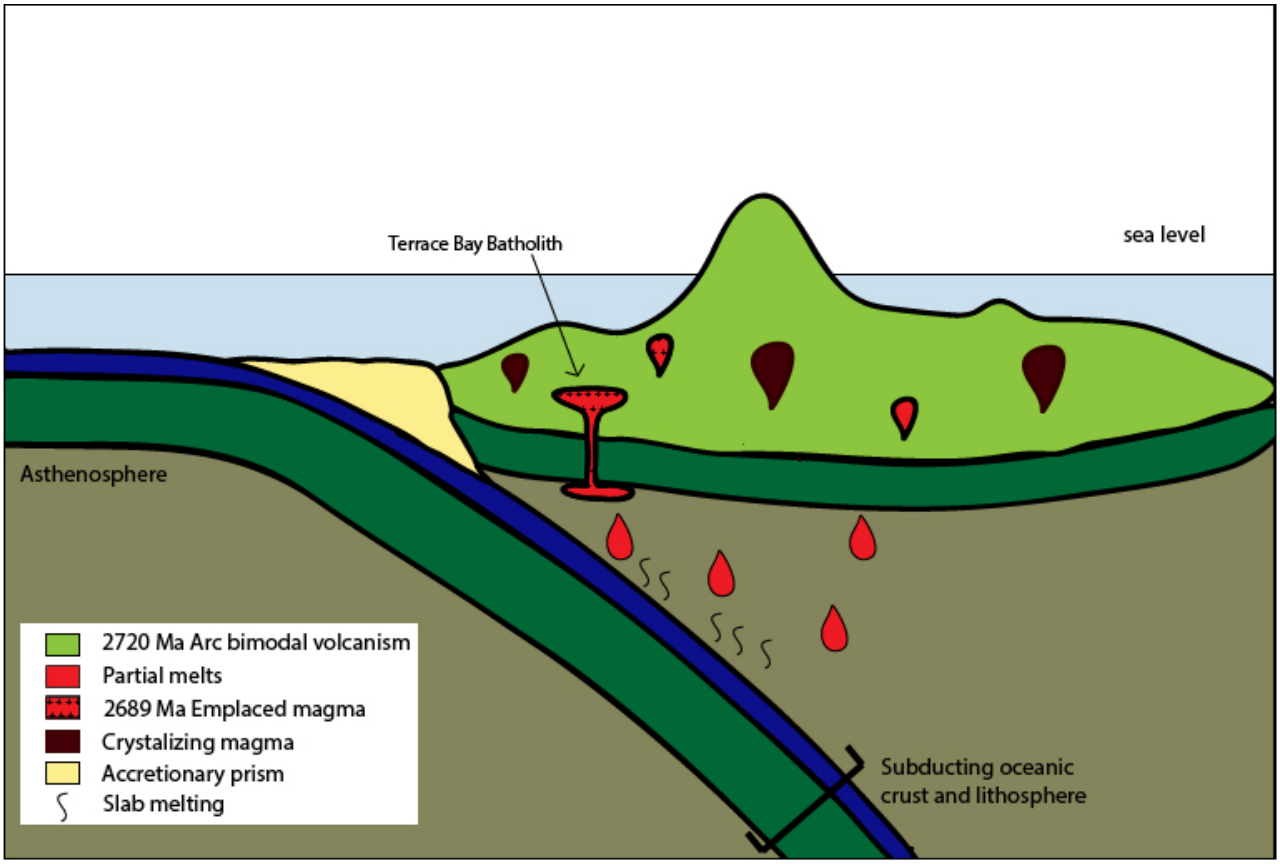

Figure 6.21 Tectonic model for the formation of Terrace Bay Batholith.

Chapter 7 - Conclusions

The Terrace Bay Batholith is a 25 km long oval shaped granitoid intrusion located in the western portion of the Schreiber-Hemlo greenstone belt, part of the larger Wawa-Abitibi terrane. The pluton, emplaced at 2689+/-1.1 Ma, intrudes *circa* 2720 Ma metavolcanic rocks. The pluton can be separated into three mineralogically distinct lithologies: granodiorite (that typically consists of medium to coarse-grained quartz and feldspar phenocrysts with a groundmass of fine-grained amphibole, biotite, disseminated magnetite, and sulphide minerals), a monzogranite (composed of medium-grained quartz and feldspar with increased amounts of potassium feldspar and amphibole relative to the granodiorite), and a diorite (that is composed of medium-grained amphibole and plagioclase with little to no quartz or potassium feldspar present). Pyroxene crystals sporadically occur in the granodiorite, some of which are rimmed by amphibole. This suggests the early crystallization of the clinopyroxene in an early, more primitive magma that subsequently evolved to crystalize amphibole. Coarse-grained potassium feldspar phenocrysts that occur sporadically throughout the pluton have orthoclase rich outer rims with albite rich cores; this suggests that the magma was initially sodium rich producing predominantly albite, and as the magma evolved as albite crystalized, the magma became more potassium rich, switching compositions to dominantly orthoclase.

Two types of hydrothermal alteration are present in the pluton: a chlorite-epidote and a pervasive hematite alteration. These are present sporadically across the pluton, and always in proximity to cross-cutting regional scale faults or shears. The chlorite-epidote occurs dominantly along faults and fractures with quartz veins, resulting in a fine-grained groundmass

of epidote and chlorite with relict feldspar and quartz phenocrysts. The very fine-grained hematite alteration overprints all primary mineralogy and textures, leaving the granodiorite deep red to purple in colour. The faults and shear zones in the pluton likely act as pathways for the hydrothermal fluids.

Geochemically, the Terrace Bay Batholith is a calc-alkaline homogenous pluton, showing minimal geochemical change between lithologies. The pluton exhibits trace element signatures that are characteristic of arc-related signatures including: fractionated HREE, negative HFSE anomalies, enrichment of Th over LREE and enrichment of LREEs. The fractionated HREEs and the Th-Nb-La systematics are consistent with the formation in a subduction zone at depths where garnet is stable. The Sr/Y and La/Yb signatures agree with formation within the garnet stability field and suggest a minimal amount of slab-derived melt incorporated in to the mantle wedge. The marginal monzogranite shows slight decreases in $\boldsymbol{\varepsilon}_{Nd}$values towards enrichment, likely due to minimal contamination of supracrustal rocks during emplacement. The supracrustal contaminants were derived from a similar source as the pluton, making it difficult to distinguish a true contamination signature.

The magma emplacement of the pluton was determined to be through multiple injections in to the intrusion from a single source. The pluton underwent fractional crystallization, creating subtle mineralogical lithologies with no geochemical differences. The homogeneous nature of the pluton suggests it is unlikely that there were numerous pulses because several pulses as this would result in more variation across the pluton

Rhenium-osmium isotopes were completed to obtain an age of mineralization for the pluton, returning a value of 2671 +/- 12 Ma. The molybdenum mineralization is spatially associated with gold mineralization in the pluton, suggesting that they were deposited from the same hydrothermal event. As is common in Archean cratons, this age of mineralization is syn- to post- both D_2 and regional metamorphism, as well as postdating the emplacement of the pluton. The mineralization in the pluton generally exhibits elevated gold and molybdenum values but no distinct mineralization style associated with gold deposits. These features can be explained by the magmatic vapor-disperse system theory which occurs when a pluton is emplaced at depth, as the aqueous phase will remain dispersed throughout the pluton instead of concentrating in areas in economic amounts.

Regionally, the Terrace Bay Batholith is comparable to the surrounding intrusions in the western Schreiber side of the belt but also comparable to the post- D_1, syn-D_2 intrusions of the eastern Hemlo side of the greenstone belt. Two stages of plutonism are recognized in the western Schreiber-Hemlo greenstone belt based on the new geochronological data and field interpretations: a syn-tectonic stage which is represented by the Terrace Bay Batholith, Steel River pluton, and Syenite Lake pluton (2690 to 2882 Ma) and a post-tectonic stage of plutonism which is represented by the Foxtrap, Little Pic River and the Santoy Lake plutons (2674 to 2667 Ma). The regional plutons show similar arc related geochemical signatures, to the Terrace Bay Batholith.

Overall, this study of the Terrace Bay Batholith has helped further define and expand the knowledge of the plutonism and mineralization on the Schreiber side of the greenstone

belt. The isotopic work adds valuable knowledge to the region, where only minimal amounts of isotopic work have been done on the basalts and komatities, and further confirms the tectonic models for the greenstone belt. This study also helps to link the plutonism between the western Schreiber side of the belt and the eastern Hemlo assemblage by showing geochemical, geochronological and isotopic connections between the two.

References

Annen, C. 2009. From plutons to magma chambers: Thermal constraints on the accumulation of eruptible silicic magma in the upper crust. Earth and Planetary Science Letters, vol. 284, p. 409-416.

Barbarin, B. 1999. A review of the relationships between granitoid types, their origins and their geodynamic environments. Lithos, vol. 46, p. 605-626.

Beakhouse, G.P. 2001. Nature, timing and significance of intermediate to felsic intrusive rocks associated with the Hemlo greenstone belt and implications for the regional geological setting of the Hemlo gold deposit; Ontario Geological Survey, Open File Report 6020, p. 1-248.

Beakhouse, G. P., & Davis, D. W. 2005. Evolution and tectonic significance of intermediate to felsic plutonism associated with the Hemlo greenstone belt, Superior Province, Canada. Precambrian Research, vol. 137, p. 61-92.

Beakhouse, G.P. 2007. Structurally controlled, magmatic hydrothermal model for Archean lode gold deposits: a working hypothesis; Ontario Geological Survey, Open File Report 6193, p. 1-133

Beakhouse, G. P., Heaman, L. M., & Creaser, R. A. 1999. Geochemical and U–Pb zircon geochronological constraints on the development of a Late Archean greenstone belt at Birch Lake, Superior Province, Canada. Precambrian Research, vol. 97, p. 77-97.

Belkabir, A., Robert, F., Vu, L., & Hubert, C. 1993. The influence of dikes on auriferous shear zone development within granitoid intrusions: the Bourlamaque pluton, Val-d'Or district, Abitibi greenstone belt. Canadian Journal of Earth Sciences, vol. 30, p. 1924-1933.

Belvin, P.L., 2009. The primacy of magma compositions in determining the Re and W contents of molybdenite. Proceedings of the 24th International Applied Geochemistry Symposium, Fredericton, Canada, vol. 1 p. 119–122.

Bennett, V. C., & DePaolo, D. J. 1987. Proterozoic crustal history of the western United States as determined by neodymium isotopic mapping. Geological Society of America Bulletin, vol. 99, p. 674-685.

Berzina, A. N., Sotnikov, V. I., Economou-Eliopoulos, M., & Eliopoulos, D. G. 2005. Distribution of rhenium in molybdenite from porphyry Cu–Mo and Mo–Cu deposits of Russia (Siberia) and Mongolia. Ore Geology Reviews, vol. 26, p. 91-113.

Candela, P. A. 1991. Physics of aqueous phase evolution in plutonic environments. American Mineralogist, vol. 76, p. 1081-1091.

Card, K. D. 1990. A review of the Superior Province of the Canadian Shield, a product of Archean accretion. Precambrian Research, vol. 48, p. 99-156.

Card, K. D., & Ciesielski, A. 1986. DNAG# 1. Subdivisions of the Superior Province of the Canadian shield. Geoscience Canada, vol. 1, p. 5-13.

Cao, M., Evans, N. J., Hollings, P., Cooke, D. R., McInnes, B. I., Qin, K., & Li, G. 2018. Phenocryst zonation in porphyry-related rocks of the Baguio District, Philippines: Evidence for magmatic and metallogenic processes. Journal of Petrology, vol. 59, p. 825-848.

Castro, A., & Stephens, W. E. 1992. Amphibole-rich polycrystalline clots in calc-alkaline granitic rocks and their enclaves. The Canadian Mineralogist, vol. 30, p. 1093-1112.

Carter, M.W. 1979. Schreiber Area, District of Thunder Bay; p.44-47 in Summary of Field Work 1979, by the Ontario Geological Survey, edited by V.G. Milne, O.L. White, R.B. Barlow, and C.R. Kustra, Ontario Geological Survey, Miscellaneous Paper 90, p. 1-245.

Carter, M.W. 1980. Terrace Bay Area, District of Thunder Bay; p.42-46 in Summary of Field Work 1980, by the Ontario Geological Survey, edited by V.G. Milne, O.L. White, R.B. Barlow, J.A. Robertson, and A.C. Colvine, Ontario Geological Survey, Miscellaneous Paper 96, p. 1-201.

Carter, M.W. 1981a. Terrace Bay Area, District of Thunder Bay; p.34-36 in Summary of Field Work by the Ontario Geological Survey, edited by John Wood, O.L. White, R.B. Barlow, and A.C. Colvine, Ontario Geological Survey, Miscellaneous Paper 100, p. 1-255.

Carter, M.W. 1981b. Precambrian Geology of the Schreiber Area, East Part, Thunder Bay District; Ontario Geological Survey, Preliminary Map P.2391, Geological Series, scale 1:15,840 or l inch to 1/4 mile. Geology 1979.

Carter, M.W. 1981c. Precambrian Geology of the Terrace Bay Area, East Sheet, Thunder Bay District; Ontario Geological Survey, Preliminary Map P.2418, Geological Series, scale 1:15,840 or l inch to 1/4 mile. Geology 1980.

Carter, M.W. 1981d. Precambrian Geology of the Terrace Bay Area, West Sheet, Thunder Bay District; Ontario Geological Survey, Preliminary Map P.2417, Geological Series, scale 1:15,840 or l inch to 1/4 mile. Geology 1980.

Carter, M. W. 1988. Geology of Schreiber-Terrace Bay area, District of Thunder Bay; Ontario Geological Survey, Open File Report 5692, p. 1-287.

Cerny, P., Blevin, P. L., Cuney, M., & London, D. 2005. Granite-related ore deposits. Economic Geology, vol. 100, p. 337-370.

Champion, D. C. 2013. Neodymium depleted mantle model age map of Australia: explanatory notes and user guide. Geoscience Australia. P. 1-215

Chappell, B., & White, A. 1974. Two contrasting granite types. Pacific geology, vol. 8, p. 173-174.

Chappell, B. W., & White, A. J. R. 2001. Two contrasting granite types: 25 years later. Australian Journal of Earth Sciences, vol. 48, p. 489-499.

Clemens, J. D., & Stevens, G. 2012. What controls chemical variation in granitic magmas?. Lithos, vol. 134, p. 317-329.

Corfu, F., and Muir, T.L. 1989. The Hemlo – Heron Bay greenstone belt and Hemlo Au–Mo deposit, Superior Province, Ontario, Canada: 1. Sequence of igneous activity determined by zircon U–Pb geochronology. Chemical Geology, vol. 79: p. 183–200.

Davis, D.W., Beakhouse, G.P. and Jackson, S.L. 1998. U-Pb zircon and titanite geochronology; in Regional Geological setting of the Hemlo gold deposit; an interim progress report; Ontario Geological Survey, Open File Report 5977, part 3, p. 1-9.

Davis, D. W., & Lin, S. 2003. Unraveling the geologic history of the Hemlo Archean gold deposit, Superior Province, Canada: A U-Pb geochronological study. Economic Geology, vol. 98, p. 51-67.

Davis, D.W. and Sutcliffe, C.N. 2017. U-Pb geochronology by LA-ICPMS in samples from northern Ontario; internal report prepared for the Ontario Geological Survey, Jack Satterly Geochronology Laboratory, University of Toronto, Toronto, Ontario, p. 1-131

Defant, M. J., & Drummond, M. S. 1990. Derivation of some modern arc magmas by melting of young subducted lithosphere. nature, vol. 347, p. 662.

D'lemos, R. S., Brown, M., & Strachan, R. A. 1992. Granite magma generation, ascent and emplacement within a transpressional orogen. Journal of the Geological Society, vol. 149, p. 487-490.

DePaolo, D. J. 1981a. Neodymium isotopes in the Colorado Front Range and crust–mantle evolution in the Proterozoic. Nature, vol. 291, p. 193-196.

DePaolo, D. J. 1981b. A neodymium and strontium isotopic study of the Mesozoic calc-alkaline granitic batholiths of the Sierra Nevada and Peninsular Ranges, California. Journal of Geophysical Research: Solid Earth, vol. 86, p. 10470-10488.

DePaolo, D. J., & Wasserburg, G. J. 1976. Nd isotopic variations and petrogenetic models. Geophysical Research Letters, vol. 3, p. 249-252.

Drummond, M. S., & Defant, M. J. 1990. A model for trondhjemite-tonalite-dacite genesis and crustal growth via slab melting: Archean to modern comparisons. Journal of Geophysical Research: Solid Earth, vol. 95, p. 21503-21521.

Dubé, B., & Gosselin, P. 2007. Greenstone-hosted quartz-carbonate vein deposits. Mineral Deposits of Canada: A synthesis of major deposit-types, district metallogeny, the evolution of geological provinces, and exploration methods: Geological Association of Canada, Mineral Deposits Division, Special Publication, vol. 5, p. 49-73.

Finger, F., Roberts, M. P., Haunschmid, B., Schermaier, A., & Steyrer, H. P. 1997. Variscan granitoids of central Europe: their typology, potential sources and tectonothermal relations. Mineralogy and Petrology, vol. 61, p. 67-96.

Fralick, P., Purdon, R.J, and Davis, D.W. 2006. Neoarchean trans-subprovince sediment transport in southwestern Superior Province: Sedimentological, geochemical, and geochronological evidence; Canadian Journal of Earth Sciences, vol. 43, p. 1055-1070.

Frost, B. R., Barnes, C. G., Collins, W. J., Arculus, R. J., Ellis, D. J., & Frost, C. D. 2001. A geochemical classification for granitic rocks. Journal of petrology, vol. 42, p. 2033-2048.

Frost, C. D., Frost, B. R., Kirkwood, R., & Chamberlain, K. R. 2006. The tonalite–trondhjemite–granodiorite (TTG) to granodiorite–granite (GG) transition in the late Archean plutonic rocks of the central Wyoming Province. Canadian Journal of Earth Sciences, vol. 43, p. 1419-1444.

Goldfarb, R. J., Groves, D. I., & Gardoll, S. 2001. Orogenic gold and geologic time: a global synthesis. Ore geology reviews, vol. 18, p. 1-75.

Goldfarb, R., Baker, T., Dube, B., Groves, D. I., Hart, C. J., & Gosselin, P. 2005. Distribution, character and genesis of gold deposits in metamorphic terranes. Society of Economic Geologists. P. Economic geology 100th Anniversary volume p. 407-450.

Goodwin, A.M. 1991. Precambrian geology, the dynamic evolution of the continental crust. Academic Press, London. P. 1-681

Gorner, E. 2019. Chemical and spectral features of alteration minerals at the Hemlo Au Deposits, Masters Thesis, Geology Department, Lakehead University.

Groves, D.I., Goldfarb, R.J., Knox-Robinson, C.M., Ojala, J., Gardoll, S., Yun, G., and Holyland, P., 2000, Late-kinematic timing of orogenic gold deposits and significance for computer-based exploration techniques with emphasis on the Yilgarn block, Western Australia: Ore Geology Reviews, vol. 17, p. 1–38.

Groves, D. I., Goldfarb, R. J., Robert, F., & Hart, C. J. 2003. Gold deposits in metamorphic belts: overview of current understanding, outstanding problems, future research, and exploration significance. Economic geology, vol. 98, p. 1-29.

Groves, D. I., Goldfarb, R. J., Gebre-Mariam, M., Hagemann, S. G., & Robert, F. 1998. Orogenic gold deposits: a proposed classification in the context of their crustal distribution and relationship to other gold deposit types. Ore Geology Reviews, vol. 13, p. 7-27.

Harcourt, G. A., & Bartley, M. W. 1938. Schreiber area. Thunder Bay District: Ontario Department of Mines, Map 47j, scale, vol. 1, p. 1-31.

Hart, C.J.R., Baker, T., and Burke, M., 2000. New exploration concepts for country-rock hosted, intrusion-related gold systems, Tintina Gold Belt: British Columbia and Yukon Chamber of Mines, Special vol. 2, p. 145–172.

Hart, C. J. 2007. Reduced intrusion-related gold systems. Geological Association of Canada, Mineral Deposits Division, special publication 5, p. 95-112.

Henry, P., Stevenson, R. K., & Gariépy, C. 1998. Late Archean mantle composition and crustal growth in the western Superior Province of Canada: Neodymium and lead isotopic evidence from the Wawa, Quetico, and Wabigoon subprovinces. Geochimica et Cosmochimica Acta, vol. 62, p. 143-157.

Hildreth, W., & Moorbath, S. 1988. Crustal contributions to arc magmatism in the Andes of central Chile. Contributions to mineralogy and petrology, vol. 98, p. 455-489.

Hollings, P., Cooke, D. R., Waters, P. J., & Cousens, B. 2011. Igneous geochemistry of mineralized rocks of the Baguio district, Philippines: Implications for tectonic evolution and the genesis of porphyry-style mineralization. Economic Geology, vol. 106, p. 1317-1333.

Hopkins, P.E. 1921: Schreiber-Duck Lake area; Ontario Department of Mines, Accompanied by Map 30a, scale l inch to l mile. vol. 30, p. 1-26

Hughes, A. 2016. Petrology and geochemistry of the McKenzie Granite, Northwestern Ontario. HBS Thesis, Geology Department, Lakehead University.

Irvine, T. N. J., & Baragar, W. R. A. F. 1971. A guide to the chemical classification of the common volcanic rocks. Canadian journal of earth sciences, vol. 8, p. 523-548.

Kamo, S.L. 2016. Part A: Report on U-Pb ID-TIMS geochronology for the Ontario Geological Survey: bedrock mapping projects, Ontario, Year 1: 2015-2016; internal report prepared for the Ontario Geological Survey, Jack Satterly Geochronology Laboratory, University of Toronto, Toronto, Ontario, p. 1-48.

Kamo, S.L. 2018. Part A: Report on U-Pb ID-TIMS geochronology for the Ontario Geological Survey: bedrock mapping projects, Ontario, Year 3: 2017-2018; internal report prepared for the Ontario Geological Survey, Jack Satterly Geochronology Laboratory, University of Toronto, Toronto, Ontario, p. 1-44

Kamo, S.L. and Hamilton, M.A. 2017. Part A: Report on U-Pb ID-TIMS geochronology for the Ontario Geological Survey: bedrock mapping projects, Ontario, Year 2: 2016-2017; internal report prepared for the Ontario Geological Survey, Jack Satterly Geochronology Laboratory, University of Toronto, Toronto, Ontario, p. 1-72.

Kerrich, R., Fyfe, W. S., German, B. E., & Allison, I. 1997. Local modification of rock chemistry by deformation. Contributions to Mineralogy and Petrology, vol. 65, p. 183-190.

Kerrich, R., Polat, A., & Xie, Q. 2008. Geochemical systematics of 2.7 Ga Kinojevis Group (Abitibi), and Manitouwadge and Winston Lake (Wawa) Fe-rich basalt–rhyolite associations: Backarc rift oceanic crust?. Lithos, vol. 10, p. 1-23.

Kerrich, R., & Xie, Q. 2002. Compositional recycling structure of an Archean super-plume: Nb–Th–U–LREE systematics of Archean komatiites and basalts revisited. Contributions to Mineralogy and Petrology, vol. 142, p. 476-484.

Kerrich, R., Goldfarb, R., Groves, D., Garwin, S. 2000. The geodynamics of world-class gold deposits: characteristics, space-time distribution, and origins. This is Gold in 2000. vol. 13 p. 501-551.

Kuno, H., 1968. Differentiation of basalt magmas. In: Hess, H. H. and Poldervaart, A. A., (eds.), Basalts: The Poldervaart Treatise on Rocks of Basaltic Composition. Interscience, New York. p. 623-688.

Kuzmich, B. 2012. Geochemistry and Petrology of the Dog Lake Granite Chain, Quetico Basin, Northwestern Ontario: HBSc Thesis, Geology Department, Lakehead University.

Le Bas, M. J., & Streckeisen, A. L. 1991. The IUGS systematics of igneous rocks. Journal of the Geological Society, vol. 148, p. 825-833.

Leake, B. E., Woolley, A. R., Arps, C. E., Birch, W. D., Gilbert, M. C., Grice, J. D., Hawthorne, F.C., Kato, A., Kisch, H.J., Krivovichev, V.G., Linthout, K. 1997. Nomenclature of amphiboles; report of the Subcommittee on Amphiboles of the International Mineralogical Association Commission on new minerals and mineral names. Mineralogical magazine, vol. 61, p. 295-310.

Le Maitre, R.W., Bateman, P., Dudek, A.J. and Keller, M.J. 1989. A Classification of Igneous Rocks and Glossary of Terms, Blackwell, Oxford, p. 1-193.

Le Maitre, R. W., Streckeisen, A., Zanettin, B., Le Bas, M. J., Bonin, B., & Bateman, P. (Eds.). 2005. Igneous rocks: a classification and glossary of terms: recommendations of the International Union of Geological Sciences Subcommission on the Systematics of Igneous Rocks. Cambridge University Press. p. 1-256

Lodge, R.W.D. 2012. Winston Lake and Manitouwadge revisited: modern views of two volcanogenic massive sulphide (VMS)-endowed greenstone belts. A field trip guidebook; Ontario Geological Survey, Open File Report 6282, p. 34.

Loiselle, M. C., & Wones, D. R. 1979. Characteristics and origin of anorogenic granites. In Geological Society of America Abstracts with Programs vol. 11, p. 468.

Magnus, S.J. and Arnold, K.A. 2016. Geology and mineral potential of the western Schreiber–Hemlo greenstone belt; in Summary of Field Work and Other Activities, 2016, Ontario Geological Survey, Open File Report 6323, p.11-1 -11-7.

Magnus, S.J. and Walker, J. 2015. Geology and mineral potential of Walsh, Tuuri and Syine townships, Schreiber–Hemlo greenstone belt; in Summary of Field Work and Other Activities, 2015, Ontario Geological Survey, Open File Report 6313, p.14-1 - 14-12.

Magnus, S.J. 2017. Precambrian geology of Tuuri and Walsh townships, northwestern Ontario; Ontario Geological Survey, Preliminary Map P.3812, scale 1:20 000.

Magnus, S.J. and Hastie, E.C.G. 2018. Project NW-18-001. Geology and Mineral Potential of Priske and Strey Townships, Western Schreiber– Hemlo Greenstone Belt; in Summary of Field Work and Other Activities, 2018, Ontario Geological Survey, Open File Report 6350, p.10-1 - 10-9.

Markey, R., Stein, H., & Morgan, J. 1998. Highly precise Re–Os dating for molybdenite using alkaline fusion and NTIMS. Talanta, vol. 45, p. 935-946.

Markey, R., Stein, H. J., Hannah, J. L., Zimmerman, A., Selby, D., & Creaser, R. A. (2007). Standardizing Re–Os geochronology: a new molybdenite reference material (Henderson, USA) and the stoichiometry of Os salts. Chemical Geology, vol. 244, p. 74-87.

Marmont, S. 1984. The Terrace Bay batholith and associated mineralization; Ontario Geological Survey, Open File Report 5514, p. 1-131.

Martin, H. 1987. Petrogenesis of Archaean trondhjemites, tonalites, and granodiorites from eastern Finland: major and trace element geochemistry. Journal of Petrology, vol. 28, p. 921-953.

Martin, H., Peucat, J. J., Sabaté, P., & Cunha, J. C. 1997. Crustal evolution in the early Archaean of South America: example of the Sete Voltas Massif, Bahia State, Brazil. Precambrian Research, vol. 82, p. 35-62.

Martin, H., Smithies, R. H., Rapp, R., Moyen, J. F., & Champion, D. 2005. An overview of adakite, tonalite–trondhjemite–granodiorite (TTG), and sanukitoid: relationships and some implications for crustal evolution. Lithos, vol. 79, p. 1-24.

Myers, J. S. (1997). Geology of granite. Journal of the Royal Society of Western Australia, vol. 80, p. 87-100.

Moyen, J. F., & Martin, H. 2012. Forty years of TTG research. Lithos, vol. 148, p. 312-336.

Muir, T. L. 2002. The Hemlo gold deposit, Ontario, Canada: principal deposit characteristics and constraints on mineralization. Ore Geology Reviews, vol. 21, p. 1-66.

Oliver, N. H. 2001. Linking of regional and local hydrothermal systems in the mid-crust by shearing and faulting. Tectonophysics, vol. 335, p. 147-161.

Pašava, J., Svojtka, M., Veselovský, F., Ďurišová, J., Ackerman, L., Pour, O., Drabek, M., Halodova, P., & Haluzová, E. 2016. Laser ablation ICPMS study of trace element chemistry in molybdenite coupled with scanning electron microscopy (SEM)—An important tool for identification of different types of mineralization. Ore Geology Reviews, vol. 72, p. 874-895.

Peccerillo, A., & Taylor, S. R. 1976. Geochemistry of Eocene calc-alkaline volcanic rocks from the Kastamonu area, northern Turkey. Contributions to mineralogy and petrology, vol. 58, p. 63-81.

Pearce, J. A., Harris, N. B., & Tindle, A. G. 1984. Trace element discrimination diagrams for the tectonic interpretation of granitic rocks. Journal of petrology, vol. 25, p. 956-983.

Percival, J. A. 2007. Geology and metallogeny of the Superior Province, Canada. Mineral deposits of Canada: a synthesis of major deposit-types, district metallogeny, the evolution of geological provinces, and exploration methods, p. 903-928.

Petford, N., Cruden, A. R., McCaffrey, K. J. W., & Vigneresse, J. L. 2000. Granite magma formation, transport and emplacement in the Earth's crust. Nature, vol. 408, p. 669-673.

Polat, A., Kerrich, R., & Wyman, D. A. 1998. The late Archean Schreiber–Hemlo and White River–Dayohessarah greenstone belts, Superior Province: collages of oceanic plateaus, oceanic arcs, and subduction–accretion complexes. Tectonophysics, vol. 289, p. 295-326.

Polat, A., Kerrich, R., & Wyman, D. A. 1999. Geochemical diversity in oceanic komatiites and basalts from the late Archean Wawa greenstone belts, Superior Province, Canada: trace element and Nd isotope evidence for a heterogeneous mantle. Precambrian Research, vol. 94, p. 139-173.

Polat, A., & Kerrich, R. 2000. Archean greenstone belt magmatism and the continental growth–mantle evolution connection: constraints from Th–U–Nb–LREE systematics of the 2.7 Ga Wawa subprovince, Superior Province, Canada. Earth and Planetary Science Letters, vol. 175, p. 41-54.

Polat, A., & Kerrich, R. 2002. Nd-isotope systematics of~ 2.7 Ga adakites, magnesian andesites, and arc basalts, Superior Province: evidence for shallow crustal recycling at Archean subduction zones. Earth and Planetary Science Letters, vol. 202, p. 345-360.

Puumala, M.A., Campbell, D.A., Tuomi, R.D., Debicki, R.L., Wilson, A.C., Moses, P. and Brunelle, M.R. 2014. Report of Activities 2013, Resident Geologist Program, Thunder Bay south Regional Resident Geologist Report: Thunder Bay South District; Ontario Geological survey, Open File Report 6293, p. 1-71.

Puumala, M.A., Campbell, D.A., Tuomi, R.D., Pettigrew, T.K. and Hinz, S.L.K. 2018. Report of Activities 2017, Resident Geologist Program, Thunder Bay South Regional Resident Geologist Report: Thunder Bay South District; Ontario Geological Survey, Open File Report 6338, p. 1-101.

Puumala, M.A., Campbell, D.A., Tuomi, R.D., Tims, A., Debicki, R.L., Pettigrew, T.K. and Brunelle, M.R. 2016. Report of Activities 2015, Resident Geologist Program, Thunder Bay South Regional Resident Geologist Report: Thunder Bay South District; Ontario Geological Survey, Open File Report 6316, p. 1-85.

Richards, J. P., & Kerrich, R. 2007. Special paper: adakite-like rocks: their diverse origins and questionable role in metallogenesis. Economic geology, vol. 102, p. 537-576.

Richards, J. P. 2011. High Sr/Y arc magmas and porphyry Cu±Mo±Au deposits: just add water. Economic Geology, vol. 106, p. 1075-1081.

Ridolfi, F., Renzulli, A., & Puerini, M. 2010. Stability and chemical equilibrium of amphibole in calc-alkaline magmas: an overview, new thermobarometric formulations and application to subduction-related volcanoes. Contributions to Mineralogy and Petrology, vol. 160, p. 45-66.

Rollinson, H. R. 1993. Using geochemical data: evaluation. Presentation, interpretation. Singapore.

Sanatana Resources Inc. News Releases. Sanatana Provides Exploration Update. September, 8th, 2017.

Selby, D., & Creaser, R. A. 2004. Macroscale NTIMS and microscale LA-MC-ICP-MS Re-Os isotopic analysis of molybdenite: Testing spatial restrictions for reliable Re-Os age determinations, and implications for the decoupling of Re and Os within molybdenite. Geochimica et Cosmochimica Acta, vol. 68 p. 3897-3908.

Sial, A. N., Bettencourt, J. S., De Campos, C. P., & Ferreira, V. P. 2011. Granite-related ore deposits: an introduction. Geological Society, London, Special Publications, vol. 350, p. 1-5.

Sinclair, D.W., Jonasson, I.R., Kirkham, R.V., Soregaroli, A.E., 2009. Rhenium and other platinum-group metals in porphyry deposits. Open File 6181. Geological Survey of Canada, Ottawa, Canada.

Sisson, T. W., & Grove, T. L. 1993. Experimental investigations of the role of H 2 O in calc-alkaline differentiation and subduction zone magmatism. Contributions to mineralogy and petrology, vol. 113, p. 143-166.

Stern, R.A., Hanson, G.N. and Shirey, S.B., 1989. Petrogenesis of mantle-derived, LILE-enriched Archean monzodiorites and trachyandesites (sanukitoids) in southwestern Superior Province. Canadian Journal of Earth Sciences, vol. 26, p. 1688-1712.

Stott, G. M. 1997. The superior province, Canada. Oxford Monographs on Geology and Geophysics, vol. 35, p. 480-507.

Stott, G. M. 2010. A revised terrane subdivision of the Superior Province of Ontario. Ontario Geological Survey, Miscellaneous Release-Data, p. 278.

Stott, G.M., Corkery, M.T., Percival, J.A.., Simard, M. and J. Goutier, J. 2010. A revised terrane subdivision of the Superior Province; in Summary of Field Work and Other Activities 2010, Ontario Geological Survey, Open File Report 6260, p. 20-1 - 20-10.

Streckeisen, A. L. 1967. Classification and nomenclature of igneous rocks. N. Jb. Miner., vol. 107, p. 144-240.

Streckeisen, A. 1974. Classification and nomenclature of plutonic rocks recommendations of the IUGS subcommission on the systematics of igneous rocks. Geologische Rundschau, vol. 63, p. 773-786.

Stein, H. J., Markey, R. J., & Morgan, J. W. 2000. Robust Re-Os molybdenite ages for the Hemlo Au deposit, Superior Province, Canada. In Program with Abstracts, Goldschmidt Conference. vol. 5, p. 955

Stein, H., Markey, R., Morgan, J., Hannah, J., and Schersten, A. 2001a. The remarkable Re-Os chronometer in molybdenite: how and why it works: Terra Nova, vol. 13, p. 479-486.

Stein, H. J., Markey, R. J., Morgan, J. W., Selby, D., Creaser, R. A., McCuaig, T. C., & Behn, M. 2001b. Re–Os dating of Boddington molybdenite, SW Yilgarn: two Au mineralization events. AGSO-Geoscience Australia, Record, vol. 37, p. 469-471.

Sun, S. S., & McDonough, W. S. 1989. Chemical and isotopic systematics of oceanic basalts: implications for mantle composition and processes. Geological Society, London, Special Publications, vol. 42, p. 313-345.

Tanaka, T., Togashi, S., Kamioka, H., Amakawa, H., Kagami, H., Hamamoto, T., Yuhara, M., Orihashi, Y., Yoneda, S., Shimizu, H., Kunimaru, T., Takahashi, K., Yanagi, T., Nakano, T., Fujimaki, H., Shinjo, R., Asahara, Y., Tanimizu, M., and Dragusanu, C., .2000. JNdi-1: a neodymium isotopic reference in consistency with LaJolla neodymium. Chemical Geology, vol. 168, p. 279-281.

Thurston, P., Osamani, I., and Stone, D. 1991. Northwestern Superior Province: Review and terrane analysis, Special Volume 4, Part 1, Ontario Geological Survey, p. 81-142.

Tomlinson, K. Y., Stott, G. M., Percival, J. A., & Stone, D. 2004. Basement terrane correlations and crustal recycling in the western Superior Province: Nd isotopic character of granitoid and felsic volcanic rocks in the Wabigoon subprovince, N. Ontario, Canada. Precambrian Research, vol. 132, p. 245-274.

Wall, V.J., 2000, Pluton-related (thermal aureole) gold: Taylor, Wall, and As- sociates, Alaska Miners Association Annual Convention, Anchorage, October 30–31, 2000, Workshop Notes.

Walker, J.W. 1967. Geology of the Jackfish-Middleton Area; Ontario Department of Mines, Geological Report 50, 41p. Accompanied by Maps 2107 and 2112, scale l inch to 1/2 mile.

Whalen, J. B., McNicoll, V. J., Galley, A. G., & Longstaffe, F. J. 2004. Tectonic and metallogenic importance of an Archean composite high-and low-Al tonalite suite, Western Superior Province, Canada. Precambrian Research, vol. 132, p. 275-301.

White A. J. R. 1979. Sources of granite magma. Geological Society of America Program with Abstracts 11, p. 539.

White, D. J., Musacchio, G., Helmstaedt, H. H., Harrap, R. M., Thurston, P. C., Van der Velden, A., & Hall, K. 2003. Images of a lower-crustal oceanic slab: Direct evidence for tectonic accretion in the Archean western Superior province. Geology, vol. 31, p. 997-1000.

Williams, H.R. 1989. Geological studies in the Wabigoon, Quetico and Abitibi-Wawa subprovinces, Superior Province of Ontario, with emphasis on the structural development of the Beardmore Geraldton Belt/ Ontario Geological Survey, Open File Report 5724, p. 1-189.

Williams, H.R., Stott, G.M., Heather, K.B., Muir, T.L. and Sage, R.P. 1991. Wawa Subprovince; in Geology of Ontario, Ontario Geological Survey, Special vol. 4, p. 485-539.

APPENDIX A: Sample Locations

SAMPLE NAME	DATUM	ZONE	EASTING	NORTHING	LITHOLOGY
16KAA001A	NAD83	16U	488840	5404002	Hematite Altered Granodiorite
16KAA002A	NAD83	16U	493747	5405029	Granodiorite
16KAA003A	NAD83	16U	493979	5406132	Granodiorite
16KAA004A	NAD83	16U	494409	5408269	Granodiorite
16KAA005A	NAD83	16U	496597	5409750	Granodiorite
16KAA006A	NAD83	16U	497388	5410505	Monzogranite
16KAA006B	NAD83	16U	497388	5410505	Supracrustal Xenolith
16KAA007A	NAD83	16U	498303	5410980	Granodiorite
16KAA008C	NAD83	16U	502041	5411500	Supracrustal Xenolith
16KAA009A	NAD83	16U	503232	5411225	Monzogranite
16KAA010A	NAD83	16U	502967	5411283	Granodiorite
16KAA011	NAD83	16U	494024	5407533	Granodiorite
16KAA012A	NAD83	16U	494764	5408895	Monzogranite
16KAA013A	NAD83	16U	496976	5409849	Granodiorite
16KAA014A	NAD83	16U	502588	5411489	Granodiorite
16KAA015A	NAD83	16U	500451	5410949	Monzogranite
16KAA016A	NAD83	16U	503395	5411189	Granodiorite
16KAA017A	NAD83	16U	504238	5407585	Monzogranite
16KAA018A	NAD83	16U	504421	5408666	Granodiorite
16KAA018B	NAD83	16U	504421	5408666	Chlorite Altered Granodiorite
16KAA018C	NAD83	16U	504421	5408666	Granodiorite
16KAA019A	NAD83	16U	504678	5408537	Granodiorite
16KAA019D	NAD83	16U	504678	5408537	Granodiorite
16KAA019E	NAD83	16U	504678	5408537	Hematite Altered Granodiorite
16KAA020A	NAD83	16U	502116	5404952	Monzogranite
16KAA021A	NAD83	16U	502116	5404952	Monzogranite
16KAA021B	NAD83	16U	502116	5404952	Monzogranite
16KAA021C	NAD83	16U	502116	5404952	Pegmatite
16KAA022A	NAD83	16U	491752	5401809	Granodiorite
16KAA023A	NAD83	16U	491876	5401919	Granodiorite
16KAA024A	NAD83	16U	493391	5401990	Granodiorite
16KAA025A	NAD83	16U	493719	5402538	Granodiorite
16KAA026A	NAD83	16U	497547	5404904	Granodiorite
16KAA027A	NAD83	16U	495273	5404985	Granodiorite
16KAA028A	NAD83	16U	503515	5406806	Hematite Altered Granodiorite
16KAA029A	NAD83	16U	503709	5406312	Granodiorite
16KAA030A	NAD83	16U	503600	5406489	Granodiorite
16KAA031A	NAD83	16U	503354	5406727	Granodiorite
16KAA032A	NAD83	16U	503736	5407312	Granodiorite

SAMPLE NAME	Datum	Zone	Easting	Northing	Lithology
16KAA033A	NAD83	16U	500513	5411664	Monzogranite
16KAA033B	NAD83	16U	500513	5411664	Pegmatite
16KAA034A	NAD83	16U	505038	5408198	Granodiorite
16KAA034B	NAD83	16U	505038	5408198	Monzogranite
16KAA035A	NAD83	16U	505152	5408004	Granodiorite
16KAA036A	NAD83	16U	504854	5407572	Monzogranite
16KAA036B	NAD83	16U	504854	5407572	Quartz Vein
16KAA037A	NAD83	16U	504382	5410970	Granodiorite
16KAA038A	NAD83	16U	504881	5410851	Granodiorite
16KAA039A	NAD83	16U	483752	5404913	Granodiorite
16KAA040A	NAD83	16U	503919	5406947	Granodiorite
16KAA041A	NAD83	16U	480523	5403572	Granodiorite
16KAA042A	NAD83	16U	480781	5401791	Hematite Altered Granodiorite
16KAA043A	NAD83	16U	491641	5406128	Granodiorite
16KAA044A	NAD83	16U	496399	5410509	Granodiorite
16KAA036C	NAD83	16U	497450	5408376	Quartz Vein
17KAM001A	NAD83	16U	498753	5410933	Granodiorite
17KAM002A	NAD83	16U	498839	5411105	Granodiorite
17KAM003A	NAD83	16U	500649	5411051	Granodiorite
17KAM004A	NAD83	16U	500843	5411186	Granodiorite
17KAM005A	NAD83	16U	500642	5410843	Granodiorite
17KAM006A	NAD83	16U	500608	5410612	Monzogranite
17KAM007A	NAD83	16U	500690	5410489	Granodiorite
17KAM007B	NAD83	16U	500690	5410489	Granodiorite
17KAM008A	NAD83	16U	500790	5410208	Monzogranite
17KAM009A	NAD83	16U	500918	5410010	Granodiorite
17KAM010A	NAD83	16U	501090	5409968	Granodiorite
17KAM011A	NAD83	16U	501370	5409965	Granodiorite
17KAM012A	NAD83	16U	491508	5402238	Granodiorite
17KAM013A	NAD83	16U	491383	5402426	Granodiorite
17KAM014A	NAD83	16U	486163	5403510	Monzogranite
17KAM015A	NAD83	16U	486064	5403368	Granodiorite
17KAM016A	NAD83	16U	486161	5403043	Granodiorite
17KAM017A	NAD83	16U	486540	5402902	Granodiorite
17KAM018A	NAD83	16U	486801	5402660	Hematite Altered Granodiorite
17KAM019A	NAD83	16U	486939	5402724	Monzogranite
17KAM020A	NAD83	16U	504432	5408904	Hematite Altered Granodiorite
17KAM021A	NAD83	16U	504706	5409130	Granodiorite
17KAM022A	NAD83	16U	504847	5409295	Granodiorite

SAMPLE NAME	Datum	Zone	Easting	Northing	Lithology
17KAM022B	NAD83	16U	504847	5409295	Hematite Altered Granodiorite
17KAM023A	NAD83	16U	504412	5409221	Granodiorite
17KAM024A	NAD83	16U	492252	5403317	Granodiorite
17KAM025A	NAD83	16U	492139	5408522	Monzogranite
17KAM026A	NAD83	16U	492834	5408420	Pegmatite
17KAM026B	NAD83	16U	492834	5408420	Pegmatite
17KAM027B	NAD83	16U	504199	5409152	Monzogranite
17KAM028A	NAD83	16U	502368	5405098	Granodiorite
17KAM029A	NAD83	16U	502146	5404997	Granodiorite
17KAM030A	NAD83	16U	502461	5405593	Granodiorite
17KAM031A	NAD83	16U	502827	5405822	Granodiorite
17KAM032A	NAD83	16U	503185	5406166	Monzogranite
17KAM033A	NAD83	16U	504108	5407599	Granodiorite
17KAM034A	NAD83	16U	496276	5409348	Monzogranite
17KAM035A	NAD83	16U	497337	5408566	Granodiorite
17KAM035B	NAD83	16U	497337	5408566	Granodiorite
17KAM036A	NAD83	16U	497450	5408376	Granodiorite
17KAM037A	NAD83	16U	497780	5408006	Granodiorite
17KAM038A	NAD83	16U	498009	5407647	Granodiorite
17KAM038B	NAD83	16U	498009	5407647	Aplite dyke
17KAM039A	NAD83	16U	498239	5407615	Granodiorite
17KAM039B	NAD83	16U	498239	5407615	Diorite
17KAM040A	NAD83	16U	496665	5407541	Granodiorite
17KAM040B	NAD83	16U	496665	5407541	Monzogranite
17KAM040C	NAD83	16U	496665	5407541	Granodiorite
17KAM041A	NAD83	16U	503660	5406132	Hematite Altered Granodiorite
17KAM042A	NAD83	16U	503217	5406677	Granodiorite
17KAM043A	NAD83	16U	503326	5407135	Granodiorite
17KAM044A	NAD83	16U	499039	5407506	Monzogranite
17KAM044B	NAD83	16U	499039	5407506	Hematite Altered Granodiorite
17KAM045A	NAD83	16U	499287	5407305	Monzogranite
17KAM045B	NAD83	16U	499361	5407252	Hematite Altered Granodiorite
17KAM046A	NAD83	16U	490416	5407269	Hematite Altered Granodiorite
17KAM047A	NAD83	16U	499802	5407086	Granodiorite
17KAM048A	NAD83	16U	500365	5406774	Hematite Altered Granodiorite
17KAM049A	NAD83	16U	500789	5406888	Granodiorite
17KAM050A	NAD83	16U	500778	5407273	Granodiorite
17KAM051A	NAD83	16U	501034	5407236	Granodiorite
17KAM052A	NAD83	16U	485963	5403389	Granodiorite

SAMPLE NAME	Datum	Zone	Easting	Northing	Lithology
17KAM053A	NAD83	16U	485818	5404050	Granodiorite
17KAM054A	NAD83	16U	486830	5402913	Granodiorite
17KAM055A	NAD83	16U	487032	5402642	Monzogranite
17KAM056A	NAD83	16U	500528	5410949	Granodiorite
17KAM057B	NAD83	16U	499006	5410727	Granodiorite
17KAM058A	NAD83	16U	501216	5411109	Granodiorite
17KAM058B	NAD83	16U	501216	5411109	Supracrustal Xenolith
17KAM056A	NAD83	16U	500528	5410949	Granodiorite
17KAM060A	NAD83	16U	502774	5411642	Granodiorite
17KAM061A	NAD83	16U	502918	5407209	Granodiorite
17KAM062A	NAD83	16U	502364	5406593	Granodiorite
17KAM062B	NAD83	16U	502364	5406593	Quartz Vein
17KAM063A	NAD83	16U	501865	5406188	Granodiorite
17KAM063B	NAD83	16U	501865	5406188	Quartz Vein
17KAM063C	NAD83	16U	501865	5406188	Quartz Vein
17KAM064A	NAD83	16U	501332	5406120	Monzogranite
17KAM065A	NAD83	16U	493810	5408274	Granodiorite
17KAM066A	NAD83	16U	488814	5404270	Granodiorite
17KAM066B	NAD83	16U	488814	5404270	Hematite Altered Granodiorite
17KAM067A	NAD83	16U	490106	5403796	Monzogranite
17KAM068A	NAD83	16U	496005	5410457	Granodiorite
17KAM069A	NAD83	16U	496028	5410664	Granodiorite
17KAM070A	NAD83	16U	496030	5410267	Granodiorite
17KAM071A	NAD83	16U	491430	5402304	Granodiorite
17KAM071B	NAD83	16U	491430	5402304	Quartz Vein
17KAM072A	NAD83	16U	483501	5404524	Diorite
17KAM072B	NAD83	16U	483501	5404524	Quartz Vein
17KAM072C	NAD83	16U	483501	5404524	Granite with molybdenum
17KAM073A	NAD83	16U	490597	5403648	Hematite Altered Granodiorite
17KAM073B	NAD83	16U	490597	5403648	Quartz Vein
17KAM074A	NAD83	16U	505898	5408314	Monzogranite
17KAM075A	NAD83	16U	483528	5404315	Monzogranite
17KAM076A	NAD83	16U	483430	5404215	Diorite
17KAM077A	NAD83	16U	483968	5404067	Granodiorite
17KAM078A	NAD83	16U	491166	5403713	Monzogranite
17KAM078B	NAD83	16U	491166	5403713	Quartz Vein
17KAM078C	NAD83	16U	491166	5403713	Chlorite Altered Granodiorite
17KAM079A	NAD83	16U	503392	5407453	Granodiorite
17KAM080A	NAD83	16U	483984	5403872	Hematite Altered Granodiorite

SAMPLE NAME	Datum	Zone	Easting	Northing	Lithology
17KAM081A	NAD83	16U	483911	5403509	Granodiorite
17KAM082A	NAD83	16U	482473	5403729	Monzogranite
17KAM082B	NAD83	16U	482473	5403729	Quartz Vein
17KAM083A	NAD83	16U	504995	5409481	Granodiorite
17KAM084A	NAD83	16U	505053	5409730	Granodiorite
17KAM084B	NAD83	16U	505053	5409730	Supracrustal Xenolith
17KAM085A	NAD83	16U	505388	5409625	Hematite Altered Granodiorite
17KAM085B	NAD83	16U	505388	5409625	Quartz Vein
17KAM086A	NAD83	16U	490680	5402051	Granodiorite
17KAM087A	NAD83	16U	490598	5401927	Granodiorite
17KAM088A	NAD83	16U	490598	5401927	Granodiorite
17KAM089A	NAD83	16U	490265	5401952	Monzogranite
17KAM090A	NAD83	16U	490849	5403040	Granodiorite
17KAM091A	NAD83	16U	485664	5402575	Granodiorite
17KAM092A	NAD83	16U	485467	5402675	Granodiorite
17KAM092B	NAD83	16U	485467	5402675	Hematite Altered Granodiorite
17KAM093A	NAD83	16U	485361	5402928	Hematite Altered Granodiorite
17KAM094A	NAD83	16U	485164	5403229	Granodiorite
17KAM095A	NAD83	16U	485506	5403598	Monzogranite

APPENDIX B: THIN SECTION DESCRIPTIONS

Grain sizes are reported as very fine-grained (<0.25mm), Fine-grained (0.25 to 1mm), medium-grained (1 to 5mm) and coarse-grained (5-50mm). All mineral contents are expressed as modal percent and lithology names are determined by field observations. Sericite alteration: mild <25%, Moderate 25-50%, Intense 50-75%, Completely >75%

Sample: 16KAA001A **Lithology:** Altered Granodiorite

Mineral Name and Abundance	Description
25% Quartz	Quartz crystals are anhedral and range from fine- to medium-grained. The coarser crystals characteristically exhibit undulatory extinction and sub-grain boundaries. Finer-grained crystals may be strain-free but typically also exhibit undulatory extinction and sub-grain boundaries. Finer-grained quartz occurs as euhedral interstitial material to feldspars.
35% Plagioclase	Plagioclase occurs as sub-euhedral medium- to coarse-grained crystals distributed evenly throughout the groundmass. Rare phenocrysts up to 2 mm are present. Finer-grained plagioclase but are strongly seritized in the groundmass. Seritization of plagioclase in the groundmass is common ranging from weak to strong. Seritization is patchy progressing from cores of crystals outwards. Plagioclase inclusions included chlorite, biotite, hornblendes and quartz. Concentric zoning, simple and polysynthetic twinning are common.
15% Potassium Feldspar	Potassium feldspar occurs generally as medium-grained subhedral crystals irregularly distributed throughout the groundmass. Crystals are typically altered to sericite. Wavy albite exsolution lamellae are common and produce perthitic textures when present. Rare coarse-grained crystal is can range in size up to 2 mm. the crystals generally occur interstitially between plagioclase and quartz crystals. Inclusions in the coarse crystals are of chlorite. Very fine-grained hematite alteration is disseminated across the crystals.
Trace Amphibole	Hornblende occurs as fine-to medium-grained crystals are unevenly distributed throughout the groundmass. Crystals are generally subhedral to anhedral with distinct cleavage planes present. Simple twinning is present in all crystals.
20% Chlorite	Chlorite occurs as an alteration product of fine- to medium-grained an- to subhedral amphibole crystals. Chlorite alteration of amphibole and biotite varies from weak to strong. Fine-grained calcite inclusions, as well birds eye halos. Chlorite is primarily an alteration product of amphibole.
Trace Titanite	Titanite occurs as fine-grained euhedral crystals and crystal clusters. Clusters of titanite are associated with clusters of opaque minerals, as well inclusions
Trace Epidote	Epidote occurs as fine-grained anhedral crystals included in chlorite alteration and as an alteration product of plagioclase.
Opaques	Disseminated very fine- to fine-grained pyrite with minor chalcopyrite.
5% Calcite	Calcite occurs in fractures in potassium feldspar and quartz. Also occurs as disseminated in quartz veins.

Sample:16KAA004A **Lithology:** Granodiorite **QAP Classification:** Monzogranite

Mineral Name and Abundance	Description
25% Quartz	Quartz crystals are anhedral and range from fine- to medium-grained. The coarser crystals characteristically exhibit undulatory extinction and sub-grain boundaries. Finer-grained crystals may be strain-free but typically also exhibit undulatory extinction and sub-grain boundaries. Finer-grained quartz occurs as euhedral interstitial material to feldspars. Myrmekitic textures are seen with feldspars.
25% Plagioclase	Plagioclase occurs as sub-euhedral medium- to coarse-grained crystals distributed evenly throughout the groundmass. Finer-grained plagioclase are moderately seritized in the groundmass. Seritization of plagioclase in the groundmass is common ranging from weak to strong. Seritization is patchy progressing from cores of crystals outwards. Plagioclase inclusions included chlorite, biotite, hornblendes and quartz. Concentric zoning, simple and polysynthetic twinning are common.

20% Potassium Feldspar	Potassium feldspar occurs generally as fine-grained subhedral crystals irregularly distributed throughout the groundmass. Crystals are typically altered to sericite. Wavy albite exsolution lamellae are common and produce perthitic textures when present. The crystals generally occur interstitially between plagioclase and quartz crystals. Mild to moderate sericite alteration, some crystals show myrmekitic textures present with plagioclase and quartz primarily occurs as in fine-grained clusters.
15% Amphibole	Hornblende occurs as fine-grained. to medium-grained crystals are found in clusters occurs around feldspars and quartz phenocrysts. Crystals are generally subhedral to anhedral with distinct cleavage planes present. Simple twinning is present in most crystals.
Trace Biotite	Biotite occurs as fine-grained to medium-grained. anhedral crystals. Chlorite alteration varies from weak to moderate.
5% Chlorite	Chlorite occurs as an alteration product of fine- to medium-grained an- to subhedral amphibole and biotite crystals. Chlorite alteration varies from weak to strong. Fine-grained calcite inclusions.
Trace Titanite	Titanite occurs as fine-grained euhedral crystals and crystal clusters. Clusters of titanite are associated with clusters of opaque minerals, as well inclusions
5% Epidote	Epidote occurs as fine-grained anhedral crystals included in chlorite alteration and occurs around amphiboles and plagioclase crystals.
Trace Opaques	Disseminated very fine- to fine-grained pyrite with minor chalcopyrite.
Trace Calcite	Calcite occurs in and around of chlorite alteration, very fine-grained anhedral.

Sample:16KAA006A **Lithology:** Monzogranite **QAP Classification:** Granodiorite

Mineral Name and Abundance	Description
25% Quartz	Quartz crystals are anhedral and range from fine- to medium-grained. The coarser crystals characteristically exhibit undulatory extinction and sub-grain boundaries. Finer-grained crystals may be strain-free but typically also exhibit undulatory extinction and sub-grain boundaries. Finer-grained quartz occurs as interstitial material to feldspars. Also found occurs as with very fine-grained mica inclusions.
35% Plagioclase	Plagioclase occurs as sub-euhedral medium- to coarse-grained crystals distributed evenly throughout the groundmass. Rare phenocrysts up to 2 mm are present. Seritization of plagioclase in the groundmass is common ranging from weak to strong. Concentric zoning, simple and polysynthetic twinning are common.
15% Potassium Feldspar	Potassium feldspar occurs generally as medium-grained subhedral crystals irregularly distributed throughout the groundmass. Crystals are typically altered to sericite. Wavy albite exsolution lamellae are common and produce perthitic textures when present. The crystals generally occur interstitially between plagioclase and quartz crystals. Sericite alteration is moderate, white mica crystals can range up to fine-grained. Tartan twinning more prevalent on fine-grained crystals in groundmass.
10-15% Amphibole	Hornblende occurs as fine- to medium-grained crystals are found in clusters occurs around feldspars and quartz phenocrysts. Crystals are generally subhedral to anhedral with distinct cleavage planes present. Simple twinning is present in most crystals.
5% Biotite	Biotite occurs as fine- to medium-grained anhedral crystals. Chlorite alteration varies from weak to moderate.
1% Chlorite	Chlorite occurs as an alteration product of fine- to medium-grained an- to subhedral amphibole and biotite crystals. Chlorite alteration varies from weak to strong. Fine-grained calcite inclusions.
4% Titanite	Titanite occurs as fine-grained euhedral crystals and crystal clusters. Clusters of titanite are associated with clusters of opaque minerals, as well inclusions.

1%Epidote	Epidote occurs as fine-grained anhedral crystals included in chlorite alteration and occurs around amphiboles and plagioclase crystals.
Opaques	Disseminated very fine- to fine-grained pyrite with minor chalcopyrite.
5% Calcite	Calcite occurs as cross-cutting vein. Fine- to medium-grained, anhedral crystals.

Sample:16KAA006B **Lithology:** Xenolith

Mineral Name and Abundance	Description
Trace Quartz	Quartz crystals only occur in proximity to the contact with the granodiorite. Fine-grained anhedral crystals with minimal undulose extinction.
25% Plagioclase	Plagioclase occurs as sub to euhedral medium- to coarse-grained crystals distributed evenly throughout the groundmass. Plagioclase accounts for most of phenocrysts. Rare phenocrysts up to 2 mm are present, simple and polysynthetic twinning are present in finer grained crystals in the groundmass.
40% Amphibole	Hornblende occurs as fine- to medium-grained crystals are found in clusters occurs around feldspars and quartz phenocrysts. Crystals are generally subhedral to anhedral with distinct cleavage planes present. Simple twinning is present in most crystals.
30% Biotite	Biotite occurs as fine- to medium-grained anhedral crystals. Chlorite alteration varies from weak to moderate.
Trace Epidote	Epidote occurs as fine-grained anhedral crystals included in chlorite alteration and occurs around amphiboles and plagioclase crystals.
Trace calcite	Calcite occurs as fine-grained anhedral crystals disseminated across the sample.

Sample: 16KAA009A **Lithology:** Monzogranite **QAP Classification:** Monzogranite

Mineral Name and Abundance	Description
25% Quartz	Quartz crystals are anhedral and range from fine- to medium-grained. The coarser crystals characteristically exhibit undulatory extinction and sub-grain boundaries. Finer-grained crystals may be strain-free but typically also exhibit undulatory extinction and sub-grain boundaries. Finer-grained quartz occurs as euhedral interstitial material to feldspars.
30% Plagioclase	Plagioclase occurs as sub to euhedral medium- to coarse-grained crystals are distributed evenly throughout the groundmass. Plagioclase accounts for most of phenocrysts. Rare phenocrysts up to 2 mm are present. Seritization of plagioclase in the groundmass is common ranging from moderate to intense. Simple and polysynthetic twinning are common.
20% Potassium Feldspar	Potassium feldspar occurs generally as medium-grained subhedral crystals irregularly distributed throughout the groundmass. Crystals are typically altered to sericite. Wavy albite exsolution lamellae are common and produce perthitic textures when present. The crystals generally occur interstitially between plagioclase and quartz crystals. Fine-grained Seritization of crystals, relic tartan twinning can be seen around sericite alteration.
Trace Amphibole	Hornblende occurs as fine-grained crystals are found in clusters occurs around feldspars and quartz phenocrysts. Crystals are generally subhedral to anhedral with distinct cleavage planes present. Simple twinning is present in most crystals.
Trace Chlorite	Chlorite occurs as an alteration product of fine- to medium-grained an- to subhedral amphibole and biotite crystals. Chlorite alteration varies from weak to strong. Fine-grained calcite inclusions.
5% Titanite	Titanite occurs as fine-grained euhedral crystals and crystal clusters. Clusters of titanite are associated with clusters of opaque minerals, as well inclusions.
10% Epidote	Epidote occurs as fine-grained anhedral crystals included in chlorite alteration and occurs around amphiboles and plagioclase crystals.

Opaques	Disseminated very fine- to fine-grained pyrite with minor chalcopyrite.
5% Calcite	Calcite occurs in fractures in potassium feldspar and quartz. Cross-cutting veins in and around quartz.

Sample: 16KAA011A **Lithology:** Granodiorite **QAP Classification:** Granodiorite

Mineral Name and Abundance	Description
25% Quartz	Quartz crystals are anhedral and range from fine- to medium-grained. The coarser crystals characteristically exhibit undulatory extinction and sub-grain boundaries. Finer-grained crystals may be strain-free but typically also exhibit undulatory extinction and sub-grain boundaries. Finer-grained quartz occurs as euhedral interstitial material to feldspars.
30% Plagioclase	Plagioclase occurs as sub- to euhedral medium-to coarse-grained crystals distributed evenly throughout the groundmass. Plagioclase accounts for most of phenocrysts. Rare phenocrysts up to 2 mm are present. Finer-grained plagioclase are intense sericite in the groundmass. Very fine- to fine-grained seritization of plagioclase in the groundmass is common ranging from moderate to intense, zonations are outlined with sericite alteration. Simple and polysynthetic twinning are common.
15% Potassium Feldspar	Potassium feldspar occurs generally as medium-grained subhedral crystals irregularly distributed throughout the groundmass. Fine-grained seritization of crystals. Wavy albite exsolution lamellae are common and produce perthitic textures when present. The crystals generally occur interstitially between plagioclase and quartz crystals. Relic tartan twinning can be seen around sericite alteration. Myrmekitic exsolution with plagioclase and quartz.
10% Amphibole	Hornblende occurs as fine-grained crystals are found in clusters occurs around feldspars and quartz phenocrysts. Crystals are generally subhedral to anhedral with distinct cleavage planes present. Simple twinning is present in most crystals. Mostly altered to chlorite.
10% Chlorite	Chlorite occurs as an alteration product of fine- to medium-grained an- to subhedral amphibole crystals. Chlorite alteration varies from weak to strong. Fine-grained calcite inclusions.
Trace Titanite	Titanite occurs as fine-grained euhedral crystals and crystal clusters. Clusters of titanite are associated with clusters of opaque minerals, as well inclusions.
Trace Epidote	Epidote occurs as fine-grained anhedral crystals included in chlorite alteration and occurs around amphiboles and plagioclase crystals.
Trace Opaques	Disseminated very fine- to fine-grained pyrite with minor chalcopyrite.
Trace Calcite	Calcite found occurs as in fractures of potassium feldspar and cross-cutting veins in and around quartz.

Sample: 16KAA012A **Lithology:** Monzogranite **QAP Classification:** Monzogranite

Mineral Name and Abundance	Description
20% Quartz	Quartz crystals are anhedral and range from fine- to medium-grained. The coarser crystals characteristically exhibit undulatory extinction and sub-grain boundaries. Finer-grained crystals may be strain-free but typically also exhibit undulatory extinction and sub-grain boundaries. Finer-grained quartz occurs as euhedral interstitial material to feldspars.
25% Plagioclase	Plagioclase occurs as sub- to euhedral medium- to coarse-grained crystals distributed evenly throughout the groundmass. Plagioclase accounts for most of phenocrysts. Rare phenocrysts up to 2 mm are present. Very fine- to fine-grained seritization of plagioclase in the groundmass is common ranging from moderate to intense, zonations are outlined with sericite alteration. Simple and polysynthetic twinning are common.

25% Potassium Feldspar	Potassium feldspar occurs generally as medium-grained subhedral crystals irregularly distributed throughout the groundmass. Crystals are typically altered to sericite. Wavy albite exsolution lamellae are common and produce perthitic textures in coarse grained crystals. the crystals generally occur interstitially between plagioclase and quartz crystals. Relic tartan twinning can be seen around sericite alteration. Myrmekitic exsolution with plagioclase and quartz.
1% Amphibole	Hornblende occurs as fine-grained crystals are found occurs around feldspar and quartz phenocrysts. Almost completely altered to chlorite, relic crystals are all that remain.
10% Chlorite	Chlorite occurs as an alteration product of fine- to medium-grained an- to subhedral amphibole crystals. Chlorite alteration varies from weak to strong. Fine-grained calcite inclusions.
2% Titanite	Titanite occurs as fine-grained euhedral crystals and crystal clusters. Clusters of titanite are associated with clusters of opaque minerals, as well inclusions.
1% Opaques	Disseminated very fine- to fine-grained pyrite with minor chalcopyrite.
5% Calcite	Calcite occurs in fractures in potassium feldspar and quartz. Cross-cutting veins in and around quartz. Occurs as in chlorite alteration of amphiboles.

Sample: 16KAA013A **Lithology:** Granodiorite **QAP Classification:** Granodiorite

Mineral Name and Abundance	Description
25% Quartz	Quartz crystals are anhedral and range from fine- to medium-grained. The coarser crystals characteristically exhibit undulatory extinction and sub-grain boundaries. Finer-grained crystals may be strain-free but typically also exhibit undulatory extinction and sub-grain boundaries. Finer-grained quartz occurs as euhedral interstitial material to feldspars. myrmekitic exsolution textures surrounds entire crystals
45% Plagioclase	Plagioclase occurs as sub- to euhedral medium- to coarse-grained crystals distributed evenly throughout the groundmass. Plagioclase accounts for most of phenocrysts. Rare phenocrysts up to 2 mm are present, simple and polysynthetic twinning are present in finer grained crystals in the groundmass. Sericite is very fine-grained. Phenocrysts are poikilitic feldspar and quartz. some crystals have relic zonations.
10% Potassium Feldspar	Potassium feldspar occurs generally as fine-grained subhedral crystals irregularly distributed throughout the groundmass. Crystals are typically altered to sericite. Wavy albite exsolution lamellae are common and produce perthitic textures when present. the crystals generally occur interstitially between plagioclase and quartz crystals. Mild to moderate sericite alteration, some crystals show myrmekitic textures present with plagioclase and quartz.
Trace Amphibole	Hornblende occurs as fine-grained crystals are found occurs around feldspar and quartz phenocrysts. Almost completely altered to chlorite, relic crystals are all that remain.
5% Biotite	Biotite occurs as fine-grained to medium-grained. anhedral crystals. Chlorite alteration varies from weak to moderate.
5% Chlorite	Chlorite occurs as an alteration product of fine- to medium-grained an- to subhedral amphibole and biotite crystals. Chlorite alteration varies from weak to strong. Fine-grained calcite inclusions.
1% Titanite	Titanite occurs as fine-grained euhedral crystals and crystal clusters. Clusters of titanite are associated with clusters of opaque minerals, as well inclusions.
Trace Opaques	Disseminated very fine- to fine-grained pyrite with minor chalcopyrite.

Sample: 16KAA018A **Lithology:** Granodiorite **QAP Classification:** Granodiorite

Mineral Name and Abundance	Description
25% Quartz	Quartz crystals are anhedral and range from fine- to medium-grained. The coarser crystals characteristically exhibit undulatory extinction and sub-grain boundaries. Finer-grained crystals may be strain-free but typically also exhibit undulatory extinction and sub-grain boundaries. Finer-grained quartz occurs as euhedral interstitial material to feldspars.
30% Plagioclase	Plagioclase occurs as sub- to euhedral medium- to coarse-grained crystals distributed evenly throughout the groundmass. Plagioclase accounts for most of phenocrysts. Rare phenocrysts up to 2 mm are present. Very fine- to fine-grained seritization of plagioclase in the groundmass is common ranging from moderate to intense. Simple and polysynthetic twinning are common.
15% Potassium Feldspar	Potassium feldspar occurs generally as medium-grained subhedral crystals irregularly distributed throughout the groundmass. Crystals are typically altered to sericite. Wavy albite exsolution lamellae are common and produce perthitic textures in coarse grained crystals. the crystals generally occur interstitially between plagioclase and quartz crystals. Relic tartan twinning can be seen around sericite alteration. Myrmekitic exsolution with plagioclase and quartz, some coarse-grained crystals have medium-grained chlorite.
10% Biotite	Biotite occurs as fine-grained to medium-grained. anhedral crystals. Chlorite alteration varies from weak to moderate.
Chlorite	Chlorite occurs as an alteration product of fine- to medium-grained an- to subhedral biotite crystals. Chlorite alteration varies from weak to strong.
1% Titanite	Titanite occurs as fine-grained euhedral crystals and crystal clusters. Clusters of titanite are associated with clusters of opaque minerals, as well inclusions, replaced by opaques.
5% Opaques	Disseminated very fine- to fine-grained pyrite with minor chalcopyrite.
Trace Calcite	Calcite occurs in and around biotite, very fine-grained anhedral.

Sample: 16KAA018B **Lithology:** Chlorite Alteration

Mineral Name and Abundance	Description
25% Quartz	Quartz crystals are anhedral and range from fine- to medium-grained. The coarser crystals characteristically exhibit undulatory extinction and sub-grain boundaries. Finer-grained crystals may be strain-free but typically also exhibit undulatory extinction and sub-grain boundaries. Finer-grained quartz occurs as euhedral interstitial material to feldspars.
40% Plagioclase	Plagioclase occurs as sub- to euhedral medium- to coarse-grained crystals distributed evenly throughout the groundmass. Plagioclase accounts for most of phenocrysts. Rare phenocrysts up to 2mm are present. Seritization of plagioclase in the groundmass is common ranging from moderate to intense. Simple and polysynthetic twinning are common. Sericite is very fine to fine-grained. Sericite alteration, and chlorite, sericite make it difficult to distinguish between plagioclase and potassium feldspar.
15% Potassium Feldspar	Potassium feldspar occurs generally as medium-grained subhedral crystals irregularly distributed throughout the groundmass. Crystals are typically altered to sericite. Wavy albite exsolution lamellae are common and produce perthitic textures in coarse grained crystals. the crystals generally occur interstitially between plagioclase and quartz crystals. Relic tartan twinning can be seen around sericite alteration. Myrmekitic exsolution with plagioclase and quartz, some coarse-grained crystals have medium-grained chlorite. Sericite alteration, and chlorite, sericite and hematite make it difficult to distinguish between plagioclase and potassium feldspar.

5% Biotite	Biotite occurs as fine- to medium-grained anhedral crystals. Chlorite alteration varies from moderate to intense.
10% Chlorite	Chlorite occurs as an alteration product of fine- to medium-grained an- to subhedral biotite crystals. Chlorite alteration varies from weak to strong.
1% Titanite	Titanite occurs as fine-grained euhedral crystals and crystal clusters. Clusters of titanite are associated with clusters of opaque minerals, as well inclusions, replaced by opaques.
1% Opaques	Disseminated very fine- to fine-grained pyrite with minor chalcopyrite.
10% Calcite	Calcite occurs as fine-grained crystals along feldspar grains.

Sample: 16KAA018C **Lithology:** Granodiorite **QAP Classification:** Granodiorite

Mineral Name and Abundance	Description
20% Quartz	Quartz crystals are anhedral and range from fine- to medium-grained. The coarser crystals characteristically exhibit undulatory extinction and sub-grain boundaries. Finer-grained crystals may be strain-free but typically also exhibit undulatory extinction and sub-grain boundaries. Finer-grained quartz occurs as euhedral interstitial material to feldspars.
30% Plagioclase	Plagioclase occurs as sub- to euhedral medium- to coarse-grained crystals distributed evenly throughout the groundmass. Plagioclase accounts for most of phenocrysts. Rare phenocrysts up to 2 mm are present. Very fine- to fine-grained seritization of plagioclase in the groundmass is common ranging from moderate to intense. Simple and polysynthetic twinning are common.
15% Potassium Feldspar	Potassium feldspar occurs generally as medium-grained subhedral crystals irregularly distributed throughout the groundmass. Crystals are typically altered to sericite. Wavy albite exsolution lamellae are common and produce perthitic textures in coarse grained crystals. the crystals generally occur interstitially between plagioclase and quartz crystals. Relic tartan twinning can be seen around sericite alteration. Myrmekitic exsolution with plagioclase and quartz, some coarse-grained crystals have medium-grained chlorite crystals.
Trace Amphibole	Hornblende occurs as fine-grained crystals are found in clusters occurs around feldspars and quartz phenocrysts. Crystals are generally subhedral to anhedral with distinct cleavage planes present. Simple twinning is present in most crystals.
10% Biotite	Biotite occurs as fine-grained to medium-grained. anhedral crystals. Chlorite alteration varies from moderate to intense. Mafic clusters
5% Chlorite	Chlorite occurs as an alteration product of fine- to medium-grained an- to subhedral biotite crystals. Chlorite alteration varies from weak to strong.
Trace Titanite	Titanite occurs as fine-grained euhedral crystals and crystal clusters. Clusters of titanite are associated with clusters of opaque minerals, as well inclusions, replaced by opaques.
5% Epidote	Epidote occurs as fine-grained anhedral crystals included in chlorite alteration and occurs in clusters around plagioclase crystals.
1% Opaques	Disseminated very fine- to fine-grained pyrite with minor chalcopyrite.

Sample: 16KAA019A **Lithology:** Granodiorite **QAP Classification:** Granodiorite

Mineral Name and Abundance	Description
25% Quartz	Quartz crystals are anhedral and range from fine- to medium-grained. Coarser crystals characteristically exhibit undulatory extinction and sub-grain boundaries. Finer-grained crystals may be strain-free but typically also exhibit undulatory extinction and sub-grain boundaries. Finer-grained quartz occurs as euhedral interstitial material to feldspars.

40% Plagioclase	Plagioclase occurs as sub- to euhedral medium- to coarse-grained crystals distributed evenly throughout the groundmass. Plagioclase accounts for most of phenocrysts. Rare phenocrysts up to 2 mm are present. Finer-grained plagioclase are intense criticized in the groundmass. Very fine- to fine-grained seritization of plagioclase in the groundmass is common ranging from moderate to intense. Simple and polysynthetic twinning are common, medium-grained crystals have mild perthitic textures.
10% Potassium Feldspar	Potassium feldspar occurs generally as medium-grained subhedral crystals irregularly distributed throughout the groundmass. Crystals are typically altered to sericite. Wavy albite exsolution lamellae are common and produce perthitic textures when present. the crystals generally occur interstitially between plagioclase and quartz crystals. Relic tartan twinning can be seen around sericite alteration.
1% Amphibole	Hornblende occurs as fine-grained crystals are found in clusters occurs around feldspars and quartz phenocrysts. Crystals are generally subhedral to anhedral with distinct cleavage planes present. Simple twinning is present in most crystals.
5% Biotite	Biotite occurs as fine-grained to medium-grained anhedral crystals. Chlorite alteration varies from moderate to intense.
1% Chlorite	Chlorite occurs as an alteration product of fine- to medium-grained an- to subhedral biotite crystals. Chlorite alteration varies from weak to strong.
1% Opaques	Disseminated very fine- to fine-grained pyrite with minor chalcopyrite.
10% Muscovite	Muscovite occurs as fine-grained anhedral crystals.
Trace Calcite	Calcite occur as fine-grained crystals, anhedral, occur in fractures of potassium feldspar and quartz.

Sample: 16KAA019D **Lithology:** Granodiorite **QAP Classification:** Monzogranite

Mineral Name and Abundance	Description
25% Quartz	Quartz crystals are anhedral and range from fine- to medium-grained. The coarser crystals characteristically exhibit undulatory extinction and sub-grain boundaries. Finer-grained crystals may be strain-free but typically also exhibit undulatory extinction and sub-grain boundaries. Finer-grained quartz occurs as euhedral interstitial material to feldspars.
30% Plagioclase	Plagioclase occurs as sub- to euhedral medium- to coarse-grain crystals distributed evenly throughout the groundmass. Plagioclase accounts for most of phenocrysts. Rare phenocrysts up to 2 mm are present. Seritization of plagioclase in the groundmass is common ranging from moderate to intense. Simple and polysynthetic twinning are common. sericite is very fine to fine-grained. Medium-grained crystals have mild perthitic textures. mild sericite alteration, phenocrysts can be poikilitic with amphibole, titanite. sericite outlines zonations
20% Potassium Feldspar	Potassium feldspar occurs generally as medium-grained. Subhedral crystals irregularly distributed throughout the groundmass. Crystals are typically altered to sericite. Wavy albite exsolution lamellae are common and produce perthitic textures when present. The crystals generally occur interstitially between plagioclase and quartz crystals. Relic tartan twinning can be seen around sericite alteration.
5% Amphibole	Hornblende occurs as fine-grained crystals are found in clusters occurs around feldspars and quartz phenocrysts. Crystals are generally subhedral to anhedral with distinct cleavage planes present. Simple twinning is present in most crystals.
5% Biotite	Biotite occurs as fine-grained to medium-grained anhedral crystals. Chlorite alteration varies from moderate to intense.
5% Chlorite	Chlorite occurs as an alteration product of fine- to medium-grained an- to subhedral biotite crystals. Chlorite alteration varies moderate to strong.
Trace Titanite	Titanite occurs as fine-grained euhedral crystals and crystal clusters. Clusters of titanite are associated with clusters of opaque minerals, as well inclusions.

5% Epidote	Epidote occurs as fine-grained anhedral crystals included in chlorite alteration and occurs in clusters around plagioclase crystals.
1% Opaques	Fine-grained disseminated pyrite.

Sample: 16KAA020A **Lithology:** Monzogranite **QAP Classification:** Monzogranite

Mineral Name and Abundance	Description
20% Quartz	Quartz crystals are anhedral and range from fine- to medium-grained. The coarser crystals characteristically exhibit undulatory extinction and sub-grain boundaries. Finer-grained crystals may be strain-free but typically also exhibit undulatory extinction and sub-grain boundaries. Finer-grained quartz occurs as euhedral interstitial material to feldspars.
25% Plagioclase	Plagioclase occurs as sub- to euhedral medium-grained. to coarse-grained crystals distributed evenly throughout the groundmass. Plagioclase accounts for most of phenocrysts. Rare phenocrysts up to 2 mm are present. Fine-grained seritization of plagioclase in the groundmass is common ranging from moderate to intense. Simple and polysynthetic twinning are common, the larger crystals have mild perthitic textures.
15% Potassium Feldspar	Potassium feldspar occurs generally as medium-grained subhedral crystals irregularly distributed throughout the groundmass. Crystals are typically altered to sericite. Wavy albite exsolution lamellae are common and produce perthitic textures when present. The crystals generally occur interstitially between plagioclase and quartz crystals. Relic tartan twinning can be seen around sericite alteration. Moderate sericite alteration, sericite to very fine- to fine-grained.
30% Amphibole	Hornblende occurs as fine-grained. Crystals are found in clusters occurs around feldspars and quartz phenocrysts. Crystals are generally subhedral to anhedral with distinct cleavage planes present. Simple twinning is present in most crystals.
1-2% Chlorite	Chlorite occurs as an alteration product of fine- to medium-grained an- to subhedral biotite crystals. Chlorite alteration varies moderate to strong.
Trace Titanite	Titanite occurs as fine-grained euhedral crystals and crystal clusters. Clusters of titanite are associated with clusters of opaque minerals, as well inclusions.
5% Epidote	Epidote occurs as fine-grained anhedral crystals included in chlorite alteration and occurs in clusters around plagioclase crystals.
1% Opaques	Disseminated very fine- to fine-grained pyrite with minor chalcopyrite.

Sample: 16KAA021B **Lithology:** Monzogranite **QAP Classification:** Granodiorite

Mineral Name and Abundance	Description
20% Quartz	Quartz crystals are anhedral and range from fine- to medium-grained. The coarser crystals characteristically exhibit undulatory extinction and sub-grain boundaries. Finer-grained crystals may be strain-free but typically also exhibit undulatory extinction and sub-grain boundaries. Finer-grained quartz occurs as euhedral interstitial material to feldspars.
30%Plagioclase	Plagioclase occurs as sub- to euhedral medium- to coarse-grained crystals distributed evenly throughout the groundmass. Plagioclase accounts for most of phenocrysts. Rare phenocrysts up to 2 mm are present. Fine-grained seritization of plagioclase in the groundmass is common ranging from moderate to intense. Simple and polysynthetic twinning are common.
15% Potassium Feldspar	Potassium feldspar occurs generally as medium-grained subhedral crystals irregularly distributed throughout the groundmass. Crystals are typically altered to sericite. Wavy albite exsolution lamellae are common and produce perthitic textures when present. the crystals generally occur interstitially between plagioclase and quartz crystals. Relic tartan

	twinning can be seen around sericite alteration. grainsize reduction, clusters of very fine-grained crystals.
25% Amphibole	Hornblende occurs as fine-grained crystals are found in clusters occurs around feldspars and quartz phenocrysts. Crystals are generally subhedral to anhedral with distinct cleavage planes present. Simple twinning is present in most crystals. poikilitic with sulphides, titanite, quartz, epidote.
5% Biotite	Biotite occurs as fine-grained to medium-grained anhedral crystals. Chlorite alteration varies from moderate to intense.
1% Titanite	Titanite occurs as fine-grained euhedral crystals and crystal clusters. Clusters of titanite are associated with clusters of opaque minerals, as well inclusions.
1% Epidote	Epidote occurs as fine-grained anhedral crystals included in chlorite alteration and occurs in clusters around plagioclase crystals.
2% Opaques	Disseminated very fine- to fine-grained pyrite with minor chalcopyrite.

Sample: 16KAA021C **Lithology:** Pegmatite

Mineral Name and Abundance	Description
30% Quartz	Quartz crystals are anhedral, coarse-grained occurs as graphic textures with feldspars.
30% Plagioclase	Plagioclase occurs as sub- to euhedral coarse-grained crystals occurs as graphic texture with potassium feldspar and quartz.
30% Potassium Feldspar	Potassium feldspar occurs generally as coarse-grained subhedral crystals, with quartz and plagioclase creating a graphic texture. Tartan twinning is present.
4% Chlorite	Chlorite occurs as fine-grained along fractures.
1% Opaques	Disseminated very fine- to fine-grained pyrite with minor chalcopyrite.
5% Calcite vein	Occurs as fine-grained anhedral crystals and cross-cutting veins.

Sample: 16KAA022A **Lithology:** Granodiorite **QAP Classification:** Granodiorite

Mineral Name and Abundance	Description
25% Quartz	Quartz crystals are anhedral and range from fine- to medium-grained. The coarser crystals characteristically exhibit undulatory extinction and sub-grain boundaries. Finer-grained crystals may be strain-free but typically also exhibit undulatory extinction and sub-grain boundaries. Finer-grained quartz occurs as euhedral interstitial material to feldspars. graphic texture with feldspar.
35% Plagioclase	Plagioclase occurs as sub- to euhedral medium- to coarse-grained crystals distributed evenly throughout the groundmass. Plagioclase accounts for most of phenocrysts. Rare phenocrysts up to 2 mm are present. Mild seritization of plagioclase in the groundmass is common ranging from moderate to intense. Simple and polysynthetic twinning are common. Medium-grained crystals have mild perthitic textures.
15% Potassium Feldspar	Potassium feldspar occurs generally as medium-grained subhedral crystals irregularly distributed throughout the groundmass. Crystals are typically altered to sericite. Wavy albite exsolution lamellae are common and produce perthitic textures when present. the crystals generally occur interstitially between plagioclase and quartz crystals. Relic tartan twinning can be seen around. grainsize reduction, clusters of very fine-grained crystals. Coarse-grained phenocrysts are poikilitic with amphibole, and quartz
10% Amphibole	Hornblende occurs as fine-grained crystals are found in clusters occurs around feldspars and quartz phenocrysts. Crystals are generally subhedral to anhedral with distinct cleavage planes present. Simple twinning is present in most crystals. Some phenocrysts are poikilitic with quartz and sulphides, minimal chlorite alteration, mafic clusters with opaques and titanite.

5% Biotite	Biotite occurs as fine- to medium-grained anhedral crystals. Chlorite alteration varies from moderate to intense.
Trace Chlorite	Chlorite occurs as an alteration product of fine- to medium-grained an- to subhedral biotite crystals. Chlorite alteration varies moderate to strong.
1% Titanite	Titanite occurs as fine-grained euhedral crystals and crystal clusters. Clusters of titanite are associated with clusters of opaque minerals, as well inclusions.
Trace Epidote	Epidote occurs as fine-grained anhedral crystals included in chlorite alteration and occurs in clusters around plagioclase crystals.
Trace Opaques	Disseminated very fine- to fine-grained pyrite with minor chalcopyrite.

Sample: 16KAA025A **Lithology:** Granodiorite **QAP Classification:** Granodiorite

Mineral Name and Abundance	Description
25% Quartz	Quartz crystals are anhedral and range from fine- to medium-grained. The coarser crystals characteristically exhibit undulatory extinction and sub-grain boundaries. Finer-grained crystals may be strain-free but typically also exhibit undulatory extinction and sub-grain boundaries. Finer-grained quartz occurs as euhedral interstitial material to feldspars. graphic exsolution textures with feldspar, fractures are filled with micas.
40% Plagioclase	Plagioclase occurs as sub- to euhedral medium- to coarse-grained crystals distributed evenly throughout the groundmass. Plagioclase accounts for most of phenocrysts. Rare phenocrysts up to 2 mm are present. Fine-grained plagioclase are intense seritized in the groundmass. Seritization of plagioclase in the groundmass is common ranging from moderate to intense. Simple and polysynthetic twinning are common. sericite is very fine to fine-grained. Medium-grained crystals have mild perthitic textures. Mild to moderate sericite zonations are outlined by sericite.
15%Potassium Feldspar	Potassium feldspar occurs generally as medium-grained subhedral crystals irregularly distributed throughout the groundmass. Crystals are typically altered to sericite. Wavy albite exsolution lamellae are common and produce perthitic textures when present. the crystals generally occur interstitially between plagioclase and quartz crystals. Relic tartan twinning can be seen around. grainsize reduction, clusters of very fine-grained crystals. Mild sericite alteration very fine-grained.
5% Amphibole	Hornblende occurs as fine-grained crystals are found in clusters occurs around feldspars and quartz phenocrysts. Crystals are generally subhedral to anhedral with distinct cleavage planes present. Simple twinning is present in most crystals. Some phenocrysts are poikilitic with quartz and sulphides, minimal chlorite alteration, mafic clusters with opaques and titanite.
5% Biotite	Biotite occurs as fine- to medium-grained anhedral crystals. Chlorite alteration varies from moderate to intense.
1% Titanite	Titanite occurs as fine-grained euhedral crystals and crystal clusters. Clusters of titanite are associated with clusters of opaque minerals, as well inclusions.
1% Opaques	Disseminated very fine- to fine-grained pyrite with minor chalcopyrite.

Sample: 16KAA026A **Lithology:** Granodiorite **QAP Classification:** Granodiorite

Mineral Name and Abundance	Description
20% Quartz	Quartz crystals are anhedral and range from fine- to medium-grained. The coarser crystals characteristically exhibit undulatory extinction and sub-grain boundaries. Finer-grained crystals may be strain-free but typically also exhibit undulatory extinction and sub-grain boundaries. Finer-grained quartz occurs as euhedral interstitial material to feldspars.

30% Plagioclase	Plagioclase occurs as sub- to euhedral medium- to coarse-grain crystals distributed evenly throughout the groundmass. Plagioclase accounts for most of phenocrysts. Rare phenocrysts up to 2 mm are present. Finer-grained plagioclase are intensely seritized in the groundmass. Seritization of plagioclase in the groundmass is common ranging from mild. Simple and polysynthetic twinning are common. Medium-grained crystals have mild perthitic textures.
15% Potassium Feldspar	Potassium feldspar occurs generally as medium- to fine-grained subhedral crystals irregularly distributed throughout the groundmass. Crystals are only mild to moderate Seritization. Some coarser grained crystals show perthitic exsolution textures. Crystals are commonly interstitially between plagioclase and quartz.
20% Amphibole	Hornblende occurs as fine-grained crystals are found in clusters occurs around feldspars and quartz phenocrysts. Crystals are generally subhedral to anhedral with distinct cleavage planes present. Simple twinning is present in most crystals.
5% Biotite	Biotite occurs as fine- to medium-grained anhedral crystals. Chlorite alteration varies from moderate to intense.
1% Titanite	Titanite occurs as fine-grained euhedral crystals and crystal clusters. Clusters of titanite are associated with clusters of opaque minerals, as well inclusions.
Trace Epidote	Epidote occurs as fine-grained anhedral crystals included in chlorite alteration and occurs in clusters around plagioclase crystals.
1% Opaques	Disseminated very fine- to fine-grained pyrite with minor chalcopyrite.

Sample: 16KAA028A **Lithology:** Hematite Altered Granodiorite

Mineral Name and Abundance	Description
20% Quartz	Quartz crystals are anhedral and range from medium-to fine-grained. The coarser crystals characteristically exhibit undulatory extinction and sub-grain boundaries. Finer-grained quartz occurs as euhedral interstitial material to feldspars. Crystals exhibit foliations, creating stringers between amphiboles and feldspars.
15%Plagioclase	Plagioclase occurs as sub- to euhedral medium- to fine-grained crystals distributed throughout the groundmass. Plagioclase are intensely seritized but over printed by hematite alteration. Sericite is very fine. the larger crystals have mild perthitic textures. Difficult to distinguished between feldspars, little to no twinning present.
15%Potassium Feldspar	K-feldspar occurs as sub- to euhedral medium- to fine-grained crystals distributed throughout the groundmass. Crystals are intensely seritized but over printed by hematite alteration. Sericite is very fine. The larger crystals have mild perthitic textures. Difficult to distinguish between feldspars.
40% Amphibole	Hornblende occurs as medium-to fine-grained laths are that foliated through the thin section. Occurs as between feldspar and quartz crystals. Crystals are subhedral to anhedral with cleavage planes.
10% Chlorite	Occurs as fine-grained laths surrounding amphibole crystals.

Sample: 16KAA031A **Lithology:** Granodiorite **QAP Classification:** Granodiorite

Mineral Name and Abundance	Description
20% Quartz	Quartz crystals are anhedral and range from fine- to medium-grained. The coarser crystals characteristically exhibit undulatory extinction and sub-grain boundaries. Finer-grained quartz occurs as euhedral interstitial material to feldspars.
35% Plagioclase	Plagioclase occurs as sub- to euhedral medium- to fine-grained phenocrysts with very fine-grained anhedral crystals in the groundmass. Intensely sericite altered, sericite is very fine to fine-grained full crystals laths can be seen. Sericite outline zonations in medium-grained phenocrysts.

15% Potassium Feldspar	K-feldspar occurs as sub- to euhedral medium- to fine-grained crystals distributed throughout the groundmass. Very few phenocrysts, primarily interstitial groundmass. Crystals experience mild sericite alteration, less than plagioclase.
5% Biotite	Biotite occurs as fine- to medium-grained anhedral crystals. Chlorite alteration is intense to complete.
5% Chlorite	Chlorite occurs as an alteration product of fine- to medium-grained an- to subhedral biotite crystals. Chlorite alteration is tense.
1% Titanite	Titanite occurs as fine-grained euhedral crystals and crystal clusters. Clusters of titanite are associated with clusters of opaque minerals, as well inclusions.
1% Epidote	Epidote occurs as fine-grained anhedral crystals included in chlorite alteration and occurs in clusters around plagioclase crystals.
Trace Opaques	Disseminated very fine- to fine-grained pyrite with minor chalcopyrite.
1% Calcite	Calcite occurs as fine-grained anhedral crystals, occurs as in fractures of potassium feldspar and quartz.

Sample: 16KAA032A **Lithology:** Granodiorite **QAP Classification:** Monzogranite

Mineral Name and Abundance	Description
25% Quartz	Quartz crystals occur as fine-grained interstitial material crystals exhibit undulose extinction with minor grainsize reduction.
35% Plagioclase	Plagioclase occurs as sub- to euhedral medium- to fine-grained phenocrysts with very fine-grained anhedral crystals in the groundmass. Moderately sericite alteration, sericite is very fine- to fine-grained. Sericite outline zonations in medium-grained phenocrysts. Simple twinning is present in phenocrysts.
20% Potassium Feldspar	K-felspars occur as anhedral medium- to fine-grained interstitial material. Tartan twinning common in medium-grained crystals with little to no sericite alteration.
9% Amphibole	Hornblende occurs as fine-grained found in clusters occurs around feldspars and quartz phenocrysts. Crystals are generally subhedral to anhedral with distinct cleavage planes present. Simple twinning is present in most crystals. poikilitic with sulphides, titanite, quartz, epidote. Occurs as clusters with biotite around quartz and feldspars.
8% Biotite	Biotite occurs as fine-to medium-grained anhedral crystals. Chlorite alteration is weak. Occurs as clusters with amphiboles, surrounding quartz and feldspars crystals.
Trace Chlorite	Chlorite occurs as an alteration product of fine- to medium-grained an- to subhedral biotite and amphibole crystals. Chlorite alteration is weak.
1% Titanite	Titanite occurs as fine-grained euhedral crystals and crystal clusters. Clusters of titanite are associated with clusters of opaque minerals, as well inclusions.
2% Epidote	Epidote occurs as fine-grained anhedral crystals included in chlorite alteration and occurs in clusters around plagioclase crystals.
Trace Opaques	Disseminated very fine- to fine-grained pyrite with minor chalcopyrite.

Sample: 16KAA033B **Lithology:** Pegmatite

Mineral Name and Abundance	Description
33% Quartz	Quartz crystals are anhedral, coarse-grained occurs as graphic exsolution textures with feldspars.
34%Plagioclase	Plagioclase occurs as sub- to euhedral coarse-grained crystals occurs as graphic texture with potassium feldspar and quartz. Mild very fine-grained sericite alteration.
30% Potassium Feldspar	Potassium Feldspar occurs generally as coarse-grained subhedral crystals, with quartz and plagioclase creating a graphic texture. Tartan twinning is present. Crystals up to 1cm

	wide. Coarse crystals are surrounded by fine- grained k-feldspars and quartz graphic texture.
1% Amphibole	Hornblende occurs as very fine-grained crystals disseminated throughout the thin section.
1% Epidote	Epidote occurs as very fine-grained anhedral crystals.
1% Opaques	Fine-grained pyrite in fractures.

Sample: 16KAA033C **Lithology:** Altered Granodiorite

Mineral Name and Abundance	Description
trace Quartz	Quartz crystals are anhedral and fine-grained. Crystals typically also exhibit undulatory extinction and sub-grain boundaries. Finer-grained quartz occurs as euhedral interstitial material to feldspars. No phenocrysts present
23% Plagioclase	Plagioclase occurs as sub- to euhedral medium- to coarse-grained crystals distributed evenly throughout the groundmass. Plagioclase accounts for most of phenocrysts. Rare phenocrysts up to 2 mm are present. Intense Seritization alteration is present, only relic simple twinning. sericite is very fine-grained to fine-grained. Crystals are intensely seritized, to the point that is difficult to distinguish between feldspars.
22% Potassium Feldspar	Potassium Feldspar occurs generally as medium- to fine-grained subhedral crystals irregularly distributed throughout the groundmass. Crystals are intensely seritized, to the point that is difficult to distinguish between feldspars.
30% Amphibole	Hornblende occurs as fine-grained. Crystals are found in clusters occurs around feldspars and quartz phenocrysts. Crystals are generally subhedral to anhedral with distinct cleavage planes present. Simple twinning is present in most crystals. Mafic mineral clusters occurs around feldspars
5% Chlorite	Chlorite occurs as fine-grained alteration product of amphiboles. Chlorite occurs as an alteration product of fine- to medium-grained an- to subhedral amphibole crystals. Chlorite alteration varies moderate to strong.
Trace Titanite	Titanite occurs as fine-grained euhedral crystals and crystal clusters. Clusters of titanite are associated with clusters of opaque minerals, as well inclusions.
5% Epidote	Epidote occurs as fine-grained anhedral crystals included in chlorite alteration and occurs in clusters around amphibole crystals.
Trace Opaques	Disseminated very fine- to fine-grained pyrite with minor chalcopyrite.
1% Calcite	Calcite is secondary fine-grained anhedral crystals.

Sample: 16KAA033D **Lithology:** Altered Granodiorite

Mineral Name and Abundance	Description
15% Quartz	Quartz crystals are anhedral and range from fine- to medium-grained. The coarser crystals characteristically exhibit undulatory extinction and sub-grain boundaries. Finer-grained crystals may be strain-free but typically also exhibit undulatory extinction and sub-grain boundaries. Finer-grained quartz occurs as euhedral interstitial material to feldspars.
30% Plagioclase	Plagioclase occurs as sub- to euhedral medium- to coarse-grained crystals distributed evenly throughout the groundmass. Plagioclase accounts for most of phenocrysts. Rare phenocrysts up to 2 mm are present. Intense Seritization alteration is present, only relic simple twinning. sericite is very fine- to fine-grained. Crystals are intensely seritized.
20% Potassium Feldspar	Potassium Feldspar occurs generally as medium- to fine-grained subhedral crystals irregularly distributed throughout the groundmass. Crystals have tartan twinning and coarser grained

	crystals have perthitic twinning. Crystals commonly occur interstitially to plagioclase and quartz phenocrysts.
25% Amphibole	Hornblende occurs as fine-grained crystals are found in clusters occurs around feldspars and quartz phenocrysts. Crystals are generally subhedral to anhedral with distinct cleavage planes present. Simple twinning is present in most crystals. Mafic mineral clusters occurs around feldspars. Has replacement by titanite and sulphides.
5-6% Chlorite	Chlorite occurs as fine-grained alteration product of amphiboles. Chlorite occurs as an alteration product of fine- to medium-grained an- to subhedral amphibole crystals. Chlorite alteration varies moderate to strong.
1% Titanite	Titanite occurs as fine-grained euhedral crystals and crystal clusters. Clusters of titanite are associated with clusters of opaque minerals, as well inclusions.
5% Epidote	Epidote occurs as fine-grained anhedral crystals included in chlorite alteration and occurs in clusters around amphibole crystals.
1% Opaques	Disseminated very fine- to fine-grained pyrite with minor chalcopyrite.
1% Calcite	Calcite occurs as fine-grained anhedral crystals, occurs as in fractures of potassium feldspar and quartz.

Sample: 16KAA034A **Lithology:** Monzogranite

Mineral Name and Abundance	Description
20% Quartz	Quartz crystals are anhedral and range from fine- to medium-grained. The crystals commonly exhibit undulose extinction and sub-grain boundaries. Phenocrystals are surrounded by very fine-grained groundmass of feldspar and quartz. Occurs as quartz veins.
35% Plagioclase	Plagioclase occurs as sub- to euhedral medium- to fine-grained crystals distributed throughout thin section with fine-grained crystals occurs as in the groundmass with k-feldspar and quartz. Crystals have mild sericite alteration, with relic twinning present.
30% Potassium Feldspar	K-feldspar occur as very fine- to fine-grained anhedral crystals in interstitial to quartz and plagioclase in the groundmass. Crystals have tartan twinning in coarser crystals and perthitic twinning.
Trace Chlorite	Chlorite occurs as very fine-grained along fractures as laths. Sulphides and chlorite occurs together.
Trace Opaques	Very fine- to fine-grained occurs around fractures.
5% Calcite	Calcite occurs as fine-grained anhedral crystals, occurs as in fractures of potassium feldspar and quartz.

Sample: 16KAA034B **Lithology:** Monzogranite

Mineral Name and Abundance	Description
35% Quartz	Quartz crystals are anhedral and range from fine- to medium-grained. The crystals commonly exhibit undulatory extinction and sub-grain boundaries. Occurs as quartz veins.
30% Plagioclase	Plagioclase occurs as sub- to euhedral medium- to coarse-grain crystals distributed throughout thin section. Fine-grained crystals occur in the groundmass with k-feldspar and quartz. Crystals have moderate very fine- to fine-grained sericite alteration, with relic twinning present. Phenocrysts are surrounded by fine-grained feldspar and quartz.

20% Potassium Feldspar	K-feldspar occur as very fine- to fine-grained anhedral crystals in interstitial to quartz and plagioclase in the groundmass. Crystals have tartan twinning in coarser crystals and perthitic twinning.
10%Chlorite	Chlorite occurs as very fine-grained along fractures as laths.
1% Opaques	Disseminated very fine- to fine-grained pyrite with minor chalcopyrite.
1% Calcite	Calcite occurs as fine-grained anhedral crystals, occurs as in fractures of potassium feldspar and quartz.

Sample: 16KAA035A **Lithology:** Granodiorite **QAP Classification:** Granodiorite

Mineral Name and Abundance	Description
30% Quartz	Quartz crystals are anhedral and range from fine- to medium-grained. The crystals commonly exhibit undulatory extinction and sub-grain boundaries. Occurs as quartz veins. Thin section cross-cut by quartz calcite veins.
30% Plagioclase	Plagioclase occurs as sub- to euhedral medium- to coarse-grained crystals, with fine-grained crystals in the groundmass. Crystals have minor fine-grained sericite alteration. Crystals show polysynthetic twinning, some deformed twins. Perthitic textures seen along contacts with k-feldspar.
15%Potassium Feldspar	K-feldspar occur as very fine- to fine-grained anhedral crystals in interstitial to quartz and plagioclase in the groundmass. Crystals have tartan twinning in coarser crystals and perthitic twinning.
Trace Biotite	Biotite occurs as very fine-grained anhedral crystals.
Trace Titanite	Titanite occurs as fine-grained euhedral crystals and crystal clusters. Clusters of titanite are associated with clusters of opaque minerals, as well inclusions.
5% Opaques	Disseminated very fine- to fine-grained pyrite with minor chalcopyrite.
10% Calcite	Calcite occurs as fine-grained anhedral crystals, occurs as in fractures of potassium feldspar and quartz.

Sample: 16KAA038A **Lithology:** Granodiorite **QAP Classification:** Granodiorite

Mineral Name and Abundance	Description
20% Quartz	Quartz crystals are anhedral and range from fine- to medium-grained. The crystals commonly exhibit undulatory extinction and sub-grain boundaries.
30% Plagioclase	Plagioclase occurs as sub- to euhedral medium- to coarse-grained crystals, with fine-grained crystals in the groundmass. Crystals have minor fine-grained sericite and calcite alteration. Crystals show polysynthetic twinning, some deformed twins.
15% Potassium Feldspar	K-feldspar occur as very fine- to fine-grained anhedral crystals in interstitial to quartz and plagioclase in the groundmass. Crystals have tartan twinning in coarser crystals and perthitic twinning.
30% Biotite	Biotite occurs as very fine- to fine-grained lath crystals. Crystals occur along plagioclase crystals.
Trace Opaques	Disseminated very fine- to fine-grained pyrite with minor chalcopyrite.
5% Calcite	Calcite occurs as fine-grained anhedral crystals, occurs as secondary alteration along feldspar crystals.

Sample: 16KAA039A **Lithology:** Granodiorite **QAP Classification:** Monzogranite

Mineral Name and Abundance	Description

30% Quartz	Quartz crystals are anhedral and range from fine- to medium-grained. The coarser crystals characteristically exhibit undulatory extinction and sub-grain boundaries. Finer-grained quartz occurs as euhedral interstitial material to feldspars.
35% Plagioclase	Plagioclase occurs as sub- to euhedral medium- to coarse-grained crystals, with fine-grained crystals in the groundmass. Crystals have mild fine-grained sericite alteration. Crystals show polysynthetic twinning, some deformed twins.
25%Potassium Feldspar	K-feldspar occur as fine-grained anhedral crystals in interstitial to quartz and plagioclase in the groundmass. Crystals have tartan twinning in coarser crystals and perthitic twinning lamellae exsolution.
1% Amphibole	Hornblende occurs as fine-grained subhedral crystals. Crystals are found in clusters occurs around feldspars and quartz phenocrysts. Crystals are generally subhedral to anhedral with distinct cleavage planes present. Simple twinning is present in most crystals.
5% Biotite	Biotite occurs as very fine- to fine-grained lath crystals.
5% Chlorite	Chlorite occurs as anhedral fine-grained alteration product of amphibole crystals.
1% Opaques	Disseminated very fine- to fine-grained pyrite with minor chalcopyrite.

Sample: 16KAA042A **Lithology:** Dyke

Mineral Name and Abundance	Description
20% Quartz	Quartz crystals are anhedral and fine-grained. Quartz occurs as interstitial material to plagioclase. No phenocrysts present.
60% Plagioclase	Plagioclase occurs as medium- to fine-grained phenocrysts in a cumulate texture. Crystals are mildly sericite altered.
15% Chlorite	Chlorite occurs as fine- to medium-grained laths and alteration product of amphiboles and along fractures.
5% Calcite	Calcite occurs as fine-grained anhedral crystals, occurs as secondary alteration along feldspar crystals.

Sample: 17KAM022B **Lithology:** Hematite Altered Granodiorite

Mineral Name and Abundance	Description
25% Quartz	Quartz crystals are anhedral and range from fine- to medium-grained. The crystals commonly exhibit undulatory extinction and sub-grain boundaries. Crystals in groundmass occurs as in clusters along feldspars.
30% Plagioclase	Plagioclase occurs as sub- to euhedral medium- to coarse-grained crystals distributed throughout thin section. Fine-grained crystals occur in the groundmass with k-feldspar and quartz. Sericite alteration is over printed by hematite. Crystals are completely over printed by very fine-grained hematite alteration. Phenocrystal are poikilitic with amphibole, epidote and feldspars.
15% Potassium Feldspar	K-feldspar occur as fine-grained anhedral crystals in interstitial to quartz and plagioclase in the groundmass. Crystals have tartan twinning in coarser crystals and perthitic twinning lamellae exsolution. Crystals have over printing fine-grained hematite alteration.
5% Amphibole	Hornblende occurs as fine-grained crystals are found in clusters occurs around feldspars and quartz phenocrysts. Crystals are generally subhedral to anhedral with distinct cleavage planes present. Simple twinning is present in most crystals. Chlorite alteration of crystals, up to 50%.
5% Biotite	Biotite occurs as fine- to medium-grained anhedral crystals. Chlorite alteration varies from weak to moderate. Crystals are pleochroic, with kinked layers.
5% Chlorite	Chlorite occurs as fine- to medium-grained laths and alteration product of amphiboles and biotite.

Trace Titanite	Titanite occurs as fine-grained euhedral crystals and crystal clusters. Clusters of titanite are associated with clusters of opaque minerals, as well inclusions.
1% Epidote	Epidote occurs as fine-grained anhedral crystals included in chlorite alteration and occurs in clusters around amphibole crystals.
Trace Opaques	Disseminated very fine- to fine-grained pyrite with minor chalcopyrite
Trace Calcite	Calcite occurs as fine-grained anhedral crystals, occurs as secondary alteration along feldspar crystals.
Trace Rutile	Rutile occurs as fine-grained anhedral crystal, with high relief occurs as inclusions in plagioclase.

Sample: 17KAM026A **Lithology:** Pegmatite

Mineral Name and Abundance	Description
20% Quartz	Quartz crystals are anhedral and range from fine- to medium-grained. The crystals commonly exhibit undulatory extinction and sub-grain boundaries.
25% Plagioclase	Plagioclase occurs as sub- to euhedral medium- to fine-grained crystals. Carls bad twinning in combination with simple twins. Intense fine-grained sericite alteration. Sericite alteration outlines zonations in medium-grained phenocryst. Granophyric exsolution textures occur with quartz and potassium feldspar crystals.
15% Potassium Feldspar	K-feldspar occur as fine- to medium-grained anhedral crystals in interstitial to quartz and plagioclase in the groundmass. Crystals have tartan twinning in coarser crystals and perthitic twinning. Medium-grained crystal commonly has perthitic lamellae.
5-10% Amphibole	Hornblende occurs as fine-grained crystals are found in clusters occurs around feldspars and quartz phenocrysts. Crystals are generally subhedral to anhedral with distinct cleavage planes present. Simple twinning is present in most crystals. Mild chlorite alteration of crystals.
5% Biotite	Biotite occurs as fine- to medium-grained anhedral crystals. Chlorite alteration varies from moderate to intense. Crystals exhibit kinked layers.
Trace Chlorite	Chlorite occurs as fine- to medium-grained laths and alteration product of amphiboles and biotite.
Trace Titanite	Titanite occurs as fine-grained euhedral crystals and crystal clusters. Clusters of titanite are associated with clusters of opaque minerals, as well inclusions.
Trace Opaques	Disseminated very fine- to fine-grained pyrite with minor chalcopyrite.

Sample: 17KAM030A **Lithology:** Granodiorite **QAP Classification:** Monzogranite

Mineral Name and Abundance	Description
25% Quartz	Quartz crystals are anhedral and range from fine- to medium-grained. The crystals commonly exhibit undulatory extinction and sub-grain boundaries. Primarily occurs as interstitial to phenocrysts in groundmass.
35% Plagioclase	Plagioclase occurs as sub- to euhedral medium- to fine-grained crystals. Carls bad twinning in combination with simple twins. Mild sericite alteration of phenocrysts. Sericite alteration outlines zonations in medium-grained phenocryst.
20% Potassium Feldspar	K-feldspar occur as fine-to medium-grained anhedral crystals in interstitial to quartz and plagioclase in the groundmass. Crystals have tartan twinning in coarser crystals and perthitic twinning. Medium-grained crystal commonly has perthitic lamellae. Less than 5% sericite alteration.
10% Amphibole	Hornblende occurs as fine-grained crystals are found in clusters occurs around feldspars and quartz phenocrysts. Crystals are generally subhedral to anhedral with distinct cleavage

	planes present. Simple twinning is present in most crystals. Mild chlorite alteration of crystals. Occurs as in mafic clusters with biotite.
5% Biotite	Biotite occurs as fine-to medium-grained anhedral crystals. Chlorite alteration varies from moderate to intense. Occurs as in mafic crystal clusters with amphiboles. Mild chlorite alteration of crystals.
2% Chlorite	Chlorite occurs as fine- to medium-grained laths and alteration product of amphiboles and biotite.
1% Titanite	Titanite occurs as fine-grained euhedral crystals and crystal clusters. Clusters of titanite are associated with clusters of opaque minerals, as well inclusions.
1% Epidote	Epidote occurs as fine-grained anhedral crystals included in chlorite alteration and occurs in clusters around amphibole crystals.
1% Opaques	Disseminated very fine- to fine-grained pyrite with minor chalcopyrite.

Sample: 17KAM032C **Lithology:** Monzogranite **QAP Classification:** Monzogranite

Mineral Name and Abundance	Description
25% Quartz	Quartz crystals are anhedral and range from fine- to medium-grained. The crystals commonly exhibit undulatory extinction and sub-grain boundaries. Primarily occurs as interstitial to phenocrysts in groundmass.
30%Plagioclase	Plagioclase occurs as sub- to euhedral medium- to fine-grained crystals. Carls bad twinning in combination with simple twins. Moderate sericite alteration of phenocrysts. Sericite alteration outlines zonations in medium-grained phenocryst.
25%Potassium Feldspar	K-feldspar occur as fine- to medium-grained anhedral crystals in interstitial to quartz and plagioclase in the groundmass. Crystals have tartan twinning in coarser crystals and perthitic twinning. Medium-grained crystal commonly has perthitic lamellae. Less than 5% sericite alteration.
5% Biotite	Biotite occurs as fine- to medium-grained anhedral crystals. Chlorite alteration varies from moderate to intense. Occurs as in mafic crystal clusters with amphiboles. Mild chlorite alteration of crystals.
10% Chlorite	Chlorite occurs as fine- to medium-grained laths and alteration product of biotite.
Trace Epidote	Epidote occurs as fine-grained anhedral crystals included in chlorite alteration and occurs in clusters around amphibole crystals.
5% Calcite	Calcite occurs as fine-grained anhedral crystals, occurs as secondary alteration along fractures.

Sample: 17KAM036A **Lithology:** Granodiorite **QAP Classification:** Granodiorite

Mineral Name and Abundance	Description
20% Quartz	Quartz crystals are anhedral and range from fine- to very fine-grained. The crystals commonly exhibit undulatory extinction and sub-grain boundaries. Primarily occurs as interstitial to phenocrysts in groundmass. Graphic textures seen along plagioclase crystals.
30% Plagioclase	Plagioclase occurs as sub- to euhedral medium- to fine-grained crystals. Intense fine-grained sericite alteration. Simple twins are present but disrupted by poikilitic minerals with quartz and feldspars. Sericite alteration outlines zonations in medium-grained phenocryst. Graphic textures seen along contacts with quartz crystals.
10%Potassium Feldspar	K-feldspar occur as fine- to medium-grained anhedral crystals in interstitial to quartz and plagioclase in the groundmass. Crystals have tartan twinning in coarser crystals and perthitic twinning. 80% of crystals are primarily perthitic lamella exsolution textures. Less than 5% sericite alteration.

20% Amphibole	Amphiboles occurs as fine- to medium-grained crystals, sub- to euhedral. 70% of amphiboles occur as rims around pyroxene crystals. Simple twins and distinct cleavage seen in phenocrysts.
10% Biotite	Biotite occurs as fine- to medium-grained anhedral crystals. Birds eye extinction seen in laths.
Trace Titanite	Titanite occurs as fine-grained euhedral crystals and crystal clusters. Clusters of titanite are associated with clusters of opaque minerals, as well inclusions.
Trace Opaques	Disseminated very fine- to fine-grained pyrite with minor chalcopyrite.
10% Pyroxenes	Pyroxenes occur as fine- to medium-grained anhedral crystals being rimmed by amphibole crystals.

Sample: 17KAM038B **Lithology:** Aplite Dyke

Mineral Name and Abundance	Description
20% Quartz	Quartz occurs as anhedral fine-grained crystals, phenocrysts are poikilitic with epidote and feldspars.
45%Plagioclase	Plagioclase occurs as very fine-grained anhedral crystals with simple and polysynthetic twinning. Phenocrysts have mild sericite alteration, with one coarse-grained phenocryst (7mm x 11mm) that was sericite altered and poikilitic with quartz and feldspar.
1% Chlorite	Chlorite occurs as fine- to medium-grained laths.
1% Epidote	Epidote occurs as fine-grained anhedral crystals around feldspars.
23% Groundmass	Groundmass is composed of very fine-grained feldspars and quartz. It is too fine-grained to distinguish percentages of minerals.

Sample: 17KAM039B **Lithology:** Diorite **QAP Classification:** Quartz Monzodiorite

Mineral Name and Abundance	Description
10% Quartz	Quartz occurs as anhedral fine-grained crystals. Crystals commonly exhibit undulatory extinction and sub-grain boundaries. Primarily occurs as interstitial to phenocrysts in groundmass.
45% Plagioclase	Plagioclase occurs as sub- to euhedral medium- to fine-grained crystals. Intense fine-grained sericite alteration. Carls bad twinning in combination with simple twins. Mild fine- to very fine-grained sericite alteration of phenocrysts. Sericite alteration outlines zonations in medium-grained phenocryst.
10% Potassium Feldspar	K-feldspar occur as fine- to medium-grained anhedral crystals in interstitial to quartz and plagioclase in the groundmass. Crystals have tartan twinning in coarser crystals and perthitic twinning. Medium-grained crystal commonly has perthitic lamellae. Less than 5% sericite alteration.
19% Amphibole	Hornblende occurs as fine-grained crystals are found in clusters occurs around feldspars and quartz phenocrysts. Crystals are generally subhedral to anhedral with distinct cleavage planes present. Simple twinning is present in most crystals. Mild chlorite alteration of crystals.
5% Biotite	Biotite occurs as fine- to medium-grained anhedral crystals occurs as typically with amphibole crystals.
1%Titanite	Titanite occurs as fine-grained anhedral crystals and crystal clusters. Clusters of titanite are associated with clusters of opaque minerals, as well inclusions.
Trace Opaques	Disseminated very fine- to fine-grained pyrite with minor chalcopyrite.

Sample: 17KAM040C **Lithology:** Granodiorite **QAP Classification:** Granodiorite

Mineral Name and Abundance	Description
20% Quartz	Quartz occurs as anhedral fine-grained crystals. Crystals commonly exhibit undulatory extinction and sub-grain boundaries. Primarily occurs as interstitial to phenocrysts in groundmass. Granophyric exsolution textures along plagioclase crystals.
40% Plagioclase	Plagioclase occurs as sub- to euhedral medium- to fine-grained crystals. Carls bad twinning in combination with simple twins. Intense fine-grained sericite alteration. Sericite alteration outlines zonations in medium-grained phenocryst. Granophyric exsolution textures along quartz crystals.
15% Potassium Feldspar	K-feldspar occur as fine- to medium-grained anhedral crystals in interstitial to quartz and plagioclase in the groundmass. Crystals have tartan twinning in coarser crystals and perthitic twinning. Medium-grained crystal commonly has perthitic lamellae. Less than 5% sericite alteration.
5% Amphibole	Hornblende occurs as fine-grained crystals are found in clusters occurs around feldspars and quartz phenocrysts. Crystals are generally subhedral to anhedral with distinct cleavage planes present. Simple twinning is present in crystals. Mild chlorite alteration of crystals. Occurs as in clusters with biotite crystals.
5% Biotite	Biotite occurs as fine- to medium-grained anhedral crystals. Occurs typically with amphibole crystals. Occurs as in clusters of mafic minerals. Crystals have mild chlorite alteration.
10% Chlorite	Chlorite occurs as fine- to medium-grained laths and alteration product of amphiboles and biotite.
Trace Titanite	Titanite occurs as fine-grained euhedral crystals and crystal clusters.
1% Opaques	Disseminated very fine- to fine-grained pyrite with minor chalcopyrite.
Trace Rutile	Rutile occurs as fine-grained anhedral crystal, with high relief occurs as inclusions in plagioclase.

Sample: 17KAM041A **Lithology:** Altered Granodiorite

Mineral Name and Abundance	Description
30% Plagioclase	Plagioclase occurs as fine-grained crystals that are completed alternated and overprinted with hematite, rare relic twinning seen in crystals. Alteration seems to be mixture of chlorite, hematite and sericite complete destroying any primary features.
15% Chlorite	Chlorite occurs as a fine-grained lath that are aligned with pyroxene phenocrysts.
5% Opaques	Disseminated very fine- to fine-grained pyrite with minor chalcopyrite.
40% Pyroxene	Pyroxene occurs as medium- to fine-grained phenocrysts that aligned through the thin section and are poikilitic with pyrite.
10% Groundmass	Groundmass is very fine-grained mix of chlorite and felspar with trace calcite.

Sample: 17KAM042A **Lithology:** Granodiorite **QAP Classification:** Monzogranite

Mineral Name and Abundance	Description
30% Quartz	Quartz occurs as anhedral fine-grained crystals. Crystals commonly exhibit undulatory extinction and sub-grain boundaries. Primarily occurs as interstitial to phenocrysts in groundmass. Granophyric exsolution textures along plagioclase crystals.
25% Plagioclase	Plagioclase occurs as sub- to euhedral medium- to fine-grained crystals. Intense fine-grained sericite alteration. Carls bad twinning in combination with simple twins. Mild fine-grained to very fine-grained sericite alteration of phenocrysts. Sericite alteration outlines zonations in medium-grained phenocryst. Granophyric exsolution textures along quartz crystals.

15% Potassium Feldspar	K-feldspar occur as fine- to medium-grained anhedral crystals in interstitial to quartz and plagioclase in the groundmass. Crystals have tartan twinning in coarser crystals and perthitic twinning. Medium-grained crystal commonly has perthitic lamellae. Less than 5% sericite alteration. Granophyric exsolution textures along quartz crystals.
10% Amphibole	Hornblende occurs as fine-grained crystals are found in clusters occurs around feldspars and quartz phenocrysts. Crystals are generally subhedral to anhedral with distinct cleavage planes present. Simple twinning is present in most crystals. Mild chlorite alteration of crystals. Occurs as in clusters with biotite crystals.
5% Biotite	Biotite occurs as fine-to medium-grained anhedral crystals. Occurs typically with amphibole crystals. Occurs as in clusters of mafic minerals. Crystals have mild chlorite alteration. Kinked layers are common.
Trace Titanite	Titanite occurs as fine-grained euhedral crystals and crystal clusters. Clusters of titanite are associated with clusters of opaque minerals, as well inclusions.
Trace Epidote	Epidote occurs as fine-grained anhedral crystals around feldspars.
Trace Opaques	Disseminated very fine- to fine-grained pyrite with minor chalcopyrite.
Trace pyroxene	Pyroxene occurs as anhedral fine-grained crystals sporadically through thin sections.
Trace rutile	Rutile occurs as fine-grained anhedral crystal, with high relief occurs as inclusions in plagioclase.

Sample: 17KAM045B **Lithology:** Hematite Altered Granodiorite

Mineral Name and Abundance	Description
40% Quartz	Quartz occurs as fine- to medium- grained anhedral crystals. Primary textures and crystals are over printed by hematite alteration.
30% Plagioclase	Plagioclase occurs as very fine- to fine-grained subhedral crystals. Crystals form in cumulate textures, has mild fine-grained sericite alteration. Crystals and primary textures over printed by intense very fine-grained hematite alteration. Extremely difficult to differentiate between plagioclase and k-feldspar because of over printing hematite alteration.
15% Potassium Feldspar	K-feldspar occurs as fine-grained sub- to anhedral crystals. Minimal Perthitic Lamellae present showing the present of k-feldspar and plagioclase, hematite alteration over prints primary textures.
4% Amphibole	Amphibole is very fine-grained anhedral crystals disseminated throughout thin section. Hematite alteration over prints primary textures.
1% Opaques	Disseminated very fine- to fine-grained pyrite with minor chalcopyrite.
10% Hematite	Hematite occurs as a secondary hydrothermal alteration that over prints all primary mineralogy.

Sample: 17KAM046A **Lithology:** Hematite Altered Granodiorite

Mineral Name and Abundance	Description
30% Quartz	Quartz occurs as medium-grained phenocrysts, crystals are fractured and infilled with fine-grained groundmass. Phenocrysts exhibit undulatory extinction and sub-grain boundaries. The grain boundaries are serrated. Very fine-grained anhedral crystals occur as part of the groundmass.
40% Plagioclase	Feldspar occurs very fine-grained anhedral crystals in the groundmass. Very fine-grained sericite alteration can be seen along feldspar crystals. Hematite alteration over prints the feldspars. With sericite and hematite alteration no primary textures are seen, making it impossible to distinguished between feldspars.
1% Titanite	Titanite occurs as fine-grained euhedral crystals and crystal clusters. Clusters of titanite are associated with clusters of opaque minerals, as well inclusions.

5% Opaques	Over prints titanite, occurs along fractures with hematite.
10% Hematite	Hematite occurs around fractures overprinting feldspars and quartz crystals.
10% Sericite	Sericite occurs as fine-grained crystals, produced by the alteration product of feldspar.

Sample: 17KAM048A **Lithology:** Hematite Altered Granodiorite

Mineral Name and Abundance	Description
25% Quartz	Quartz occurs as anhedral medium- to fine-grained crystals interstitially to feldspars. Crystals commonly exhibit undulatory extinction and sub-grain boundaries. Primarily occurs as interstitial to phenocrysts in groundmass.
30% Plagioclase	Plagioclase occurs as sub- to euhedral medium- to coarse-grain crystals distributed throughout thin section. With fine-grained crystals occurs in the groundmass with k-feldspar and quartz. Crystals have moderate to intense very fine- to fine-grained sericite alteration, with relic twinning present. Phenocrysts are surrounded by fine-grained feldspar and quartz.
30% Potassium Feldspar	K-feldspar occur as fine- to medium-grained anhedral crystals in interstitial to quartz and plagioclase in the groundmass. Crystals have tartan twinning in coarser crystals and perthitic twinning. Medium-grained crystal has minimal perthitic lamellae.
4% Amphibole	Hornblende occurs as fine-grained crystals are found in clusters occurs around feldspars and quartz phenocrysts. Simple twinning is present in some crystals. Intense chlorite alteration.
10% Chlorite	Chlorite occurs as fine-grained laths and alteration product of amphiboles.
1% Opaques	Disseminated very fine- to fine-grained pyrite with minor chalcopyrite.
5% calcite	Hematite occurs around fractures overprinting feldspars and quartz crystals. Occurs with chlorite alteration.

Sample: 17KAM072V **Lithology:** Quartz Vein

Mineral Name and Abundance	Description
30% Quartz	Occurs as coarse-grained anhedral crystals. A quartz vein takes up 30% of thin section.
40% Plagioclase	Plagioclase occurs as coarse-grained subhedral crystals. Forming graphic textures with quartz and k-feldspar.
30% Potassium Feldspar	K-feldspar occurs as coarse-grained subhedral crystals. Forming graphic textures with quartz and plagioclase.

Sample: 17KAM073A **Lithology:** Monzogranite **QAP Classification:** Granodiorite

Mineral Name and Abundance	Description
25% Quartz	Quartz crystals are anhedral and range from fine- to medium-grained. The crystals commonly exhibit undulatory extinction and sub-grain boundaries. Phenocrysts can range up to coarse-grained.
40% Plagioclase	Feldspar occurs medium- to fine-grained anhedral crystals in the groundmass. Very fine-grained sericite alteration can be seen along feldspar crystals. Sericite alteration makes it difficult to distinguished between feldspars. Mild hematite over printing present. Some Carlsbad and simple twins can be seen.
10% Potassium Feldspar	K-feldspar occur as fine- to medium-grained anhedral crystals in interstitial to quartz and plagioclase in the groundmass. Crystals have tartan twinning in coarser crystals and perthitic twinning. Medium-grained crystals have minimal perthitic lamellae.
5% Amphibole	Hornblende occurs as fine-grained crystals are found in clusters occurs around feldspars and quartz phenocrysts. Simple twinning is present in some crystals. Intense chlorite alteration.

10% Chlorite	Chlorite occurs as fine-grained laths and alteration product of amphiboles.
1% Titanite	Titanite occurs as fine-grained euhedral crystals and crystal clusters. Clusters of titanite are associated with clusters of opaque minerals, as well inclusions.
1% Opaques	Disseminated very fine- to fine-grained pyrite with minor chalcopyrite.
Trace Calcite	Calcite occurs as fine-grained anhedral crystals, occurs as secondary alteration along fractures.

Sample: 17KAM073B **Lithology:** Quartz Vein
Thins section is cross-cut by quartz veins, quartz show exhibit undulatory extinction and sub-grain boundaries. The other veins are composed of very fine-grained quartz and feldspars. The feldspar veins are sericite and chlorite alteration, making it impossible to distinguished between feldspars.

Sample: 17KAM078A **Lithology:** Monzogranite **QAP Classification:** Monzogranite

Mineral Name and Abundance	Description
30% Quartz	Quartz occurs as very fine- to medium-grained anhedral crystals. The crystals commonly exhibit undulatory extinction and sub-grain boundaries.
35% Plagioclase	Plagioclase occurs as sub- to euhedral medium- to fine-grained crystals. Intense fine-grained sericite alteration. Carls bad twinning in combination with simple twins, some deformation twins seen. Mild sericite alteration of phenocrysts. Sericite alteration outlines zonations in medium-grained phenocryst.
25% Potassium Feldspar	K-feldspar occur as fine-grained anhedral crystals in interstitial to quartz and plagioclase in the groundmass. Crystals exhibit some tartan twinning.
15% Chlorite	Chlorite occurs as fine-grained laths and alteration product of amphiboles. No primary amphiboles left form chlorite.
5% Opaques	Occurs along veins and intermixed with hematite.

Sample: 17KAM082A **Lithology:** Monzogranite **QAP Classification:** Monzogranite

Mineral Name and Abundance	Description
30% Quartz	Quartz occur as fine- to medium-grained interstitial material and phenocrysts. The phenocrysts are cross-cut by quartz veins.
35% Plagioclase	Plagioclase occurs as sub-to euhedral medium- to fine-grained crystals. Intense fine-grained sericite alteration. Carls bad twinning in combination with simple twins. Mild sericite alteration of phenocrysts.
25% Potassium Feldspar	K-feldspar occurs as fine-grained anhedral crystal interstitial to quartz and plagioclase in the groundmass. Perthitic exsolution textures seen coarser crystals.
5% Chlorite	Chlorite occurs as fine-grained laths and alteration product of amphiboles. No primary amphiboles left form chlorite.
1% Titanite	Titanite occurs as fine-grained euhedral crystals and crystal clusters. Clusters of titanite are associated with clusters of opaque minerals, as well inclusions.
Trace Opaques	Disseminated very fine- to fine-grained pyrite with minor chalcopyrite.
4% Calcite	Calcite occurs as fine-grained anhedral crystals, occurs as secondary alteration along fractures.

Sample: 17KAM085A **Lithology:** Hematite Altered Granodiorite

Mineral Name and Abundance	Description

25% Quartz	Quartz occurs as anhedral medium- to fine-grained phenocrysts. The phenocrysts are surrounded by 1 mm graphic exsolution textures.
60% Plagioclase	Plagioclase occurs as sub- to euhedral medium- to fine-grained crystals. Intense fine-grained sericite alteration. Carls bad twinning in combination with simple twins. Mild sericite alteration of phenocrysts. Moderate hematite overprinting alteration.
5% Amphibole	Hornblende occurs as fine-grained crystals are found in clusters occurs around feldspars and quartz phenocrysts. Simple twinning is rare. Intense chlorite alteration and replacement of sulphides.
5% Chlorite	Chlorite occurs as fine-grained laths and alteration product of amphiboles occurs as with sulphides.
5% Opaques	Disseminated very fine- to fine-grained pyrite with minor chalcopyrite.

Sample: 17KAM089A **Lithology:** Monzogranite **QAP Classification:** Monzogranite

Mineral Name and Abundance	Description
20% Quartz	Quartz crystals are anhedral and range from fine- to medium-grained. The crystals commonly exhibit undulatory extinction and sub-grain boundaries. Phenocrysts can range up to coarse-grained.
35% Plagioclase	Plagioclase occurs as sub- to euhedral medium- to fine-grained crystals. Intense fine-grained sericite alteration. Carls bad twinning in combination with simple twins. Intense sericite alteration of phenocrysts. Moderate hematite overprinting alteration.
30% Potassium Feldspar	K-feldspar occur as fine- to medium-grained anhedral crystals in interstitial to quartz and plagioclase in the groundmass. Crystals have tartan twinning in coarser crystals and perthitic twinning. Medium-grained crystals have minimal perthitic lamellae.
Trace Biotite	Biotite is fine-grained, completed alteration by chlorite.
10% Chlorite	Chlorite occurs as fine-grained laths, alteration product of biotite.
1% Opaques	Occurs around fractures.

Sample: 17KAM092B **Lithology:** Hematite Altered Granodiorite

Mineral Name and Abundance	Description
50% Plagioclase	Plagioclase occurs as very fine-to fine-grained subhedral crystals have mild fine-grained sericite alteration. Crystals and primary textures over printed by intense very fine-grained hematite alteration. Extremely difficult to differentiate between plagioclase and k-feldspar because of over printing hematite alteration.
20% Amphibole	Hornblende occurs as fine-grained crystals are found in clusters occurs around feldspars phenocrysts. Simple twinning is rare in crystals.
20% Biotite	Biotite occurs as subhedral fine-grained crystals in clusters with amphibole crystal.
1% Epidote	Epidote occurs as fine-grained anhedral crystals around feldspars.
Trace Opaques	Disseminated very fine- to fine-grained pyrite with minor chalcopyrite.

Sample: 17KAM095A **Lithology:** Monzogranite **QAP Classification:** Monzogranite

Mineral Name and Abundance	Description
20% Quartz	Quartz occurs as very fine-grained anhedral crystals. The crystals commonly exhibit undulatory extinction and sub-grain boundaries.
35% Plagioclase	Plagioclase occurs as fine-grained anhedral crystals. Intense fine-grained sericite alteration. Crystals and primary textures over printed by intense very fine-grained hematite alteration.

35% Potassium Feldspar	K-feldspar occurs as very fine-grained anhedral crystals. Crystals have tartan twinning in coarser crystals and perthitic twinning. K-feldspar occurs in clusters with quartz and plagioclase.
5% Chlorite	Chlorite occurs as fine- to very fine-grained occurs as stringers, alteration product of biotite or amphibole but no primary mineralogy present.
1% Opaques	Occurs as fine-grained crystals with chlorite.
5% Calcite	Calcite occurs as fine-grained anhedral crystals, occurs as secondary alteration along fractures.

APPENDIX C: Mineral Chemistry

Plagioclase Chemistry- Structural formulae based on eight oxygens

Sample	16KAA026A-6	16KAA026A-7	17KAM036B-1	17KAM036B-2
Lithology	Granodiorite	Granodiorite	Granodiorite	Granodiorite
SiO_2	63.53	65.3	62.13	63.25
Al_2O_3	17.74	18.32	22.54	18.53
FeO	n.d	n.d	0.3	n.d
CaO	n.d	n.d	4.23	n.d
Na_2O	0.38	0.48	9.21	0.93
K_2O	16.47	16.44	0.34	15.44
BaO	n.d	n.d	n.d	0.76
Total	98.11	100.55	98.75	98.91
Si	3.00	3.00	2.79	2.97
Al	0.99	0.99	1.19	1.03
Fe(ii)	0.00	0.00	0.01	0.00
Ca	0.00	0.00	0.20	0.00
Na	0.03	0.04	0.80	0.08
K	0.99	0.96	0.02	0.93
Ba	0.00	0.00	0.00	0.01
Total	5.02	5.00	5.02	5.02
An%	0.00	0.00	19.86	0.00
Ab%	3.39	4.25	78.24	8.39
Or%	96.61	95.75	1.90	91.61

n.d = not detected n.m= not measured

Plagioclase Chemistry- Structural formulae based on eight oxygens

Sample	16KAA020A-3	16KAA020A-8	16KAA020A-13	16KAA020A-14
Lithology	Monzogranite	Monzogranite	Monzogranite	Monzogranite
SiO_2	62.84	63.07	63.21	63.26
Al_2O_3	18.72	18.95	22.99	22.92
CaO	n.d	n.d	1.88	4.03
Na_2O	0.25	1.72	9.44	9.49
K_2O	17.09	15.12	1.12	n.d
BaO	1.02	0.8	n.d	n.d
Total	99.91	99.66	98.63	99.69
Si	2.95	2.95	2.83	2.80
Al	1.04	1.04	1.21	1.20
Ca	0.00	0.00	0.09	0.19
Na	0.02	0.16	0.82	0.82
K	1.02	0.90	0.06	0.00
Ba	0.02	0.01	0.00	0.00
Total	5.05	5.06	5.01	5.01
An%	0.00	0.00	9.26	19.01
Ab%	2.17	14.74	84.17	80.99
Or%	97.83	85.26	6.57	0.00

n.d = not detected n.m= not measured

Plagioclase Chemistry- Structural formulae based on eight oxygens

Sample	16KAA020A-15	17KAM042A-1	17KAM042A-2	17KAM042A-3
Lithology	Monzogranite	Granodiorite	Granodiorite	Granodiorite
SiO_2	62.65	62.83	63	63.66
Al_2O_3	22.43	18.09	18.34	18.33
CaO	3.96	n.d	n.d	n.d
Na_2O	9.41	0	0.45	1.95
K_2O	0.26	16.92	15.94	14.15
BaO	n.d	0.51	1.3	1.09
Total	98.7	98.35	99.03	99.18
Si	2.81	2.98	2.97	2.98
Al	1.18	1.01	1.02	1.01
Ca	0.19	0.00	0.00	0.00
Na	0.82	0.00	0.04	0.18
K	0.01	1.02	0.96	0.84
Ba	0.00	0.01	0.02	0.02
Total	5.02	5.03	5.02	5.03
An%	18.59	0.00	0.00	0.00
Ab%	79.95	0.00	4.11	17.32
Or%	1.45	100.00	95.89	82.68

n.d = not detected n.m= not measured

Plagioclase Chemistry- Structural formulae based on eight oxygens

Sample	17KAM042A-4	17KAM042A-5	17KAM042A-6	17KAM042A-7
Lithology	Granodiorite	Granodiorite	Granodiorite	Granodiorite
SiO_2	64.08	61.84	63.09	64.75
Al_2O_3	18.6	18.7	22.79	18.2
CaO	n.d	n.d	4.44	n.d
Na_2O	2.53	0.9	9.34	0.33
K_2O	13.26	14.84	0.31	16.94
BaO	1.53	2.98	n.d	n.d
Total	100	99.26	99.98	100.22
Si	2.97	2.94	2.80	3.00
Al	1.02	1.05	1.19	0.99
Ca	0.00	0.00	0.21	0.00
Na	0.23	0.08	0.80	0.03
K	0.78	0.90	0.02	1.00
Ba	0.03	0.06	0.00	0.00
Total	5.03	5.03	5.02	5.02
An%	0.00	0.00	20.45	0.00
Ab%	22.48	8.44	77.85	2.88
Or%	77.52	91.56	1.70	97.12

n.d = not detected n.m= not measured

Plagioclase Chemistry- Structural formulae based on eight oxygens

Sample	17KAM042A-8	17KAM042A-9	17KAM042A-10	17KAM042A-11	17KAM042A-12
Lithology	Granodiorite	Granodiorite	Granodiorite	Granodiorite	Granodiorite
SiO_2	64.86	64.48	64.51	64.3	64.08
Al_2O_3	18.73	18.51	18.42	18.2	18.27
Na_2O	2.66	0.38	0.38	0.3	1.16
K_2O	12.86	16.61	16.35	16.77	14.79
BaO	0.76	0.61	0.8	0.73	1.85
Total	99.85	100.58	100.46	100.31	100.15
Si	2.98	2.98	2.99	2.99	2.98
Al	1.02	1.01	1.01	1.00	1.00
Na	0.24	0.03	0.03	0.03	0.10
K	0.75	0.98	0.97	0.99	0.88
Ba	0.01	0.01	0.01	0.01	0.03
Total	5.00	5.02	5.01	5.02	5.01
An%	0.00	0.00	0.00	0.00	0.00
Ab%	23.92	3.36	3.41	2.65	10.65
Or%	76.08	96.64	96.59	97.35	89.35

n.d = not detected n.m= not measured

Amphibole Chemistry- Structural formulae based on 23 oxygens

Sample number	17KAM036b-1	17KAM036b-2	17KAM036b-3	17KAM036b-4
Lithology	Granodiorite	Granodiorite	Granodiorite	Granodiorite
SiO_2	49.52	50.16	50.53	50.8
TiO_2	1.22	1.16	0.71	0.79
Al_2O_3	5.1	4.97	4.09	4.06
FeO	11.32	11.69	11.6	11.62
MnO	0.3	0.3	0.29	0.27
MgO	16.52	17.03	16.65	16.67
CaO	11.71	11.81	12.23	12.26
Na_2O	1.36	1.47	0.96	0.98
K_2O	0.62	0.54	0.47	0.46
Total	97.66	99.12	97.53	97.91
Si	7.090	7.064	7.246	7.259
Al iv	0.861	0.825	0.691	0.684
Al vi	0.000	0.000	0.000	0.000
Ti	0.131	0.123	0.077	0.085
Fe3+	0.613	0.739	0.552	0.519
Fe2+	0.743	0.638	0.839	0.870
Mn	0.036	0.036	0.035	0.033
Mg	3.526	3.575	3.559	3.551
Ca	1.796	1.782	1.879	1.877
Na	0.378	0.401	0.267	0.272
K	0.113	0.097	0.086	0.084
F	n.m	n.m	n.m	n.m
Cl	n.m	n.m	n.m	n.m
OH*	2.000	2.000	2.000	2.000
Total	17.287	17.280	17.232	17.232

Hydrous components and Fe3+ and Fe2+ are estimated.
n.d = not detected n.m= not measured

Amphibole Chemistry- Structural formulae based on 23 oxygens

Sample number	16KAA026a-1	16KAA026a-2	16KAA026a-3	16KAA020a-1
Lithology	Granodiorite	Granodiorite	Granodiorite	Monzogranite
SiO_2	49.25	48.02	47.89	49.27
TiO_2	0.50	0.68	0.78	0.63
Al_2O_3	4.62	5.38	5.49	4.62
FeO	13.12	13.69	13.43	12.22
MnO	0.53	0.49	0.46	0.36
MgO	15.47	15.03	14.76	16.02
CaO	11.86	11.64	11.58	12.32
Na_2O	1.19	1.41	1.35	0.89
K2O	0.57	0.56	0.56	0.45
Total	97.11	96.89	96.29	96.78
Si	7.149	7.003	7.029	7.149
Al iv	0.790	0.925	0.950	0.790
Al vi	0.000	0.000	0.000	0.000
Ti	0.055	0.075	0.086	0.069
Fe3+	0.672	0.780	0.689	0.610
Fe2+	0.921	0.890	0.959	0.872
Mn	0.065	0.061	0.057	0.044
Mg	3.348	3.268	3.230	3.465
Ca	1.845	1.819	1.821	1.915
Na	0.335	0.399	0.384	0.250
K	0.106	0.104	0.105	0.083
F	n.m	n.m	n.m	n.m
Cl	n.m	n.m	n.m	n.m
OH*	2.000	2.000	2.000	2.000
Total	17.285	17.322	17.310	17.249

Hydrous components and Fe3+ and Fe2+ are estimated.
n.d = not detected n.m= not measured

Amphibole Chemistry- Structural formulae based on 23 oxygens

Sample number	16KAA020a-3	16KAA020a-4	16KAA020a-7
Lithology	Monzogranite	Monzogranite	Monzogranite
SiO_2	48.89	48.51	51.7
TiO_2	1.21	1.04	0.89
Al_2O_3	5.09	5.02	4.21
FeO	12.5	12.55	12.06
MnO	n.d	n.d	n.d
MgO	16.21	15.79	17.06
CaO	11.86	12.02	12.53
Na_2O	1.41	1.13	1
K_2O	0.49	0.54	0.38
Total	97.65	96.61	99.83
Si	7.029	7.066	7.239
Al iv	0.863	0.862	0.695
Al vi	0.000	0.000	0.000
Ti	0.131	0.114	0.094
Fe3+	0.680	0.606	0.542
Fe2+	0.823	0.923	0.870
Mg	3.474	3.429	3.561
Ca	1.827	1.876	1.880
Na	0.393	0.319	0.271
K	0.090	0.100	0.068
F	n.m	n.m	n.m
Cl	n.m	n.m	n.m
OH*	2.000	2.000	2.000
Total	17.310	17.295	17.219

Hydrous components and Fe3+ and Fe2+ are estimated.
n.d = not detected n.m= not measured

Pyroxene Chemistry- Structural formulae based on 6 oxygen

Sample number	17KAM036B-1	17KAM036B-2	17KAM036B-3	17KAM036B-4
Lithology	Granodiorite	Granodiorite	Granodiorite	Granodiorite
SiO_2	51.76	51.53	52.41	52.45
Al_2O_3	1.11	2.1	1.21	1.26
FeO	7.3	7.86	7.25	7.33
MnO	0.41	0.25	0.34	0.36
MgO	14.93	15.19	14.38	14.31
CaO	22.53	20.72	22.9	22.93
Na_2O	0.7	0.75	0.74	0.7
Total	98.74	98.38	99.23	99.36
Si	1.95	1.94	1.97	1.97
Al	0.05	0.06	0.03	0.03
Al	0.00	0.04	0.02	0.02
Fe(iii)	0.14	0.11	0.10	0.10
Cr	0.00	0.00	0.00	0.00
Ti	0.00	0.00	0.00	0.00
Fe(ii)	0.09	0.13	0.12	0.13
Mn	0.01	0.01	0.01	0.01
Mg	0.84	0.85	0.80	0.80
Ca	0.91	0.84	0.92	0.92
Na	0.05	0.05	0.05	0.05
K	0.00	0.00	0.00	0.00
TOTAL	4.05	4.04	4.03	4.03
Wo	45.74	43.05	46.94	46.98
En	42.18	43.92	41.01	40.80
Fs	12.09	13.04	12.05	12.21

Fe3+ and Fe2+ are estimated.
n.d = not detected n.m= not measured

APPENDIX F: Trench Maps

Trench # 1

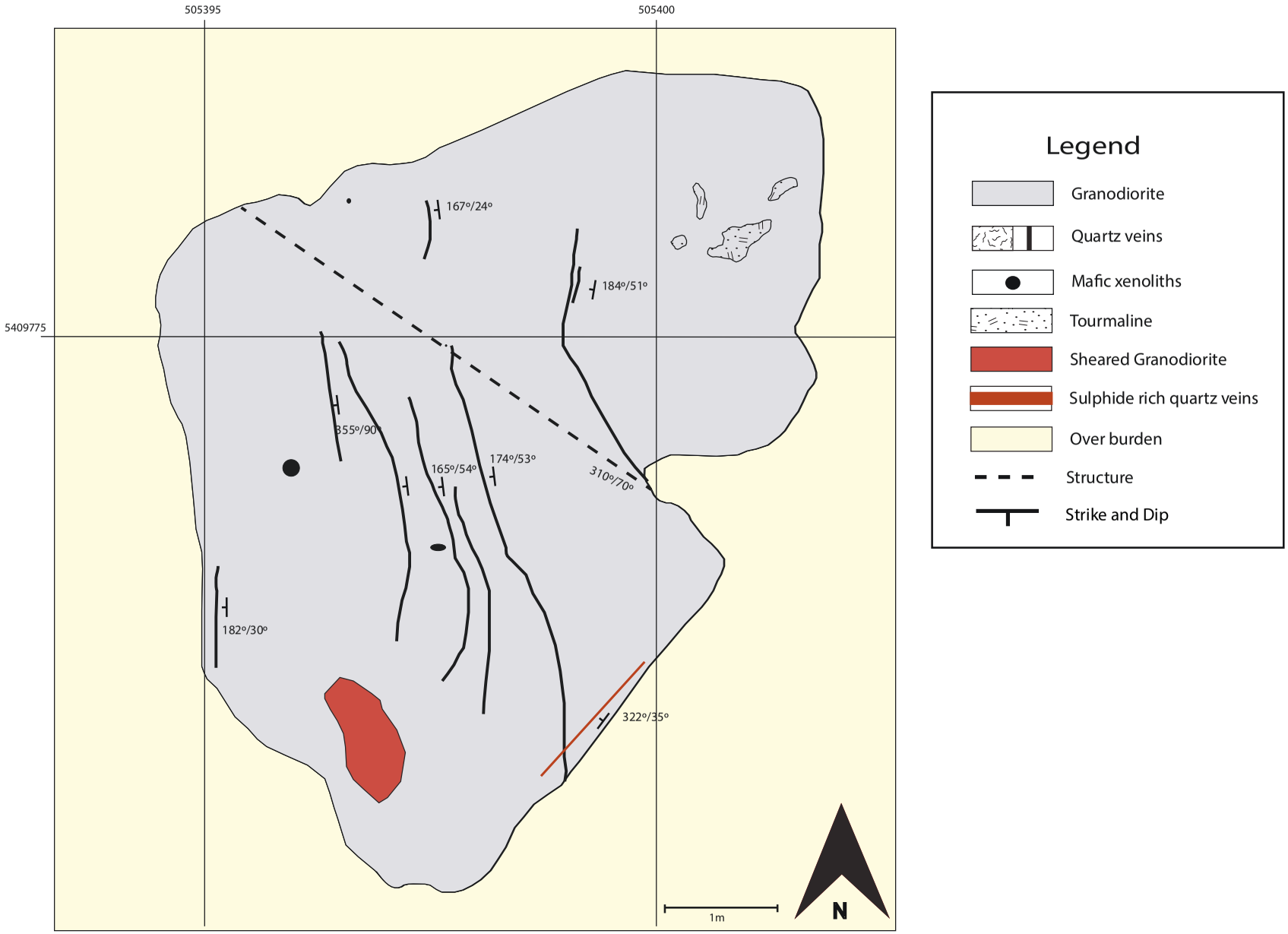
505395
505400
5409775
167°/24°
184°/51°
355°/90°
165°/54°
174°/53°
310°/70°
182°/30°
322°/35°
1m
N
Legend
Granodiorite
Quartz veins
Mafic xenoliths
Tourmaline
Sheared Granodiorite
Sulphide rich quartz veins
Over burden
Structure
Strike and Dip

Trench #2

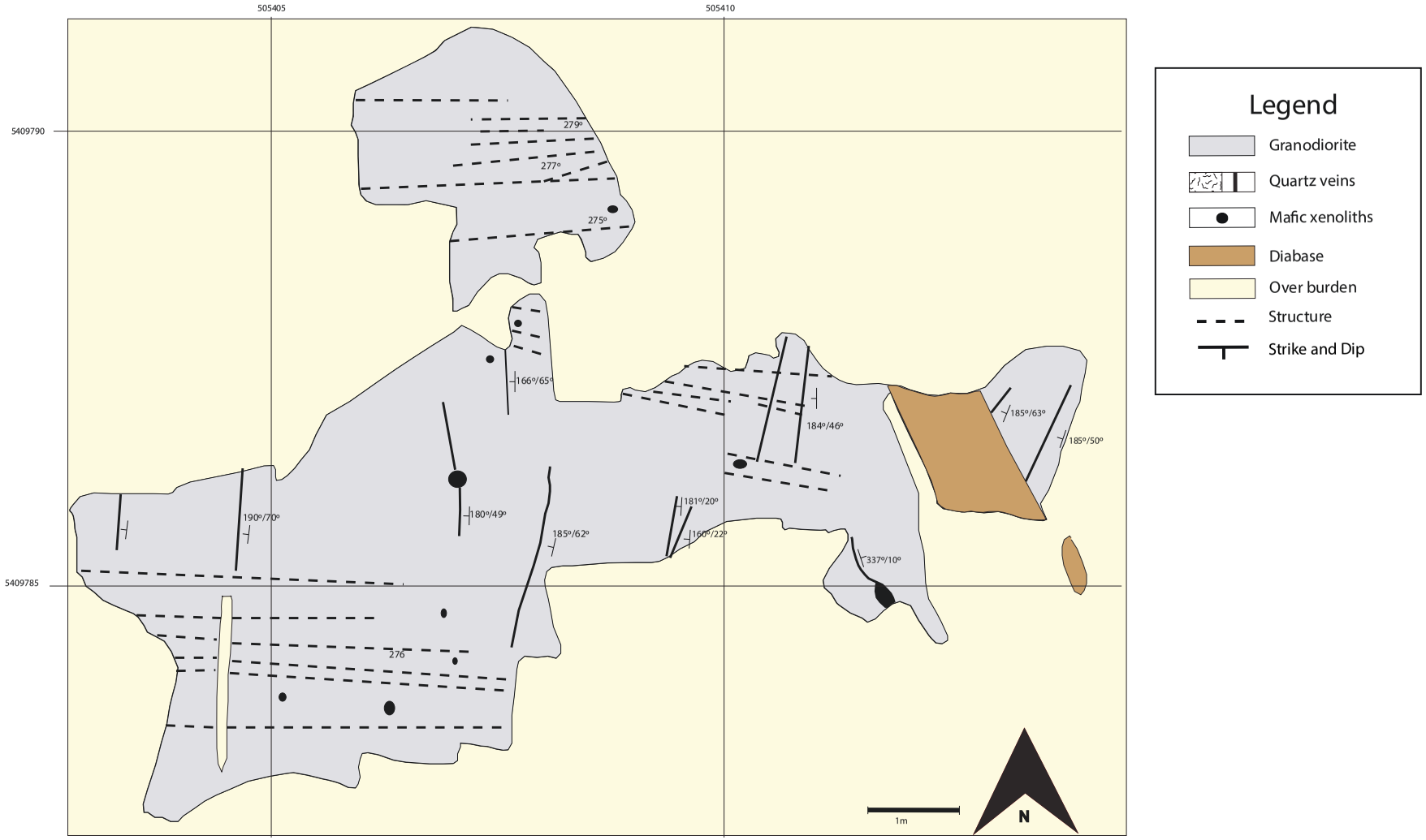
505405
505410
5409790
5409785
279°
277°
275°
166°/65°
184°/46°
185°/63°
185°/50°
190°/70°
180°/49°
185°/62°
181°/20°
160°/22°
337°/10°
276
1m
N
Legend
Granodiorite
Quartz veins
Mafic xenoliths
Diabase
Over burden
Structure
Strike and Dip

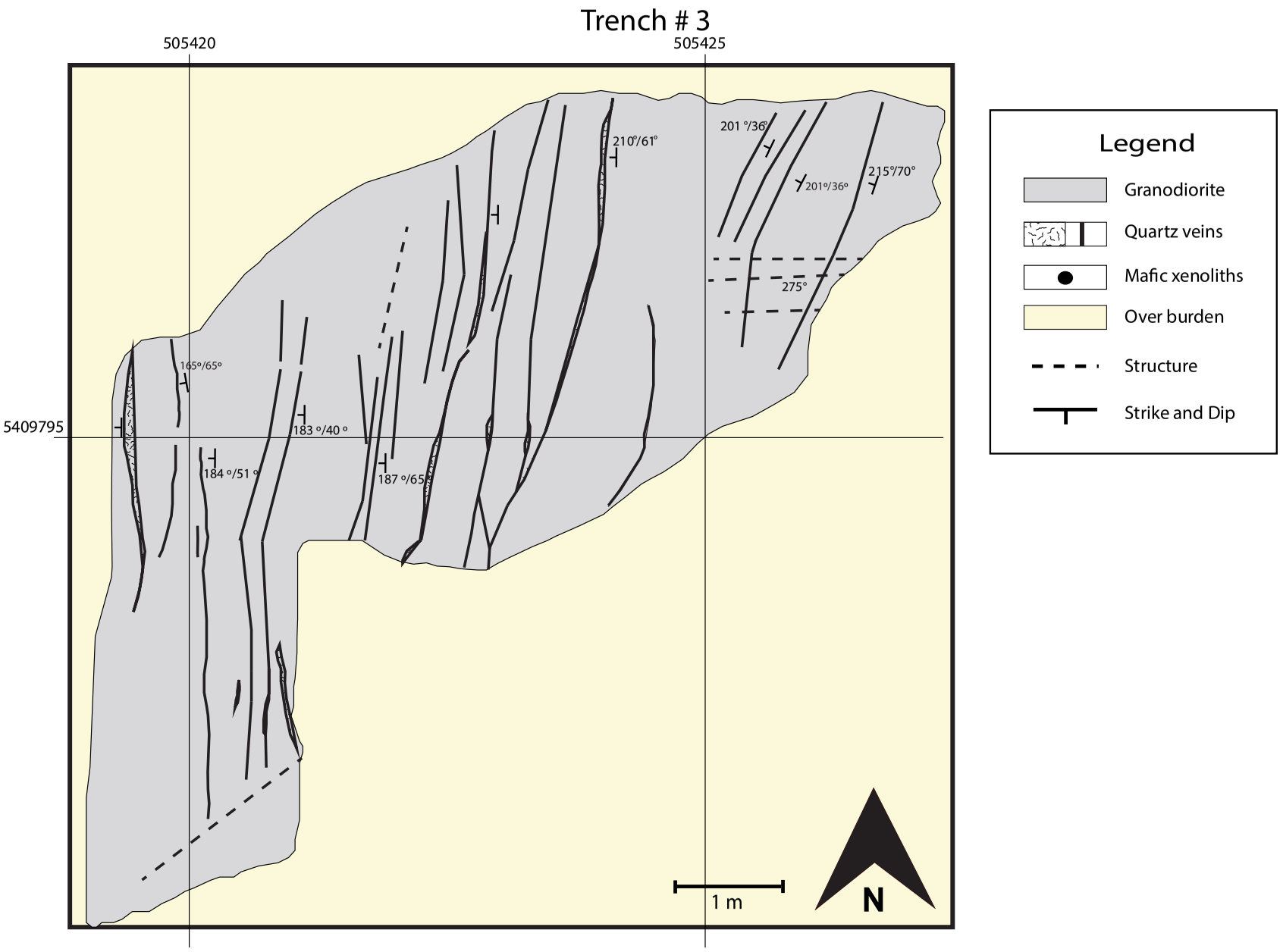
Trench # 3
505420
505425
5409795
210°/61°
201 °/36°
201°/36°
215°/70°
275°
165°/65°
183 °/40 °
184 °/51 °
187 °/65°
1 m
N
Legend
Granodiorite
Quartz veins
Mafic xenoliths
Over burden
Structure
Strike and Dip

Trench #7

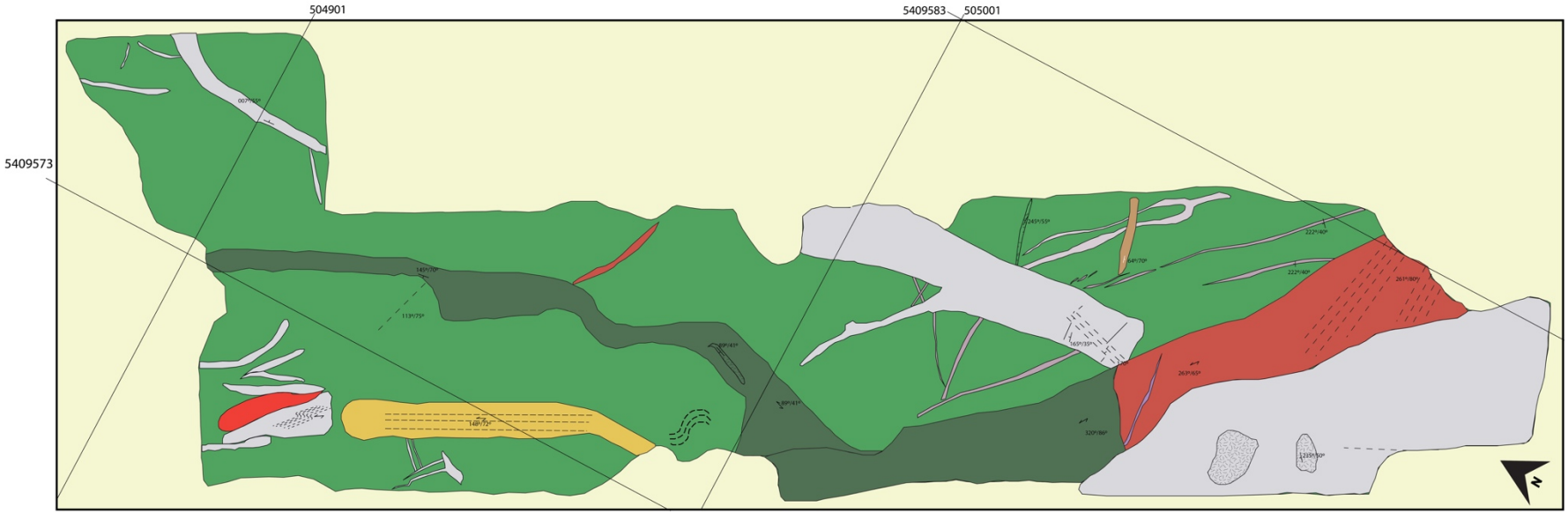

Legend

- Granodiorite
- Quartz veins
- Sheared granodiorite
- Mafic Volcanic
- Sheared mafic volcanics
- Sulphide rich mafic volcanics
- Diabase
- Pegmatitic veins
- Mafic xenoliths
- Overburden
- Structure
- Strike and Dip
- Foliation

APPENDIX E: Whole-rock geochemical data

Method		Units	Detect Limit	16KAA001 A	16KAA004 A	16KAA006 A	16KAA006 B	16KAA008 C	16KAA009 A
SG				2.67	2.66	2.66	2.79	2.71	2.68
SG DWT		g		1295.4	637.1	671.6	118.6	982.7	1724.2
SG WWT		g		810.7	398	419.4	76.1	620.5	1079.9
FEO-ION	FeO	wt%	0.06	1.18	0.98	1.35	4.98	7.99	1.16
IRC-100	CO_2	wt%	0.023	0.183	1.01	1.235	0.54	0.042	0.027
IRC-101	S	wt%	0.003	0.004	0.003	0.013	0.016	0.019	0.046
IMP-101	Au	ppb	1.6	<1.6	<1.6	<1.6	<1.6	5	<1.6
IMP-101	Pd	ppb	1.3	<1.3	<1.3	<1.3	<1.3	17.3	<1.3
IMP-101	Pt	ppb	0.4	<0.4	<0.4	<0.4	0.9	5.9	<0.4
XRF-M01	Al_2O_3	wt%	0.02	15.74	15.82	15.35	15.56	15.54	17.28
XRF-M01	BaO	wt%	0.004	0.1	0.07	0.1	0.05	0.02	0.11
XRF-M01	CaO	wt%	0.006	2.09	2.564	2.952	6.301	6.169	3.042
XRF-M01	Cr_2O_3	wt%	0.002	0.01	<0.002	0.01	0.03	0.02	0.01
XRF-M01	Fe_2O_3	wt%	0.01	2.71	2.13	2.46	8.9	13.11	2.55
XRF-M01	K_2O	wt%	0.01	2.74	2.24	2.53	1.6	0.62	2.87
XRF-M01	LOI	wt%	0.05	1.41	2.24	2.32	1.93	5.96	1.14
XRF-M01	MgO	wt%	0.01	1.55	1.16	1.2	6.39	7.31	1.28
XRF-M01	MnO	wt%	0.002	0.047	0.041	0.039	0.191	0.237	0.035
XRF-M01	Na_2O	wt%	0.02	5.06	5.28	5.25	4.48	2.49	4.81
XRF-M01	P_2O_5	wt%	0.002	0.149	0.106	0.132	0.501	0.165	0.126
XRF-M01	SiO_2	wt%	0.04	67.69	67.73	66.74	53.79	45.98	66.4
XRF-M01	TiO_2	wt%	0.01	0.31	0.24	0.28	0.68	1.51	0.27
	Total	wt%		99.6	99.63	99.36	100.41	99.15	99.92
XRF-T02	As	ppm	6	<6	<6	<6	<6	<6	<6
XRF-T02	Br	ppm	1.2	2	2	2	<1.2	<1.2	16
XRF-T02	Cu	ppm	9	<9	<9	<9	18	234	<9
XRF-T02	Ga	ppm	1.3	20	20	19	26	20	20
XRF-T02	Mo	ppm	0.8	1	1	1	1	<0.8	1
XRF-T02	Nb	ppm	0.7	4	3	6	7	5	3
XRF-T02	Ni	ppm	1.6	18	16	21	131	98	21
XRF-T02	Pb	ppm	1.7	6	9	11	9	3	10
XRF-T02	Rb	ppm	0.8	78	54	57	73	13	59
XRF-T02	Sr	ppm	0.8	713	584	613	525	359	758
XRF-T02	Th	ppm	1.5	4	3	3	6	<1.5	3
XRF-T02	U	ppm	1.6	<1.6	<1.6	<1.6	2	<1.6	<1.6
XRF-T02	Y	ppm	0.7	10	9	11	20	30	9
XRF-T02	Zn	ppm	1	49	44	52	201	94	33
XRF-T02	Zr	ppm	1.8	122	101	119	165	124	110
IMC-100	Ba	ppm	0.8	880.3	802.3	833.1	874.7	956	172.4
IMC-100	Be	ppm	0.04	1.58	1.45	1.72	1.6	1.74	0.7

Method		Units	Detect Limit	16KAA001 A	16KAA004 A	16KAA006 A	16KAA006 B	16KAA008 C	16KAA009 A
IMC-100	Bi	ppm	0.47	<0.47	<0.47	<0.47	<0.47	<0.47	<0.47
IMC-100	Cd	ppm	0.013	0.025	0.026	<0.013	0.032	0.067	0.118
IMC-100	Ce	ppm	0.12	67.09	49.9	51.17	54.77	64.66	32.72
IMC-100	Co	ppm	0.13	7.16	5.52	6.38	7.92	6.92	44.62
IMC-100	Cr	ppm	3	61	33	42	68	48	104
IMC-100	Cs	ppm	0.013	1.46	0.479	0.656	1.001	0.814	0.649
IMC-100	Cu	ppm	1.4	4.5	2	1.9	3	2.8	232.7
IMC-100	Dy	ppm	0.009	2.09	1.731	1.681	2.173	2.264	5.609
IMC-100	Er	ppm	0.007	1.057	0.895	0.897	1.13	1.186	3.401
IMC-100	Eu	ppm	0.0031	1.2985	0.9556	0.8965	1.0904	1.2446	1.5356
IMC-100	Ga	ppm	0.04	20.76	20.49	21.18	21.05	20.38	19.36
IMC-100	Gd	ppm	0.009	3.502	2.663	2.444	3.185	3.334	5.366
IMC-100	Hf	ppm	0.14	3.64	3.09	3.39	3.34	3.37	3.41
IMC-100	Ho	ppm	0.0025	0.373	0.3222	0.3132	0.3987	0.4185	1.1452
IMC-100	In	ppm	0.0018	0.0191	0.018	0.0208	0.0301	0.0211	0.0882
IMC-100	La	ppm	0.1	30.82	23.72	23.4	24.62	30.03	16.43
IMC-100	Li	ppm	0.4	17.1	12.3	13.7	14.6	12.6	24.6
IMC-100	Lu	ppm	0.002	0.1466	0.1254	0.1347	0.1607	0.1628	0.4449
IMC-100	Mo	ppm	0.08	2.57	0.9	1.02	1.76	1.09	0.69
IMC-100	Nb	ppm	0.028	5.056	3.665	4.409	4.35	6.385	6.354
IMC-100	Nd	ppm	0.06	31.58	23.1	22	25.9	28.27	17.8
IMC-100	Ni	ppm	0.7	18.4	15.2	17.5	22.4	22.1	92
IMC-100	Pb	ppm	0.18	6.8	6.4	8.3	10.8	11.4	4.4
IMC-100	Pr	ppm	0.014	8.286	6.064	5.832	6.749	7.593	4.063
IMC-100	Rb	ppm	0.11	77.94	65.3	63.37	61.86	58.69	11.39
IMC-100	Sb	ppm	0.04	0.04	0.05	0.09	0.06	0.08	0.11
IMC-100	Sc	ppm	1.1	5	4.3	4.5	6.3	5.4	37.9
IMC-100	Sm	ppm	0.026	5.038	3.927	3.629	4.478	4.948	4.546
IMC-100	Sn	ppm	0.16	0.93	0.83	0.91	1.01	0.85	1.27
IMC-100	Sr	ppm	0.6	743.5	502.5	560.5	973.6	636.2	350.8
IMC-100	Ta	ppm	0.007	0.332	0.275	0.311	0.296	0.306	0.433
IMC-100	Tb	ppm	0.0023	0.3961	0.3339	0.307	0.3803	0.4183	0.8697
IMC-100	Th	ppm	0.018	4.965	4.041	3.682	4.992	4.059	2.57
IMC-100	Ti	ppm	7	1925	1618	1717	1922	1799	9012
IMC-100	Tl	ppm	0.002	0.308	0.225	0.247	0.28	0.229	0.098
IMC-100	Tm	ppm	0.0019	0.1505	0.1301	0.1355	0.161	0.1657	0.4735
IMC-100	U	ppm	0.011	1.548	1.137	0.973	1.356	1.249	0.706
IMC-100	V	ppm	0.8	44.2	32.7	38.1	48.2	41.1	336.8
IMC-100	W	ppm	0.05	2.56	0.28	0.19	0.11	0.68	0.54
IMC-100	Y	ppm	0.05	11.18	9.34	9.1	11.83	12.16	30.64
IMC-100	Yb	ppm	0.009	0.983	0.863	0.878	1.057	1.079	2.975
IMC-100	Zn	ppm	1.8	46	43	46	58	52	85
IMC-100	Zr	ppm	6	134	112	128	127	133	122

Method		Units	Detect Limit	16KAA011A	16KAA012A	16KAA013A	16KAA016A	16KAA018A	16KAA018B
SG				2.65	2.64	2.67	2.66	2.58	2.5
SG DWT		g		570.5	763.7	1471.6	959.3	172.3	137.5
SG WWT		g		355.6	474.6	919.9	598	105.6	82.6
FEO-ION	FeO	wt%	0.06	0.92	1.09	1.37	1.33	0.86	2.03
IRC-100	CO_2	wt%	0.023	0.39	0.414	0.078	0.704	0.711	2.18
IRC-101	S	wt%	0.003	<0.003	<0.003	0.006	0.028	0.007	0.007
IMP-101	Au	ppb	1.6	<1.6	<1.6	2	<1.6	2	<1.6
IMP-101	Pd	ppb	1.3	<1.3	<1.3	<1.3	<1.3	<1.3	<1.3
IMP-101	Pt	ppb	0.4	<0.4	<0.4	0.4	<0.4	<0.4	<0.4
XRF-M01	Al_2O_3	wt%	0.02	15.62	15.78	15.54	15.85	16.09	18.05
XRF-M01	BaO	wt%	0.004	0.09	0.09	0.09	0.08	0.07	0.12
XRF-M01	CaO	wt%	0.006	1.786	1.578	2.834	2.344	1.26	2.724
XRF-M01	Cr_2O_3	wt%	0.002	<0.002	<0.002	0.01	<0.002	<0.002	<0.002
XRF-M01	Fe_2O_3	wt%	0.01	2.26	2.44	3.02	2.57	2.47	4.03
XRF-M01	K_2O	wt%	0.01	2.59	2.6	2.58	1.97	2.11	2.44
XRF-M01	LOI	wt%	0.05	1.58	1.77	1.18	1.99	2.55	7.31
XRF-M01	MgO	wt%	0.01	1.27	1.25	1.6	1.42	0.78	1.05
XRF-M01	MnO	wt%	0.002	0.038	0.038	0.053	0.043	0.038	0.063
XRF-M01	Na_2O	wt%	0.02	5.6	5.15	5.07	5.85	4.84	1.4
XRF-M01	P_2O_5	wt%	0.002	0.112	0.116	0.137	0.137	0.116	0.15
XRF-M01	SiO_2	wt%	0.04	68.34	68.61	67.29	67.05	68.89	61.61
XRF-M01	TiO_2	wt%	0.01	0.26	0.27	0.3	0.3	0.31	0.3
	Total	wt%		99.55	99.69	99.71	99.62	99.53	99.25
XRF-T02	As	ppm	6	<6	<6	<6	<6	<6	<6
XRF-T02	Br	ppm	1.2	3	<1.2	2	5	<1.2	<1.2
XRF-T02	Cu	ppm	9	<9	<9	<9	<9	<9	<9
XRF-T02	Ga	ppm	1.3	20	20	20	20	22	22
XRF-T02	Mo	ppm	0.8	1	1	1	<0.8	1	<0.8
XRF-T02	Nb	ppm	0.7	3	3	3	5	6	4
XRF-T02	Ni	ppm	1.6	16	18	22	23	17	45
XRF-T02	Pb	ppm	1.7	6	8	11	15	8	6
XRF-T02	Rb	ppm	0.8	66	61	61	49	62	49
XRF-T02	Sr	ppm	0.8	483	535	941	761	441	157
XRF-T02	Th	ppm	1.5	2	2	3	4	6	3
XRF-T02	U	ppm	1.6	<1.6	<1.6	<1.6	<1.6	<1.6	<1.6
XRF-T02	Y	ppm	0.7	9	8	10	11	11	13
XRF-T02	Zn	ppm	1	45	49	58	54	53	119
XRF-T02	Zr	ppm	1.8	111	111	114	115	136	139
IMC-100	Ba	ppm	0.8	768	977.8	>1740	73.4	783.8	390
IMC-100	Be	ppm	0.04	2.02	1.31	1.58	0.15	1.44	1

Method		Units	Detect Limit	16KAA011A	16KAA012 A	16KAA013 A	16KAA016 A	16KAA018 A	16KAA018 B
IMC-100	Bi	ppm	0.47	<0.47	<0.47	0.56	2.11	<0.47	<0.47
IMC-100	Cd	ppm	0.013	0.063	0.068	0.057	0.05	0.041	0.021
IMC-100	Ce	ppm	0.12	81.01	134.57	50.34	44.65	48.91	25.1
IMC-100	Co	ppm	0.13	7.1	19.45	9.12	5.83	5.52	2.53
IMC-100	Cr	ppm	3	46	33	34	90	97	55
IMC-100	Cs	ppm	0.013	0.614	2.16	1.903	0.21	2.463	3.709
IMC-100	Cu	ppm	1.4	14.1	<1.4	8	<1.4	3.6	5.4
IMC-100	Dy	ppm	0.009	2.203	2.774	2.203	0.428	1.759	0.936
IMC-100	Er	ppm	0.007	1.093	1.293	1.145	0.105	0.95	0.479
IMC-100	Eu	ppm	0.0031	1.3095	1.9916	1.0987	0.7558	0.9005	0.4411
IMC-100	Ga	ppm	0.04	20.06	23.08	22.26	2.33	20.53	9.87
IMC-100	Gd	ppm	0.009	3.405	5.153	3.134	1.606	2.378	1.165
IMC-100	Hf	ppm	0.14	3.42	3.65	3.44	0.31	3.52	1.34
IMC-100	Ho	ppm	0.0025	0.394	0.4771	0.3987	0.0487	0.3216	0.1671
IMC-100	In	ppm	0.0018	0.021	0.0256	0.0175	<0.0018	0.0168	0.0105
IMC-100	La	ppm	0.1	36.75	59.43	22.12	20.69	21.43	12.76
IMC-100	Li	ppm	0.4	15.5	23.7	15.2	0.7	14.4	70.8
IMC-100	Lu	ppm	0.002	0.1608	0.1968	0.1548	0.0089	0.1493	0.0674
IMC-100	Mo	ppm	0.08	0.82	0.66	41.19	34.4	2.5	2.72
IMC-100	Nb	ppm	0.028	6	4.576	6.952	0.465	4.189	1.788
IMC-100	Nd	ppm	0.06	34.12	54.75	23.16	19.97	20.94	10.15
IMC-100	Ni	ppm	0.7	23	44.6	16.1	4.6	16	9.7
IMC-100	Pb	ppm	0.18	14.8	7.6	12.7	301.3	9.4	4.7
IMC-100	Pr	ppm	0.014	9.131	15.596	5.883	5.318	5.444	2.77
IMC-100	Rb	ppm	0.11	48.24	37.24	27.79	2.46	71.57	52.61
IMC-100	Sb	ppm	0.04	0.06	0.08	0.1	0.04	0.1	1.55
IMC-100	Sc	ppm	1.1	5.3	4.7	4.2	<1.1	4.2	2.4
IMC-100	Sm	ppm	0.026	5.355	8.288	4.363	3.244	3.508	1.705
IMC-100	Sn	ppm	0.16	0.93	0.99	0.75	0.17	0.83	0.47
IMC-100	Sr	ppm	0.6	787.4	153.8	418.7	11.9	558.2	38.2
IMC-100	Ta	ppm	0.007	0.342	0.341	0.329	0.026	0.339	0.12
IMC-100	Tb	ppm	0.0023	0.4022	0.5584	0.4177	0.1359	0.3176	0.1575
IMC-100	Th	ppm	0.018	5.93	4.214	8.744	1.196	4.492	1.892
IMC-100	Ti	ppm	7	1810	1854	1532	99	1485	619
IMC-100	Tl	ppm	0.002	0.24	0.228	0.149	0.017	0.35	0.243
IMC-100	Tm	ppm	0.0019	0.1588	0.1852	0.163	0.0123	0.1456	0.0656
IMC-100	U	ppm	0.011	1.407	0.817	1.085	0.079	0.947	0.77
IMC-100	V	ppm	0.8	43.7	42.6	32.1	3.8	33.2	31
IMC-100	W	ppm	0.05	1.15	0.78	9.45	1.1	1.2	4.76
IMC-100	Y	ppm	0.05	11.53	13.09	12.32	1.29	9.3	4.79
IMC-100	Yb	ppm	0.009	1.017	1.295	1.024	0.068	0.959	0.432
IMC-100	Zn	ppm	1.8	52	113	45	3	40	15
IMC-100	Zr	ppm	6	129	134	122	11	126	48

Method		Units	Detect Limit	16KAA018C	16KAA019A	16KAA019B	16KAA019D	16KAA019E	16KAA020A
SG				2.66	2.54	2.64	2.64	2.6	2.72
SG DWT		g		358.5	228.7	168.7	152	246.5	157.7
SG WWT		g		223.8	138.8	104.8	94.4	151.6	99.7
FEO-ION	FeO	wt%	0.06	0.92	0.84		0.85	0.17	1.93
IRC-100	CO_2	wt%	0.023	0.381	0.367		0.11	0.31	0.097
IRC-101	S	wt%	0.003	<0.003	0.236		<0.003	0.009	0.004
IMP-101	Au	ppb	1.6	<1.6	90	1407	3	15	<1.6
IMP-101	Pd	ppb	1.3	<1.3	<1.3	<1.3	<1.3	<1.3	<1.3
IMP-101	Pt	ppb	0.4	<0.4	<0.4	<0.4	<0.4	<0.4	0.4
XRF-M01	Al_2O_3	wt%	0.02	17.05	16.76		15.69	6.41	15.42
XRF-M01	BaO	wt%	0.004	0.1	0.31		0.09	0.04	0.14
XRF-M01	CaO	wt%	0.006	2.16	0.544		1.607	0.424	3.747
XRF-M01	Cr_2O_3	wt%	0.002	0.01	0.01		<0.002	0.01	0.01
XRF-M01	Fe_2O_3	wt%	0.01	2.32	2.35		2.23	3.44	3.9
XRF-M01	K_2O	wt%	0.01	2.54	1.03		3	1.46	2.82
XRF-M01	LOI	wt%	0.05	1.59	1.59		1.43	2.19	1.26
XRF-M01	MgO	wt%	0.01	1.03	1.01		1.01	0.36	2.84
XRF-M01	MnO	wt%	0.002	0.033	0.037		0.035	0.009	0.065
XRF-M01	Na_2O	wt%	0.02	4.88	7.59		4.72	0.12	4.64
XRF-M01	P_2O_5	wt%	0.002	0.121	0.148		0.108	0.049	0.241
XRF-M01	SiO_2	wt%	0.04	68.55	67.67		69.47	84.89	64.11
XRF-M01	TiO_2	wt%	0.01	0.26	0.23		0.24	0.1	0.38
	Total	wt%		100.63	99.28		99.61	99.5	99.58
XRF-T02	As	ppm	6	<6	<6	<6	<6	<6	<6
XRF-T02	Br	ppm	1.2	2	<1.2	<1.2	2	<1.2	<1.2
XRF-T02	Cu	ppm	9	<9	<9	<9	<9	<9	<9
XRF-T02	Ga	ppm	1.3	20	20	2	20	9	18
XRF-T02	Mo	ppm	0.8	1	37	29	1	1	1
XRF-T02	Nb	ppm	0.7	3	6	<0.7	3	1	3
XRF-T02	Ni	ppm	1.6	16	15	4	16	10	47
XRF-T02	Pb	ppm	1.7	9	11	290	9	3	13
XRF-T02	Rb	ppm	0.8	59	27	3	73	51	61
XRF-T02	Sr	ppm	0.8	639	397	12	547	37	1018
XRF-T02	Th	ppm	1.5	3	6	<1.5	3	<1.5	4
XRF-T02	U	ppm	1.6	<1.6	<1.6	<1.6	<1.6	<1.6	<1.6
XRF-T02	Y	ppm	0.7	9	12	1	8	4	12
XRF-T02	Zn	ppm	1	50	45	1	42	14	63
XRF-T02	Zr	ppm	1.8	113	114	11	106	46	139

Method		Units	Detect Limit	16KAA018C	16KAA019A	16KAA019B	16KAA019D	16KAA019E	16KAA020A
IMC-100	Ba	ppm	0.8	1254.8	647.2	972.1	590.9	444.1	891.4
IMC-100	Be	ppm	0.04	1.73	1.57	1.64	1.64	3.16	1.47
IMC-100	Bi	ppm	0.47	<0.47	<0.47	<0.47	<0.47	<0.47	<0.47
IMC-100	Cd	ppm	0.013	0.064	0.037	0.045	0.058	0.14	0.027
IMC-100	Ce	ppm	0.12	81.7	48.52	55.91	41.37	108.57	48.29
IMC-100	Co	ppm	0.13	13.22	5.5	7.27	5.75	29.34	5.52
IMC-100	Cr	ppm	3	109	38	55	42	224	48
IMC-100	Cs	ppm	0.013	0.678	0.586	0.828	2.532	4.77	2.02
IMC-100	Cu	ppm	1.4	6.8	1.5	3.1	3.8	19.2	2.1
IMC-100	Dy	ppm	0.009	2.54	1.812	1.899	2.014	3.643	1.648
IMC-100	Er	ppm	0.007	1.186	0.971	0.973	1.183	1.997	0.849
IMC-100	Eu	ppm	0.0031	1.6904	0.9734	1.0735	0.8679	1.6531	0.9428
IMC-100	Ga	ppm	0.04	19.25	20.61	20.99	21.66	27.39	21.59
IMC-100	Gd	ppm	0.009	4.415	2.628	2.941	2.527	5.392	2.524
IMC-100	Hf	ppm	0.14	4.2	3.36	3.43	4.07	4.69	3.25
IMC-100	Ho	ppm	0.0025	0.4503	0.3388	0.3449	0.3968	0.7097	0.3137
IMC-100	In	ppm	0.0018	0.0316	0.0174	0.0212	0.0197	0.1422	0.0171
IMC-100	La	ppm	0.1	37.28	21.97	26.38	20.26	52.63	23.12
IMC-100	Li	ppm	0.4	12	14.9	8.9	23.5	55.2	15
IMC-100	Lu	ppm	0.002	0.1595	0.1516	0.1473	0.1757	0.3306	0.1321
IMC-100	Mo	ppm	0.08	1.75	0.96	1.34	1.15	0.84	1.54
IMC-100	Nb	ppm	0.028	4.065	4.122	4.119	6.073	7.27	3.759
IMC-100	Nd	ppm	0.06	40.9	22.37	24.86	19.76	48.67	22.15
IMC-100	Ni	ppm	0.7	49.3	15.6	22.3	15.7	133.3	15.5
IMC-100	Pb	ppm	0.18	12.6	10.3	11.4	8.6	8.7	9.2
IMC-100	Pr	ppm	0.014	10.128	5.805	6.672	5.181	12.654	5.786
IMC-100	Rb	ppm	0.11	61.57	54.5	59.73	61.61	75.87	58.56
IMC-100	Sb	ppm	0.04	0.07	0.07	<0.04	0.1	0.1	0.11
IMC-100	Sc	ppm	1.1	8.8	4.4	5.3	5.1	25.5	4
IMC-100	Sm	ppm	0.026	7.002	3.71	4.214	3.373	7.749	3.683
IMC-100	Sn	ppm	0.16	0.98	0.84	0.89	1.02	2.36	0.83
IMC-100	Sr	ppm	0.6	1037.3	594.1	774.1	440.2	547.9	651.9
IMC-100	Ta	ppm	0.007	0.286	0.304	0.305	0.434	0.345	0.281
IMC-100	Tb	ppm	0.0023	0.5108	0.3296	0.3642	0.355	0.6444	0.3068
IMC-100	Th	ppm	0.018	5.456	4.356	5.032	6.957	6.717	3.628
IMC-100	Ti	ppm	7	2332	1503	1691	1863	4244	1524
IMC-100	Tl	ppm	0.002	0.285	0.194	0.329	0.302	0.418	0.262
IMC-100	Tm	ppm	0.0019	0.1632	0.1356	0.1407	0.1777	0.2987	0.1268

Method		Units	Detect Limit	16KAA018C	16KAA019A	16KAA019B	16KAA019D	16KAA019E	16KAA020A
IMC-100	U	ppm	0.011	0.88	1.259	1.268	1.242	1.439	0.939
IMC-100	V	ppm	0.8	66.8	33.3	39.9	36.8	145.3	33.4
IMC-100	W	ppm	0.05	0.19	0.87	0.1	3.26	0.66	0.19
IMC-100	Y	ppm	0.05	12.95	10.09	10.37	11.5	21.46	9.08
IMC-100	Yb	ppm	0.009	1.036	0.971	0.976	1.194	1.995	0.868
IMC-100	Zn	ppm	1.8	61	44	35	52	194	47
IMC-100	Zr	ppm	6	170	124	125	142	177	124
Method		Units	Detect Limit	16KAA020A	16KAA020B	16KAA020C	16KAA022A	16KAA024A	16KAA025A
SG				2.67	2.74	2.61	2.64	2.64	2.64
SG DWT		g		113.5	254.8	172.2	394.4	133.3	108.5
SG WWT		g		71	161.9	106.1	245.2	82.8	67.4
FEO-ION	FeO	wt%	0.06	1.15	2.9	0.21	1.24	1.19	1
IRC-100	CO_2	wt%	0.023	0.289	1.494	0.168	0.512	0.285	0.371
IRC-101	S	wt%	0.003	0.003	0.003	<0.003	0.003	<0.003	<0.003
IMP-101	Au	ppb	1.6	<1.6	2	<1.6	<1.6	<1.6	<1.6
IMP-101	Pd	ppb	1.3	<1.3	<1.3	<1.3	<1.3	<1.3	<1.3
IMP-101	Pt	ppb	0.4	<0.4	0.8	<0.4	<0.4	<0.4	<0.4
XRF-M01	Al_2O_3	wt%	0.02	15.87	15.52	13.49	15.58	15.79	15.78
XRF-M01	BaO	wt%	0.004	0.1	0.12	0.02	0.09	0.09	0.09
XRF-M01	CaO	wt%	0.006	2.362	4.993	0.656	2.266	2.55	2.303
XRF-M01	Cr_2O_3	wt%	0.002	0.01	0.02	<0.002	<0.002	0.01	0.01
XRF-M01	Fe_2O_3	wt%	0.01	2.86	5.75	0.59	2.35	2.46	2.28
XRF-M01	K_2O	wt%	0.01	2.27	2.95	5.53	2.62	2.4	2.72
XRF-M01	LOI	wt%	0.05	1.5	2.88	0.58	1.59	1.13	1.21
XRF-M01	MgO	wt%	0.01	1.5	4.05	0.13	1.5	1.28	1.2
XRF-M01	MnO	wt%	0.002	0.044	0.083	0.008	0.048	0.045	0.043
XRF-M01	Na_2O	wt%	0.02	5.03	4.21	3.18	5.3	5.17	5.18
XRF-M01	P_2O_5	wt%	0.002	0.145	0.371	0.003	0.128	0.125	0.12
XRF-M01	SiO_2	wt%	0.04	69.07	58.94	76.18	68.96	69.42	68.69
XRF-M01	TiO_2	wt%	0.01	0.31	0.57	0.07	0.28	0.28	0.26
	Total	wt%		101.06	100.46	100.45	100.71	100.73	99.88
XRF-T02	As	ppm	6	<6	<6	<6	<6	<6	<6
XRF-T02	Br	ppm	1.2	3	<1.2	<1.2	3	2	<1.2
XRF-T02	Cu	ppm	9	<9	41	<9	<9	<9	<9
XRF-T02	Ga	ppm	1.3	20	18	17	20	20	19
XRF-T02	Mo	ppm	0.8	1	3	1	2	1	1
XRF-T02	Nb	ppm	0.7	4	6	2	4	3	3
XRF-T02	Ni	ppm	1.6	22	54	2	21	19	18
XRF-T02	Pb	ppm	1.7	8	18	30	43	9	8
XRF-T02	Rb	ppm	0.8	53	103	154	78	65	87

Method		Units	Detect Limit	16KAA020A	16KAA020B	16KAA020C	16KAA022A	16KAA024A	16KAA025A
XRF-T02	Sr	ppm	0.8	697	948	138	648	761	761
XRF-T02	Th	ppm	1.5	3	10	28	4	4	4
XRF-T02	U	ppm	1.6	<1.6	3	6	<1.6	<1.6	<1.6
XRF-T02	Y	ppm	0.7	11	15	2	10	10	9
XRF-T02	Zn	ppm	1	52	71	8	55	50	45
XRF-T02	Zr	ppm	1.8	123	187	80	114	117	111
IMC-100	Ba	ppm	0.8	910.1	1079.5	230.8	851.9	791.1	829.1
IMC-100	Be	ppm	0.04	1.58	2.11	1.75	1.63	1.73	1.69
IMC-100	Bi	ppm	0.47	<0.47	<0.47	<0.47	<0.47	<0.47	<0.47
IMC-100	Cd	ppm	0.013	<0.013	0.062	0.065	0.072	0.062	0.068
IMC-100	Ce	ppm	0.12	61.81	112.18	23.96	55.72	55.88	55.23
IMC-100	Co	ppm	0.13	7.75	20.13	0.46	6.83	6.61	6.34
IMC-100	Cr	ppm	3	60	189	31	45	48	50
IMC-100	Cs	ppm	0.013	0.684	4.137	3.239	1.178	1.013	1.828
IMC-100	Cu	ppm	1.4	1.4	44.8	4.9	1.9	7	7.1
IMC-100	Dy	ppm	0.009	2.221	3.137	0.289	1.918	1.956	1.78
IMC-100	Er	ppm	0.007	1.206	1.505	0.24	1.016	1.01	0.929
IMC-100	Eu	ppm	0.0031	1.1944	2.0213	0.1758	1.0993	1.0518	0.9887
IMC-100	Ga	ppm	0.04	20.97	19.27	18.35	20.53	21.02	20.85
IMC-100	Gd	ppm	0.009	3.261	5.251	0.353	2.802	2.803	2.585
IMC-100	Hf	ppm	0.14	3.62	5.27	3.47	3.55	3.34	3.21
IMC-100	Ho	ppm	0.0025	0.4165	0.5622	0.0697	0.3584	0.3679	0.3328
IMC-100	In	ppm	0.0018	0.0213	0.0374	0.002	<0.0018	0.0215	0.022
IMC-100	La	ppm	0.1	29.23	54.57	17.22	27.48	26.64	27.88
IMC-100	Li	ppm	0.4	12.8	18.8	1.2	22	19.9	19.5
IMC-100	Lu	ppm	0.002	0.1694	0.2095	0.1132	0.1493	0.1529	0.1403
IMC-100	Mo	ppm	0.08	1.71	2.86	1.71	1.88	1.48	1.49
IMC-100	Nb	ppm	0.028	4.323	6.531	2.63	4.491	4.54	4.313
IMC-100	Nd	ppm	0.06	28.5	51.67	4.93	25.06	25.56	23.87
IMC-100	Ni	ppm	0.7	22.6	57.7	0.7	21.5	19.3	19.1
IMC-100	Pb	ppm	0.18	8.2	18.2	30.6	138.1	9.2	8.2
IMC-100	Pr	ppm	0.014	7.401	13.553	1.822	6.542	6.635	6.265
IMC-100	Rb	ppm	0.11	54.71	107.13	162.38	79.26	65.44	89.79
IMC-100	Sb	ppm	0.04	0.08	0.23	0.19	0.06	<0.04	0.06
IMC-100	Sc	ppm	1.1	5.6	13.4	<1.1	5	4.7	4.7
IMC-100	Sm	ppm	0.026	4.719	8.368	0.497	4.106	4.259	3.907
IMC-100	Sn	ppm	0.16	0.92	1.37	0.41	>14	0.93	0.83
IMC-100	Sr	ppm	0.6	725.9	973.3	143.4	668.1	781.8	806.5
IMC-100	Ta	ppm	0.007	0.328	0.448	0.172	0.337	0.335	0.301
IMC-100	Tb	ppm	0.0023	0.4128	0.6216	0.0459	0.3506	0.3592	0.324
IMC-100	Th	ppm	0.018	3.841	10.318	31.695	5.532	4.725	4.988
IMC-100	Ti	ppm	7	1937	3455	372	1721	1706	1636

Method		Units	Detect Limit	16KAA020A	16KAA020B	16KAA020C	16KAA022A	16KAA024A	16KAA025A
IMC-100	Tl	ppm	0.002	0.212	0.552	0.793	0.351	0.303	0.434
IMC-100	Tm	ppm	0.0019	0.1734	0.2147	0.049	0.1447	0.148	0.1348
IMC-100	U	ppm	0.011	0.679	2.52	6.549	1.316	1.004	1.325
IMC-100	V	ppm	0.8	45.8	114.1	5.2	41.3	40	38.2
IMC-100	W	ppm	0.05	0.06	0.66	0.27	0.2	0.07	0.14
IMC-100	Y	ppm	0.05	12.21	15.91	2.66	10.51	10.79	9.83
IMC-100	Yb	ppm	0.009	1.13	1.413	0.479	0.966	1.011	0.907
IMC-100	Zn	ppm	1.8	56	71	11	64	49	47
IMC-100	Zr	ppm	6	142	217	84	131	124	120
Method		Units	Detect Limit	16KAA026A	16KAA028A	16KAA031A	16KAA033A	16KAA033B	16KAA033C
SG				2.67	2.67	2.62	2.74	2.59	2.96
SG DWT		g		382.1	154.5	148	127.9	118.8	263.5
SG WWT		g		238.8	96.6	91.6	81.2	72.9	174.5
FEO-ION	FeO	wt%	0.06	1.25	2.1	1.04	2.88	0.11	5.61
IRC-100	CO_2	wt%	0.023	<0.023	0.043	0.618	0.26	0.129	0.313
IRC-101	S	wt%	0.003	<0.003	<0.003	0.007	<0.003	<0.003	0.01
IMP-101	Au	ppb	1.6	<1.6	<1.6	<1.6	<1.6	<1.6	<1.6
IMP-101	Pd	ppb	1.3	<1.3	<1.3	<1.3	<1.3	<1.3	<1.3
IMP-101	Pt	ppb	0.4	<0.4	0.5	<0.4	0.4	<0.4	2.8
XRF-M01	Al_2O_3	wt%	0.02	15.85	15.31	16.53	16.86	13.44	14.24
XRF-M01	BaO	wt%	0.004	0.09	0.14	0.09	0.09	0.05	0.02
XRF-M01	CaO	wt%	0.006	2.72	3.48	2.005	3.877	0.5	9.69
XRF-M01	Cr_2O_3	wt%	0.002	0.01	0.02	<0.002	0.01	<0.002	0.02
XRF-M01	Fe_2O_3	wt%	0.01	2.73	4.06	2.3	5.13	0.28	9.95
XRF-M01	K_2O	wt%	0.01	2.47	4.01	2.41	2.31	4.77	0.74
XRF-M01	LOI	wt%	0.05	0.89	1.39	1.71	1.83	0.43	1.62
XRF-M01	MgO	wt%	0.01	1.42	3.17	1.07	3.6	0.04	6.76
XRF-M01	MnO	wt%	0.002	0.049	0.069	0.033	0.088	0.008	0.167
XRF-M01	Na_2O	wt%	0.02	5.23	4.59	5.06	5.79	4.09	4.1
XRF-M01	P_2O_5	wt%	0.002	0.143	0.243	0.115	0.325	0.003	0.581
XRF-M01	SiO_2	wt%	0.04	69.09	63.53	69.18	60.12	76.71	51.64
XRF-M01	TiO_2	wt%	0.01	0.3	0.39	0.26	0.55	0.03	0.88
	Total	wt%		100.98	100.42	100.77	100.58	100.36	100.39
XRF-T02	As	ppm	6	<6	<6	<6	<6	<6	<6
XRF-T02	Br	ppm	1.2	3	3	<1.2	5	2	12
XRF-T02	Cu	ppm	9	<9	<9	<9	<9	<9	<9
XRF-T02	Ga	ppm	1.3	21	17	20	22	20	21
XRF-T02	Mo	ppm	0.8	1	1	1	1	<0.8	1
XRF-T02	Nb	ppm	0.7	4	4	3	4	2	5
XRF-T02	Ni	ppm	1.6	18	54	16	59	2	50
XRF-T02	Pb	ppm	1.7	11	10	9	5	11	4

Method		Units	Detect Limit	16KAA026A	16KAA028A	16KAA031A	16KAA033A	16KAA033B	16KAA033C
XRF-T02	Rb	ppm	0.8	64	118	54	63	116	18
XRF-T02	Sr	ppm	0.8	780	912	587	643	113	865
XRF-T02	Th	ppm	1.5	3	7	3	4	5	2
XRF-T02	U	ppm	1.6	<1.6	<1.6	<1.6	<1.6	2	<1.6
XRF-T02	Y	ppm	0.7	11	11	10	18	1	23
XRF-T02	Zn	ppm	1	53	48	42	75	2	109
XRF-T02	Zr	ppm	1.8	120	136	119	193	25	78
IMC-100	Ba	ppm	0.8	820.9	1309.3	850.3	851.9	494.9	185.8
IMC-100	Be	ppm	0.04	1.63	1.67	1.68	1.66	2.42	2.13
IMC-100	Bi	ppm	0.47	<0.47	<0.47	<0.47	<0.47	<0.47	<0.47
IMC-100	Cd	ppm	0.013	0.048	0.086	0.062	0.131	0.017	0.082
IMC-100	Ce	ppm	0.12	59.83	90.65	52.48	112.45	10.66	117.21
IMC-100	Co	ppm	0.13	7.32	15.2	5.98	17.31	0.43	35.42
IMC-100	Cr	ppm	3	42	137	39	101	26	170
IMC-100	Cs	ppm	0.013	0.697	0.927	0.978	0.307	1.058	0.287
IMC-100	Cu	ppm	1.4	<1.4	4	<1.4	3.1	7.5	1.5
IMC-100	Dy	ppm	0.009	2.111	2.273	1.742	3.695	0.152	4.653
IMC-100	Er	ppm	0.007	1.148	1.03	0.955	1.724	0.115	2.24
IMC-100	Eu	ppm	0.0031	1.1823	1.6227	0.9658	2.3802	0.0912	2.9622
IMC-100	Ga	ppm	0.04	21.14	18.02	21.65	22.7	20.21	21.55
IMC-100	Gd	ppm	0.009	3.052	4.189	2.577	5.98	0.182	7.608
IMC-100	Hf	ppm	0.14	3.66	3.88	3.35	4.92	2.14	2.59
IMC-100	Ho	ppm	0.0025	0.4146	0.39	0.3382	0.6633	0.0332	0.82
IMC-100	In	ppm	0.0018	0.0239	0.0253	0.0166	0.0383	<0.0018	0.0664
IMC-100	La	ppm	0.1	27.7	44.13	26.32	50.49	8.83	46.7
IMC-100	Li	ppm	0.4	16.9	11.2	20.1	13.4	0.9	13.6
IMC-100	Lu	ppm	0.002	0.1731	0.1453	0.1451	0.2259	0.0365	0.2923
IMC-100	Mo	ppm	0.08	1.04	1.02	0.96	0.77	1.37	0.64
IMC-100	Nb	ppm	0.028	4.97	4.681	3.937	5.098	2.562	5.535
IMC-100	Nd	ppm	0.06	28.22	41.13	23.47	56.49	2.07	66.34
IMC-100	Ni	ppm	0.7	19.5	57.2	16.4	61.3	1	51
IMC-100	Pb	ppm	0.18	10.7	10	9.2	4.7	12.2	3.4
IMC-100	Pr	ppm	0.014	7.296	10.784	6.154	14.094	0.759	15.612
IMC-100	Rb	ppm	0.11	65.71	121.34	56.11	64.78	119.63	16.82
IMC-100	Sb	ppm	0.04	0.04	<0.04	0.07	0.04	0.04	0.05
IMC-100	Sc	ppm	1.1	5.2	9.6	4.1	10.3	<1.1	27.9
IMC-100	Sm	ppm	0.026	4.712	6.671	3.762	9.372	0.282	11.607
IMC-100	Sn	ppm	0.16	0.93	1.01	0.82	1.22	0.17	1.66
IMC-100	Sr	ppm	0.6	810.9	941	614.7	676.6	117.3	904.6
IMC-100	Ta	ppm	0.007	0.349	0.279	0.299	0.288	0.142	0.262
IMC-100	Tb	ppm	0.0023	0.3862	0.4539	0.3216	0.7216	0.0278	0.8865
IMC-100	Th	ppm	0.018	5.08	7.582	4.225	4.873	6.583	2.69

Method		Units	Detect Limit	16KAA026A	16KAA028A	16KAA031A	16KAA033A	16KAA033B	16KAA033C
IMC-100	Ti	ppm	7	1902	2498	1587	3323	203	5126
IMC-100	Tl	ppm	0.002	0.283	0.485	0.207	0.183	0.34	0.069
IMC-100	Tm	ppm	0.0019	0.1693	0.1426	0.1378	0.233	0.0198	0.3071
IMC-100	U	ppm	0.011	1.146	1.957	0.999	1.3	2.591	0.945
IMC-100	V	ppm	0.8	43.6	78	36.1	88.4	2.9	210.5
IMC-100	W	ppm	0.05	0.08	0.38	0.32	0.21	0.19	0.18
IMC-100	Y	ppm	0.05	12	11.53	9.76	18.78	1.22	23.19
IMC-100	Yb	ppm	0.009	1.135	0.949	0.927	1.539	0.187	1.932
IMC-100	Zn	ppm	1.8	54	48	43	74	4	103
IMC-100	Zr	ppm	6	136	156	128	217	26	91
Method		Units	Detect Limit	16KAA034A	16KAA034B	16KAA035A	16KAA036A	16KAA036B	16KAA038A
SG				2.58	2.58	2.61	2.54	2.71	2.68
SG DWT		g		173.2	148	190.6	101	815.2	216.4
SG WWT		g		106.1	90.7	117.6	61.2	514.9	135.8
FEO-ION	FeO	wt%	0.06	0.86	1.02	0.54	1.39	0.56	2.27
IRC-100	CO_2	wt%	0.023	0.19	0.355	2.184	0.551	0.084	0.759
IRC-101	S	wt%	0.003	0.003	0.009	0.439	<0.003	2.785	0.163
IMP-101	Au	ppb	1.6	<1.6	32	500	2	39	2
IMP-101	Pd	ppb	1.3	<1.3	<1.3	<1.3	<1.3	<1.3	<1.3
IMP-101	Pt	ppb	0.4	<0.4	<0.4	<0.4	<0.4	<0.4	0.4
XRF-M01	Al_2O_3	wt%	0.02	10.24	9.94	14.71	15.16	1.7	16.25
XRF-M01	BaO	wt%	0.004	0.05	0.06	0.09	0.11	0.01	0.18
XRF-M01	CaO	wt%	0.006	0.294	0.464	2.593	0.848	0.076	2.385
XRF-M01	Cr_2O_3	wt%	0.002	0.01	0.01	0.01	0.01	0.01	0.01
XRF-M01	Fe_2O_3	wt%	0.01	1.29	1.55	1.98	2.37	4.29	4.11
XRF-M01	K_2O	wt%	0.01	1.96	1.15	1.62	3.54	0.05	2.47
XRF-M01	LOI	wt%	0.05	1.12	1.4	2.82	1.62	2.1	2.51
XRF-M01	MgO	wt%	0.01	0.86	0.86	0.41	1.39	0.1	3.16
XRF-M01	MnO	wt%	0.002	0.019	0.023	0.034	0.037	0.004	0.067
XRF-M01	Na_2O	wt%	0.02	3.13	3.46	5.66	4.7	0.12	4.77
XRF-M01	P_2O_5	wt%	0.002	0.067	0.071	0.116	0.13	0.009	0.302
XRF-M01	SiO_2	wt%	0.04	81.56	80.78	69.71	69.46	91.78	63.08
XRF-M01	TiO_2	wt%	0.01	0.16	0.17	0.26	0.28	0.03	0.44
	Total	wt%		100.76	99.94	100.01	99.65	100.29	99.74
XRF-T02	As	ppm	6	<6	<6	<6	<6	<6	<6
XRF-T02	Br	ppm	1.2	3	2	<1.2	<1.2	<1.2	<1.2
XRF-T02	Cu	ppm	9	<9	<9	51	<9	1732	96
XRF-T02	Ga	ppm	1.3	10	12	18	17	<1.3	19
XRF-T02	Mo	ppm	0.8	1	1	6	1	2	3
XRF-T02	Nb	ppm	0.7	2	2	3	3	<0.7	5
XRF-T02	Ni	ppm	1.6	11	13	15	19	8	48

Method		Units	Detect Limit	16KAA034A	16KAA034B	16KAA035A	16KAA036A	16KAA036B	16KAA038A
XRF-T02	Pb	ppm	1.7	<1.7	3	63	5	15	9
XRF-T02	Rb	ppm	0.8	39	26	39	83	1	73
XRF-T02	Sr	ppm	0.8	103	166	531	517	15	1819
XRF-T02	Th	ppm	1.5	<1.5	<1.5	3	4	<1.5	7
XRF-T02	U	ppm	1.6	<1.6	<1.6	<1.6	<1.6	<1.6	<1.6
XRF-T02	Y	ppm	0.7	5	4	9	7	<0.7	15
XRF-T02	Zn	ppm	1	24	24	40	39	<1	72
XRF-T02	Zr	ppm	1.8	71	72	115	103	4	167
IMC-100	Ba	ppm	0.8	429.4	571.2	799.4	993.4	74	1652.4
IMC-100	Be	ppm	0.04	0.54	0.67	1.29	1.27	<0.04	1.74
IMC-100	Bi	ppm	0.47	<0.47	0.73	0.8	<0.47	15.74	<0.47
IMC-100	Cd	ppm	0.013	0.015	0.02	0.22	0.043	0.062	0.067
IMC-100	Ce	ppm	0.12	29.2	33.19	50.99	44.1	1.12	124.51
IMC-100	Co	ppm	0.13	3.71	5.67	7.44	7.32	34.58	14.41
IMC-100	Cr	ppm	3	47	53	49	46	71	95
IMC-100	Cs	ppm	0.013	0.64	0.816	1.195	1.067	0.036	2.019
IMC-100	Cu	ppm	1.4	7.9	1.9	54	3.8	1842.2	98
IMC-100	Dy	ppm	0.009	0.958	0.899	1.675	1.461	0.039	3.096
IMC-100	Er	ppm	0.007	0.491	0.497	0.884	0.747	0.022	1.494
IMC-100	Eu	ppm	0.0031	0.5335	0.5119	0.8811	0.826	0.0262	2.1947
IMC-100	Ga	ppm	0.04	10.16	12.06	18.57	18.69	1.35	20.23
IMC-100	Gd	ppm	0.009	1.459	1.327	2.418	2.22	0.054	5.182
IMC-100	Hf	ppm	0.14	1.95	1.9	3.17	3.04	<0.14	4.65
IMC-100	Ho	ppm	0.0025	0.1813	0.1756	0.3274	0.2762	0.0086	0.5533
IMC-100	In	ppm	0.0018	0.0082	0.0109	0.0201	0.016	0.0673	0.0308
IMC-100	La	ppm	0.1	13.47	15.54	24.56	20.58	0.35	58.09
IMC-100	Li	ppm	0.4	6.7	5.5	8.7	6.9	0.5	22.2
IMC-100	Lu	ppm	0.002	0.066	0.0739	0.1313	0.1222	0.0036	0.2023
IMC-100	Mo	ppm	0.08	1.93	2.28	7.01	1.05	3.97	1.33
IMC-100	Nb	ppm	0.028	2.403	2.608	3.907	3.717	0.144	6.172
IMC-100	Nd	ppm	0.06	13.08	13.73	21.93	19.73	0.42	55.48
IMC-100	Ni	ppm	0.7	10.5	12.4	15	18.2	9.2	49.3
IMC-100	Pb	ppm	0.18	2.3	4.9	61	5.6	16.3	8
IMC-100	Pr	ppm	0.014	3.36	3.668	5.816	5.066	0.102	14.56
IMC-100	Rb	ppm	0.11	39.55	26.7	39.1	85.64	1.08	72.92
IMC-100	Sb	ppm	0.04	<0.04	<0.04	0.19	0.08	<0.04	0.08
IMC-100	Sc	ppm	1.1	2.4	2.7	4	4.6	<1.1	8.9
IMC-100	Sm	ppm	0.026	2.097	2.162	3.563	3.392	0.08	8.587
IMC-100	Sn	ppm	0.16	0.5	0.59	0.99	0.73	0.2	1.14
IMC-100	Sr	ppm	0.6	106	168.4	544.2	527.6	14.6	>1560
IMC-100	Ta	ppm	0.007	0.182	0.187	0.285	0.317	<0.007	0.466
IMC-100	Tb	ppm	0.0023	0.1812	0.1625	0.3032	0.2714	0.0069	0.6164

Method		Units	Detect Limit	16KAA034A	16KAA034B	16KAA035A	16KAA036A	16KAA036B	16KAA038A
IMC-100	Th	ppm	0.018	2.715	2.61	3.865	4.598	0.079	7.987
IMC-100	Ti	ppm	7	926	954	1530	1648	91	2665
IMC-100	Tl	ppm	0.002	0.202	0.135	0.156	0.365	0.007	0.347
IMC-100	Tm	ppm	0.0019	0.0696	0.0727	0.1297	0.1092	0.0036	0.2102
IMC-100	U	ppm	0.011	0.512	0.664	1.014	1.048	0.017	1.326
IMC-100	V	ppm	0.8	18.5	28.1	33	40.9	11	75.1
IMC-100	W	ppm	0.05	0.46	1.02	13.68	1.07	0.68	0.95
IMC-100	Y	ppm	0.05	5.09	4.65	9.41	7.41	0.22	15.74
IMC-100	Yb	ppm	0.009	0.449	0.503	0.834	0.756	0.028	1.41
IMC-100	Zn	ppm	1.8	28	26	39	39	5	69
IMC-100	Zr	ppm	6	72	71	126	112	<6	191
Method		Units	Detect Limit	16KAA039B	16KAA041A	16KAA042A			
SG				2.62	4.08	2.68			
SG DWT		g		188.5	423.5	334			
SG WWT		g		116.5	319.7	209.6			
FEO-ION	FeO	wt%	0.06	0.62		4.26			
IRC-100	CO_2	wt%	0.023	0.209	0.215	2.167			
IRC-101	S	wt%	0.003	0.01	35.983	0.181			
IMP-101	Au	ppb	1.6	<1.6	13	4			
IMP-101	Pd	ppb	1.3	<1.3	<1.3	<1.3			
IMP-101	Pt	ppb	0.4	<0.4	1.4	<0.4			
XRF-M01	Al_2O_3	wt%	0.02	14.05	1.19	17.52			
XRF-M01	BaO	wt%	0.004	0.12	<0.004	0.03			
XRF-M01	CaO	wt%	0.006	0.754	0.042	3.126			
XRF-M01	Cr_2O_3	wt%	0.002	<0.002	0.01	<0.002			
XRF-M01	Fe_2O_3	wt%	0.01	0.93	74.09	5.91			
XRF-M01	K_2O	wt%	0.01	4.83	0.04	1.82			
XRF-M01	LOI	wt%	0.05	0.85	15.52	4.15			
XRF-M01	MgO	wt%	0.01	0.25	0.22	2.89			
XRF-M01	MnO	wt%	0.002	0.012	0.027	0.092			
XRF-M01	Na_2O	wt%	0.02	3.57	<0.02	4.78			
XRF-M01	P_2O_5	wt%	0.002	0.025	0.008	0.301			
XRF-M01	SiO_2	wt%	0.04	75.05	9.55	58.85			
XRF-M01	TiO_2	wt%	0.01	0.13	0.05	0.53			
	Total	wt%		100.57	100.77	100.01			
XRF-T02	As	ppm	6	<6	<6	<6			
XRF-T02	Br	ppm	1.2	<1.2	<1.2	<1.2			
XRF-T02	Cu	ppm	9	<9	447	19			
XRF-T02	Ga	ppm	1.3	14	<1.3	20			
XRF-T02	Mo	ppm	0.8	2	10	1			
XRF-T02	Nb	ppm	0.7	3	<0.7	4			

Method		Units	Detect Limit	16KAA039B	16KAA041A	16KAA042A			
XRF-T02	Ni	ppm	1.6	4	114	12			
XRF-T02	Pb	ppm	1.7	18	5	3			
XRF-T02	Rb	ppm	0.8	124	3	62			
XRF-T02	Sr	ppm	0.8	308	3	382			
XRF-T02	Th	ppm	1.5	17	<1.5	3			
XRF-T02	U	ppm	1.6	<1.6	<1.6	<1.6			
XRF-T02	Y	ppm	0.7	3	1	13			
XRF-T02	Zn	ppm	1	14	31	82			
XRF-T02	Zr	ppm	1.8	74	9	134			
IMC-100	Ba	ppm	0.8	1102.5	11.7	311			
IMC-100	Be	ppm	0.04	1.54	0.28	1.3			
IMC-100	Bi	ppm	0.47	<0.47	4.31	<0.47			
IMC-100	Cd	ppm	0.013	0.028	0.063	0.056			
IMC-100	Ce	ppm	0.12	73.98	2.64	73.19			
IMC-100	Co	ppm	0.13	1.68	1	16.48			
IMC-100	Cr	ppm	3	41	65	31			
IMC-100	Cs	ppm	0.013	2.914	0.316	2.423			
IMC-100	Cu	ppm	1.4	4	402.9	22			
IMC-100	Dy	ppm	0.009	0.677	0.213	2.406			
IMC-100	Er	ppm	0.007	0.381	0.111	1.264			
IMC-100	Eu	ppm	0.0031	0.6551	0.0742	1.4192			
IMC-100	Ga	ppm	0.04	15.73	1.33	21.25			
IMC-100	Gd	ppm	0.009	1.218	0.215	3.829			
IMC-100	Hf	ppm	0.14	2.52	0.25	3.48			
IMC-100	Ho	ppm	0.0025	0.1262	0.0411	0.4555			
IMC-100	In	ppm	0.0018	<0.0018	0.0138	0.0182			
IMC-100	La	ppm	0.1	42.94	1.18	34.58			
IMC-100	Li	ppm	0.4	3.6	7.1	33.4			
IMC-100	Lu	ppm	0.002	0.0629	0.0165	0.2027			
IMC-100	Mo	ppm	0.08	2.8	0.82	1.15			
IMC-100	Nb	ppm	0.028	3.607	0.421	4.27			
IMC-100	Nd	ppm	0.06	20.87	1.41	36.28			
IMC-100	Ni	ppm	0.7	3.4	72.6	12.4			
IMC-100	Pb	ppm	0.18	18.9	6.9	3.1			
IMC-100	Pr	ppm	0.014	6.849	0.329	9.22			
IMC-100	Rb	ppm	0.11	128.02	1.98	62.82			
IMC-100	Sb	ppm	0.04	0.17	0.11	0.09			
IMC-100	Sc	ppm	1.1	1.2	1.4	11.9			
IMC-100	Sm	ppm	0.026	2.432	0.267	5.837			
IMC-100	Sn	ppm	0.16	0.29	0.38	0.85			
IMC-100	Sr	ppm	0.6	317.3	2.5	393.5			
IMC-100	Ta	ppm	0.007	0.309	0.025	0.277			

Method		Units	Detect Limit	16KAA039B	16KAA041A	16KAA042A			
IMC-100	Tb	ppm	0.0023	0.1402	0.0348	0.4569			
IMC-100	Th	ppm	0.018	18.518	0.235	3.652			
IMC-100	Ti	ppm	7	835	273	3253			
IMC-100	Tl	ppm	0.002	0.552	0.067	0.433			
IMC-100	Tm	ppm	0.0019	0.0562	0.0162	0.1915			
IMC-100	U	ppm	0.011	1.676	0.236	0.857			
IMC-100	V	ppm	0.8	10.7	7.4	104.7			
IMC-100	W	ppm	0.05	0.79	11.73	0.63			
IMC-100	Y	ppm	0.05	3.81	0.99	12.83			
IMC-100	Yb	ppm	0.009	0.39	0.107	1.262			
IMC-100	Zn	ppm	1.8	16	19	85			
IMC-100	Zr	ppm	6	84	10	140			
Method		Units	Detect Limit	16KAM036C	17KAM001A	17KAM002A	17KAM003A	17KAM006A	17KAM007A
SG				4.591	2.68	1.842	2.62		2.64
SG DWT		g		0.004	189	0.051	163		103.5
SG WWT		g			118.5		100.7		64.3
IRC-100	CO_2	wt%	0.023	4.591	0.281	1.842	0.199	0.395	0.033
IRC-101	S	wt%	0.003	0.004	0.003	0.051	0.003	0.004	<0.003
IMP-101	Au	ppb	0.6	0.8	1.3	2	1.6	1	1.4
IMP-101	Pd	ppb	0.14	<0.14	<0.14	<0.14	<0.14	<0.14	<0.14
IMP-101	Pt	ppb	0.06	0.06	0.13	0.1	0.1	<0.06	<0.06
XRF-M01	Al_2O_3	wt%	0.02	1.05	15.9	16.84	16.08	16.26	15.99
XRF-M01	BaO	wt%	0.004	0.006	0.129	0.104	0.09	0.11	0.101
XRF-M01	CaO	wt%	0.006	4.946	2.716	2.554	2.215	2.23	2.423
XRF-M01	Cr_2O_3	wt%	0.002	0.024	0.01	0.008	0.008	0.005	0.006
XRF-M01	Fe_2O_3	wt%	0.01	0.47	2.87	3.06	2.55	2.27	2.26
XRF-M01	K_2O	wt%	0.01	0.13	2.76	2.48	2.33	2.82	2.65
XRF-M01	MgO	wt%	0.01	0.29	1.64	1.41	1.29	1.08	1.11
XRF-M01	MnO	wt%	0.002	0.026	0.05	0.043	0.042	0.036	0.04
XRF-M01	Na_2O	wt%	0.02	0.06	4.93	5.28	5.5	4.93	5.01
XRF-M01	Nitrogen 105	wt%		0.08	0.29	0.25	0.4	0.28	0.28
XRF-M01	P_2O_5	wt%	0.002	0.005	0.15	0.175	0.126	0.111	0.108
XRF-M01	SiO_2	wt%	0.04	89.91	67.07	64.83	69.19	69.09	69.79
XRF-M01	TiO_2	wt%	0.01	0.02	0.32	0.35	0.29	0.26	0.26
XRF-M01	Total	wt%		101.12	100.11	100.07	101.03	100.3	100.57
XRF-M01	Total LOI 1000	wt%		4.19	1.56	2.94	1.32	1.1	0.84
XRF-T02	As	ppm	6	<6	<6	<6	<6	<6	<6
XRF-T02	Br	ppm	1.2	2	2	2	<1.2	4	<1.2
XRF-T02	Cu	ppm	9	18	<9	146	19	<9	<9

Method		Units	Detect Limit	16KAM036C	17KAM001A	17KAM002A	17KAM003A	17KAM006A	17KAM007A
XRF-T02	Ga	ppm	1.3	20	19	19	20	20	20
XRF-T02	Mo	ppm	0.8	6	1	2	2	1	1
XRF-T02	Nb	ppm	0.7	4	3	4	3	3	4
XRF-T02	Ni	ppm	1.6	26	16	24	28	15	16
XRF-T02	Pb	ppm	1.7	9	11	6	11	17	12
XRF-T02	Rb	ppm	0.8	72	77	94	62	77	67
XRF-T02	Sr	ppm	0.8	737	592	578	878	531	757
XRF-T02	Th	ppm	1.5	4	4	5	4	3	12
XRF-T02	U	ppm	1.6	<1.6	<1.6	<1.6	2	<1.6	<1.6
XRF-T02	Y	ppm	0.7	12	9	11	11	10	10
XRF-T02	Zn	ppm	1	41	45	36	106	36	45
XRF-T02	Zr	ppm	1.8	126	110	124	129	114	113
IMC-100	Ba	ppm	0.8	1040.7	877.3	1336.9	958.1	891.4	1038.7
IMC-100	Be	ppm	0.04	1.41	1.16	1.79	1.62	1.17	1.8
IMC-100	Bi	ppm	0.47	<0.47	<0.47	2.39	<0.47	<0.47	<0.47
IMC-100	Cd	ppm	0.013	0.027	0.049	0.04	0.05	0.045	0.033
IMC-100	Ce	ppm	0.12	64.32	50.28	66.62	65.22	44.89	55.75
IMC-100	Co	ppm	0.13	7.98	4.71	6.83	10.29	5.06	5.43
IMC-100	Cr	ppm	3	72	41	56	54	33	37
IMC-100	Cs	ppm	0.013	1.505	1.652	1.625	2.306	0.831	1.841
IMC-100	Cu	ppm	1.4	20.3	1.6	163.7	20.3	1.7	<1.4
IMC-100	Dy	ppm	0.009	2.219	1.647	2.104	2.147	1.793	1.909
IMC-100	Er	ppm	0.007	1.158	0.904	1.106	1.073	0.971	0.968
IMC-100	Eu	ppm	0.0031	1.2644	0.8667	1.3083	1.3357	0.9289	1.0827
IMC-100	Ga	ppm	0.04	20.18	19.47	20.37	20.13	20.14	20.8
IMC-100	Gd	ppm	0.009	3.55	2.369	3.369	3.514	2.547	2.85
IMC-100	Hf	ppm	0.14	3.79	3.05	3.83	3.47	3.23	3.08
IMC-100	Ho	ppm	0.0025	0.4172	0.314	0.3946	0.4015	0.3465	0.3478
IMC-100	In	ppm	0.0018	0.0187	0.0174	0.0192	0.0278	0.0191	0.0192
IMC-100	La	ppm	0.1	30	25.49	32.63	31.23	21.54	25.8
IMC-100	Li	ppm	0.4	15.3	10.7	19.5	17.2	12.3	19.6
IMC-100	Lu	ppm	0.002	0.165	0.1431	0.1645	0.1532	0.1559	0.1373
IMC-100	Mo	ppm	0.08	6.65	1.52	1.94	1.88	1.04	1.11
IMC-100	Nb	ppm	0.028	4.346	3.819	5.001	4.023	4.001	4.885
IMC-100	Nd	ppm	0.06	30.55	20.9	31.12	31.57	20.43	26.57
IMC-100	Ni	ppm	0.7	25.5	14.4	23.1	28.2	13.3	15.2
IMC-100	Pb	ppm	0.18	10.1	10.9	6.7	11.2	17.8	12.7
IMC-100	Pr	ppm	0.014	7.936	5.69	8.118	8.064	5.366	6.844
IMC-100	Rb	ppm	0.11	71.29	76.09	97.63	60.05	75.33	65.95
IMC-100	Sb	ppm	0.04	0.12	0.06	0.07	0.52	0.05	0.11
IMC-100	Sc	ppm	1.1	4.9	3.2	5.2	7.3	3.6	3.9
IMC-100	Sm	ppm	0.026	5.057	3.346	5.121	5.259	3.405	4.347

Method		Units	Detect Limit	16KAM036C	17KAM001A	17KAM002A	17KAM003A	17KAM006A	17KAM007A
IMC-100	Sn	ppm	0.16	1.03	0.94	1.1	0.96	0.94	0.88
IMC-100	Sr	ppm	0.6	740.7	599.9	589.1	880.3	532	772.2
IMC-100	Ta	ppm	0.007	0.339	0.298	0.38	0.287	0.297	0.293
IMC-100	Tb	ppm	0.0023	0.4291	0.3061	0.3989	0.4225	0.3312	0.3555
IMC-100	Th	ppm	0.018	6.416	4.957	6.608	5.238	4.093	12.765
IMC-100	Ti	ppm	7	1761	1306	1788	2225	1434	1499
IMC-100	Tl	ppm	0.002	0.345	0.363	0.419	0.357	0.377	0.252
IMC-100	Tm	ppm	0.0019	0.1598	0.1337	0.1564	0.152	0.1506	0.1387
IMC-100	U	ppm	0.011	1.505	0.914	1.807	1.572	1.204	1.171
IMC-100	V	ppm	0.8	43.3	27.6	42.2	55.6	29.9	33.8
IMC-100	W	ppm	0.05	2.24	0.61	2.18	4.87	0.21	0.36
IMC-100	Y	ppm	0.05	11.62	8.9	11.31	10.95	9.89	9.88
IMC-100	Yb	ppm	0.009	1.091	0.889	0.995	1.032	0.977	0.934
IMC-100	Zn	ppm	1.8	41	46	38	101	37	46
IMC-100	Zr	ppm	6	139	106	143	126	117	112
Method		**Units**	**Detect Limit**	**17KAM007B**	**17KAM008A**	**17KAM010A**	**17KAM011A**	**17KAM013A**	**17KAM014A**
SG				0.394			0.091	2.64	
SG DWT		g		0.004			<0.003	125.7	
SG WWT		g						78	
IRC-100	CO_2	wt%	0.023	0.394	0.364	0.322	0.091	0.1	0.544
IRC-101	S	wt%	0.003	0.004	0.005	<0.003	<0.003	<0.003	0.018
IMP-101	Au	ppb	0.6	0.8	1	1	10.1	1.5	14
IMP-101	Pd	ppb	0.14	<0.14	<0.14	<0.14	<0.14	<0.14	<0.14
IMP-101	Pt	ppb	0.06	<0.06	0.1	0.1	0.09	0.07	0.2
XRF-M01	Al_2O_3	wt%	0.02	15.67	15.99	16.07	16.39	15.62	16.32
XRF-M01	BaO	wt%	0.004	0.1	0.092	0.085	0.094	0.08	0.144
XRF-M01	CaO	wt%	0.006	1.72	2.228	2.786	2.632	2.419	1.418
XRF-M01	Cr_2O_3	wt%	0.002	0.008	0.005	0.005	0.006	0.009	0.007
XRF-M01	Fe_2O_3	wt%	0.01	2.13	2.7	2.76	2.68	2.49	2.34
XRF-M01	K_2O	wt%	0.01	2.74	2.36	2.43	2.61	2.6	3.13
XRF-M01	MgO	wt%	0.01	0.97	1.32	1.38	1.34	1.39	1.33
XRF-M01	MnO	wt%	0.002	0.039	0.067	0.052	0.045	0.053	0.03
XRF-M01	Na_2O	wt%	0.02	5.35	5.14	5.09	4.94	5	4.8
XRF-M01	Nitrogen 105	wt%		0.34	0.37	0.25	0.32	0.31	0.36
XRF-M01	P_2O_5	wt%	0.002	0.107	0.152	0.148	0.141	0.131	0.142
XRF-M01	SiO_2	wt%	0.04	69.18	68.66	68.83	68.91	69.53	68.63
XRF-M01	TiO_2	wt%	0.01	0.26	0.31	0.32	0.3	0.28	0.31
XRF-M01	Total	wt%		99.64	100.53	100.97	101.02	100.72	100.6
XRF-M01	Total LOI 1000	wt%		1.37	1.5	1.02	0.93	1.11	2

Method		Units	Detect Limit	17KAM007B	17KAM008A	17KAM010A	17KAM011A	17KAM013A	17KAM014A
XRF-T02	As	ppm	6	<6	<6	<6	<6	6	<6
XRF-T02	Br	ppm	1.2	<1.2	2	3	<1.2	<1.2	4
XRF-T02	Cu	ppm	9	<9	<9	<9	<9	93	<9
XRF-T02	Ga	ppm	1.3	23	20	20	19	15	20
XRF-T02	Mo	ppm	0.8	1	1	1	2	3	1
XRF-T02	Nb	ppm	0.7	6	3	4	4	130	5
XRF-T02	Ni	ppm	1.6	2	14	24	27	481	19
XRF-T02	Pb	ppm	1.7	16	8	11	12	14	18
XRF-T02	Rb	ppm	0.8	178	46	69	62	75	60
XRF-T02	Sr	ppm	0.8	37	582	679	695	850	590
XRF-T02	Th	ppm	1.5	24	2	5	7	14	4
XRF-T02	U	ppm	1.6	5	<1.6	<1.6	2	4	<1.6
XRF-T02	Y	ppm	0.7	3	8	10	11	27	11
XRF-T02	Zn	ppm	1	6	35	57	51	110	53
XRF-T02	Zr	ppm	1.8	68	118	127	130	290	133
IMC-100	Ba	ppm	0.8	58.6	695.8	877.1	877.8	775.8	949.5
IMC-100	Be	ppm	0.04	2.42	1.32	1.42	1.66	3.17	1.54
IMC-100	Bi	ppm	0.47	<0.47	<0.47	<0.47	<0.47	1.4	<0.47
IMC-100	Cd	ppm	0.013	0.042	0.039	0.058	0.032	0.214	0.051
IMC-100	Ce	ppm	0.12	13.04	54.17	58.7	69.12	198.98	60.62
IMC-100	Co	ppm	0.13	0.34	5.04	7.55	8.26	65.32	6.97
IMC-100	Cr	ppm	3	29	48	64	67	662	41
IMC-100	Cs	ppm	0.013	3.963	1.415	0.92	0.902	6.002	0.485
IMC-100	Cu	ppm	1.4	2	1.5	<1.4	1.9	93.2	1.6
IMC-100	Dy	ppm	0.009	0.186	1.605	1.985	2.061	6.832	2.021
IMC-100	Er	ppm	0.007	0.218	0.871	0.984	1.084	2.48	1.155
IMC-100	Eu	ppm	0.0031	0.066	0.923	1.1442	1.2553	4.5722	1.1547
IMC-100	Ga	ppm	0.04	23.01	21.04	19.77	19.72	15.32	20.59
IMC-100	Gd	ppm	0.009	0.211	2.327	3.046	3.394	11.575	3.029
IMC-100	Hf	ppm	0.14	4.03	3.3	3.51	3.87	6.81	3.65
IMC-100	Ho	ppm	0.0025	0.0521	0.2914	0.3604	0.385	1.0738	0.3858
IMC-100	In	ppm	0.0018	0.0026	0.0204	0.0229	0.02	0.0735	0.0234
IMC-100	La	ppm	0.1	7.99	24.64	26.65	33.83	93.64	28.82
IMC-100	Li	ppm	0.4	1	14.6	10.9	14.2	112.8	13.5
IMC-100	Lu	ppm	0.002	0.1145	0.143	0.1456	0.1611	0.2468	0.1765
IMC-100	Mo	ppm	0.08	1.82	1.81	1.77	1.66	2.62	1.08
IMC-100	Nb	ppm	0.028	6.209	3.831	4.576	4.914	122.475	5.328
IMC-100	Nd	ppm	0.06	2.28	23.72	26.4	30.35	95.91	27.07
IMC-100	Ni	ppm	0.7	0.9	12.9	23.4	26	464.5	18.1
IMC-100	Pb	ppm	0.18	17.4	8.6	10.6	12.6	13.9	17.9
IMC-100	Pr	ppm	0.014	0.866	6.427	6.916	8.147	24.43	7.23
IMC-100	Rb	ppm	0.11	183.67	44.84	69.05	61.89	76.94	60.68

Method		Units	Detect Limit	17KAM007B	17KAM008A	17KAM010A	17KAM011A	17KAM013A	17KAM014A
IMC-100	Sb	ppm	0.04	0.34	0.07	0.11	0.08	0.25	0.06
IMC-100	Sc	ppm	1.1	<1.1	3.7	5	5.3	18.4	4.9
IMC-100	Sm	ppm	0.026	0.295	3.737	4.492	4.937	16.476	4.47
IMC-100	Sn	ppm	0.16	0.65	0.97	0.93	0.96	2.61	0.96
IMC-100	Sr	ppm	0.6	36.7	599.9	688.4	705.1	875.4	610.1
IMC-100	Ta	ppm	0.007	0.542	0.284	0.352	0.358	6.933	0.347
IMC-100	Tb	ppm	0.0023	0.0312	0.2994	0.367	0.3964	1.4034	0.3759
IMC-100	Th	ppm	0.018	26.38	3.727	5.676	7.844	14.535	4.864
IMC-100	Ti	ppm	7	332	1475	1821	1812	18453	1754
IMC-100	Tl	ppm	0.002	0.577	0.173	0.294	0.294	0.273	0.251
IMC-100	Tm	ppm	0.0019	0.0485	0.1305	0.1405	0.153	0.3113	0.1713
IMC-100	U	ppm	0.011	5.622	1.042	1.211	2.082	3.817	1.08
IMC-100	V	ppm	0.8	5.6	33	41.6	46	244.2	41.6
IMC-100	W	ppm	0.05	0.32	0.49	0.29	0.27	6.66	1.46
IMC-100	Y	ppm	0.05	2.19	7.85	9.86	10.95	27.86	11.16
IMC-100	Yb	ppm	0.009	0.468	0.92	0.975	1.037	1.803	1.179
IMC-100	Zn	ppm	1.8	8	35	56	51	120	54
IMC-100	Zr	ppm	6	69	120	131	140	284	136
Method		Units	Detect Limit	17KAM015A	17KAM016A	17KAM018A	17KAM019A	17KAM020A	17KAM022A
SG				2.65	2.65				0.642
SG DWT		g		133.4	118.1				0.065
SG WWT		g		83.1	73.5				
IRC-100	CO_2	wt%	0.023	<0.023	<0.023	0.211	0.498	0.565	0.642
IRC-101	S	wt%	0.003	<0.003	0.005	0.009	0.042	0.004	0.065
IMP-101	Au	ppb	0.6	1.2	6.5	2	1	1	1.3
IMP-101	Pd	ppb	0.14	<0.14	<0.14	<0.14	0.3	<0.14	<0.14
IMP-101	Pt	ppb	0.06	0.12	0.18	0.1	0.2	0.1	<0.06
XRF-M01	Al_2O_3	wt%	0.02	15.47	15.59	16.21	15.79	15.89	15.81
XRF-M01	BaO	wt%	0.004	0.109	0.095	0.101	0.112	0.094	0.084
XRF-M01	CaO	wt%	0.006	2.978	2.734	3.193	2.046	1.283	1.494
XRF-M01	Cr_2O_3	wt%	0.002	0.011	0.01	0.008	0.014	0.005	0.008
XRF-M01	Fe_2O_3	wt%	0.01	2.53	2.83	3.43	2.88	2.21	2.14
XRF-M01	K_2O	wt%	0.01	2.43	2.72	2.17	2.57	3.24	2.21
XRF-M01	MgO	wt%	0.01	1.53	1.69	2.01	1.68	1.02	0.75
XRF-M01	MnO	wt%	0.002	0.049	0.049	0.067	0.045	0.033	0.03
XRF-M01	Na_2O	wt%	0.02	5.04	4.88	4.93	4.99	4.99	5.59
XRF-M01	Nitrogen 105	wt%		0.25	0.26	0.29	0.31	0.44	0.33
XRF-M01	P_2O_5	wt%	0.002	0.149	0.152	0.173	0.143	0.103	0.117
XRF-M01	SiO_2	wt%	0.04	68.73	68.06	66.24	68.19	69.65	70.63
XRF-M01	TiO_2	wt%	0.01	0.31	0.33	0.4	0.3	0.26	0.28
XRF-M01	Total	wt%		100.26	100.26	100.34	100.67	100.75	100.91

Method		Units	Detect Limit	17KAM015A	17KAM016A	17KAM018A	17KAM019A	17KAM020A	17KAM022A
XRF-M01	Total LOI 1000	wt%		0.92	1.12	1.42	1.91	1.99	1.76
XRF-T02	As	ppm	6	<6	<6	<6	<6	<6	<6
XRF-T02	Br	ppm	1.2	<1.2	<1.2	2	2	4	<1.2
XRF-T02	Cu	ppm	9	<9	<9	<9	<9	<9	<9
XRF-T02	Ga	ppm	1.3	20	19	20	20	19	20
XRF-T02	Mo	ppm	0.8	1	1	1	1	1	1
XRF-T02	Nb	ppm	0.7	4	3	4	4	5	4
XRF-T02	Ni	ppm	1.6	17	11	16	17	19	19
XRF-T02	Pb	ppm	1.7	12	13	13	11	17	10
XRF-T02	Rb	ppm	0.8	63	85	61	57	61	55
XRF-T02	Sr	ppm	0.8	866	475	764	774	591	796
XRF-T02	Th	ppm	1.5	4	6	3	4	4	3
XRF-T02	U	ppm	1.6	<1.6	2	<1.6	<1.6	<1.6	<1.6
XRF-T02	Y	ppm	0.7	12	6	11	11	11	10
XRF-T02	Zn	ppm	1	56	27	44	56	53	44
XRF-T02	Zr	ppm	1.8	132	79	124	129	132	119
IMC-100	Ba	ppm	0.8	810.4	431.6	833.3	880.2	1011.8	801.9
IMC-100	Be	ppm	0.04	1.53	1.6	1.49	1.31	1.49	1.46
IMC-100	Bi	ppm	0.47	<0.47	<0.47	<0.47	<0.47	<0.47	<0.47
IMC-100	Cd	ppm	0.013	0.059	0.033	0.04	0.089	0.051	0.048
IMC-100	Ce	ppm	0.12	62.08	35.59	58.1	60.2	63.39	54.79
IMC-100	Co	ppm	0.13	7.16	3.49	6.19	6.83	7.09	5.73
IMC-100	Cr	ppm	3	38	30	44	42	41	42
IMC-100	Cs	ppm	0.013	1.987	0.636	0.985	1.199	0.498	0.726
IMC-100	Cu	ppm	1.4	5.6	<1.4	1.7	2.4	1.4	<1.4
IMC-100	Dy	ppm	0.009	2.244	1.037	2.161	2.21	2.079	1.93
IMC-100	Er	ppm	0.007	1.149	0.599	1.099	1.16	1.15	1.002
IMC-100	Eu	ppm	0.0031	1.2197	0.5605	1.1703	1.1959	1.177	1.0235
IMC-100	Ga	ppm	0.04	20.86	19.33	20.37	20.67	20.36	21.1
IMC-100	Gd	ppm	0.009	3.441	1.534	3.217	3.211	3.128	2.815
IMC-100	Hf	ppm	0.14	3.57	2.91	3.61	3.62	3.88	3.34
IMC-100	Ho	ppm	0.0025	0.4122	0.1967	0.4059	0.4153	0.3939	0.351
IMC-100	In	ppm	0.0018	0.0233	0.0117	0.0209	0.0248	0.0224	0.0213
IMC-100	La	ppm	0.1	29.06	18.84	26.31	27.18	30.3	26.56
IMC-100	Li	ppm	0.4	31.8	7	16	15.7	13	18.8
IMC-100	Lu	ppm	0.002	0.1705	0.1099	0.161	0.163	0.1872	0.1519
IMC-100	Mo	ppm	0.08	0.86	1.04	1.41	1.12	1.14	1.21
IMC-100	Nb	ppm	0.028	5.081	3.769	5.142	4.886	5.638	4.138
IMC-100	Nd	ppm	0.06	28.71	13.47	26.99	28.37	28.51	24.01
IMC-100	Ni	ppm	0.7	17.5	10.2	15.7	17.2	18.3	16.7

Method		Units	Detect Limit	17KAM015A	17KAM016A	17KAM018A	17KAM019A	17KAM020A	17KAM022A
IMC-100	Pb	ppm	0.18	12.4	13.1	13.2	11.6	18.4	10.2
IMC-100	Pr	ppm	0.014	7.569	3.761	7.027	7.302	7.502	6.397
IMC-100	Rb	ppm	0.11	65.48	85.08	60.59	55.45	60.52	52.81
IMC-100	Sb	ppm	0.04	0.08	<0.04	<0.04	0.06	0.06	0.04
IMC-100	Sc	ppm	1.1	5	2.7	4.4	4.7	4.8	4.2
IMC-100	Sm	ppm	0.026	4.915	2.176	4.499	4.77	4.565	3.978
IMC-100	Sn	ppm	0.16	0.97	0.66	0.91	1	1.03	1
IMC-100	Sr	ppm	0.6	893.9	478.3	781	792.1	603.2	806.2
IMC-100	Ta	ppm	0.007	0.347	0.317	0.332	0.353	0.364	0.315
IMC-100	Tb	ppm	0.0023	0.4249	0.1889	0.3931	0.4093	0.3878	0.3525
IMC-100	Th	ppm	0.018	4.952	7.513	4.792	5.341	5.046	4.391
IMC-100	Ti	ppm	7	1834	922	1680	1784	1772	1498
IMC-100	Tl	ppm	0.002	0.318	0.324	0.285	0.235	0.243	0.218
IMC-100	Tm	ppm	0.0019	0.17	0.0947	0.1652	0.1645	0.1737	0.1486
IMC-100	U	ppm	0.011	1.038	1.973	1.231	1.087	1.138	0.724
IMC-100	V	ppm	0.8	41.3	21.4	38.1	39.1	41.4	33.7
IMC-100	W	ppm	0.05	0.06	0.09	0.15	0.28	1.53	0.05
IMC-100	Y	ppm	0.05	12.15	5.79	11.51	11.42	11.3	10.35
IMC-100	Yb	ppm	0.009	1.103	0.65	1.059	1.143	1.194	0.988
IMC-100	Zn	ppm	1.8	58	29	44	55	53	41
IMC-100	Zr	ppm	6	135	81	135	134	142	121
Method		Units	Detect Limit	17KAM022B	17KAM022C	17KAM024A	17KAM025A	17KAM026A	17KAM026B
SG						0.425			
SG DWT		g				<0.003			
SG WWT		g							
IRC-100	CO_2	wt%	0.023	0.582	21.547	0.425	0.222	0.096	0.09
IRC-101	S	wt%	0.003	0.003	0.246	<0.003	<0.003	<0.003	<0.003
IMP-101	Au	ppb	0.6	1	6	1	1	1	1
IMP-101	Pd	ppb	0.14	0.3	0.4	<0.14	<0.14	<0.14	<0.14
IMP-101	Pt	ppb	0.06	0.1	0.4	0.1	0.1	<0.06	<0.06
XRF-M01	Al_2O_3	wt%	0.02	15.54	6.05	17.05	15.88	14.32	14.78
XRF-M01	BaO	wt%	0.004	0.096	0.083	0.106	0.093	0.006	0.046
XRF-M01	CaO	wt%	0.006	1.341	14.141	2.039	2.122	0.365	1.669
XRF-M01	Cr_2O_3	wt%	0.002	0.005	0.101	0.006	0.009	0.003	0.004
XRF-M01	Fe_2O_3	wt%	0.01	1.97	12.1	2.48	2.72	0.58	1.51
XRF-M01	K_2O	wt%	0.01	3.53	1.52	2.74	2.78	5.32	3.59
XRF-M01	MgO	wt%	0.01	1.08	11.56	1.28	1.67	0.06	0.73
XRF-M01	MnO	wt%	0.002	0.037	0.221	0.044	0.057	0.01	0.026
XRF-M01	Na_2O	wt%	0.02	4.88	0.31	5.03	5.11	3.72	5.04
XRF-M01	Nitrogen 105	wt%		0.42	0.67	0.27	0.29	0.13	0.19
XRF-M01	P_2O_5	wt%	0.002	0.094	0.831	0.131	0.149	0.002	0.062

Method		Units	Detect Limit	17KAM022B	17KAM022C	17KAM024A	17KAM025A	17KAM026A	17KAM026B
XRF-M01	SiO_2	wt%	0.04	69.55	26.72	68.26	68.4	75.46	72.62
XRF-M01	TiO_2	wt%	0.01	0.23	3.17	0.28	0.32	0.06	0.17
XRF-M01	Total	wt%		100.25	99.3	100.76	100.59	100.28	100.96
XRF-M01	Total LOI 1000	wt%		1.9	22.49	1.32	1.28	0.37	0.71
XRF-T02	As	ppm	6	<6	<6	<6	<6	<6	<6
XRF-T02	Br	ppm	1.2	2	4	<1.2	2	<1.2	3
XRF-T02	Cu	ppm	9	<9	<9	<9	<9	<9	<9
XRF-T02	Ga	ppm	1.3	21	20	21	21	21	20
XRF-T02	Mo	ppm	0.8	1	1	1	2	1	1
XRF-T02	Nb	ppm	0.7	4	4	4	4	2	4
XRF-T02	Ni	ppm	1.6	19	19	20	20	4	18
XRF-T02	Pb	ppm	1.7	9	8	10	10	17	8
XRF-T02	Rb	ppm	0.8	39	53	47	67	55	65
XRF-T02	Sr	ppm	0.8	891	739	845	623	669	611
XRF-T02	Th	ppm	1.5	4	3	3	3	<1.5	4
XRF-T02	U	ppm	1.6	<1.6	<1.6	<1.6	<1.6	<1.6	<1.6
XRF-T02	Y	ppm	0.7	12	9	10	11	5	12
XRF-T02	Zn	ppm	1	55	42	54	51	79	52
XRF-T02	Zr	ppm	1.8	134	132	132	123	98	129
IMC-100	Ba	ppm	0.8	924.9	1422.2	973.4	990.8	768	852.7
IMC-100	Be	ppm	0.04	1.4	1.28	1.17	1.4	1.2	1.37
IMC-100	Bi	ppm	0.47	<0.47	<0.47	<0.47	<0.47	<0.47	<0.47
IMC-100	Cd	ppm	0.013	0.045	0.021	0.036	0.05	0.051	0.035
IMC-100	Ce	ppm	0.12	67.85	52.14	82.74	57.8	21.8	63.66
IMC-100	Co	ppm	0.13	7.54	7.18	7.95	6.89	1.99	6.82
IMC-100	Cr	ppm	3	43	49	45	64	18	40
IMC-100	Cs	ppm	0.013	0.812	0.615	0.972	1.451	0.943	0.471
IMC-100	Cu	ppm	1.4	1.4	3.5	1.6	1.5	1.9	1.9
IMC-100	Dy	ppm	0.009	2.341	1.907	2.281	2.136	0.972	2.365
IMC-100	Er	ppm	0.007	1.219	0.94	1.15	1.186	0.509	1.238
IMC-100	Eu	ppm	0.0031	1.3515	1.136	1.3568	1.1216	0.5891	1.2733
IMC-100	Ga	ppm	0.04	21.1	20.64	21.19	20.75	21.46	20.64
IMC-100	Gd	ppm	0.009	3.678	2.862	3.628	3.137	1.477	3.573
IMC-100	Hf	ppm	0.14	3.73	3.81	3.65	3.65	2.74	3.43
IMC-100	Ho	ppm	0.0025	0.4334	0.3453	0.3921	0.4099	0.1798	0.4415
IMC-100	In	ppm	0.0018	0.0233	0.0232	0.0245	0.0268	0.0141	0.0245
IMC-100	La	ppm	0.1	30.81	22.08	37.81	27.36	10.56	29.29
IMC-100	Li	ppm	0.4	22.7	15.5	20.7	17.5	6.6	11.8
IMC-100	Lu	ppm	0.002	0.1618	0.1455	0.152	0.1699	0.0767	0.1702
IMC-100	Mo	ppm	0.08	1.2	1.49	1.18	1.77	0.89	1.12

Method		Units	Detect Limit	17KAM022B	17KAM022C	17KAM024A	17KAM025A	17KAM026A	17KAM026B
IMC-100	Nb	ppm	0.028	4.927	4.883	4.921	4.702	2.511	4.808
IMC-100	Nd	ppm	0.06	31.77	25.33	35.73	26.44	10.19	29.92
IMC-100	Ni	ppm	0.7	18.6	18.3	19.8	18.9	2.8	16.3
IMC-100	Pb	ppm	0.18	9.8	9.1	10.5	11.1	17.8	9.7
IMC-100	Pr	ppm	0.014	8.213	6.604	9.602	7.103	2.679	7.748
IMC-100	Rb	ppm	0.11	38.11	52.32	45.95	66.23	54.51	64.03
IMC-100	Sb	ppm	0.04	<0.04	<0.04	<0.04	0.04	0.04	0.07
IMC-100	Sc	ppm	1.1	5.1	4.7	4.7	5.3	1.8	4.6
IMC-100	Sm	ppm	0.026	5.34	4.32	5.575	4.457	1.996	4.974
IMC-100	Sn	ppm	0.16	0.97	1	1.03	1	0.72	0.96
IMC-100	Sr	ppm	0.6	907.1	755.4	860.7	632.7	694	621.9
IMC-100	Ta	ppm	0.007	0.32	0.344	0.344	0.344	0.185	0.342
IMC-100	Tb	ppm	0.0023	0.4399	0.3575	0.4385	0.3946	0.1809	0.4511
IMC-100	Th	ppm	0.018	4.643	4.328	4.236	4.441	2.299	4.851
IMC-100	Ti	ppm	7	1895	1874	1890	1730	999	1751
IMC-100	Tl	ppm	0.002	0.192	0.32	0.26	0.285	0.283	0.238
IMC-100	Tm	ppm	0.0019	0.1668	0.1469	0.1588	0.1742	0.0739	0.1741
IMC-100	U	ppm	0.011	1.207	1.244	0.851	1.35	0.9	1.25
IMC-100	V	ppm	0.8	43.4	44	43.5	42.9	15.9	39.7
IMC-100	W	ppm	0.05	0.05	0.07	0.07	0.96	0.17	0.23
IMC-100	Y	ppm	0.05	12.17	9.02	10.15	11.08	5.27	12.06
IMC-100	Yb	ppm	0.009	1.093	0.997	1.051	1.185	0.507	1.154
IMC-100	Zn	ppm	1.8	54	44	54	50	77	52
IMC-100	Zr	ppm	6	139	141	137	133	97	122
Method		Units	Detect Limit	17KAM027B	17KAM028A	17KAM029A	17KAM030A	17KAM031A	17KAM032A
SG					2.7	0.348	<0.023	0.728	
SG DWT		g			162.3	<0.003	0.003	0.003	
SG WWT		g			102.2				
IRC-100	CO_2	wt%	0.023	0.717	0.146	0.348	<0.023	0.728	1.198
IRC-101	S	wt%	0.003	0.011	<0.003	<0.003	0.003	0.003	<0.003
IMP-101	Au	ppb	0.6	1	1.3	1	0.9	2	1
IMP-101	Pd	ppb	0.14	<0.14	<0.14	<0.14	<0.14	0.2	<0.14
IMP-101	Pt	ppb	0.06	<0.06	0.23	0.2	0.09	0.6	0.1
XRF-M01	Al_2O_3	wt%	0.02	16.64	15.64	15.8	15.12	16.02	15.55
XRF-M01	BaO	wt%	0.004	0.074	0.108	0.127	0.091	0.078	0.094
XRF-M01	CaO	wt%	0.006	2.531	3.137	2.739	2.519	2.353	3.175
XRF-M01	Cr_2O_3	wt%	0.002	0.005	0.013	0.009	0.012	0.008	0.009
XRF-M01	Fe_2O_3	wt%	0.01	2.44	3.42	3.17	2.53	3.09	2.89
XRF-M01	K_2O	wt%	0.01	1.48	2.44	3.64	2.66	2.89	2.59
XRF-M01	MgO	wt%	0.01	1	2.08	1.89	1.54	1.68	1.82
XRF-M01	MnO	wt%	0.002	0.032	0.066	0.058	0.049	0.045	0.049

Method		Units	Detect Limit	17KAM027B	17KAM028A	17KAM029A	17KAM030A	17KAM031A	17KAM032A
XRF-M01	Na_2O	wt%	0.02	5.58	4.84	4.74	4.94	4.61	4.77
XRF-M01	Nitrogen 105	wt%		0.31	0.31	0.32	0.32	0.35	0.34
XRF-M01	P_2O_5	wt%	0.002	0.105	0.192	0.176	0.139	0.12	0.152
XRF-M01	SiO_2	wt%	0.04	69.03	66.87	66.65	69.25	67.61	66.89
XRF-M01	TiO_2	wt%	0.01	0.26	0.36	0.35	0.3	0.3	0.33
XRF-M01	Total	wt%		101.23	100.51	100.68	100.34	100.77	100.91
XRF-M01	Total LOI 1000	wt%		2.06	1.34	1.34	1.18	1.97	2.6
XRF-T02	As	ppm	6	<6	<6	<6	<6	<6	<6
XRF-T02	Br	ppm	1.2	3	<1.2	6	10	2	<1.2
XRF-T02	Cu	ppm	9	<9	10	<9	12	<9	<9
XRF-T02	Ga	ppm	1.3	22	22	20	19	20	20
XRF-T02	Mo	ppm	0.8	1	1	1	1	1	4
XRF-T02	Nb	ppm	0.7	5	3	5	4	5	5
XRF-T02	Ni	ppm	1.6	22	102	18	23	18	26
XRF-T02	Pb	ppm	1.7	13	10	7	3	8	7
XRF-T02	Rb	ppm	0.8	50	72	74	82	57	76
XRF-T02	Sr	ppm	0.8	946	898	568	553	629	691
XRF-T02	Th	ppm	1.5	5	4	4	5	3	5
XRF-T02	U	ppm	1.6	<1.6	<1.6	<1.6	<1.6	<1.6	<1.6
XRF-T02	Y	ppm	0.7	12	10	12	11	8	12
XRF-T02	Zn	ppm	1	61	88	48	47	57	35
XRF-T02	Zr	ppm	1.8	142	134	135	127	129	120
IMC-100	Ba	ppm	0.8	715.2	486.2	779.2	912.9	807.1	886.7
IMC-100	Be	ppm	0.04	1.61	1.56	1.23	1.43	1.59	1.58
IMC-100	Bi	ppm	0.47	<0.47	<0.47	<0.47	<0.47	<0.47	<0.47
IMC-100	Cd	ppm	0.013	0.044	0.08	0.043	0.039	0.064	0.02
IMC-100	Ce	ppm	0.12	78.29	63.65	62.69	62.15	51.58	74.79
IMC-100	Co	ppm	0.13	8.15	16.65	6.53	7.83	7.51	7.58
IMC-100	Cr	ppm	3	44	169	38	54	52	56
IMC-100	Cs	ppm	0.013	0.476	2.871	0.534	2.078	1.014	1.202
IMC-100	Cu	ppm	1.4	3.4	10.7	3.5	14.4	<1.4	6.7
IMC-100	Dy	ppm	0.009	2.435	1.902	2.395	2.078	1.539	2.453
IMC-100	Er	ppm	0.007	1.187	0.971	1.277	1.085	0.811	1.214
IMC-100	Eu	ppm	0.0031	1.464	1.2767	1.2606	1.1678	0.9004	1.3888
IMC-100	Ga	ppm	0.04	21.36	21.53	20.45	19.92	20.42	20.22
IMC-100	Gd	ppm	0.009	3.994	3.3	3.591	3.263	2.271	3.97
IMC-100	Hf	ppm	0.14	4.06	3.51	3.8	3.57	3.43	3.93
IMC-100	Ho	ppm	0.0025	0.4451	0.3443	0.4464	0.3848	0.2881	0.439
IMC-100	In	ppm	0.0018	0.0276	0.0412	0.0226	0.0207	0.0223	0.0174

Method		Units	Detect Limit	17KAM027B	17KAM028A	17KAM029A	17KAM030A	17KAM031A	17KAM032A
IMC-100	La	ppm	0.1	36.32	31.63	28.99	28.47	20.75	34.66
IMC-100	Li	ppm	0.4	15.7	37.3	8.9	17.8	12.6	13
IMC-100	Lu	ppm	0.002	0.1736	0.1669	0.1834	0.1567	0.124	0.1712
IMC-100	Mo	ppm	0.08	1.15	0.99	0.93	1.56	1.38	4.04
IMC-100	Nb	ppm	0.028	5.606	3.673	5.031	4.681	5.558	5.61
IMC-100	Nd	ppm	0.06	37.06	27.66	30.25	27.97	21.24	34.82
IMC-100	Ni	ppm	0.7	20.9	99.7	16.8	23.5	17.4	25.7
IMC-100	Pb	ppm	0.18	13.2	10.6	7.5	4.3	7.9	7.4
IMC-100	Pr	ppm	0.014	9.64	7.25	7.815	7.367	5.537	9.177
IMC-100	Rb	ppm	0.11	47.3	69.74	71.96	84.61	59.02	76.63
IMC-100	Sb	ppm	0.04	<0.04	0.07	0.08	0.1	<0.04	0.12
IMC-100	Sc	ppm	1.1	5.2	9.7	4.6	5	4.8	5.3
IMC-100	Sm	ppm	0.026	5.991	4.681	5.183	4.659	3.536	5.824
IMC-100	Sn	ppm	0.16	1.07	1.02	0.98	1	1.01	1.2
IMC-100	Sr	ppm	0.6	955.3	902.9	579.1	570.5	650.4	710.2
IMC-100	Ta	ppm	0.007	0.395	0.148	0.354	0.351	0.351	0.465
IMC-100	Tb	ppm	0.0023	0.4785	0.3817	0.4362	0.4082	0.2868	0.4597
IMC-100	Th	ppm	0.018	5.93	4.978	5.221	6.417	4.784	6.87
IMC-100	Ti	ppm	7	2015	2560	1771	1796	1817	1890
IMC-100	Tl	ppm	0.002	0.214	0.436	0.276	0.434	0.224	0.339
IMC-100	Tm	ppm	0.0019	0.1695	0.1354	0.18	0.1625	0.1162	0.1752
IMC-100	U	ppm	0.011	1.454	0.597	1.209	1.224	1.302	1.399
IMC-100	V	ppm	0.8	44.9	75.1	37.8	42.6	42.4	43.9
IMC-100	W	ppm	0.05	0.1	0.08	0.14	0.66	0.18	2.43
IMC-100	Y	ppm	0.05	12.34	9.59	12.55	11.4	8.01	12.37
IMC-100	Yb	ppm	0.009	1.117	0.944	1.169	1.023	0.816	1.151
IMC-100	Zn	ppm	1.8	60	86	49	49	56	37
IMC-100	Zr	ppm	6	146	130	137	133	131	147
Method		Units	Detect Limit	17KAM034A	17KAM035A	17KAM035B	17KAM036A	17KAM037A	17KAM038A
SG				2.62	2.66	0.216		2.67	2.67
SG DWT		g		147.1	104.2	<0.003		285.4	105.3
SG WWT		g		91	65			178.6	65.8
IRC-100	CO_2	wt%	0.023	<0.023	<0.023	0.216	0.153	1.007	<0.023
IRC-101	S	wt%	0.003	<0.003	<0.003	<0.003	<0.003	0.004	<0.003
IMP-101	Au	ppb	0.6	1.2	1.1	1	1	1.2	1
IMP-101	Pd	ppb	0.14	<0.14	0.17	<0.14	<0.14	<0.14	<0.14
IMP-101	Pt	ppb	0.06	<0.06	0.09	<0.06	0.1	0.12	<0.06
XRF-M01	Al_2O_3	wt%	0.02	14.69	15.92	16.82	16.64	15.8	16.11
XRF-M01	BaO	wt%	0.004	0.068	0.088	0.083	0.091	0.107	0.1
XRF-M01	CaO	wt%	0.006	1.715	2.97	1.763	2.017	2.865	2.737
XRF-M01	Cr_2O_3	wt%	0.002	0.007	0.009	0.004	0.005	0.007	0.006

Method		Units	Detect Limit	17KAM034A	17KAM035A	17KAM035B	17KAM036A	17KAM037A	17KAM038A
XRF-M01	Fe_2O_3	wt%	0.01	1.55	2.82	2.42	2.73	2.47	2.55
XRF-M01	K_2O	wt%	0.01	3.23	2.33	2.77	2.71	2.66	2.53
XRF-M01	MgO	wt%	0.01	0.64	1.41	1.38	1.5	1.24	1.3
XRF-M01	MnO	wt%	0.002	0.028	0.049	0.047	0.051	0.046	0.047
XRF-M01	Na_2O	wt%	0.02	4.54	5.07	5.13	5.28	4.88	5.12
XRF-M01	Nitrogen 105	wt%		0.23	0.27	0.44	0.3	0.27	0.24
XRF-M01	P_2O_5	wt%	0.002	0.069	0.152	0.144	0.146	0.153	0.142
XRF-M01	SiO_2	wt%	0.04	73.33	68.4	67.54	66.64	68.07	68.76
XRF-M01	TiO_2	wt%	0.01	0.17	0.32	0.31	0.32	0.32	0.3
XRF-M01	Total	wt%		100.75	100.36	99.89	99.43	100.57	100.49
XRF-M01	Total LOI 1000	wt%		0.72	0.83	1.48	1.3	1.95	0.78
XRF-T02	As	ppm	6	<6	<6	<6	<6	<6	<6
XRF-T02	Br	ppm	1.2	3	3	<1.2	<1.2	<1.2	2
XRF-T02	Cu	ppm	9	33	<9	10	<9	<9	19
XRF-T02	Ga	ppm	1.3	18	20	22	20	19	19
XRF-T02	Mo	ppm	0.8	3	1	1	2	2	1
XRF-T02	Nb	ppm	0.7	4	5	3	3	4	2
XRF-T02	Ni	ppm	1.6	21	19	100	7	27	47
XRF-T02	Pb	ppm	1.7	12	7	11	12	14	3
XRF-T02	Rb	ppm	0.8	87	60	73	64	79	45
XRF-T02	Sr	ppm	0.8	369	740	903	538	535	599
XRF-T02	Th	ppm	1.5	6	3	4	3	9	<1.5
XRF-T02	U	ppm	1.6	<1.6	<1.6	<1.6	<1.6	<1.6	<1.6
XRF-T02	Y	ppm	0.7	9	11	10	4	9	20
XRF-T02	Zn	ppm	1	41	43	86	35	47	88
XRF-T02	Zr	ppm	1.8	123	122	125	104	117	79
IMC-100	Ba	ppm	0.8	690.7	861.3	495.7	797.3	733.5	814.4
IMC-100	Be	ppm	0.04	1.57	1.53	1.56	1.19	1.38	1.19
IMC-100	Bi	ppm	0.47	<0.47	<0.47	<0.47	<0.47	<0.47	<0.47
IMC-100	Cd	ppm	0.013	0.021	0.033	0.067	0.031	0.051	0.159
IMC-100	Ce	ppm	0.12	62.56	67.9	63.52	24.99	56.73	91.17
IMC-100	Co	ppm	0.13	7.33	7.19	17.02	3.55	9.02	35.07
IMC-100	Cr	ppm	3	54	53	173	48	61	184
IMC-100	Cs	ppm	0.013	1.123	0.618	2.902	1.819	1.248	0.433
IMC-100	Cu	ppm	1.4	39.2	<1.4	10.9	6.8	6.2	21.6
IMC-100	Dy	ppm	0.009	1.767	2.125	2.003	0.787	1.823	4.029
IMC-100	Er	ppm	0.007	0.943	1.113	0.994	0.377	0.939	1.907
IMC-100	Eu	ppm	0.0031	1.0607	1.19	1.2525	0.5352	1.0429	2.6201
IMC-100	Ga	ppm	0.04	18.53	20.46	21.68	20.81	19.47	18.55

Method		Units	Detect Limit	17KAM034A	17KAM035 A	17KAM035 B	17KAM036 A	17KAM037 A	17KAM038 A
IMC-100	Gd	ppm	0.009	2.924	3.218	3.341	1.235	2.796	7.029
IMC-100	Hf	ppm	0.14	3.61	3.38	3.73	2.78	3.65	2.17
IMC-100	Ho	ppm	0.0025	0.3274	0.3941	0.3513	0.1364	0.3386	0.7205
IMC-100	In	ppm	0.0018	0.0156	0.0229	0.0382	0.0133	0.0219	0.0634
IMC-100	La	ppm	0.1	28.69	34.09	31.72	11.89	28.01	39.76
IMC-100	Li	ppm	0.4	17.4	16.5	38.1	15.2	12.6	22.9
IMC-100	Lu	ppm	0.002	0.146	0.1559	0.1629	0.0536	0.1569	0.2439
IMC-100	Mo	ppm	0.08	3.44	1.52	1.13	2.41	2.1	1.1
IMC-100	Nb	ppm	0.028	4.441	5.555	3.868	3.403	4.238	2.744
IMC-100	Nd	ppm	0.06	28.19	29.64	28.43	10.37	24.44	53.59
IMC-100	Ni	ppm	0.7	21.8	17.9	99.9	6	26.1	45.2
IMC-100	Pb	ppm	0.18	13.4	7.9	10.8	12.2	14.1	3.5
IMC-100	Pr	ppm	0.014	7.499	7.858	7.265	2.847	6.561	12.494
IMC-100	Rb	ppm	0.11	86.72	60.1	72.28	62.69	77.27	44.37
IMC-100	Sb	ppm	0.04	0.06	0.19	0.08	<0.04	0.12	<0.04
IMC-100	Sc	ppm	1.1	4.4	5.2	9.9	2.3	5.6	29.1
IMC-100	Sm	ppm	0.026	4.321	4.787	4.783	1.808	4.005	10.149
IMC-100	Sn	ppm	0.16	1.05	0.95	1.06	0.71	0.98	1.55
IMC-100	Sr	ppm	0.6	374.2	765.5	919.2	550.3	543.9	601.3
IMC-100	Ta	ppm	0.007	0.344	0.321	0.16	0.159	0.315	0.145
IMC-100	Tb	ppm	0.0023	0.3385	0.4044	0.3901	0.1577	0.3471	0.822
IMC-100	Th	ppm	0.018	6.442	4.503	4.766	4.392	10.325	2.268
IMC-100	Ti	ppm	7	1709	1749	2629	1313	1642	4723
IMC-100	Tl	ppm	0.002	0.387	0.23	0.445	0.339	0.38	0.243
IMC-100	Tm	ppm	0.0019	0.1386	0.1591	0.1441	0.0524	0.1402	0.2518
IMC-100	U	ppm	0.011	1.561	1.458	0.62	1.155	1.729	0.586
IMC-100	V	ppm	0.8	35.8	43.7	77.9	23.4	45.3	220.4
IMC-100	W	ppm	0.05	1.42	0.21	0.08	0.22	0.57	0.31
IMC-100	Y	ppm	0.05	8.42	11.08	10.08	3.79	9.31	19.94
IMC-100	Yb	ppm	0.009	0.949	1.061	0.957	0.366	0.961	1.65
IMC-100	Zn	ppm	1.8	41	43	85	37	47	91
IMC-100	Zr	ppm	6	130	129	145	101	124	78
Method		Units	Detect Limit	17KAM038B	17KAM039 A	17KAM039 B	17KAM039 B SP	17KAM040 A	17KAM040 B
SG						0.135	0.085		
SG DWT		g				0.006	0.007		
SG WWT		g							
IRC-100	CO_2	wt%	0.023	0.153	0.14	0.135	0.085	0.087	0.481
IRC-101	S	wt%	0.003	<0.003	<0.003	0.006	0.007	<0.003	0.012
IMP-101	Au	ppb	0.6	2	1	3	1	1	1
IMP-101	Pd	ppb	0.14	<0.14	<0.14	0.2	0.3	<0.14	<0.14
IMP-101	Pt	ppb	0.06	<0.06	0.1	0.4	0.3	0.1	0.1

Method		Units	Detect Limit	17KAM038B	17KAM039 A	17KAM039 B	17KAM039 B SP	17KAM040 A	17KAM040 B
XRF-M01	Al_2O_3	wt%	0.02	15.83	16.54	15.23	15.38	17.53	16.04
XRF-M01	BaO	wt%	0.004	0.082	0.077	0.051	0.052	0.098	0.15
XRF-M01	CaO	wt%	0.006	1.488	3.051	4.38	4.359	2.733	2.095
XRF-M01	Cr_2O_3	wt%	0.002	0.002	0.007	0.025	0.025	0.016	0.007
XRF-M01	Fe_2O_3	wt%	0.01	1.26	3.07	4.67	4.58	2.87	2.91
XRF-M01	K_2O	wt%	0.01	2.28	1.95	2.01	2.07	1.95	2.57
XRF-M01	MgO	wt%	0.01	0.34	1.67	4.07	4.01	1.57	1.4
XRF-M01	MnO	wt%	0.002	0.02	0.055	0.09	0.09	0.05	0.038
XRF-M01	Na_2O	wt%	0.02	6.01	5.28	4.58	4.62	5.13	5.05
XRF-M01	Nitrogen 105	wt%		0.25	0.27	0.22	0.16	0.37	0.5
XRF-M01	P_2O_5	wt%	0.002	0.055	0.178	0.223	0.218	0.156	0.149
XRF-M01	SiO_2	wt%	0.04	71.07	67.03	63.24	63.43	66.73	67.14
XRF-M01	TiO_2	wt%	0.01	0.17	0.36	0.46	0.46	0.33	0.32
XRF-M01	Total	wt%		99.44	100.59	99.96	100.15	100.34	99.89
XRF-M01	Total LOI 1000	wt%		0.84	1.31	0.92	0.86	1.18	2.03
XRF-T02	As	ppm	6	<6	<6	<6	<6	<6	<6
XRF-T02	Br	ppm	1.2	2	<1.2	<1.2	<1.2	3	<1.2
XRF-T02	Cu	ppm	9	<9	<9	<9	<9	<9	<9
XRF-T02	Ga	ppm	1.3	18	21	17	20	20	20
XRF-T02	Mo	ppm	0.8	2	1	1	1	1	1
XRF-T02	Nb	ppm	0.7	5	6	3	4	3	4
XRF-T02	Ni	ppm	1.6	30	10	15	29	17	32
XRF-T02	Pb	ppm	1.7	8	4	4	11	14	11
XRF-T02	Rb	ppm	0.8	106	49	42	60	67	71
XRF-T02	Sr	ppm	0.8	814	50	40	742	647	792
XRF-T02	Th	ppm	1.5	5	5	2	3	4	3
XRF-T02	U	ppm	1.6	<1.6	<1.6	<1.6	<1.6	<1.6	<1.6
XRF-T02	Y	ppm	0.7	11	7	7	11	9	10
XRF-T02	Zn	ppm	1	44	12	21	57	44	53
XRF-T02	Zr	ppm	1.8	143	135	94	139	110	121
IMC-100	Ba	ppm	0.8	1167.5	93.4	55.6	985	874.4	990.4
IMC-100	Be	ppm	0.04	1.48	0.91	1.2	2.07	1.36	1.23
IMC-100	Bi	ppm	0.47	<0.47	<0.47	<0.47	<0.47	<0.47	<0.47
IMC-100	Cd	ppm	0.013	0.075	0.029	0.02	0.094	0.045	0.048
IMC-100	Ce	ppm	0.12	75.87	61.09	46.43	75.08	49.84	54.2
IMC-100	Co	ppm	0.13	9.12	2.57	5.63	8.56	5.87	6.33
IMC-100	Cr	ppm	3	71	65	61	56	34	52
IMC-100	Cs	ppm	0.013	0.508	1.837	1.633	2.946	0.541	1.34
IMC-100	Cu	ppm	1.4	1.6	<1.4	1.9	1.9	<1.4	5.4

Method		Units	Detect Limit	17KAM038B	17KAM039 A	17KAM039 B	17KAM039 B SP	17KAM040 A	17KAM040 B
IMC-100	Dy	ppm	0.009	2.295	1.222	1.252	2.29	1.724	1.898
IMC-100	Er	ppm	0.007	1.151	0.715	0.676	1.215	0.921	0.991
IMC-100	Eu	ppm	0.0031	1.4335	0.5228	0.6625	1.3209	1.0027	1.0112
IMC-100	Ga	ppm	0.04	19.16	20.92	17.29	20.08	20.36	20.5
IMC-100	Gd	ppm	0.009	3.887	1.35	1.753	3.617	2.693	2.782
IMC-100	Hf	ppm	0.14	3.91	3.94	2.66	3.78	3.24	3.76
IMC-100	Ho	ppm	0.0025	0.4291	0.2332	0.2391	0.4369	0.3217	0.3575
IMC-100	In	ppm	0.0018	0.0242	0.0212	0.0175	0.027	0.0189	0.0238
IMC-100	La	ppm	0.1	35.34	28.16	20.91	35.18	23.12	25.22
IMC-100	Li	ppm	0.4	5.4	28.6	44.8	21.7	10.9	21.7
IMC-100	Lu	ppm	0.002	0.1655	0.1177	0.0975	0.1636	0.1365	0.152
IMC-100	Mo	ppm	0.08	1.52	2.28	2.32	1.04	0.81	1.53
IMC-100	Nb	ppm	0.028	5.105	5.751	3.609	4.45	3.816	4.427
IMC-100	Nd	ppm	0.06	34.19	23.09	19.9	32.98	22.71	23.61
IMC-100	Ni	ppm	0.7	30.9	9.5	14.7	28.4	16.5	19.7
IMC-100	Pb	ppm	0.18	8.6	5.8	5.7	12.4	14.8	10.8
IMC-100	Pr	ppm	0.014	8.977	6.646	5.36	8.621	5.869	6.247
IMC-100	Rb	ppm	0.11	109.16	48.78	41.71	58.41	64.79	68.3
IMC-100	Sb	ppm	0.04	0.05	0.07	0.14	0.09	0.04	0.09
IMC-100	Sc	ppm	1.1	6.4	4.4	3.1	5.8	4	4.4
IMC-100	Sm	ppm	0.026	5.706	2.496	2.856	5.355	3.842	3.906
IMC-100	Sn	ppm	0.16	1.11	1.01	0.79	1.03	0.86	0.95
IMC-100	Sr	ppm	0.6	855	50.2	40.9	751	662.5	800.9
IMC-100	Ta	ppm	0.007	0.377	0.392	0.252	0.356	0.277	0.336
IMC-100	Tb	ppm	0.0023	0.4548	0.203	0.2192	0.4331	0.3295	0.3536
IMC-100	Th	ppm	0.018	6.276	6.767	3.537	4.365	6.046	4.774
IMC-100	Ti	ppm	7	2047	1904	1317	1973	1511	1591
IMC-100	Tl	ppm	0.002	0.471	0.198	0.174	0.237	0.25	0.381
IMC-100	Tm	ppm	0.0019	0.1646	0.1111	0.0951	0.1634	0.1355	0.1468
IMC-100	U	ppm	0.011	1.285	1.017	0.871	0.811	0.998	0.852
IMC-100	V	ppm	0.8	53.4	34.8	21.3	54	34.3	34
IMC-100	W	ppm	0.05	0.11	0.32	0.61	16.81	0.14	0.24
IMC-100	Y	ppm	0.05	12.21	6.35	6.63	11.71	9.28	10
IMC-100	Yb	ppm	0.009	1.103	0.735	0.657	1.065	0.897	1.035
IMC-100	Zn	ppm	1.8	46	13	26	57	44	52
IMC-100	Zr	ppm	6	151	137	97	144	114	134
Method		Units	Detect Limit	17KAM040C	17KAM041 A	17KAM042 A	17KAM043 A	17KAM044 A	17KAM044 B
SG					0.347				0.315
SG DWT		g			0.007				0.004
SG WWT		g							
IRC-100	CO_2	wt%	0.023	0.136	0.347	0.236	0.172	0.556	0.315

Method		Units	Detect Limit	17KAM040C	17KAM041A	17KAM042A	17KAM043A	17KAM044A	17KAM044B
IRC-101	S	wt%	0.003	<0.003	0.007	0.003	<0.003	0.003	0.004
IMP-101	Au	ppb	0.6	1	1	11	1	1	3
IMP-101	Pd	ppb	0.14	<0.14	2.1	<0.14	<0.14	<0.14	<0.14
IMP-101	Pt	ppb	0.06	<0.06	2.9	<0.06	<0.06	0.1	<0.06
XRF-M01	Al_2O_3	wt%	0.02	16.5	14.22	15.94	16.79	15.95	15.93
XRF-M01	BaO	wt%	0.004	0.1	0.086	0.101	0.086	0.087	0.084
XRF-M01	CaO	wt%	0.006	2.105	9.659	1.932	2.772	2.457	1.807
XRF-M01	Cr_2O_3	wt%	0.002	0.006	0.026	0.009	0.006	0.005	0.006
XRF-M01	Fe_2O_3	wt%	0.01	3.09	10.02	2.86	2.39	2.45	1.56
XRF-M01	K_2O	wt%	0.01	2.32	1.66	2.65	2.3	2.56	2.63
XRF-M01	MgO	wt%	0.01	1.23	6.69	1.44	1.18	0.96	0.54
XRF-M01	MnO	wt%	0.002	0.037	0.151	0.039	0.04	0.036	0.019
XRF-M01	Na_2O	wt%	0.02	5.08	3.66	5.19	5.07	5.03	5.34
XRF-M01	Nitrogen 105	wt%		0.53	1.12	0.42	0.2	0.31	0.38
XRF-M01	P_2O_5	wt%	0.002	0.152	0.538	0.144	0.115	0.128	0.067
XRF-M01	SiO_2	wt%	0.04	67.57	49.57	67.78	68.07	69.5	71.05
XRF-M01	TiO_2	wt%	0.01	0.33	0.81	0.3	0.27	0.29	0.23
XRF-M01	Total	wt%		100.1	100.33	99.99	99.89	100.87	100.33
XRF-M01	Total LOI 1000	wt%		1.58	3.24	1.6	0.8	1.42	1.07
XRF-T02	As	ppm	6	<6	<6	<6	<6	<6	<6
XRF-T02	Br	ppm	1.2	1.5	<1.2	<1.2	<1.2	2.7	11
XRF-T02	Cu	ppm	9	<9	<9	<9	<9	<9	<9
XRF-T02	Ga	ppm	1.3	19.8	19.6	20	20.6	19.5	19.3
XRF-T02	Mo	ppm	0.8	2.4	2.3	1.4	2	1.5	1.8
XRF-T02	Nb	ppm	0.7	4	3.8	5.2	4.4	3.5	3.8
XRF-T02	Ni	ppm	1.6	24.2	22.2	13	19.6	11.6	18.3
XRF-T02	Pb	ppm	1.7	9.5	12.4	11.8	20	8.8	3.4
XRF-T02	Rb	ppm	0.8	51.4	62.1	55.1	68	68.9	66.2
XRF-T02	Sr	ppm	0.8	794.3	736.8	469.7	857	601.8	694.8
XRF-T02	Th	ppm	1.5	3.7	5.7	5	3.3	3.2	3.2
XRF-T02	U	ppm	1.6	<1.6	<1.6	<1.6	<1.6	<1.6	<1.6
XRF-T02	Y	ppm	0.7	11.8	10.7	13.4	12.5	10.3	11.7
XRF-T02	Zn	ppm	1	54	50	40	55	39	44
XRF-T02	Zr	ppm	1.8	129.9	129.5	128.4	137.6	124	132.4
IMC-100	Ba	ppm	0.8	967.9	854.4	791.2	1026.2	932.5	866.5
IMC-100	Be	ppm	0.04	1.59	1.66	1.69	1.66	1.53	1.16
IMC-100	Bi	ppm	0.47	<0.47	<0.47	<0.47	<0.47	<0.47	<0.47
IMC-100	Cd	ppm	0.013	0.069	0.053	0.085	0.066	0.056	0.028
IMC-100	Ce	ppm	0.12	64.3	61.36	68.58	64.69	44.6	56.48

Method		Units	Detect Limit	17KAM040C	17KAM041A	17KAM042A	17KAM043A	17KAM044A	17KAM044B
IMC-100	Co	ppm	0.13	8.19	7.37	5.05	7.86	4.9	6.28
IMC-100	Cr	ppm	3	87	131	53	64	55	92
IMC-100	Cs	ppm	0.013	1.107	0.852	3.973	1.355	1.049	0.333
IMC-100	Cu	ppm	1.4	4	5.2	3.3	1.4	1.5	3
IMC-100	Dy	ppm	0.009	2.132	2.03	2.282	2.334	1.819	2.1
IMC-100	Er	ppm	0.007	1.098	1.028	1.233	1.223	1.008	1.123
IMC-100	Eu	ppm	0.0031	1.273	1.1383	1.3181	1.3015	0.927	1.0667
IMC-100	Ga	ppm	0.04	20.93	20.16	21.26	21.33	21	20.5
IMC-100	Gd	ppm	0.009	3.281	3.126	3.513	3.506	2.534	3.002
IMC-100	Hf	ppm	0.14	3.61	3.76	3.32	3.72	3.35	3.49
IMC-100	Ho	ppm	0.0025	0.4007	0.3691	0.4291	0.4276	0.3376	0.3891
IMC-100	In	ppm	0.0018	0.0233	0.0224	0.0215	0.027	0.0198	0.0228
IMC-100	La	ppm	0.1	30.7	29.8	30.8	30	20.5	27.2
IMC-100	Li	ppm	0.4	16.2	21.3	12.1	14.6	10.1	13
IMC-100	Lu	ppm	0.002	0.159	0.153	0.171	0.178	0.14	0.16
IMC-100	Mo	ppm	0.08	2.95	3.19	1.94	1.97	2.24	2.35
IMC-100	Nb	ppm	0.028	4.667	4.72	5.855	5.296	4.148	4.309
IMC-100	Nd	ppm	0.06	29.73	27.21	32.12	31.29	21.04	26.56
IMC-100	Ni	ppm	0.7	24.9	23.5	13.1	19.7	11.8	18.7
IMC-100	Pb	ppm	0.18	10.1	12.26	12.45	19.62	8.75	4.41
IMC-100	Pr	ppm	0.014	7.63	7.159	8.42	7.918	5.437	6.908
IMC-100	Rb	ppm	0.11	52.62	62.87	56.93	70.21	71.48	67.77
IMC-100	Sb	ppm	0.04	0.11	0.05	0.12	0.23	0.08	0.06
IMC-100	Sc	ppm	1.1	5.8	5.4	4.4	5.9	3.9	4.7
IMC-100	Sm	ppm	0.026	4.979	4.564	5.269	5.314	3.59	4.302
IMC-100	Sn	ppm	0.16	0.87	0.88	0.79	0.9	0.76	0.83
IMC-100	Sr	ppm	0.6	814.7	746.2	482.6	884.9	622.4	715.7
IMC-100	Ta	ppm	0.007	0.343	0.361	0.326	0.358	0.303	0.317
IMC-100	Tb	ppm	0.0023	0.4059	0.3737	0.4306	0.4265	0.3242	0.3741
IMC-100	Th	ppm	0.018	4.929	7.129	6.525	4.651	4.411	4.178
IMC-100	Ti	ppm	7	1942	1815	1628	1995	1555	1704
IMC-100	Tl	ppm	0.002	0.234	0.27	0.258	0.242	0.273	0.28
IMC-100	Tm	ppm	0.0019	0.1605	0.1531	0.1794	0.1726	0.1419	0.1655
IMC-100	U	ppm	0.011	1.012	1.076	0.788	1.093	1.197	1.035
IMC-100	V	ppm	0.8	45.5	42.5	35.9	47.6	32.6	34.8
IMC-100	W	ppm	0.05	0.3	0.12	7.71	0.1	0.26	0.18
IMC-100	Y	ppm	0.05	11.98	10.92	13.21	12.83	10.27	11.38
IMC-100	Yb	ppm	0.009	1.078	1.006	1.154	1.171	0.962	1.069
IMC-100	Zn	ppm	1.8	57.9	53.4	45.4	57.7	43	46.3
IMC-100	Zr	ppm	6	138	139	126	141	125	131

Method		Units	Detect Limit	17KAM045A	17KAM045A SP	17KAM045B	17KAM046A	17KAM047A	17KAM048A
SG						0.162	0.155	0.607	0.31
SG DWT		g				0.003	0.004	0.004	<0.003
SG WWT		g							
IRC-100	CO_2	wt%	0.023	1.201	1.192	0.162	0.155	0.607	0.31
IRC-101	S	wt%	0.003	0.014	0.014	0.003	0.004	0.004	<0.003
IMP-101	Au	ppb	0.6	1	1	<0.6	1	1	1
IMP-101	Pd	ppb	0.14	<0.14	<0.14	<0.14	<0.14	<0.14	<0.14
IMP-101	Pt	ppb	0.06	0.1	0.1	<0.06	<0.06	0.1	0.1
XRF-M01	Al_2O_3	wt%	0.02	16.24	15.76	13.09	16.55	16.21	16.09
XRF-M01	BaO	wt%	0.004	0.098	0.106	0.006	0.011	0.09	0.086
XRF-M01	CaO	wt%	0.006	2.444	2.399	0.06	0.061	2.329	1.536
XRF-M01	Cr_2O_3	wt%	0.002	0.005	0.008	0.008	0.009	0.007	0.007
XRF-M01	Fe_2O_3	wt%	0.01	2.61	2.66	2.17	2.08	2.77	2.84
XRF-M01	K_2O	wt%	0.01	2.5	2.65	0.64	0.74	2.37	2.63
XRF-M01	MgO	wt%	0.01	1.27	1.29	0.18	0.14	1.52	0.93
XRF-M01	MnO	wt%	0.002	0.058	0.056	0.006	0.004	0.043	0.049
XRF-M01	Na_2O	wt%	0.02	5.24	5.23	0.07	0.08	5.13	5.08
XRF-M01	Nitrogen 105	wt%		0.42	0.38	0.79	0.72	0.35	0.41
XRF-M01	P_2O_5	wt%	0.002	0.148	0.152	0.048	0.033	0.155	0.144
XRF-M01	SiO_2	wt%	0.04	67.18	67.96	79.1	74.21	67.43	68.54
XRF-M01	TiO_2	wt%	0.01	0.31	0.31	0.23	0.34	0.31	0.31
XRF-M01	Total	wt%		100.57	100.95	100.54	100.37	100.23	99.87
XRF-M01	Total LOI 1000	wt%		2.48	2.38	4.93	6.12	1.87	1.63
XRF-T02	As	ppm	6	<6	<6	<6	<6	<6	<6
XRF-T02	Br	ppm	1.2	<1.2	1.5	1.9	3.3	1.6	2.6
XRF-T02	Cu	ppm	9	104	<9	25	<9	<9	<9
XRF-T02	Ga	ppm	1.3	21.3	19.8	20	19.7	6.6	19.2
XRF-T02	Mo	ppm	0.8	1.5	1.9	6.9	1.9	4.7	1.9
XRF-T02	Nb	ppm	0.7	10.9	3	4.6	4.2	<0.7	3.8
XRF-T02	Ni	ppm	1.6	68.2	16.8	14.1	14.2	6.5	15.1
XRF-T02	Pb	ppm	1.7	3.9	11.6	24.2	2.1	<1.7	<1.7
XRF-T02	Rb	ppm	0.8	20.2	56.3	75.5	76.2	29.8	71.7
XRF-T02	Sr	ppm	0.8	337.6	683.8	684.7	528.5	16.4	262.2
XRF-T02	Th	ppm	1.5	2.4	3.1	4.2	3.9	<1.5	3.2
XRF-T02	U	ppm	1.6	<1.6	<1.6	<1.6	<1.6	<1.6	<1.6
XRF-T02	Y	ppm	0.7	32.8	10.7	9.6	9.7	19.1	4.8
XRF-T02	Zn	ppm	1	126	44	37	58	15	28
XRF-T02	Zr	ppm	1.8	190.5	122.9	124.8	158.2	27.9	113.2
IMC-100	Ba	ppm	0.8	409.1	1010.3	984.7	792.6	89.3	381.6

Method		Units	Detect Limit	17KAM045A	17KAM045A SP	17KAM045B	17KAM046A	17KAM047A	17KAM048A
IMC-100	Be	ppm	0.04	1.27	1.4	1.52	1.39	2.85	1.11
IMC-100	Bi	ppm	0.47	<0.47	<0.47	3.65	<0.47	<0.47	<0.47
IMC-100	Cd	ppm	0.013	0.106	0.073	0.084	0.051	0.02	0.028
IMC-100	Ce	ppm	0.12	62.25	52.85	56.26	78.59	11.16	13.66
IMC-100	Co	ppm	0.13	44.11	6.05	7.41	8.49	3.11	4.87
IMC-100	Cr	ppm	3	96	75	76	68	156	70
IMC-100	Cs	ppm	0.013	0.352	0.401	2	1.068	0.396	0.863
IMC-100	Cu	ppm	1.4	105.1	2.2	27.8	5.2	2	3
IMC-100	Dy	ppm	0.009	5.906	1.865	1.666	1.917	3.748	0.693
IMC-100	Er	ppm	0.007	3.293	1.028	0.821	0.837	1.96	0.46
IMC-100	Eu	ppm	0.0031	2.1573	1.0139	1.0892	1.4058	1.2712	0.3595
IMC-100	Ga	ppm	0.04	21.05	21.24	20.94	20.22	6.83	19.03
IMC-100	Gd	ppm	0.009	6.618	2.696	2.676	3.504	4.329	0.861
IMC-100	Hf	ppm	0.14	4.65	3.25	3.39	3.87	0.79	3.41
IMC-100	Ho	ppm	0.0025	1.201	0.3607	0.3123	0.331	0.7148	0.1463
IMC-100	In	ppm	0.0018	0.0786	0.0205	0.0149	0.0228	0.0202	0.01
IMC-100	La	ppm	0.1	29.3	25.8	27.6	36.2	3.8	6.1
IMC-100	Li	ppm	0.4	9.9	12.4	20.5	34.1	35.4	24.2
IMC-100	Lu	ppm	0.002	0.453	0.143	0.119	0.111	0.241	0.095
IMC-100	Mo	ppm	0.08	1.71	2.96	7.89	3.05	8.22	3.05
IMC-100	Nb	ppm	0.028	11.675	4.004	5.082	5.169	1.174	4.177
IMC-100	Nd	ppm	0.06	32.81	23.91	25.62	35.85	10.22	6.48
IMC-100	Ni	ppm	0.7	67.4	17	15	13.9	6	14.8
IMC-100	Pb	ppm	0.18	4.46	10.88	23.36	2.98	0.78	2.42
IMC-100	Pr	ppm	0.014	7.903	6.261	6.73	9.341	1.886	1.636
IMC-100	Rb	ppm	0.11	19.77	58.19	77.68	78.46	31.71	72.95
IMC-100	Sb	ppm	0.04	<0.04	0.04	0.14	0.09	0.1	0.05
IMC-100	Sc	ppm	1.1	28.8	4.6	4.6	5.8	3.7	4
IMC-100	Sm	ppm	0.026	6.9	3.866	4.072	5.662	4.203	1.207
IMC-100	Sn	ppm	0.16	1.44	0.75	0.72	0.86	0.45	0.76
IMC-100	Sr	ppm	0.6	340.3	703.9	700	543.4	17.2	259.4
IMC-100	Ta	ppm	0.007	0.72	0.284	0.37	0.315	0.061	0.307
IMC-100	Tb	ppm	0.0023	0.9915	0.3472	0.3261	0.391	0.6498	0.1171
IMC-100	Th	ppm	0.018	3.004	3.987	5.543	5.649	0.685	4.537
IMC-100	Ti	ppm	7	11891	1649	1765	2381	747	1459
IMC-100	Tl	ppm	0.002	0.095	0.206	0.387	0.302	0.11	0.315
IMC-100	Tm	ppm	0.0019	0.4739	0.1478	0.1165	0.1153	0.2773	0.0781
IMC-100	U	ppm	0.011	0.573	0.878	1.949	1.208	0.884	0.634
IMC-100	V	ppm	0.8	277.2	37.3	36.5	49.9	31.1	33.9
IMC-100	W	ppm	0.05	0.18	0.06	1.61	2.34	0.99	0.83
IMC-100	Y	ppm	0.05	32.51	10.34	9.03	9.2	18.69	4.28
IMC-100	Yb	ppm	0.009	3.022	0.96	0.766	0.742	1.792	0.575
IMC-100	Zn	ppm	1.8	144.7	49.4	40	62.3	18.3	29.5

Method		Units	Detect Limit	17KAM045A	17KAM045A SP	17KAM045B	17KAM046A	17KAM047A	17KAM048A
IMC-100	Zr	ppm	6	183	122	122	153	29	123
Method		Units	Detect Limit	17KAM049A	17KAM049B	17KAM050A	17KAM051A	17KAM051A SP	17KAM052A
SG				0.201	<0.023	0.028	2.63		0.432
SG DWT		g		<0.003	0.084	0.006	159.5		0.007
SG WWT		g					98.9		
IRC-100	CO_2	wt%	0.023	0.201	<0.023	0.028	0.307	0.319	0.432
IRC-101	S	wt%	0.003	<0.003	0.084	0.006	<0.003	<0.003	0.007
IMP-101	Au	ppb	0.6	1	1.6	0.9	1.8	1	2
IMP-101	Pd	ppb	0.14	<0.14	1.07	<0.14	<0.14	<0.14	<0.14
IMP-101	Pt	ppb	0.06	<0.06	1.15	0.06	0.09	0.13	0.2
XRF-M01	Al_2O_3	wt%	0.02	16.4	15.39	16.1	15.78	15.67	15.78
XRF-M01	BaO	wt%	0.004	0.094	0.043	0.106	0.097	0.098	0.093
XRF-M01	CaO	wt%	0.006	1.833	8.326	2.647	2.431	2.42	1.772
XRF-M01	Cr_2O_3	wt%	0.002	0.004	0.013	0.008	0.008	0.009	0.008
XRF-M01	Fe_2O_3	wt%	0.01	2.32	12.77	2.88	2.72	2.72	2.78
XRF-M01	K_2O	wt%	0.01	2.69	0.91	2.52	2.6	2.6	2.49
XRF-M01	MgO	wt%	0.01	1.28	4.75	1.5	1.33	1.34	1.89
XRF-M01	MnO	wt%	0.002	0.047	0.174	0.054	0.051	0.051	0.053
XRF-M01	Na_2O	wt%	0.02	5.18	2.8	5.14	4.96	4.92	5.56
XRF-M01	Nitrogen 105	wt%		0.43	1.47	0.31	0.3	0.31	0.42
XRF-M01	P_2O_5	wt%	0.002	0.114	0.325	0.154	0.148	0.148	0.134
XRF-M01	SiO_2	wt%	0.04	68.9	50.45	68.13	69.03	68.84	65.99
XRF-M01	TiO_2	wt%	0.01	0.27	1.99	0.33	0.3	0.3	0.3
XRF-M01	Total	wt%		100.5	100.46	100.66	100.54	100.23	98.72
XRF-M01	Total LOI 1000	wt%		1.37	2.52	1.1	1.06	1.1	1.86
XRF-T02	As	ppm	6	<6	31	<6	<6	<6	14
XRF-T02	Br	ppm	1.2	<1.2	1.3	<1.2	<1.2	1.9	<1.2
XRF-T02	Cu	ppm	9	12	6680	<9	<9	<9	1117
XRF-T02	Ga	ppm	1.3	17.7	15.7	19.5	<1.3	1.8	3
XRF-T02	Mo	ppm	0.8	2.1	872.9	2.3	5.5	44.8	>2000
XRF-T02	Nb	ppm	0.7	4.4	2.8	3.6	<0.7	<0.7	<0.7
XRF-T02	Ni	ppm	1.6	22.7	52	23.8	2.5	3	11.4
XRF-T02	Pb	ppm	1.7	15.4	197	10.2	<1.7	2.5	42.1
XRF-T02	Rb	ppm	0.8	94	79.4	51.2	2.2	1.1	12
XRF-T02	Sr	ppm	0.8	994.5	312.5	789.9	4.4	28	41.4
XRF-T02	Th	ppm	1.5	5.3	11.6	4.1	<1.5	<1.5	14
XRF-T02	U	ppm	1.6	<1.6	<1.6	<1.6	<1.6	<1.6	<1.6
XRF-T02	Y	ppm	0.7	10.3	11.8	11.7	<0.7	0.7	2
XRF-T02	Zn	ppm	1	39	90	54	<1	1	32
XRF-T02	Zr	ppm	1.8	139	105.3	129.7	<1.8	6.9	<1.8

Method		Units	Detect Limit	17KAM049A	17KAM049 B	17KAM050 A	17KAM051 A	17KAM051 A SP	17KAM052 A
IMC-100	Ba	ppm	0.8	1285.1	630.9	962.7	21.6	368.1	96.7
IMC-100	Be	ppm	0.04	1.52	1.3	1.48	0.04	0.11	0.19
IMC-100	Bi	ppm	0.47	<0.47	>47	<0.47	<0.47	<0.47	8.52
IMC-100	Cd	ppm	0.013	0.066	0.959	0.054	0.019	0.048	<0.013
IMC-100	Ce	ppm	0.12	69.04	107.77	65.81	0.52	2.48	15.95
IMC-100	Co	ppm	0.13	7.58	18.6	8	0.35	0.99	4.99
IMC-100	Cr	ppm	3	69	159	76	169	196	179
IMC-100	Cs	ppm	0.013	1.8	1.972	1.111	0.029	0.028	0.284
IMC-100	Cu	ppm	1.4	9.1	>2900	7	<1.4	1.6	1154.8
IMC-100	Dy	ppm	0.009	1.943	2.607	2.154	0.023	0.105	0.323
IMC-100	Er	ppm	0.007	0.942	1.057	1.115	0.018	0.049	0.137
IMC-100	Eu	ppm	0.0031	1.3935	1.9334	1.295	0.0128	0.0466	0.2933
IMC-100	Ga	ppm	0.04	19.1	16.1	20.32	1.06	1.94	2.59
IMC-100	Gd	ppm	0.009	3.109	5.158	3.389	0.018	0.121	0.694
IMC-100	Hf	ppm	0.14	3.97	3.2	3.64	<0.14	0.25	0.36
IMC-100	Ho	ppm	0.0025	0.3409	0.4108	0.4035	0.0053	0.0157	0.0556
IMC-100	In	ppm	0.0018	0.0187	0.1281	0.0244	<0.0018	0.0029	0.026
IMC-100	La	ppm	0.1	32.4	52	31.2	0.2	1.1	9.1
IMC-100	Li	ppm	0.4	7.4	51.6	15.9	<0.4	0.8	5.5
IMC-100	Lu	ppm	0.002	0.135	0.133	0.161	0.003	0.007	0.015
IMC-100	Mo	ppm	0.08	2.37	>44	3.1	8.69	>44	>44
IMC-100	Nb	ppm	0.028	5.522	3.816	4.491	0.226	0.509	0.646
IMC-100	Nd	ppm	0.06	29.42	51.82	29.96	0.16	0.93	6.5
IMC-100	Ni	ppm	0.7	23.6	52.9	23.9	1.8	2.8	11.1
IMC-100	Pb	ppm	0.18	14.73	188.26	10.34	0.5	3.95	38.66
IMC-100	Pr	ppm	0.014	7.907	12.948	7.765	0.038	0.251	1.733
IMC-100	Rb	ppm	0.11	97.29	81.38	52.56	2.31	1.06	11.15
IMC-100	Sb	ppm	0.04	0.15	0.69	0.11	<0.04	0.04	0.51
IMC-100	Sc	ppm	1.1	5.4	10.4	5.7	<1.1	<1.1	1.9
IMC-100	Sm	ppm	0.026	4.806	8.621	4.953	0.033	0.166	1.064
IMC-100	Sn	ppm	0.16	0.9	1.06	0.84	<0.16	<0.16	0.27
IMC-100	Sr	ppm	0.6	1020.4	312.2	808.4	5.7	29.4	39.1
IMC-100	Ta	ppm	0.007	0.493	0.274	0.334	<0.007	0.018	0.026
IMC-100	Tb	ppm	0.0023	0.3757	0.5622	0.4119	0.004	0.0153	0.0721
IMC-100	Th	ppm	0.018	6.502	9.315	5.229	0.039	0.297	0.802
IMC-100	Ti	ppm	7	1749	2587	1870	48	111	325
IMC-100	Tl	ppm	0.002	0.465	0.467	0.234	0.011	0.014	0.078
IMC-100	Tm	ppm	0.0019	0.1381	0.1414	0.1567	0.0027	0.0082	0.0194
IMC-100	U	ppm	0.011	1.189	2.372	0.988	0.052	0.065	0.236
IMC-100	V	ppm	0.8	42.3	102.5	44.3	2	2.6	21.9
IMC-100	W	ppm	0.05	0.47	18.59	0.29	<0.05	2.02	2.78
IMC-100	Y	ppm	0.05	10.15	11.46	11.73	0.13	0.49	1.6

Method		Units	Detect Limit	17KAM049A	17KAM049B	17KAM050A	17KAM051A	17KAM051A SP	17KAM052A
IMC-100	Yb	ppm	0.009	0.916	0.872	1.061	0.014	0.049	0.11
IMC-100	Zn	ppm	1.8	42.2	116.4	56.3	3.1	3.7	37.8
IMC-100	Zr	ppm	6	154	118	137	6	9	14
Method		Units	Detect Limit	17KAM053A	17KAM054A	17KAM055A	17KAM056A	17KAM057B	17KAM058A
SG				2.68	0.15	0.293	0.205	2.84	2.68
SG DWT		g		232.6	0.004	0.164	<0.003	135.6	129.5
SG WWT		g		145.7				87.9	81.2
IRC-100	CO_2	wt%	0.023	<0.023	0.15	0.293	0.205	<0.023	0.058
IRC-101	S	wt%	0.003	0.003	0.004	0.164	<0.003	0.006	<0.003
IMP-101	Au	ppb	0.6	2.6	1	3	0.7	1.2	2
IMP-101	Pd	ppb	0.14	<0.14	<0.14	1	<0.14	0.67	<0.14
IMP-101	Pt	ppb	0.06	0.19	0.1	0.3	0.13	0.84	0.09
XRF-M01	Al_2O_3	wt%	0.02	15.55	16.26	15.63	15.8	14.27	15.95
XRF-M01	BaO	wt%	0.004	0.095	0.091	0.072	0.093	0.03	0.09
XRF-M01	CaO	wt%	0.006	2.73	2.225	0.667	1.609	6.196	2.722
XRF-M01	Cr_2O_3	wt%	0.002	0.01	0.008	0.007	0.008	0.03	0.009
XRF-M01	Fe_2O_3	wt%	0.01	2.62	2.71	2.46	2.38	7.97	2.51
XRF-M01	K_2O	wt%	0.01	2.63	2.7	2.81	2.59	1.05	2.43
XRF-M01	MgO	wt%	0.01	1.46	1.77	1.88	1.43	6.34	1.33
XRF-M01	MnO	wt%	0.002	0.045	0.044	0.037	0.045	0.195	0.044
XRF-M01	Na_2O	wt%	0.02	4.94	5.09	5.07	5.86	5.15	5.11
XRF-M01	Nitrogen 105	wt%		0.25	0.23	0.24	0.37	0.32	0.24
XRF-M01	P_2O_5	wt%	0.002	0.132	0.149	0.137	0.125	0.379	0.123
XRF-M01	SiO_2	wt%	0.04	68.94	67.5	68.43	68.21	56.78	69.51
XRF-M01	TiO_2	wt%	0.01	0.29	0.33	0.3	0.29	0.62	0.28
XRF-M01	Total	wt%		100.44	100.12	99.21	100.08	100.65	101.04
XRF-M01	Total LOI 1000	wt%		1	1.24	1.71	1.64	1.64	0.94
XRF-T02	As	ppm	6	<6	<6	<6	<6	<6	<6
XRF-T02	Br	ppm	1.2	1.5	<1.2	<1.2	<1.2	2.7	1.3
XRF-T02	Cu	ppm	9	1190	18	<9	<9	<9	9
XRF-T02	Ga	ppm	1.3	2	20.6	18.6	17.6	19.4	19.2
XRF-T02	Mo	ppm	0.8	365.2	3.9	2.3	3.3	1.8	1.9
XRF-T02	Nb	ppm	0.7	<0.7	4.2	3.4	2.9	3.7	2.8
XRF-T02	Ni	ppm	1.6	3.2	24.7	57.9	13.1	16.5	30.3
XRF-T02	Pb	ppm	1.7	22.1	11.1	13.9	<1.7	2.8	13.8
XRF-T02	Rb	ppm	0.8	11.9	60.5	113	29.9	62.1	100.7
XRF-T02	Sr	ppm	0.8	9.6	791.8	951.4	157.2	393.5	976.9
XRF-T02	Th	ppm	1.5	<1.5	2.4	16.7	1.7	3.8	13.1
XRF-T02	U	ppm	1.6	<1.6	<1.6	<1.6	<1.6	<1.6	<1.6

Method		Units	Detect Limit	17KAM053A	17KAM054A	17KAM055A	17KAM056A	17KAM057B	17KAM058A
XRF-T02	Y	ppm	0.7	1.2	14.1	11.3	8.3	10.2	8.3
XRF-T02	Zn	ppm	1	3	67	66	50	44	49
XRF-T02	Zr	ppm	1.8	5.1	154.5	148.1	102.3	119.8	117.9
IMC-100	Ba	ppm	0.8	52.4	818.9	957.1	137.6	604.3	610
IMC-100	Be	ppm	0.04	0.1	1.46	1.88	1.91	1.33	1.86
IMC-100	Bi	ppm	0.47	3.16	<0.47	<0.47	<0.47	<0.47	<0.47
IMC-100	Cd	ppm	0.013	<0.013	0.07	0.075	0.029	0.028	0.087
IMC-100	Ce	ppm	0.12	1.36	71.19	112.95	38.39	54.96	99.47
IMC-100	Co	ppm	0.13	0.82	8.81	15.2	7.1	6.03	9.66
IMC-100	Cr	ppm	3	184	81	131	98	61	95
IMC-100	Cs	ppm	0.013	0.152	1.996	1.297	1.308	1.456	1.56
IMC-100	Cu	ppm	1.4	1309.1	18.2	5.3	5.8	4.1	9.7
IMC-100	Dy	ppm	0.009	0.138	2.707	2.419	1.257	1.858	1.72
IMC-100	Er	ppm	0.007	0.079	1.45	0.951	0.84	0.958	0.831
IMC-100	Eu	ppm	0.0031	0.047	1.3675	1.9297	0.545	0.9877	1.4331
IMC-100	Ga	ppm	0.04	1.73	20.93	19.01	17.85	19.53	19.81
IMC-100	Gd	ppm	0.009	0.159	3.932	4.823	1.463	2.713	3.132
IMC-100	Hf	ppm	0.14	0.34	4.19	4.07	2.86	3.48	3.31
IMC-100	Ho	ppm	0.0025	0.0244	0.5176	0.3814	0.2679	0.3361	0.3036
IMC-100	In	ppm	0.0018	0.0728	0.0313	0.0304	0.0228	0.0169	0.0207
IMC-100	La	ppm	0.1	0.6	33.1	58.3	18.3	27	61.9
IMC-100	Li	ppm	0.4	1.2	18	6.8	111.1	23.5	11.5
IMC-100	Lu	ppm	0.002	0.012	0.199	0.124	0.154	0.134	0.119
IMC-100	Mo	ppm	0.08	>44	4.59	2.43	5.27	2.66	2.48
IMC-100	Nb	ppm	0.028	0.528	5.295	4.332	3.53	4.15	3.771
IMC-100	Nd	ppm	0.06	0.57	34.24	48.58	15.89	24.51	33.16
IMC-100	Ni	ppm	0.7	2.1	24.5	60.1	12.5	16	32.3
IMC-100	Pb	ppm	0.18	24.01	11.27	13.07	1.99	4.09	13.3
IMC-100	Pr	ppm	0.014	0.134	8.842	13.003	4.379	6.474	9.851
IMC-100	Rb	ppm	0.11	12.19	61.77	114.85	30.84	63.44	104.73
IMC-100	Sb	ppm	0.04	0.06	0.05	0.34	0.15	0.06	0.13
IMC-100	Sc	ppm	1.1	<1.1	6.4	9.4	4.6	4.1	6.2
IMC-100	Sm	ppm	0.026	0.175	5.766	7.731	2.268	3.982	5.048
IMC-100	Sn	ppm	0.16	0.36	0.96	0.94	0.76	0.74	1.89
IMC-100	Sr	ppm	0.6	10.4	814.5	964.5	159.9	398.1	997.6
IMC-100	Ta	ppm	0.007	0.029	0.38	0.245	0.252	0.3	0.27
IMC-100	Tb	ppm	0.0023	0.0198	0.5248	0.5111	0.1979	0.3379	0.3577
IMC-100	Th	ppm	0.018	0.609	4.455	18.616	3.597	4.692	15.746
IMC-100	Ti	ppm	7	29	2212	2570	1317	1509	1778
IMC-100	Tl	ppm	0.002	0.128	0.278	0.571	0.117	0.31	0.476
IMC-100	Tm	ppm	0.0019	0.0124	0.2037	0.1318	0.136	0.1328	0.1142
IMC-100	U	ppm	0.011	1.22	0.699	1.209	1.332	0.898	2.052

Method		Units	Detect Limit	17KAM053A	17KAM054 A	17KAM055 A	17KAM056 A	17KAM057 B	17KAM058 A
IMC-100	V	ppm	0.8	2.3	50.6	74.9	42.7	31.3	50.9
IMC-100	W	ppm	0.05	0.07	0.36	0.64	1.42	0.38	0.21
IMC-100	Y	ppm	0.05	0.99	14.23	11.07	8.26	9.86	8.95
IMC-100	Yb	ppm	0.009	0.075	1.371	0.809	0.979	0.859	0.734
IMC-100	Zn	ppm	1.8	10.9	103.1	65.2	52.3	47.2	52.1
IMC-100	Zr	ppm	6	10	159	154	106	123	117
Method		Units	Detect Limit	17KAM058B	17KAM060 A	17KAM060 A SP	17KAM062 A	17KAM062 B	17KAM062 B SP
SG				2.8	0.087	0.09	2.65	3.924	4.449
SG DWT		g		160.6	<0.003	<0.003	214.3	0.036	0.033
SG WWT		g		103.2			133.5		
IRC-100	CO_2	wt%	0.023	0.088	0.087	0.09	<0.023	3.924	4.449
IRC-101	S	wt%	0.003	0.017	<0.003	<0.003	0.003	0.036	0.033
IMP-101	Au	ppb	0.6	0.8	1	1.1	1.3	2.3	4.5
IMP-101	Pd	ppb	0.14	1.42	<0.14	<0.14	<0.14	<0.14	<0.14
IMP-101	Pt	ppb	0.06	1.06	0.15	0.15	0.12	<0.06	<0.06
XRF-M01	Al_2O_3	wt%	0.02	16.01	15.82	15.79	15.98	15.79	15.98
XRF-M01	BaO	wt%	0.004	0.041	0.103	0.104	0.097	0.104	0.097
XRF-M01	CaO	wt%	0.006	6.066	2.63	2.617	2.687	2.617	2.687
XRF-M01	Cr_2O_3	wt%	0.002	0.016	0.013	0.012	0.01	0.012	0.01
XRF-M01	Fe_2O_3	wt%	0.01	7.05	2.8	2.83	2.37	2.83	2.37
XRF-M01	K_2O	wt%	0.01	1.1	2.43	2.42	2.41	2.42	2.41
XRF-M01	MgO	wt%	0.01	4.47	1.64	1.64	1.13	1.64	1.13
XRF-M01	MnO	wt%	0.002	0.144	0.049	0.048	0.042	0.048	0.042
XRF-M01	Na_2O	wt%	0.02	5.48	4.89	4.93	5.11	4.93	5.11
XRF-M01	Nitrogen 105	wt%		0.23	0.25	0.23	0.29	0.23	0.29
XRF-M01	P_2O_5	wt%	0.002	0.473	0.15	0.153	0.114	0.153	0.114
XRF-M01	SiO_2	wt%	0.04	57.07	68.18	68.72	69.64	68.72	69.64
XRF-M01	TiO_2	wt%	0.01	0.67	0.32	0.32	0.26	0.32	0.26
XRF-M01	Total	wt%		99.93	100.41	100.94	100.75	100.94	100.75
XRF-M01	Total LOI 1000	wt%		1.33	1.39	1.35	0.89	1.35	0.89
XRF-T02	As	ppm	6	<6	<6	<6	<6	<6	<6
XRF-T02	Br	ppm	1.2	1.2	<1.2	2.4	1.2	<1.2	1.3
XRF-T02	Cu	ppm	9	<9	<9	271	<9	<9	<9
XRF-T02	Ga	ppm	1.3	18.8	19.1	19.4	1.3	19.4	6.6
XRF-T02	Mo	ppm	0.8	2.3	1.8	138.3	6	2.3	3.6
XRF-T02	Nb	ppm	0.7	4.6	4.5	3.7	<0.7	4	<0.7
XRF-T02	Ni	ppm	1.6	26.4	36.2	16	3.5	37.3	10
XRF-T02	Pb	ppm	1.7	12.6	8.3	29.5	<1.7	12	<1.7
XRF-T02	Rb	ppm	0.8	75.5	70.8	65.9	3.5	62.6	19.9

Method		Units	Detect Limit	17KAM058B	17KAM060 A	17KAM060 A SP	17KAM062 A	17KAM062 B	17KAM062 B SP
XRF-T02	Sr	ppm	0.8	830.5	980.9	362.1	182.5	1039.3	73.8
XRF-T02	Th	ppm	1.5	4.6	4.5	5.6	<1.5	3.7	<1.5
XRF-T02	U	ppm	1.6	<1.6	<1.6	<1.6	<1.6	<1.6	<1.6
XRF-T02	Y	ppm	0.7	11.3	14	9.4	2.6	14.3	4.2
XRF-T02	Zn	ppm	1	57	53	52	6	62	24
XRF-T02	Zr	ppm	1.8	138.7	163.6	109.1	2.4	159.6	16.5
IMC-100	Ba	ppm	0.8	1006.8	1252.6	540.5	53.9	1216.1	244.8
IMC-100	Be	ppm	0.04	1.45	1.7	1.39	0.04	1.6	0.34
IMC-100	Bi	ppm	0.47	<0.47	<0.47	<0.47	<0.47	<0.47	<0.47
IMC-100	Cd	ppm	0.013	0.08	0.051	0.069	0.059	0.069	0.028
IMC-100	Ce	ppm	0.12	79.08	86.36	45.6	1.94	82.45	6.01
IMC-100	Co	ppm	0.13	8.46	11.59	5.43	2.14	11.62	6.08
IMC-100	Cr	ppm	3	86	98	77	170	97	113
IMC-100	Cs	ppm	0.013	1.067	0.784	0.451	0.065	0.658	0.485
IMC-100	Cu	ppm	1.4	3.2	2	294.2	3	2.9	7.6
IMC-100	Dy	ppm	0.009	2.079	2.819	1.634	0.36	2.76	0.621
IMC-100	Er	ppm	0.007	1.073	1.334	0.901	0.17	1.346	0.345
IMC-100	Eu	ppm	0.0031	1.2906	1.7707	0.9266	0.183	1.712	0.2351
IMC-100	Ga	ppm	0.04	19.63	20.11	19.26	1.36	20.55	6.7
IMC-100	Gd	ppm	0.009	3.325	4.468	2.431	0.556	4.545	0.709
IMC-100	Hf	ppm	0.14	3.99	4.32	3.42	<0.14	4.18	0.47
IMC-100	Ho	ppm	0.0025	0.3779	0.5073	0.3075	0.0704	0.5003	0.1254
IMC-100	In	ppm	0.0018	0.0264	0.026	0.0319	0.005	0.0297	0.0108
IMC-100	La	ppm	0.1	43.2	40.4	22.3	0.7	37.6	3.1
IMC-100	Li	ppm	0.4	15	9	13.9	3.2	10.3	16.5
IMC-100	Lu	ppm	0.002	0.155	0.184	0.142	0.023	0.176	0.054
IMC-100	Mo	ppm	0.08	2.92	2.41	>44	9.27	2.24	5.86
IMC-100	Nb	ppm	0.028	5.303	5.415	4.396	0.392	4.856	0.537
IMC-100	Nd	ppm	0.06	32.16	41.54	20.3	1.72	41.1	3.51
IMC-100	Ni	ppm	0.7	27.6	36.2	15.7	3.2	38.5	10.5
IMC-100	Pb	ppm	0.18	12.57	8.19	29.72	0.93	11.38	1.21
IMC-100	Pr	ppm	0.014	8.842	10.58	5.29	0.339	10.543	0.873
IMC-100	Rb	ppm	0.11	78.22	72.2	67.82	3.36	64.16	20.68
IMC-100	Sb	ppm	0.04	0.15	<0.04	0.05	<0.04	0.04	0.1
IMC-100	Sc	ppm	1.1	6.4	7.7	4.1	1.7	7.5	2.6
IMC-100	Sm	ppm	0.026	5.042	6.773	3.373	0.526	6.93	0.798
IMC-100	Sn	ppm	0.16	0.96	1	0.95	0.17	0.96	0.29
IMC-100	Sr	ppm	0.6	849.5	984.4	363.4	186.5	1061.6	76.8
IMC-100	Ta	ppm	0.007	0.43	0.395	0.315	0.008	0.35	0.034
IMC-100	Tb	ppm	0.0023	0.398	0.5322	0.3039	0.0699	0.5412	0.1054
IMC-100	Th	ppm	0.018	6.203	5.961	6.521	0.067	5.22	0.526
IMC-100	Ti	ppm	7	1950	2350	1405	122	2354	402

Method		Units	Detect Limit	17KAM058B	17KAM060 A	17KAM060 A SP	17KAM062 A	17KAM062 B	17KAM062 B SP
IMC-100	Tl	ppm	0.002	0.369	0.235	0.462	0.019	0.295	0.082
IMC-100	Tm	ppm	0.0019	0.1544	0.1887	0.1313	0.0213	0.1878	0.0491
IMC-100	U	ppm	0.011	1.048	1.178	1.378	0.015	0.831	0.146
IMC-100	V	ppm	0.8	47.8	63.4	31	7.8	62.8	22.9
IMC-100	W	ppm	0.05	0.13	0.13	0.29	0.19	0.1	0.59
IMC-100	Y	ppm	0.05	11.26	14.45	9.21	2.28	14.38	3.47
IMC-100	Yb	ppm	0.009	0.995	1.284	0.897	0.142	1.216	0.344
IMC-100	Zn	ppm	1.8	57.8	52.8	51.1	8	60.2	26.8
IMC-100	Zr	ppm	6	150	166	112	<6	167	17
Method		Units	Detect Limit	17KAM063B	17KAM063 C	17KAM064 A	17KAM065 A	17KAM066 B	17KAM067 A
SG						0.179	2.63	<0.023	0.204
SG DWT		g				0.004	111.5	0.003	0.257
SG WWT		g					69.1		
IRC-100	CO_2	wt%	0.023			0.179	0.205	<0.023	0.204
IRC-101	S	wt%	0.003			0.004	<0.003	0.003	0.257
IMP-101	Au	ppb	0.6	0.8	345.1	<0.6	4.4	1.3	9.2
IMP-101	Pd	ppb	0.14	7.42	<0.14	<0.14	<0.14	<0.14	<0.14
IMP-101	Pt	ppb	0.06	<0.06	0.07	0.09	0.27	<0.06	0.08
XRF-M01	Al_2O_3	wt%	0.02			15.89	15.84	15.75	15.82
XRF-M01	BaO	wt%	0.004			0.109	0.088	0.085	0.104
XRF-M01	CaO	wt%	0.006			1.907	2.5	1.21	1.913
XRF-M01	Cr_2O_3	wt%	0.002			0.009	0.009	0.009	0.011
XRF-M01	Fe_2O_3	wt%	0.01			2.38	2.44	3.28	2.3
XRF-M01	K_2O	wt%	0.01			2.7	2.71	2.24	2.87
XRF-M01	MgO	wt%	0.01			1.26	1.23	1.97	1.18
XRF-M01	MnO	wt%	0.002			0.038	0.046	0.044	0.029
XRF-M01	Na_2O	wt%	0.02			5.06	5.05	5.53	4.91
XRF-M01	Nitrogen 105	wt%				0.34	0.28	0.28	0.32
XRF-M01	P_2O_5	wt%	0.002			0.117	0.127	0.199	0.131
XRF-M01	SiO_2	wt%	0.04			69.61	69.73	67.13	68.77
XRF-M01	TiO_2	wt%	0.01			0.27	0.28	0.39	0.29
XRF-M01	Total	wt%				100.78	101.11	99.57	99.93
XRF-M01	Total LOI 1000	wt%				1.44	1.05	1.73	1.61
XRF-T02	As	ppm	6	<6	<6	<6	<6	<6	<6
XRF-T02	Br	ppm	1.2	8.1	1.3	<1.2	<1.2	1.7	<1.2
XRF-T02	Cu	ppm	9	<9	<9	<9	34	<9	<9
XRF-T02	Ga	ppm	1.3	4.1	6.6	20.1	24.1	22.8	19.6
XRF-T02	Mo	ppm	0.8	6.4	3.8	1.8	1.8	<0.8	2.1
XRF-T02	Nb	ppm	0.7	<0.7	<0.7	4.5	8.1	6	4.1

Method		Units	Detect Limit	17KAM063B	17KAM063C	17KAM064A	17KAM065A	17KAM066B	17KAM067A
XRF-T02	Ni	ppm	1.6	5.3	10.2	19.4	52.8	129.5	21.5
XRF-T02	Pb	ppm	1.7	<1.7	<1.7	12.4	9.9	6.1	10.8
XRF-T02	Rb	ppm	0.8	9.4	19.8	73.9	39.8	35.4	66.4
XRF-T02	Sr	ppm	0.8	14.9	72.5	737.3	672.7	628.3	789.1
XRF-T02	Th	ppm	1.5	<1.5	<1.5	6.3	6.6	3.5	5.1
XRF-T02	U	ppm	1.6	<1.6	<1.6	<1.6	<1.6	<1.6	<1.6
XRF-T02	Y	ppm	0.7	1.6	3.8	10.4	24.4	22.1	11.1
XRF-T02	Zn	ppm	1	7	23	49	147	162	45
XRF-T02	Zr	ppm	1.8	3.4	16.7	126.3	167.6	139.3	129.4
IMC-100	Ba	ppm	0.8	141.7	250.1	861.4	374.1	278.3	898.9
IMC-100	Be	ppm	0.04	0.53	0.4	1.73	2.27	2.97	1.46
IMC-100	Bi	ppm	0.47	<0.47	<0.47	<0.47	<0.47	<0.47	<0.47
IMC-100	Cd	ppm	0.013	0.025	0.03	0.052	0.113	0.116	0.05
IMC-100	Ce	ppm	0.12	3.96	5.41	55.1	157.61	109.44	56.69
IMC-100	Co	ppm	0.13	1.5	6.13	6.6	22.37	29.25	7.28
IMC-100	Cr	ppm	3	162	132	66	113	236	72
IMC-100	Cs	ppm	0.013	0.267	0.489	1.88	1.006	0.302	1.192
IMC-100	Cu	ppm	1.4	1.9	8.1	<1.4	35.8	4.6	2.4
IMC-100	Dy	ppm	0.009	0.275	0.613	1.861	4.462	4.027	1.941
IMC-100	Er	ppm	0.007	0.149	0.355	0.999	2.297	2.124	0.985
IMC-100	Eu	ppm	0.0031	0.1354	0.2333	1.0634	2.2303	1.5795	1.0857
IMC-100	Ga	ppm	0.04	3.89	6.58	20.86	24.78	22.82	20.52
IMC-100	Gd	ppm	0.009	0.373	0.69	2.717	7.113	5.872	2.877
IMC-100	Hf	ppm	0.14	0.15	0.52	3.42	4.26	3.43	3.47
IMC-100	Ho	ppm	0.0025	0.0532	0.1121	0.345	0.8254	0.7605	0.3556
IMC-100	In	ppm	0.0018	0.0035	0.0121	0.0212	0.0891	0.0963	0.0216
IMC-100	La	ppm	0.1	1.8	2.8	25.8	74.1	52.8	26.4
IMC-100	Li	ppm	0.4	59.8	15.7	15	29.8	18.8	14.9
IMC-100	Lu	ppm	0.002	0.018	0.054	0.143	0.343	0.315	0.153
IMC-100	Mo	ppm	0.08	8.87	6.79	2.35	1.53	0.94	2.52
IMC-100	Nb	ppm	0.028	0.274	0.616	5.022	8.127	6.743	4.383
IMC-100	Nd	ppm	0.06	2.07	3.27	24.92	71.92	50.87	25.87
IMC-100	Ni	ppm	0.7	4.3	10	19.8	52.7	131.5	22.7
IMC-100	Pb	ppm	0.18	0.62	1.14	12.67	10.1	5.96	10.89
IMC-100	Pr	ppm	0.014	0.476	0.791	6.419	18.385	12.726	6.594
IMC-100	Rb	ppm	0.11	9.91	20.48	75.66	39.17	35.81	62.01
IMC-100	Sb	ppm	0.04	0.21	0.15	0.07	0.08	0.05	<0.04
IMC-100	Sc	ppm	1.1	<1.1	2.9	4.7	15.8	22.1	5
IMC-100	Sm	ppm	0.026	0.469	0.709	4.17	10.924	8.288	4.279
IMC-100	Sn	ppm	0.16	<0.16	0.35	1.01	1.68	1.71	0.82
IMC-100	Sr	ppm	0.6	14.9	75.8	749.3	680.6	645	793.7
IMC-100	Ta	ppm	0.007	<0.007	0.039	0.388	0.61	0.241	0.328

Method		Units	Detect Limit	17KAM063B	17KAM063C	17KAM064A	17KAM065A	17KAM066B	17KAM067A
IMC-100	Tb	ppm	0.0023	0.0526	0.1036	0.3518	0.8676	0.7345	0.3731
IMC-100	Th	ppm	0.018	0.135	0.514	7.227	7.486	4.818	5.938
IMC-100	Ti	ppm	7	38	449	1676	3946	3663	1750
IMC-100	Tl	ppm	0.002	0.037	0.08	0.289	0.206	0.144	0.299
IMC-100	Tm	ppm	0.0019	0.0216	0.0539	0.1452	0.3414	0.3025	0.1495
IMC-100	U	ppm	0.011	0.089	0.146	1.356	1.347	1.115	1.153
IMC-100	V	ppm	0.8	9.8	25.1	38	171.4	156.9	41.7
IMC-100	W	ppm	0.05	0.29	0.6	0.27	0.19	0.41	0.21
IMC-100	Y	ppm	0.05	1.48	3.33	10.17	24.15	21.75	10.38
IMC-100	Yb	ppm	0.009	0.146	0.354	0.952	2.264	2.024	0.972
IMC-100	Zn	ppm	1.8	8.5	25.5	48.3	134.6	148.9	44.6
IMC-100	Zr	ppm	6	6	19	121	168	131	128
Method		Units	Detect Limit	17KAM068A	17KAM069A	17KAM071A	17KAM071B	17KAM072A	17KAM072B
SG				<0.023	0.108	0.201	0.189	0.375	0.98
SG DWT		g		0.003	0.003	0.025	0.146	0.003	0.585
SG WWT		g							
IRC-100	CO_2	wt%	0.023	<0.023	0.108	0.201	0.189	0.375	0.98
IRC-101	S	wt%	0.003	0.003	0.003	0.025	0.146	0.003	0.585
IMP-101	Au	ppb	0.6	1.1	0.8	2.4	23.9	1.1	159.1
IMP-101	Pd	ppb	0.14	<0.14	<0.14	<0.14	0.28	<0.14	1.42
IMP-101	Pt	ppb	0.06	0.28	0.32	0.18	0.18	0.12	0.58
XRF-M01	Al_2O_3	wt%	0.02	16.3	16.07	14.52	1.86	15.83	2.06
XRF-M01	BaO	wt%	0.004	0.129	0.134	0.058	0.007	0.136	0.011
XRF-M01	CaO	wt%	0.006	3.589	3.471	1.296	0.167	2.163	1.106
XRF-M01	Cr_2O_3	wt%	0.002	0.012	0.014	0.012	0.024	0.009	0.024
XRF-M01	Fe_2O_3	wt%	0.01	3.71	3.81	2.07	0.34	2.51	1.22
XRF-M01	K_2O	wt%	0.01	2.63	2.88	2.49	0.54	3.6	0.37
XRF-M01	MgO	wt%	0.01	2.32	2.34	1.32	0.07	1.48	0.47
XRF-M01	MnO	wt%	0.002	0.063	0.067	0.044	0.005	0.043	0.017
XRF-M01	Na_2O	wt%	0.02	4.95	4.85	5.04	0.2	4.62	0.1
XRF-M01	Nitrogen 105	wt%		0.14	0.2	0.31	0.07	0.33	0.13
XRF-M01	P_2O_5	wt%	0.002	0.216	0.218	0.106	0.002	0.137	0.047
XRF-M01	SiO_2	wt%	0.04	65.96	65.84	71.33	97.09	68.85	93.02
XRF-M01	TiO_2	wt%	0.01	0.39	0.4	0.24	0.01	0.29	0.07
XRF-M01	Total	wt%		101.1	101	100	100.72	100.92	99.8
XRF-M01	Total LOI 1000	wt%		0.83	0.92	1.49	0.41	1.25	1.29
XRF-T02	As	ppm	6	<6	<6	<6	<6	<6	<6
XRF-T02	Br	ppm	1.2	<1.2	1.2	1.3	3.9	<1.2	<1.2
XRF-T02	Cu	ppm	9	132	<9	<9	<9	<9	<9

Method		Units	Detect Limit	17KAM068A	17KAM069A	17KAM071A	17KAM071B	17KAM072A	17KAM072B
XRF-T02	Ga	ppm	1.3	19.9	20.1	19.5	20.1	20.7	20.3
XRF-T02	Mo	ppm	0.8	5.3	1.4	1.7	1.9	1.5	1.3
XRF-T02	Nb	ppm	0.7	4.2	4.1	3.8	3.4	3.6	3.1
XRF-T02	Ni	ppm	1.6	26.5	16.7	19.8	25.6	17.9	15.4
XRF-T02	Pb	ppm	1.7	16.8	13.2	10.1	9	7.7	10.4
XRF-T02	Rb	ppm	0.8	74.5	66.3	70	68.2	52.7	63.8
XRF-T02	Sr	ppm	0.8	784.1	886.8	699.1	862.7	726	782.7
XRF-T02	Th	ppm	1.5	5.3	3.7	5.9	2.6	2.4	3.1
XRF-T02	U	ppm	1.6	<1.6	<1.6	<1.6	<1.6	<1.6	<1.6
XRF-T02	Y	ppm	0.7	11.3	10.4	10.4	11.9	10.4	9.5
XRF-T02	Zn	ppm	1	47	51	51	47	40	47
XRF-T02	Zr	ppm	1.8	132.4	129.1	122.3	136.7	131.2	118.9
IMC-100	Ba	ppm	0.8	902.2	955.9	768.5	1214.7	838.9	952.7
IMC-100	Be	ppm	0.04	1.67	1.5	1.46	1.39	1.52	1.46
IMC-100	Bi	ppm	0.47	<0.47	<0.47	<0.47	<0.47	<0.47	<0.47
IMC-100	Cd	ppm	0.013	0.058	0.048	0.055	0.041	0.059	0.048
IMC-100	Ce	ppm	0.12	73.78	64.45	54.18	60.19	55.08	49.19
IMC-100	Co	ppm	0.13	8.25	6.74	6.62	7.97	6.07	5.53
IMC-100	Cr	ppm	3	71	49	83	69	56	43
IMC-100	Cs	ppm	0.013	1.012	1.089	1.176	0.416	0.88	2.046
IMC-100	Cu	ppm	1.4	135.4	4	3	<1.4	1.4	<1.4
IMC-100	Dy	ppm	0.009	2.111	1.856	1.896	2.184	1.924	1.675
IMC-100	Er	ppm	0.007	1.081	0.933	1.011	1.1	1.032	0.885
IMC-100	Eu	ppm	0.0031	1.2996	1.1886	1.0625	1.2467	1.0883	0.9258
IMC-100	Ga	ppm	0.04	20.23	20.8	19.95	20.62	21	20.73
IMC-100	Gd	ppm	0.009	3.444	2.992	2.902	3.169	2.832	2.416
IMC-100	Hf	ppm	0.14	3.81	3.61	3.6	3.68	3.5	3.25
IMC-100	Ho	ppm	0.0025	0.3882	0.3383	0.3544	0.4029	0.3664	0.3219
IMC-100	In	ppm	0.0018	0.0224	0.022	0.022	0.0234	0.0212	0.0211
IMC-100	La	ppm	0.1	35.1	29.6	23.9	27.6	25.4	23.3
IMC-100	Li	ppm	0.4	10.5	20.1	14.7	12.2	10.8	20.4
IMC-100	Lu	ppm	0.002	0.157	0.134	0.158	0.158	0.142	0.14
IMC-100	Mo	ppm	0.08	5.96	1.76	3.39	2.1	1.99	1.47
IMC-100	Nb	ppm	0.028	5.014	4.952	4.625	4.365	4.488	3.84
IMC-100	Nd	ppm	0.06	31.72	28.79	24.85	28.64	25.1	21.73
IMC-100	Ni	ppm	0.7	27.4	16.5	20.8	24.9	17.7	14.9
IMC-100	Pb	ppm	0.18	16.52	13.6	10.42	8.62	7.76	10.05
IMC-100	Pr	ppm	0.014	8.35	7.3	6.395	7.256	6.484	5.641
IMC-100	Rb	ppm	0.11	73.3	65.15	64.83	67.08	51.52	63.48
IMC-100	Sb	ppm	0.04	0.04	<0.04	0.04	0.05	0.06	0.06
IMC-100	Sc	ppm	1.1	5.5	4.5	4.6	5.4	4.4	4
IMC-100	Sm	ppm	0.026	5.081	4.541	4.124	4.72	4.007	3.552

Method		Units	Detect Limit	17KAM068A	17KAM069 A	17KAM071 A	17KAM071 B	17KAM072 A	17KAM072 B
IMC-100	Sn	ppm	0.16	0.83	0.71	0.78	0.82	0.78	0.71
IMC-100	Sr	ppm	0.6	791.1	891.7	699.1	871.7	727.4	788.9
IMC-100	Ta	ppm	0.007	0.392	0.322	0.361	0.31	0.309	0.288
IMC-100	Tb	ppm	0.0023	0.4044	0.3652	0.3517	0.4099	0.3621	0.3031
IMC-100	Th	ppm	0.018	6.614	5.236	7.795	3.623	3.855	4.345
IMC-100	Ti	ppm	7	1895	1736	1604	1882	1645	1484
IMC-100	Tl	ppm	0.002	0.339	0.334	0.336	0.28	0.193	0.268
IMC-100	Tm	ppm	0.0019	0.1567	0.1344	0.146	0.1648	0.1477	0.1318
IMC-100	U	ppm	0.011	1.295	1.059	0.896	0.811	0.747	1.181
IMC-100	V	ppm	0.8	46.3	39.3	37.2	46.8	40.1	32.6
IMC-100	W	ppm	0.05	1.46	0.05	0.09	0.48	0.23	0.16
IMC-100	Y	ppm	0.05	11.32	9.96	10.09	11.53	10.25	9.2
IMC-100	Yb	ppm	0.009	1.022	0.879	0.988	1.073	0.998	0.895
IMC-100	Zn	ppm	1.8	45.3	49.1	48.6	44.4	37.6	44.2
IMC-100	Zr	ppm	6	141	130	125	135	127	120
Method		Units	Detect Limit	17KAM072C	17KAM073 A	17KAM073 B	17KAM074 A	17KAM075 A	17KAM076 A
SG				1.438	0.515	0.654	0.706	0.182	0.122
SG DWT		g		0.696	<0.003	0.003	0.009	0.003	<0.003
SG WWT		g							
IRC-100	CO_2	wt%	0.023	1.438	0.515	0.654	0.706	0.182	0.122
IRC-101	S	wt%	0.003	0.696	<0.003	0.003	0.009	0.003	<0.003
IMP-101	Au	ppb	0.6	58	0.9	2.6	1.4	1	1.9
IMP-101	Pd	ppb	0.14	1.42	<0.14	<0.14	0.15	<0.14	<0.14
IMP-101	Pt	ppb	0.06	0.91	0.09	0.15	0.15	0.55	0.41
XRF-M01	Al_2O_3	wt%	0.02	12.33	14.83	3.93	15.81	14.97	15.68
XRF-M01	BaO	wt%	0.004	0.068	0.042	0.012	0.085	0.104	0.065
XRF-M01	CaO	wt%	0.006	2.062	0.958	0.879	2.811	3.701	2.991
XRF-M01	Cr_2O_3	wt%	0.002	0.022	0.01	0.021	0.011	0.018	0.014
XRF-M01	Fe_2O_3	wt%	0.01	6.83	2.17	1.15	3.33	4.17	2.8
XRF-M01	K_2O	wt%	0.01	2.99	2.83	0.97	2.28	3.4	3.01
XRF-M01	MgO	wt%	0.01	3.76	1.84	1.41	1.77	3.38	2.03
XRF-M01	MnO	wt%	0.002	0.114	0.024	0.02	0.052	0.07	0.059
XRF-M01	Na_2O	wt%	0.02	2.56	5.04	0.36	4.93	4.7	4.94
XRF-M01	Nitrogen 105	wt%		0.46	0.33	0.23	0.28	0.25	0.28
XRF-M01	P_2O_5	wt%	0.002	0.354	0.108	0.047	0.162	0.278	0.164
XRF-M01	SiO_2	wt%	0.04	63.29	68.36	90.66	66.51	64.61	67.87
XRF-M01	TiO_2	wt%	0.01	0.45	0.25	0.14	0.37	0.43	0.29
XRF-M01	Total	wt%		98.84	98.63	101.37	99.92	100.9	101.18
XRF-M01	Total LOI 1000	wt%		4.01	2.18	1.77	1.8	1.07	1.26

Method		Units	Detect Limit	17KAM072C	17KAM073A	17KAM073B	17KAM074A	17KAM075A	17KAM076A
XRF-T02	As	ppm	6	<6	<6	<6	<6	<6	<6
XRF-T02	Br	ppm	1.2	<1.2	2.3	<1.2	<1.2	<1.2	3.3
XRF-T02	Cu	ppm	9	<9	<9	<9	<9	<9	<9
XRF-T02	Ga	ppm	1.3	19.3	20.3	19.8	18.4	19.6	20
XRF-T02	Mo	ppm	0.8	2.1	2.1	1.9	1.5	1.9	1.9
XRF-T02	Nb	ppm	0.7	4	4	4.5	2.7	4.3	3.5
XRF-T02	Ni	ppm	1.6	23.3	17.9	17.7	8.6	16.5	18.1
XRF-T02	Pb	ppm	1.7	10.3	11.8	13.7	11.7	11.3	12.2
XRF-T02	Rb	ppm	0.8	63.7	60.1	70.6	81.5	66.9	69.7
XRF-T02	Sr	ppm	0.8	864.8	897.3	835.3	555.7	817.7	802.4
XRF-T02	Th	ppm	1.5	4.5	3.5	4.3	3.3	2.8	3.1
XRF-T02	U	ppm	1.6	<1.6	<1.6	<1.6	<1.6	<1.6	<1.6
XRF-T02	Y	ppm	0.7	11.7	12.6	11.4	7.5	12	11.1
XRF-T02	Zn	ppm	1	39	54	54	31	59	49
XRF-T02	Zr	ppm	1.8	128.2	140	133.4	92.4	132	123.1
IMC-100	Ba	ppm	0.8	1035.6	840.5	1008.9	635.4	898.6	836.6
IMC-100	Be	ppm	0.04	1.48	1.55	1.4	1.25	1.5	1.36
IMC-100	Bi	ppm	0.47	<0.47	<0.47	<0.47	<0.47	<0.47	<0.47
IMC-100	Cd	ppm	0.013	0.036	0.046	0.043	0.033	0.058	0.042
IMC-100	Ce	ppm	0.12	64.86	64.56	67.21	36.05	61.58	55.92
IMC-100	Co	ppm	0.13	7.07	7.36	7.12	3.36	6.88	6.55
IMC-100	Cr	ppm	3	71	67	54	51	62	67
IMC-100	Cs	ppm	0.013	1.116	1.727	2.332	1.343	1.051	2.275
IMC-100	Cu	ppm	1.4	7.3	4.7	4.5	<1.4	<1.4	2.4
IMC-100	Dy	ppm	0.009	2.064	2.258	1.994	1.222	2.127	1.921
IMC-100	Er	ppm	0.007	1.083	1.173	0.981	0.686	1.14	1.025
IMC-100	Eu	ppm	0.0031	1.2434	1.2491	1.2822	0.679	1.2141	1.05
IMC-100	Ga	ppm	0.04	19.64	20.74	20.13	18.28	20.27	20.47
IMC-100	Gd	ppm	0.009	3.252	3.355	3.386	1.717	3.245	2.802
IMC-100	Hf	ppm	0.14	3.77	3.61	3.56	2.63	3.66	3.47
IMC-100	Ho	ppm	0.0025	0.3849	0.4212	0.3628	0.2464	0.4056	0.3665
IMC-100	In	ppm	0.0018	0.0248	0.0263	0.0226	0.0119	0.0241	0.0229
IMC-100	La	ppm	0.1	29.2	29.5	31.5	17	26.9	26.3
IMC-100	Li	ppm	0.4	11.4	17.8	29.2	9.5	23.2	17.2
IMC-100	Lu	ppm	0.002	0.159	0.168	0.145	0.119	0.163	0.152
IMC-100	Mo	ppm	0.08	2.73	2.47	2.07	2.41	2.3	2.27
IMC-100	Nb	ppm	0.028	4.763	5.13	5.076	3.411	5.104	4.289
IMC-100	Nd	ppm	0.06	29.74	29.92	31.27	15.57	28.96	25.11
IMC-100	Ni	ppm	0.7	23.5	18	17.1	8.1	17	18.7
IMC-100	Pb	ppm	0.18	10.08	11.48	13.36	11.7	11.57	11.66
IMC-100	Pr	ppm	0.014	7.681	7.56	8.058	4.061	7.255	6.483
IMC-100	Rb	ppm	0.11	62.75	60.03	69.65	80.92	65.27	69.52

Method		Units	Detect Limit	17KAM072C	17KAM073A	17KAM073B	17KAM074A	17KAM075A	17KAM076A
IMC-100	Sb	ppm	0.04	0.05	0.11	0.04	<0.04	<0.04	0.08
IMC-100	Sc	ppm	1.1	5	5.1	4.5	2.3	4.7	4.3
IMC-100	Sm	ppm	0.026	4.781	4.904	5.053	2.516	4.676	4.1
IMC-100	Sn	ppm	0.16	0.94	0.8	0.96	0.54	0.8	0.86
IMC-100	Sr	ppm	0.6	872.3	908.2	831.9	560	826.3	810.2
IMC-100	Ta	ppm	0.007	0.378	0.354	0.348	0.242	0.338	0.315
IMC-100	Tb	ppm	0.0023	0.3974	0.4277	0.4063	0.2226	0.3994	0.3568
IMC-100	Th	ppm	0.018	5.658	4.721	4.847	4.331	4.305	4.529
IMC-100	Ti	ppm	7	1808	1872	1804	985	1771	1617
IMC-100	Tl	ppm	0.002	0.297	0.306	0.38	0.319	0.269	0.368
IMC-100	Tm	ppm	0.0019	0.1592	0.167	0.143	0.1014	0.1621	0.1488
IMC-100	U	ppm	0.011	0.99	1.015	1.125	1.05	1.081	0.707
IMC-100	V	ppm	0.8	42.5	44.2	40.5	21	42.2	37.5
IMC-100	W	ppm	0.05	0.28	0.11	0.36	0.12	0.09	0.13
IMC-100	Y	ppm	0.05	10.98	12.25	10.12	7.02	11.59	10.48
IMC-100	Yb	ppm	0.009	1.004	1.114	0.923	0.713	1.086	0.993
IMC-100	Zn	ppm	1.8	37.3	51.7	51.2	30.8	56.4	47.4
IMC-100	Zr	ppm	6	137	134	128	89	135	127
Method		Units	Detect Limit	17KAM077A	17KAM078A	17KAM078B	17KAM078C	17KAM080A	17KAM081A
SG				0.24	0.836	<0.023	0.14	0.471	<0.023
SG DWT		g		0.003	0.003	0.006	0.003	0.003	0.013
SG WWT		g							
IRC-100	CO_2	wt%	0.023	0.24	0.836	<0.023	0.14	0.471	<0.023
IRC-101	S	wt%	0.003	0.003	0.003	0.006	0.003	0.003	0.013
IMP-101	Au	ppb	0.6	0.7	1.6	0.8	1.8	2.6	2.3
IMP-101	Pd	ppb	0.14	<0.14	<0.14	<0.14	<0.14	<0.14	<0.14
IMP-101	Pt	ppb	0.06	0.18	0.08	<0.06	0.13	0.22	0.15
XRF-M01	Al_2O_3	wt%	0.02	15.6	15.67		12.34	15.72	15.78
XRF-M01	BaO	wt%	0.004	0.108	0.066		0.017	0.106	0.175
XRF-M01	CaO	wt%	0.006	2.485	1.461		0.48	2.672	2.554
XRF-M01	Cr_2O_3	wt%	0.002	0.013	0.008		0.013	0.01	0.008
XRF-M01	Fe_2O_3	wt%	0.01	2.97	2.3		3.73	2.9	2.83
XRF-M01	K_2O	wt%	0.01	3.14	2.23		0.69	2.75	2.82
XRF-M01	MgO	wt%	0.01	1.69	1.44		8.74	1.63	1.6
XRF-M01	MnO	wt%	0.002	0.055	0.036		0.032	0.049	0.05
XRF-M01	Na_2O	wt%	0.02	4.81	5.78		3.01	4.89	4.89
XRF-M01	Nitrogen 105	wt%		0.23	0.26		0.51	0.24	0.26
XRF-M01	P_2O_5	wt%	0.002	0.163	0.113		0.1	0.157	0.15
XRF-M01	SiO_2	wt%	0.04	68.74	69.83		66.44	68.03	68.21
XRF-M01	TiO_2	wt%	0.01	0.33	0.26		0.23	0.33	0.31
XRF-M01	Total	wt%		101.36	101.38		100.48	100.74	100.45

Method		Units	Detect Limit	17KAM077A	17KAM078A	17KAM078B	17KAM078C	17KAM080A	17KAM081A
XRF-M01	Total LOI 1000	wt%		1.27	2.2		4.65	1.5	1.08
XRF-T02	As	ppm	6	<6	<6	<6	<6	<6	<6
XRF-T02	Br	ppm	1.2	<1.2	<1.2	<1.2	<1.2	2.2	2.1
XRF-T02	Cu	ppm	9	<9	<9	<9	<9	<9	19
XRF-T02	Ga	ppm	1.3	20.1	19.3	19.8	21.5	19	17.2
XRF-T02	Mo	ppm	0.8	2	2.1	1.8	2.1	1	3.4
XRF-T02	Nb	ppm	0.7	3.2	4.5	4.4	3.9	4	1.4
XRF-T02	Ni	ppm	1.6	16.2	33.9	17.1	11.9	12.1	5.8
XRF-T02	Pb	ppm	1.7	10.8	12.7	11.8	8.4	40.7	83.9
XRF-T02	Rb	ppm	0.8	52.2	53.3	67	83.5	82.4	71.3
XRF-T02	Sr	ppm	0.8	808	898.5	815.7	207.4	456.5	415.1
XRF-T02	Th	ppm	1.5	2.6	6	3.2	3.2	3.4	4.9
XRF-T02	U	ppm	1.6	<1.6	<1.6	<1.6	<1.6	14.8	<1.6
XRF-T02	Y	ppm	0.7	11.3	12.1	11.5	10	12.1	3.6
XRF-T02	Zn	ppm	1	46	58	60	42	21	36
XRF-T02	Zr	ppm	1.8	123.1	147.7	133.7	122.7	129.8	89.4
IMC-100	Ba	ppm	0.8	893.4	1019.3	909.8	214.4	441.9	652.8
IMC-100	Be	ppm	0.04	1.33	1.57	1.42	1.3	1.48	1.07
IMC-100	Bi	ppm	0.47	<0.47	<0.47	<0.47	<0.47	<0.47	<0.47
IMC-100	Cd	ppm	0.013	0.059	0.066	0.05	<0.013	0.29	0.096
IMC-100	Ce	ppm	0.12	52.46	74.07	61.45	22.83	26.94	19.42
IMC-100	Co	ppm	0.13	5.86	9.84	6.84	5.96	10.59	2.86
IMC-100	Cr	ppm	3	65	91	59	76	43	69
IMC-100	Cs	ppm	0.013	0.607	0.596	1.025	5.822	0.522	2.332
IMC-100	Cu	ppm	1.4	2	5.1	<1.4	3.9	5.4	21
IMC-100	Dy	ppm	0.009	1.943	2.25	2.13	1.326	2.031	0.577
IMC-100	Er	ppm	0.007	1.058	1.114	1.143	0.735	1.284	0.322
IMC-100	Eu	ppm	0.0031	1.0753	1.4183	1.1788	0.577	0.7338	0.4313
IMC-100	Ga	ppm	0.04	20.44	19.49	19.99	21.64	18.57	17.3
IMC-100	Gd	ppm	0.009	2.885	3.639	3.282	1.677	2.097	0.876
IMC-100	Hf	ppm	0.14	3.34	4.24	3.49	3.38	3.71	2.69
IMC-100	Ho	ppm	0.0025	0.3772	0.4055	0.4036	0.2516	0.4147	0.1119
IMC-100	In	ppm	0.0018	0.0238	0.0288	0.0229	0.0221	0.0214	0.0065
IMC-100	La	ppm	0.1	24.2	34.3	26.8	7.6	13.2	9
IMC-100	Li	ppm	0.4	15.8	16.4	22.8	26.5	6.3	8.2
IMC-100	Lu	ppm	0.002	0.154	0.162	0.162	0.125	0.229	0.055
IMC-100	Mo	ppm	0.08	2.48	2.38	2.15	3.26	1.22	4.78
IMC-100	Nb	ppm	0.028	4.107	5.149	5.045	4.498	4.495	2.311
IMC-100	Nd	ppm	0.06	24.58	33.54	28.48	10.84	12.49	7.35
IMC-100	Ni	ppm	0.7	16.5	32.8	17.1	12.3	15.4	4.9

Method		Units	Detect Limit	17KAM077A	17KAM078 A	17KAM078 B	17KAM078 C	17KAM080 A	17KAM081 A
IMC-100	Pb	ppm	0.18	10.49	12.22	11.51	9.41	42.9	79.96
IMC-100	Pr	ppm	0.014	6.233	8.481	7.361	2.607	3.152	1.93
IMC-100	Rb	ppm	0.11	52.43	49.66	64.3	29.16	82.05	72.72
IMC-100	Sb	ppm	0.04	0.08	0.06	<0.04	0.2	0.21	0.24
IMC-100	Sc	ppm	1.1	4.1	6.2	4.6	1.8	4.1	2.2
IMC-100	Sm	ppm	0.026	4.055	5.449	4.733	2.174	2.406	1.223
IMC-100	Sn	ppm	0.16	0.82	0.97	0.82	0.89	0.54	0.45
IMC-100	Sr	ppm	0.6	814.4	899.5	819	166.5	457.3	418
IMC-100	Ta	ppm	0.007	0.31	0.393	0.336	0.341	0.333	0.213
IMC-100	Tb	ppm	0.0023	0.3666	0.4422	0.4008	0.2205	0.3296	0.111
IMC-100	Th	ppm	0.018	3.995	6.988	4.282	3.956	4.063	6.47
IMC-100	Ti	ppm	7	1529	2063	1756	1624	1765	876
IMC-100	Tl	ppm	0.002	0.22	0.246	0.275	0.294	0.461	0.342
IMC-100	Tm	ppm	0.0019	0.1533	0.1594	0.1643	0.1152	0.1977	0.0492
IMC-100	U	ppm	0.011	0.932	1.143	1.064	1.774	14.759	1.4
IMC-100	V	ppm	0.8	33.7	53.9	41.6	25.1	17	16.2
IMC-100	W	ppm	0.05	0.07	0.14	0.07	0.81	29.53	0.8
IMC-100	Y	ppm	0.05	10.73	11.41	11.34	6.61	11.29	3.24
IMC-100	Yb	ppm	0.009	1.03	1.056	1.094	0.816	1.453	0.345
IMC-100	Zn	ppm	1.8	43.6	53.4	56.3	43.5	20.8	38.6
IMC-100	Zr	ppm	6	121	156	129	117	137	91
Method		Units	Detect Limit	17KAM082A	17KAM082 A SP	17KAM082 B	17KAM083 A	17KAM084 A	17KAM084 B
SG				0.129	0.135	0.028	1.215	0.454	0.114
SG DWT		g		0.069	0.074	0.223	0.026	0.007	0.21
SG WWT		g							
IRC-100	CO_2	wt%	0.023	0.129	0.135	0.028	1.215	0.454	0.114
IRC-101	S	wt%	0.003	0.069	0.074	0.223	0.026	0.007	0.21
IMP-101	Au	ppb	0.6	2.8	3.2	185.8	3.6	2.5	2.8
IMP-101	Pd	ppb	0.14	<0.14	<0.14	<0.14	<0.14	0.88	0.31
IMP-101	Pt	ppb	0.06	<0.06	<0.06	0.09	0.06	0.85	0.39
XRF-M01	Al_2O_3	wt%	0.02	15.36	15.11		15.83	15.59	16.82
XRF-M01	BaO	wt%	0.004	0.07	0.073		0.077	0.032	0.086
XRF-M01	CaO	wt%	0.006	0.847	0.833		1.655	4.192	6.46
XRF-M01	Cr_2O_3	wt%	0.002	0.009	0.009		0.007	0.033	0.012
XRF-M01	Fe_2O_3	wt%	0.01	1.32	1.34		2.14	5.71	13.76
XRF-M01	K_2O	wt%	0.01	2.97	2.98		2.01	1.36	1.77
XRF-M01	MgO	wt%	0.01	0.54	0.56		0.93	4.22	4.78
XRF-M01	MnO	wt%	0.002	0.022	0.02		0.031	0.113	0.242
XRF-M01	Na_2O	wt%	0.02	5.02	5.01		5.92	6.05	4.16
XRF-M01	Nitrogen 105	wt%		0.35	0.34		0.28	0.86	0.57
XRF-M01	P_2O_5	wt%	0.002	0.049	0.051		0.098	0.278	0.499

Method		Units	Detect Limit	17KAM082A	17KAM082A SP	17KAM082B	17KAM083A	17KAM084A	17KAM084B
XRF-M01	SiO_2	wt%	0.04	73.15	73.17		69.33	59.69	47.81
XRF-M01	TiO_2	wt%	0.01	0.15	0.15		0.26	0.57	1.64
XRF-M01	Total	wt%		100.84	100.55		100.41	100.14	100.56
XRF-M01	Total LOI 1000	wt%		1.33	1.24		2.12	2.32	2.53
XRF-T02	As	ppm	6	<6	<6	<6	<6	<6	<6
XRF-T02	Br	ppm	1.2	<1.2	1.4	2	<1.2	2.1	3.5
XRF-T02	Cu	ppm	9	<9	<9	<9	<9	<9	21
XRF-T02	Ga	ppm	1.3	19.8	19	19.7	20.2	19.2	7.7
XRF-T02	Mo	ppm	0.8	1.8	2	1.8	1.3	2	3.1
XRF-T02	Nb	ppm	0.7	4.2	3.7	4.3	3.7	3.7	1.2
XRF-T02	Ni	ppm	1.6	24.9	24.3	18.7	14.6	18.9	9.2
XRF-T02	Pb	ppm	1.7	12.3	10.8	10.8	12.2	11.2	12.4
XRF-T02	Rb	ppm	0.8	71.2	66.7	88.9	51.8	84.1	47.6
XRF-T02	Sr	ppm	0.8	765.1	845.8	550.4	589.7	620.6	65.6
XRF-T02	Th	ppm	1.5	4.9	4.1	7	4.2	5.7	<1.5
XRF-T02	U	ppm	1.6	<1.6	<1.6	1.8	<1.6	<1.6	<1.6
XRF-T02	Y	ppm	0.7	11.8	11.2	9.4	9.7	10	4.7
XRF-T02	Zn	ppm	1	50	49	40	41	44	26
XRF-T02	Zr	ppm	1.8	138.5	132.9	107.5	121.1	116.3	46.4
IMC-100	Ba	ppm	0.8	980.4	1623.1	622.6	702.1	783.5	212.9
IMC-100	Be	ppm	0.04	1.71	1.46	1.82	1.58	1.55	0.64
IMC-100	Bi	ppm	0.47	<0.47	<0.47	<0.47	<0.47	<0.47	<0.47
IMC-100	Cd	ppm	0.013	0.048	0.047	0.024	0.045	0.045	0.046
IMC-100	Ce	ppm	0.12	66.71	65.22	56.06	42.71	55.44	10.96
IMC-100	Co	ppm	0.13	8.21	8.01	5.84	4.92	6.18	3.71
IMC-100	Cr	ppm	3	73	64	65	50	79	106
IMC-100	Cs	ppm	0.013	1.425	1.363	2.529	4.569	1.316	1.377
IMC-100	Cu	ppm	1.4	4.3	4.3	6.5	2.4	2.8	23.8
IMC-100	Dy	ppm	0.009	2.105	2.073	1.706	1.577	1.751	0.645
IMC-100	Er	ppm	0.007	1.048	1.089	0.923	0.865	0.893	0.413
IMC-100	Eu	ppm	0.0031	1.3	1.2751	1.0813	0.8541	1.0449	0.2389
IMC-100	Ga	ppm	0.04	19.98	19.57	20.27	20.41	19.61	7.83
IMC-100	Gd	ppm	0.009	3.384	3.248	2.736	2.333	2.789	0.79
IMC-100	Hf	ppm	0.14	3.88	3.77	3.3	3.45	3.28	1.23
IMC-100	Ho	ppm	0.0025	0.3937	0.3775	0.3232	0.3202	0.3338	0.1392
IMC-100	In	ppm	0.0018	0.0251	0.0215	0.0196	0.021	0.0199	0.0088
IMC-100	La	ppm	0.1	32	31.6	27.8	20.7	27.1	4.5
IMC-100	Li	ppm	0.4	13.8	14.5	20.8	14.8	12.5	43.2
IMC-100	Lu	ppm	0.002	0.158	0.154	0.145	0.138	0.146	0.072
IMC-100	Mo	ppm	0.08	2.39	1.91	2.49	1.79	2.99	5.48

Method		Units	Detect Limit	17KAM082A	17KAM082A SP	17KAM082B	17KAM083A	17KAM084A	17KAM084B
IMC-100	Nb	ppm	0.028	5.016	4.435	4.792	4.347	4.548	1.64
IMC-100	Nd	ppm	0.06	30.27	29.54	24.11	18.64	23.56	5.31
IMC-100	Ni	ppm	0.7	25.3	24.7	18.8	14.1	19.9	9
IMC-100	Pb	ppm	0.18	11.75	10.63	11.07	12.48	11.36	13.12
IMC-100	Pr	ppm	0.014	7.92	7.671	6.248	4.913	6.354	1.291
IMC-100	Rb	ppm	0.11	71.15	65.37	88.92	51.55	85.12	49.2
IMC-100	Sb	ppm	0.04	0.11	0.06	0.14	0.06	0.06	0.27
IMC-100	Sc	ppm	1.1	5.5	5.4	4.3	3.8	4.3	2.1
IMC-100	Sm	ppm	0.026	4.922	4.821	3.908	3.107	4.042	1.026
IMC-100	Sn	ppm	0.16	1.09	0.79	0.75	0.79	0.73	0.33
IMC-100	Sr	ppm	0.6	768.9	856.5	555	591.7	629.8	66.4
IMC-100	Ta	ppm	0.007	0.375	0.331	0.395	0.313	0.349	0.111
IMC-100	Tb	ppm	0.0023	0.4104	0.3934	0.334	0.3053	0.3348	0.1089
IMC-100	Th	ppm	0.018	6.062	5.679	8.681	5.758	7.312	1.648
IMC-100	Ti	ppm	7	1919	1841	1467	1488	1540	568
IMC-100	Tl	ppm	0.002	0.34	0.315	0.414	0.224	0.377	0.183
IMC-100	Tm	ppm	0.0019	0.1557	0.1511	0.1338	0.1322	0.1346	0.0644
IMC-100	U	ppm	0.011	1.159	1.203	2.546	1.075	1.309	0.501
IMC-100	V	ppm	0.8	45.9	44	32.6	32.9	35.6	20.5
IMC-100	W	ppm	0.05	0.32	0.13	3.26	2.4	0.67	0.83
IMC-100	Y	ppm	0.05	11.43	11.07	9.48	9.17	9.62	3.95
IMC-100	Yb	ppm	0.009	1.046	1.021	0.917	0.882	0.913	0.423
IMC-100	Zn	ppm	1.8	48.5	47.8	38.1	38.7	41.8	25.2
IMC-100	Zr	ppm	6	144	146	111	122	115	46
Method		Units	Detect Limit	17KAM085A	17KAM085B	17KAM088A	17KAM089A	17KAM091A	17KAM092A
SG				0.123	0.246	0.292	0.883	<0.023	<0.023
SG DWT		g		<0.003	0.004	0.003	<0.003	0.004	0.003
SG WWT		g							
IRC-100	CO2	wt%	0.023	0.123	0.246	0.292	0.883	<0.023	<0.023
IRC-101	S	wt%	0.003	<0.003	0.004	0.003	<0.003	0.004	0.003
IMP-101	Au	ppb	0.6	2.7	4.1	2.5	2	2.1	2.5
IMP-101	Pd	ppb	0.14	<0.14	<0.14	<0.14	<0.14	<0.14	<0.14
IMP-101	Pt	ppb	0.06	0.07	0.06	0.24	0.13	0.19	0.25
XRF-M01	Al_2O_3	wt%	0.02	15.49	5.43	15.53	16.09	15.73	15.33
XRF-M01	BaO	wt%	0.004	0.079	0.022	0.085	0.064	0.099	0.098
XRF-M01	CaO	wt%	0.006	0.863	0.278	2.208	2.066	2.809	2.675
XRF-M01	Cr_2O_3	wt%	0.002	0.01	0.016	0.011	0.01	0.011	0.01
XRF-M01	Fe_2O_3	wt%	0.01	2.24	1.5	2.34	2.5	2.91	3.16
XRF-M01	K_2O	wt%	0.01	3.19	1.53	3.08	2.96	2.8	3.15
XRF-M01	MgO	wt%	0.01	1.09	0.69	1.25	1.24	1.67	1.91
XRF-M01	MnO	wt%	0.002	0.036	0.026	0.043	0.032	0.052	0.058

Method		Units	Detect Limit	17KAM085A	17KAM085B	17KAM088A	17KAM089A	17KAM091A	17KAM092A
XRF-M01	Na_2O	wt%	0.02	5.31	1.09	4.98	5.12	4.89	4.73
XRF-M01	Nitrogen 105	wt%		0.61	0.56	0.28	0.35	0.27	0.36
XRF-M01	P_2O_5	wt%	0.002	0.121	0.042	0.118	0.107	0.156	0.171
XRF-M01	SiO_2	wt%	0.04	70.48	87.82	69.85	68.29	68.66	67.63
XRF-M01	TiO_2	wt%	0.01	0.26	0.1	0.27	0.25	0.31	0.34
XRF-M01	Total	wt%		100.9	100.18	101.07	100.91	100.99	100.52
XRF-M01	Total LOI 1000	wt%		1.74	1.62	1.32	2.19	0.88	1.27
XRF-T02	As	ppm	6	<6	<6	<6	<6	<6	<6
XRF-T02	Br	ppm	1.2	2.7	1.7	1.7	1.2	<1.2	<1.2
XRF-T02	Cu	ppm	9	<9	57	138	28	26	13
XRF-T02	Ga	ppm	1.3	18.7	21.8	24.8	18.8	20.7	17.3
XRF-T02	Mo	ppm	0.8	2.1	1.1	1.6	3.6	1.8	2.4
XRF-T02	Nb	ppm	0.7	3.6	3.4	5.8	4.5	7.5	4.2
XRF-T02	Ni	ppm	1.6	15.6	67.9	59.9	30	65.7	23
XRF-T02	Pb	ppm	1.7	6.7	3.7	7.7	9	11.5	4
XRF-T02	Rb	ppm	0.8	68.6	37.7	65	85.5	67.4	113.8
XRF-T02	Sr	ppm	0.8	386.6	588.3	1034.2	835.8	1210	492.2
XRF-T02	Th	ppm	1.5	3.6	3.3	1.5	9.4	6.7	5.2
XRF-T02	U	ppm	1.6	<1.6	<1.6	<1.6	<1.6	<1.6	<1.6
XRF-T02	Y	ppm	0.7	9.9	18.2	30.1	12.2	18.9	12.1
XRF-T02	Zn	ppm	1	40	81	127	46	108	30
XRF-T02	Zr	ppm	1.8	120.6	193	270.3	139.4	222.6	124.4
IMC-100	Ba	ppm	0.8	742.5	276.9	817.1	912.1	1059	1061.6
IMC-100	Be	ppm	0.04	1.16	1.28	1.13	1.74	2.16	1.44
IMC-100	Bi	ppm	0.47	<0.47	<0.47	<0.47	<0.47	<0.47	<0.47
IMC-100	Cd	ppm	0.013	0.04	0.106	0.101	0.034	0.124	0.038
IMC-100	Ce	ppm	0.12	48.13	81.91	68.84	79.88	174.96	66.58
IMC-100	Co	ppm	0.13	5.26	18.78	32.97	9.66	22.81	6.98
IMC-100	Cr	ppm	3	71	368	83	83	117	70
IMC-100	Cs	ppm	0.013	1.573	0.395	2.113	2.662	1.313	0.869
IMC-100	Cu	ppm	1.4	2.2	63.1	129.6	28	24.5	14.5
IMC-100	Dy	ppm	0.009	1.746	3.53	5.815	2.294	4.049	2.124
IMC-100	Er	ppm	0.007	0.972	1.692	3.129	1.115	1.679	1.098
IMC-100	Eu	ppm	0.0031	0.9247	2.0444	2.5861	1.4416	3.013	1.2457
IMC-100	Ga	ppm	0.04	18.84	20.65	23.82	19.3	20.93	17.65
IMC-100	Gd	ppm	0.009	2.576	5.643	7.444	3.828	7.975	3.354
IMC-100	Hf	ppm	0.14	3.58	4.74	6.09	3.66	4.98	3.73
IMC-100	Ho	ppm	0.0025	0.3368	0.6396	1.1248	0.4196	0.6753	0.4055
IMC-100	In	ppm	0.0018	0.0223	0.0487	0.0824	0.0237	0.0467	0.0197

Method		Units	Detect Limit	17KAM085A	17KAM085B	17KAM088A	17KAM089A	17KAM091A	17KAM092A
IMC-100	La	ppm	0.1	21.3	34.9	26.6	39.9	87	33.4
IMC-100	Li	ppm	0.4	8.1	14.8	25.5	7.4	15.1	9
IMC-100	Lu	ppm	0.002	0.154	0.231	0.425	0.165	0.193	0.163
IMC-100	Mo	ppm	0.08	2.97	1.94	1.3	3.87	0.93	3.04
IMC-100	Nb	ppm	0.028	4.422	4.226	7.008	5.424	8.309	4.871
IMC-100	Nd	ppm	0.06	20.87	41.86	42.27	35.19	77.51	29.27
IMC-100	Ni	ppm	0.7	15.3	70.8	56.9	31.4	65.2	22.7
IMC-100	Pb	ppm	0.18	7.7	3.48	7.29	8.97	10.14	4.49
IMC-100	Pr	ppm	0.014	5.462	9.98	9.649	9.425	20.337	7.732
IMC-100	Rb	ppm	0.11	69.38	36.69	61.34	87.41	67.85	114.89
IMC-100	Sb	ppm	0.04	0.14	0.04	<0.04	0.06	0.24	0.05
IMC-100	Sc	ppm	1.1	3.8	12.4	22.4	6.1	13	5
IMC-100	Sm	ppm	0.026	3.54	7.792	8.649	5.698	12.407	4.821
IMC-100	Sn	ppm	0.16	0.72	1.12	1.03	0.89	1.26	1.03
IMC-100	Sr	ppm	0.6	386.1	587.5	1011.8	841.2	1228.9	489.4
IMC-100	Ta	ppm	0.007	0.333	0.149	0.4	0.396	0.471	0.44
IMC-100	Tb	ppm	0.0023	0.3244	0.6941	1.0419	0.4629	0.8882	0.4089
IMC-100	Th	ppm	0.018	5.552	4.024	1.892	10.232	8.025	6.725
IMC-100	Ti	ppm	7	1494	3284	9468	2040	4840	1657
IMC-100	Tl	ppm	0.002	0.262	0.274	0.332	0.44	0.449	0.468
IMC-100	Tm	ppm	0.0019	0.1529	0.2447	0.4401	0.1572	0.2177	0.1604
IMC-100	U	ppm	0.011	1.566	0.74	0.636	1.802	1.828	1.673
IMC-100	V	ppm	0.8	32.3	97.2	199.9	51.9	109.4	37.7
IMC-100	W	ppm	0.05	0.96	1.17	0.76	0.47	1.42	3.8
IMC-100	Y	ppm	0.05	9.85	17.9	29.52	12.11	18.86	11.87
IMC-100	Yb	ppm	0.009	0.974	1.555	2.793	1.073	1.338	1.092
IMC-100	Zn	ppm	1.8	38.7	74.7	117.7	45.2	98.2	29.4
IMC-100	Zr	ppm	6	126	196	262	137	208	136
Method		Units	Detect Limit	17KAM092B	17KAM093A	17KAM095A	17KAM200A	17KAM202A	
SG				0.301	<0.023	0.613	0.183	4.932	
SG DWT		g		0.011	<0.003	<0.003	0.004	0.842	
SG WWT		g							
IRC-100	CO2	wt%	0.023	0.301	<0.023	0.613	0.183	4.932	
IRC-101	S	wt%	0.003	0.011	<0.003	<0.003	0.004	0.842	
IMP-101	Au	ppb	0.6	1.9	3.2	2.7	2.4	75.4	
IMP-101	Pd	ppb	0.14	<0.14	<0.14	<0.14	<0.14	<0.14	
IMP-101	Pt	ppb	0.06	<0.06	0.13	0.37	<0.06	0.19	
XRF-M01	Al_2O_3	wt%	0.02	15.25	15.22	19.76	15.81	17.52	
XRF-M01	BaO	wt%	0.004	0.113	0.115	0.004	0.047	0.051	
XRF-M01	CaO	wt%	0.006	4.477	1.742	1.067	0.62	6.173	
XRF-M01	Cr_2O_3	wt%	0.002	0.017	0.009	0.008	0.011	0.007	

Method		Units	Detect Limit	17KAM092B	17KAM093A	17KAM095A	17KAM200A	17KAM202A	
XRF-M01	Fe_2O_3	wt%	0.01	6.74	2.52	3.07	1.99	2.03	
XRF-M01	K_2O	wt%	0.01	2.44	3.88	0.16	2.64	2.81	
XRF-M01	MgO	wt%	0.01	4.32	1.2	2.44	1.39	0.69	
XRF-M01	MnO	wt%	0.002	0.099	0.042	0.06	0.014	0.07	
XRF-M01	Na_2O	wt%	0.02	4.9	5.26	9.67	0.11	7.6	
XRF-M01	Nitrogen 105	wt%		0.68	0.64	0.38	1.43	0.21	
XRF-M01	P_2O_5	wt%	0.002	0.664	0.142	0.2	0.12	0.181	
XRF-M01	SiO_2	wt%	0.04	58.29	68.71	61.68	71.1	57.33	
XRF-M01	TiO_2	wt%	0.01	0.81	0.28	0.43	0.28	0.3	
XRF-M01	Total	wt%		100.41	100.49	100.98	100.33	99.16	
XRF-M01	Total LOI 1000	wt%		2.29	1.37	2.42	6.2	4.41	
XRF-T02	As	ppm	6	<6	<6	<6	<6	7	
XRF-T02	Br	ppm	1.2	<1.2	6.2	<1.2	<1.2	<1.2	
XRF-T02	Cu	ppm	9	15	<9	<9	18	1921	
XRF-T02	Ga	ppm	1.3	19.4	19.8	20.3	16.9	4.6	
XRF-T02	Mo	ppm	0.8	4.4	<0.8	1	3.8	77.8	
XRF-T02	Nb	ppm	0.7	3.9	5.7	4.1	1.6	<0.7	
XRF-T02	Ni	ppm	1.6	26.1	31.7	16.3	5.4	3.7	
XRF-T02	Pb	ppm	1.7	11.6	<1.7	14	85.6	237	
XRF-T02	Rb	ppm	0.8	90.4	6.1	66.3	72.2	27.1	
XRF-T02	Sr	ppm	0.8	799.8	267.6	847.9	415.1	26.2	
XRF-T02	Th	ppm	1.5	6.7	8.4	3.5	5.1	<1.5	
XRF-T02	U	ppm	1.6	<1.6	<1.6	<1.6	<1.6	<1.6	
XRF-T02	Y	ppm	0.7	11.9	15	11.7	3.9	1.4	
XRF-T02	Zn	ppm	1	46	63	52	37	106	
XRF-T02	Zr	ppm	1.8	129.2	172	126.5	89	23.6	
IMC-100	Ba	ppm	0.8	930.3	29.4	859.1	672.7	99.5	
IMC-100	Be	ppm	0.04	1.6	1.03	1.62	1.03	0.28	
IMC-100	Bi	ppm	0.47	<0.47	<0.47	<0.47	<0.47	>47	
IMC-100	Cd	ppm	0.013	0.036	0.041	0.049	0.106	0.55	
IMC-100	Ce	ppm	0.12	68.95	77.07	55.48	18.93	2.59	
IMC-100	Co	ppm	0.13	8.36	9.25	6.66	2.92	1.73	
IMC-100	Cr	ppm	3	87	92	49	65	146	
IMC-100	Cs	ppm	0.013	3.356	0.198	2.021	2.467	0.784	
IMC-100	Cu	ppm	1.4	16.1	2.9	4.1	22.5	2041.1	
IMC-100	Dy	ppm	0.009	2.181	2.603	2.041	0.607	0.112	
IMC-100	Er	ppm	0.007	1.119	1.43	1.1	0.355	0.065	
IMC-100	Eu	ppm	0.0031	1.2621	1.5134	1.1634	0.4254	0.0595	
IMC-100	Ga	ppm	0.04	19.88	19.83	20.3	17.29	4.79	

Method		Units	Detect Limit	17KAM092B	17KAM093A	17KAM095A	17KAM200A	17KAM202A	
IMC-100	Gd	ppm	0.009	3.424	4.43	3.228	0.904	0.151	
IMC-100	Hf	ppm	0.14	3.6	4.97	3.7	2.6	0.75	
IMC-100	Ho	ppm	0.0025	0.4068	0.5106	0.3889	0.1142	0.0254	
IMC-100	In	ppm	0.0018	0.0237	0.0262	0.0216	0.007	0.0422	
IMC-100	La	ppm	0.1	34	42.2	24.6	8.8	1.1	
IMC-100	Li	ppm	0.4	10.4	27.4	19.1	8.2	3.1	
IMC-100	Lu	ppm	0.002	0.167	0.221	0.157	0.055	0.011	
IMC-100	Mo	ppm	0.08	5.04	0.71	1.57	4.67	>44	
IMC-100	Nb	ppm	0.028	5.076	6.433	5.066	2.4	0.732	
IMC-100	Nd	ppm	0.06	29.75	38.87	26.55	7.2	1.04	
IMC-100	Ni	ppm	0.7	26.5	32.9	16.8	5	2.8	
IMC-100	Pb	ppm	0.18	11.16	1.11	13.24	84.39	236.79	
IMC-100	Pr	ppm	0.014	7.925	10.005	6.733	1.964	0.269	
IMC-100	Rb	ppm	0.11	92.88	5.91	67.85	74.39	26.23	
IMC-100	Sb	ppm	0.04	0.04	0.06	0.08	0.25	0.26	
IMC-100	Sc	ppm	1.1	5.4	6.9	4.7	2.2	<1.1	
IMC-100	Sm	ppm	0.026	5.062	6.356	4.527	1.259	0.182	
IMC-100	Sn	ppm	0.16	0.86	1.2	0.8	0.46	0.22	
IMC-100	Sr	ppm	0.6	806.3	270.1	853.7	420.6	25.5	
IMC-100	Ta	ppm	0.007	0.434	0.475	0.336	0.221	0.066	
IMC-100	Tb	ppm	0.0023	0.4196	0.5233	0.3983	0.1141	0.0206	
IMC-100	Th	ppm	0.018	8.799	10.362	5.1	6.865	0.585	
IMC-100	Ti	ppm	7	1843	2439	1732	895	212	
IMC-100	Tl	ppm	0.002	0.47	0.022	0.336	0.334	0.152	
IMC-100	Tm	ppm	0.0019	0.1616	0.2109	0.1597	0.0506	0.0104	
IMC-100	U	ppm	0.011	1.603	1.505	0.849	1.288	0.269	
IMC-100	V	ppm	0.8	45.2	45.2	40.7	16.5	4.9	
IMC-100	W	ppm	0.05	0.78	1.69	0.07	0.85	1.65	
IMC-100	Y	ppm	0.05	11.7	14.86	11.44	3.32	0.79	
IMC-100	Yb	ppm	0.009	1.066	1.38	1.068	0.345	0.072	
IMC-100	Zn	ppm	1.8	44.7	60.5	46	35.8	109.2	
IMC-100	Zr	ppm	6	136	183	137	90	25	

Appendix F: Neodymium Isotope Data

Sample	Nd (ppm)	Sm (ppm)	Age (Ma)	Nd^{143}/Nd^{144}	Sm^{147}/Nd^{144}	Nd^{143}/Nd^{144} (intial)	ε_{Ndt}	Model Age (TDMR)
17KAM024A	21.32	3.54	2689	0.511043	0.1004	0.50926	2.239	2820
17KAM007A	20.41	3.36	2689	0.51103	0.0996	0.50926	2.282	2817
17KAM038A	26.68	4.34	2689	0.51102	0.0983	0.50928	2.498	2799
16KAA020A	37.97	6.42	2689	0.511074	0.1023	0.50926	2.207	2826
17KAM074A	31.01	5.23	2689	0.511067	0.1019	0.50926	2.16	2825
17KAM025A	25.54	4.26	2689	0.511056	0.1008	0.50927	2.335	2812
17KAM039B	26.52	4.41	2690	0.511053	0.1005	0.50927	2.396	2809